# Hydrophilic $(AB)_n$-segmented copolymers for melt electrowriting as biomaterial inks

DISSERTATION

zur Erlangung des akademischen Grades eines

Doktors der Naturwissenschaften (Dr. rer. nat.)

im Promotionsprogramm „Polymer Science“

in der Bayreuther Graduiertenschule für Mathematik und Naturwissenschaften (BayNAT)

der Universität Bayreuth

vorgelegt von

**Jannik Mechau**

geboren in Bremen, Deutschland

Bayreuth, 2023

Die vorliegende Arbeit wurde in der Zeit von Juni 2015 bis Juli 2023 in Bayreuth am Lehrstuhl Makromolekulare Chemie I unter Betreuung von Herrn Prof. Dr. Hans-Werner Schmidt angefertigt. Der experimentelle Teil wurde in der Zeit von Juni 2015 bis Juli 2019 durchgeführt.

Vollständiger Abdruck der von der Bayreuther Graduiertenschule für Mathematik und Naturwissenschaften (BayNAT) der Universität Bayreuth genehmigten Dissertation zur Erlangung des akademischen Grades eines Doktors der Naturwissenschaften (Dr. rer. nat.).

Form der Dissertation: Monographie

Dissertation eingereicht am: 07.07.2023

Zulassung durch das Leitungsgremium: 18.07.2023

Wissenschaftliches Kolloquium: 07.12.2023

Amtierender Direktor: Prof. Dr. Jürgen Köhler

Prüfungsausschuss:

Prof. Dr. Hans-Werner Schmidt (Gutachter)

Prof. Dr. Seema Agarwal (Gutachterin)

Prof. Dr. Markus Retsch (Vorsitz)

Prof. Dr. Leonid Ionov

Die vorliegende Arbeit ist als Monographie verfasst.

Teile der Arbeit sind bereits in der folgenden Publikation erschienen:

*Hydrophilic $(AB)_n$ Segmented Copolymers for Melt Extrusion-Based Additive Manufacturing*

Mechau, J.; Frank, A.; Bakirci, E.; Gumbel, S.; Jungst, T.; Giesa, R.; Groll, J.; Dalton, P.D.; Schmidt, H.-W., Macromol. Chem. Phys. **2021**, *222* (1), 2000265.

**DOI:** 10.1002/macp.202000265

Diese Publikation ist in der vorliegenden Arbeit mit der Literaturstelle [139] zitiert

# Table of contents

## Abbreviations

| | |
|---|---|
| 3D | Three-dimensional |
| AM | Additive manufacturing |
| $BuNH_2$ | *n*-butylamine |
| CAD | Computer-assisted design |
| $CDCl_3$ | Deuterated chloroform |
| CHDI | *trans-1,4*-cyclohexane diisocyanate |
| CTS | Critical translation speed |
| DMF | Dimethyl form amide |
| DMTA | Dynamic mechanical thermal analysis |
| DNA | Deoxyribonucleic acid |
| DSC | Differential scanning calorimetry |
| EBP | Extrusion based printing |
| eSEM | Environmental scanning electron microscopy |
| FDM | Fused deposition modeling |
| FT-IR | Fourier transformation infrared spectroscopy |
| HM | Hexamethylene |
| HMDI | Hexamethylene diisocyanate |
| LCST | Lower critical solution temperature |
| LiBr | Lithium bromide |
| MALDI-TOF | Matrix-assistant laser desorption ionization – time of flight |
| m-b-CH | Methylene-bis-cyclohexyl |
| m-b-CHDI | Methylene-bis-cyclohexyl(isocyanate) |
| MES | Melt electrospinning |
| MEW | Melt electrowriting |
| NMR | Nuclear magnetic resonance |
| PBS | Phosphate buffered saline |
| PCL | Poly(ε-caprolactone) |
| PEG | Polyethylene glycol |
| PLA | Polylactid acid |
| PPG | Polypropylene glycol |

| | |
|---|---|
| PPG-PEG-PPG | Polypropylene glycol-*block*-polyethylene glycol-*block*-polypropylene glycol |
| PVDF | Poly(vinylidene fluoride) |
| SEC | Size exclusion chromatography |
| SEM | Scanning electron microscopy |
| TBAB | Tetrabutylammonium bromide |
| THF | Tetrahydrofuran |
| Upy | Ureido pyrimidone |
| UV | Ultraviolet |

# Symbols

| | |
|---|---|
| $c$ | Molarity |
| $\dot{\gamma}$ | Sheer velocity |
| $D_1$ | Experimentally determined fiber diameter from reference |
| $D_2$ | Calculated fiber diameter |
| $Đ$ | Polydispersion index |
| $\delta$ | Chemical shift in NMR |
| $\Delta H_{m,PEG}$ | Melting enthalpy of PEG in the $(AB)_n$-segmented copolymer |
| $\Delta H^0_{m,PEG}$ | Melting enthalpy of 100 % crystalline PEG |
| $\Delta H_{c,PEG}$ | Crystallization enthalpy of PEG in the $(AB)_n$-segmented copolymer |
| $E$ | Young's modulus |
| $E'$ | Elastic (storage) modulus in *Dynamic Mechanical Thermal Analysis* |
| $E''$ | Viscous (loss) modulus in *Dynamic Mechanical Thermal Analysis* |
| $\varepsilon_{br}$ | Elongation at break |
| $G'$ | Elastic (storage) modulus in *Oscillation Shear Rheology* |
| G'' | Viscous (loss) modulus in *Oscillation Shear Rheology* |
| $\eta$ | Steady viscosity |
| $\eta^*$ | Complex viscosity |
| $\eta^*_{100}$ | Complex viscosity at 100 °C |
| $\eta^*_{EBP,max}$ | Complex melt viscosity at maximum temperature of EBP processing window |
| $\eta^*_{EBP,min}$ | Complex melt viscosity at minimum temperature of EBP processing window |
| $\eta^*_{EBP,r}$ | Complex melt viscosity range of EBP processing window |
| $\eta^*_{MEW,max}$ | Complex melt viscosity at maximum temperature of MEW processing window |
| $\eta^*_{MEW,min}$ | Complex melt viscosity at minimum temperature of MEW processing window |
| $\eta^*_{MEW,r}$ | Complex melt viscosity range of MEW processing window |
| $M$ | Molecular weight |
| $M_{Bu}$ | Molecular weight of *n*-butylamine |

| | |
|---|---|
| $M_{DI}$ | Molecular weight of Diisocyanate |
| $M_{JA}$ | Molecular weight of Jefffamine |
| $M_n$ | Number average molecular weight |
| $M_w$ | Mass average molecular weight |
| $m_a$ | Weighted Mass of amine for titration |
| $m_d$ | Mass of dried polymer |
| $m_s$ | Mass of swollen polymer |
| $N_{Bu}$ | Molar ratio of n-butylamine added to the polyaddition reaction mixture |
| $n$ | Number of repeating units, degree of polymerization |
| $\tilde{\nu}$ | Wave numer |
| $P_1$ | Reference nitrogen pressure in MEW |
| $P_2$ | Applied nitrogen pressure in MEW |
| $r$ | Stoichiometric imbalance |
| $\sigma_{yi}$ | Strength at yield |
| $\sigma_{br}$ | Strength at break |
| $T_{c,BU}$ | Temperature for the assembly of the bisurea hydrogen bonds upon cooling |
| $T_{c,PEG}$ | Crystallization temperature of PEG units in the $(AB)_n$-segmented copolymer |
| $T_{cr}$ | Crossover temperature between storage and loss modulus |
| $T_{cr,c}$ | Crossover temperature between storage and loss modulus upon cooling |
| $T_{cr,h}$ | Crossover temperature between storage and loss modulus upon heating |
| $T_{EBP,max}$ | Maximum temperature of EBP processing window |
| $T_{EBP,min}$ | Minimum temperature of EBP processing window |
| $T_{EBP,r}$ | Temperature range of EBP processing window |
| $T_g$ | Glass transition temperature |
| $T_{g,c}$ | Glass transition temperature upon cooling |
| $T_{g,h}$ | Glass transition temperature upon heating |
| $T_{g,PPG-PEG-PPG}$ | Glass transition temperature of PPG-PEG-PPG segments |
| $T_{m,BU}$ | Temperature for the disassembly of the bisurea hydrogen bonds upon cooling |

| | |
|---|---|
| $T_{MEW,max}$ | Maximum temperature of MEW processing window |
| $T_{MEW,min}$ | Minimum temperature of MEW processing window |
| $T_{MEW,r}$ | Temperature range of MEW processing window |
| tan $\delta$ | Loss factor |
| $U_T$ | Toughness |
| $V_1$ | Reference collector velocity |
| $V_2$ | Applied collector velocity |
| $V_{eq}$ | Volume until equivalent point is reached |
| $w$ | Water content of swollen hydrogel |
| $w_{bisurea}$ | Mass ratio of the bisurea segments in the $(AB)_n$-segmented copolymer |
| $w_{hydrophil}$ | Mass ratio of the hydrophilic segments in the $(AB)_n$-segmented copolymer |
| $w_{PEG}$ | Mass ratio of PEG in the $(AB)_n$-segmented copolymer |
| $X_{C,PEG}$ | Degree of crystallinity of PEG in the $(AB)_n$-segmented copolymer |
| $X_n$ | Degree of polymerization |
| $X_{n,th}$ | Theoretical degree of polymerization |
| $z$ | Number of amine end groups in a molecule |
| $\omega$ | Angular velocity |

## Short summary

The motivation for this work arises from the developing field of biofabrication. One approach is to directly print bioinks containing cells to hierarchical three-dimensional (3D) structures to mimic human tissues. Another promising approach is the hybrid printing of cell suspensions in combination with biomaterial inks as supporting polymer constructs to achieve structural patterning and enable localized cell deposition of low viscosity bioinks. Mainly hydrophobic semicrystalline polymers, such as poly(ε-caprolactone) or materials that are chemically crosslinked after printing were previously reported as supporting materials.

In this context this thesis focuses on the *synthesis, characterization,* and *additive manufacturing* of tailored *hydrophilic $(AB)_n$-segmented copolymers* with polyethylene glycol (PEG) and bisurea segments as *biomaterial inks*. The bisurea segments form at room temperature physical crosslinks via hydrogen bonds that disassemble upon heating to form processable polymer melts. The copolymers were tailored to be applied in *melt electrowriting* (MEW) to produce defined 3D constructs with fiber dimensions below 50 µm. Additionally, initial studies with *extrusion based printing* (EBP) as second additive manufacturing technique were performed. The copolymers swell in aqueous and biological media to hydrogels that are stable or disintegrate after a certain time depending on the composition.

In the first part of this thesis the synthesis of a series of $(AB)_n$-segmented copolymers based on hydrophilic propylene glycol-*block*-polyethylene glycol-*block*-polypropylene glycol (PPG-PEG-PPG) segments and bisurea segments is described. The copolymers were prepared by polyaddition of commercially available PPG-PEG-PPG diamines (Jeffamine®) with different molecular weights and aliphatic diisocyanates, namely hexamethylene diisocyanate, *trans*-1,4-cyclohexane diisocyanate and 4,4'-methylene-bis(cyclohexyl) isocyanate, in a laboratory scale above 50 g. This synthesis route is advantaged that no byproducts are formed, and no catalysts are needed. By addition of monofunctional *n*-butylamine the degree of polymerization can be controlled. FT-IR analysis reveals that the strength of the hydrogen bonding depends on the chemical structure of the bisurea segments. The reversible melting and the disassembly of the physical crosslinks depends on the length of the hydrophilic segments, the structure of the bisurea segments and the degree of polymerization, and thus can be adjusted in the temperature range from about 10 up to 180 °C. The physical crosslinks reassemble upon cooling. The melt viscosities at 100 °C can be adjusted in the range from 15 to 8000 Pa s which opens opportunities for different additive manufacturing techniques. Tensile tests showed the highest toughness for the copolymers with hexamethylene bisurea segments.

Depending on the composition the copolymers with hexamethylene bisurea segments swell to hydrogels in aqueous media that disintegrate over time. The disintegration speed increases with rising length of the hydrophilic segments. Copolymers with 4,4'-methylene-bis(cyclohexyl) bisurea segments swell to hydrogels in aqueous media with a water content of at least 70 wt% that do not disintegrate. The biocompatibility of these two classes of $(AB)_n$-segmented copolymers was demonstrated by cytotoxicity tests.

The second part of this thesis focuses on the additive manufacturing of selected $(AB)_n$-segmented copolymers. *Melt electrowriting* (MEW) was used as the focal method. Four suitable copolymers were selected for detailed studies with MEW based on their optimum printing temperatures that are in the range of 75 – 100 °C. Isothermal rheology measurements of these copolymers at 100 and 120 °C demonstrate the long-term stability during MEW-processing by not showing any notable degradation. Depending on the copolymer the adjustment of several instrumental parameters, namely temperature, applied voltage, nitrogen pressure, collector speed, spinneret-collector distance, nozzle diameter and printed surface, results in single fiber diameters in the desired range of 5 – 50 µm. Well-defined 3D constructs with uniform fibers, controlled fiber deposition and fiber diameters of 20 – 65 µm can be realized with all tested copolymers. It was shown for a copolymer with 82 wt% PPG-PEG-PPG segments and 18 wt% hexamethylene-bisurea segments that the scaffolds swell to more than twice the fiber diameter at 100 % humidity by using environmental scanning electron microscopy and remain stable.

Two of the copolymers used for MEW were additionally optimized for *Extrusion based printing* (EBP) by adjusting the optimum processing temperatures to 110 – 120 °C. Well-defined scaffolds with high stacking accuracy and well positioned fibers with diameters of 250 – 450 µm can be realized. The addition of a soft hydrogel to a scaffold of a copolymer with 82 wt% PPG-PEG-PPG segments and 18 wt% hexamethylene-bisurea segments results in strong swelling. Nutrients were proven to diffuse through the scaffolds which enabling the creation of perfusable channels. A scaffold of a copolymer with 75 wt% PPG-PEG-PPG segments and 25 wt% 4,4'-methylene-bis(cyclo-hexyl) bisurea segments was shown to swell in aqueous solution without dissolving.

All in all, the use of hydrophilic $(AB)_n$-segmented copolymers that form physical crosslinks in extrusion-based additive manufacturing techniques expands the biofabrication window.

## Kurzzusammenfassung

Die Motivation für diese Arbeit entsteht aus dem sich entwickelnden Bereich der Biofabrikation. Ein Ansatz besteht darin, zellhaltige Biotinten direkt zu hierarchischen dreidimensionalen (3D) Strukturen zu drucken, um menschliches Gewebe nachzubilden. Ein weiterer vielversprechender Ansatz ist der Hybriddruck von Zellsuspensionen in Kombination mit Biomaterialtinten als unterstützende Polymerkonstrukte, um strukturierte Gerüste zu erreichen und eine lokalisierte Zellablagerung von niedrigviskosen Biotinten zu ermöglichen. Als Stützmaterialien wurden bisher vor allem hydrophobe teilkristalline Polymere wie zum Beispiel Poly(ε-Caprolacton) und Materialien, die nach dem Druck chemisch vernetzt werden, beschrieben.

In diesem Zusammenhang beschäftigt sich diese Arbeit mit der Synthese, Charakterisierung und additiven Fertigung von maßgeschneiderten hydrophilen $(AB)_n$-segmentierten Copolymeren mit Polyethylenglykol (PEG) und Bisharnstoff-Segmenten als Biomaterialtinten. Die Bisharnstoff-Segmente bilden bei Raumtemperatur physikalische Vernetzungen über Wasserstoffbrücken-bindungen aus, welche beim Erhitzen reversibel aufgespalten werden und verarbeitbare Polymerschmelzen ermöglichen. Die Copolymere wurden für die Anwendung im additiven Fertigungsverfahren *Melt Electrowriting* (MEW) maßgeschneidert, um definierte 3D-Konstrukte mit Faserdurchmessern unterhalb von 50 µm herzustellen. Zusätzlich wurden erste Untersuchungen mit dem *extrusionsbasierten Drucken* (*extrusion based printing*, EBP) als zweites 3D-Druck-Verfahren durchgeführt. Die Copolymere quellen in wässrigen und biologischen Medien zu Hydrogelen auf, welche je nach ihrer Zusammensetzung stabil sind oder nach einer gewissen Zeit zerfallen.

Im ersten Teil dieser Arbeit wird die Synthese einer Serie von $(AB)_n$-segmentierten Copolymeren auf der Basis von hydrophilen Propylenglykol-b-Polyethylenglykol-b-Polypropylenglykol (PPG-PEG-PPG)-Segmenten und Bisharnstoffsegmenten dargestellt. Die Copolymere wurden mittels Polyaddition von kommerziell erhältlichen PPG-PEG-PPG-Diaminen (Jeffamine®) mit unterschiedlichen Molekulargewichten und aliphatischen Diisocyanaten, namentlich Hexamethylendiisocyanat, trans-1,4-Cyclohexandiisocyanat oder 4,4'-Methylen-bis(cyclohexyl)isocyanat im Labormaßstab über 50 g hergestellt. Diese Syntheseroute hat den Vorteil, dass keine Nebenprodukte entstehen und keine Katalysatoren benötigt werden. Durch Zugabe von monofunktionellem *n*-Butylamin kann der Polymerisationsgrad gesteuert werden. Die FT-IR-Analyse zeigt, dass die Stärke der Wasserstoffbrückenbindungen von der chemischen Struktur der Bisurea-Segmente abhängig ist. Das reversible Schmelzen ist von der Länge der

hydrophilen Segmente, der Struktur der Bisharnstoffsegmente und dem Polymerisationsgrad abhängig und kann daher im Temperaturbereich von etwa 10 bis 180 °C eingestellt werden. Die physikalischen Netzwerke bilden sich beim Abkühlen wieder zurück. Die Schmelzviskositäten bei 100 °C konnten im Bereich von 15 bis 8000 Pa s eingestellt werden. Dies ermöglicht die Anwendung in verschiedenen additiven Fertigungstechniken. Zugversuche zeigten die höchsten Zugfestigkeiten für die Copolymere mit Hexamethylenbisharnstoffsegmenten. Je nach Zusammensetzung quellen die Copolymere mit Hexamethylenbisharnstoffsegmenten in wässrigen Medien zu Hydrogelen auf, welche innerhalb einer bestimmten Zeit zerfallen. Die Zerfallsgeschwindigkeit nimmt mit zunehmender Länge der hydrophilen Segmente zu. Copolymere mit 4,4'-Methylen-Bis(cyclohexyl)-Harnstoff-Segmenten quellen in wässrigen Medien zu Hydrogelen mit einem Wassergehalt von mindestens 70 % auf, die in wässrigen Medien nicht zerfallen. Die Biokompatibilität dieser beiden Klassen von $(AB)_n$-segmentierten Copolymeren wurde durch Zytotoxizitätstests nachgewiesen.

Der zweite Teil dieser Arbeit befasst sich mit der additiven Fertigung ausgewählter $(AB)_n$-segmentierter Copolymere. Als zentrale Methode wurde das *Melt electrowriting* (MEW) eingesetzt. Vier geeignete Copolymere wurden aufgrund ihrer optimalen Drucktemperaturen, die im Bereich von 75 – 100 °C liegen, für ausführlichere Untersuchungen mit MEW ausgewählt. Isotherme rheologische Messungen dieser Copolymere bei 100 und 120 °C zeigen die Langzeitstabilität während der MEW-Verarbeitung, indem sie keine nennenswerte Degradation aufweisen. Die Einstellung verschiedener instrumenteller Parameter, namentlich Temperatur, angelegte Spannung, Stickstoffdruck, Kollektorgeschwindigkeit, Düsen-Kollektor-Abstand, Düsendurchmesser und bedruckte Oberfläche, führt je nach Copolymer zu Einzelfaserdurchmessern, die im gewünschten Bereich von 5 – 50 µm liegen. Mit allen getesteten Copolymeren lassen sich gut definierte 3D-Konstrukte mit gleichmäßigen Fasern, kontrollierter Faserablage und Faserdurchmessern von 20 – 50 µm realisieren. Für ein Copolymer mit 82 Gew.- % PPG-PEG-PPG-Segmenten und 18 Gew.-% Hexamethylen-Bisharnstoff-Segmenten wurde mittels *Environmental scanning electron microscopy* gezeigt, dass die gedruckten Gerüste bei 100 % Luftfeuchtigkeit auf mehr als das Doppelte des Faserdurchmessers anschwellen und dabei stabil bleiben.

Zwei der für MEW verwendeten Copolymere wurden zusätzlich für das *extrusionsbasierte Drucken* (EBP) optimiert, indem die Verarbeitungstemperaturen auf 110 – 120 °C eingestellt wurden. Es lassen sich gut definierte Gerüste mit hoher Stapelgenauigkeit und gut positionierten Fasern mit Durchmessern von 250 – 450 µm realisieren. Die Zugabe eines weichen Hydrogels zu

einem Gerüst aus einem Copolymer mit 82 Gew.-% PPG-PEG-PPG-Segmenten und 18 Gew.-% Hexamethylen-Harnstoff-Segmenten führt zu einer starken Quellung. Es wurde nachgewiesen, dass Nährstoffe durch das Gerüst diffundieren, wodurch die Erzeugung von durchlässigen Kanälen ermöglicht wird. Ein Gerüst aus einem Copolymer mit 75 Gew.-% PPG-PEG-PPG-Segmenten und 25 Gew.-% 4,4'-Methylen-bis(Cyclohexyl)-Bisurea-Segmenten quillt in wässrigen Medien auf, ohne sich aufzulösen.

Die Arbeit zeigt, dass durch die Verwendung von hydrophilen $(AB)_n$-segmentierten Copolymeren mit physikalischen Wechselwirkungen in extrusionsbasierten additiven Fertigungsverfahren das Biofabrikationsfenster erweitert wird.

# 1 Introduction

## 1.1 Biofabrication

### 1.1.1 Definition

Biofabrication is a technique that aims the repair, replacement or regeneration of damaged or lost tissues and organs. Within this technique, bioactive materials are combined with cells and growth factors to generate hierarchial arranged cell-material composites that can be implemented or incubated in vivo. These engineered tissue constructs can deliver the cells and growth factors to a damaged tissue or organ. A key element of biofabrication is the use of automatized fabrication processes, usually based on additive manufacturing techniques.[1–3] At the state of 2016 the term biofabrication is defined as *"the automated generation of biologically functional products with structural organization from living cells, bioactive molecules, biomaterials, cell aggregates such as micro-tissues, or hybrid cell-material constructs, through Bioprinting or Bioassembly and subsequent tissue maturation processes"*.[4] The term bioprinting describes the additive manufacturing of three-dimensional (3D) biomaterials also named as *bioinks* that include living cells. Bioassembly means the printing of biomaterials as inks which are defined as *biomaterial inks* and their assembly with cells in the post-fabrication.[5] Figure 1.1 illustrates the difference between bioinks and biomaterial inks.[5]

The use of automatized fabrication processes based on additive manufacturing methods differentiates biofabrication from classic tissue engineering approaches where the cells are either seeded on the prefabricated 3D carrier surface or are suspended with a hydrogel or a gelled solution.[6] The topic of additive manufacturing will be addressed in more detail in chapter 1.3.

The automatized manufacturing of functional tissue models is seen as a promising strategy for regenerative therapeutic application on humans, for pharma- and cancer research and for the replacement of animal experiments. The field of biofabrication is rapidly growing and continuously developing with an exponential growth of published work in the past years.

In the following, the terms *bioinks* and *biomaterial inks* will be further described.

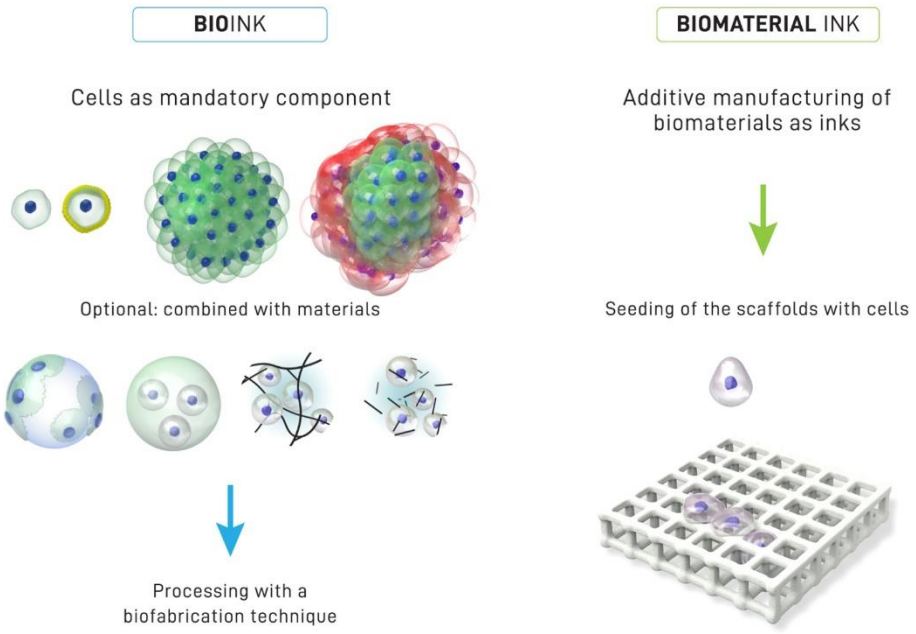


**Figure 1.1:** Differentiation between a bioink (left) where cells are an essential component of the printing formulation and a biomaterial ink (right) where a biomaterial without cells is printed and seeding with cells occurs afterwards. Adapted and reproduced with permission (© 2018 IOP Publishing Ltd).[5]

### 1.1.2 Bioinks

As defined by Groll et al., bioinks are *a formulation of cells suitable for processing by an automated biofabrication technology that may also contain biologically active components and biomaterials.*[5] By this definition, bioinks must include cells that can be organized in different forms and environments, e.g. as single cells, coated cells, cell aggregates (e.g. in spheroids), or in combination with other materials, for example formulated in a hydrogel, seeded onto microcarriers or embedded in microgels. Moreover, biomaterials and bioactive molecules, such as growth factors and DNA, can but do not have to be part of the bioinks. Bioinks can provide an instructive, aqueous 3D environment which simulates the natural extracellular matrix.[7] The biomaterials usually consist of hydrogels or hydrogel precursor formulations with high water content. The cells are dispersed in theses formulations. The term “hydrogel” will be further discribed in chapter 1.1.4.

### 1.1.3 Biomaterial inks

In contrast to bioinks, biomaterial inks do not contain living cells during processing and, thus, have less stringent physicochemical requirements. The biomaterial is printed into a 3D scaffold in which the cells are added in a post-process. Therefore, biomaterial inks have less stringent physicochemical requirements which allows the use of more variable process conditions, e.g. higher temperature, higher pressure and the use of organic solvents. However, the resulting 3D scaffold prepared from the biomaterial ink needs to be cytocompatible with cells.

One approach is the combination of bioinks with biomaterial inks where a biomaterial containing cells is printed onto a supporting scaffold which is prepared from processing of a biomaterial ink. Within this approach the biomaterial inks can be sacrificial materials as temporary support during printing. Preferably, the temporary supporting material can either be washed away from the target structure or dissolves in the biological media. One example of a sacrificial material is carbohyhydrate glass which has been used for the creation of channel networks within the hydrogel structure by combining printing and casting.[8] Another strategy is the combined printing of bioinks and thermoplastic polymers as shown in figure 1.2.[9] In this approach, the bioinks can be processed with low polymer concentration and low crosslinking density while the shape and the strength of the overall construct is tailored by the thermoplastic polymer network. This allows the manufacturing of more complex tissue structures. One example is the hybrid printing of ε-polycaprolactone (PCL) with the infusion of a hyaluronic-based hydrogel.[9,10] The PCL filaments were printed by melt extrusion based additive manufacturing and enhance the strength of the bioinks.

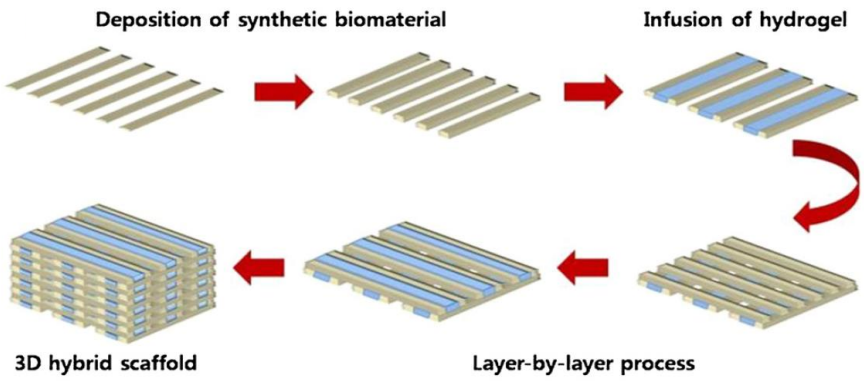


**Figure 1.2:** Schematic on the fabrication process of a hybride scaffold consisiting of a biomaterial ink as supporting material and a hydrogel as bioink. Adapted and reproduced with permission (© 2011 IOP Publishing Ltd).[9]

### 1.1.4 Hydrogels

The term hydrogel describes a three-dimensional network of a hydrophilic polymer that absorbs and holds a large amount of water without dissolving. As a consequence, the polymer swells in water. Hydrogels were first reported by Wichterle et al. defining a material as a hydrogel that constitutes of at least 10 % water of total weight or volume.[11] The network structure of a hydrogel is maintained by either chemically or physically crosslinking of individual polymer chains.

Chemically crosslinked hydrogels consist of covalent or ionic bonds between polymer chains that are non-reversible. Covalent crosslinking can be achieved by several synthesis methods including grafting, radical polymerization, click chemistry, enzymatic reactions, thermogelation and radiation crosslinking.[12,13] Ionic bond formation can be induced by ions that are added to the hydrogel precursor, such as $Ca^{2+}$ or $Mg^{2+}$. One example for ionic crosslining are hydrogels based on alginate.[11,14–16]

Physical crosslinked hydrogels, also described as supramolecular hydrogels, are made of non-covalent bonds between polymers. The crosslinking occurs by physical interactions, such as hydrogen bonding, metal-ligand corrdination, van-der-waals interactions and electrostatic interactions. Several noncovalent hydrogels show reversible gel-sol transition behavior in response to stimuli, such as temperature, pH value, light, redox reactions and enzymatic reactions. Moreover, the physical crosslinks have the ability to self-heal when a network is broken.[17–19]

Hydrogels are used in many biomedical applications due to their biocompatibility, flexibility in fabrication, variable composition and desirable physical chracterisics that are similar to physiological conditions. For instance, they can serve as 3D scaffolds for tissue engineering, as carriers for drug delivery or as adhesives between tissue and material surfaces.[20]

To be applicable for biofabrication, hydrogels and hydrogel precursors must be suitable for both additive manufacturing and cell culture. Thereby, the rheological properties and the mechanism for the crosslinking of the hydrogels are relevant physical parameters for the printability of bioinks. Moreover, the cytocompatibility of the gelation process and the resulting hydrogel is essential for the field of biofabrication. The viscosity of a bioink is predominantly determined by the polymer concentration and its molecular weight. Low molecular weights and low concentrations resulting in a low vscosity are favorable conditions for cell proliferation, migration and tissue formation. An increase of the viscosity generally results in a higher printing fidelity. However, the applied shear stress of the bioink also increases with rising viscosity which may be harmful to cells. Most polymeric systems reveal non-Newtonian behavior leading to a decrease of the viscosity with increasing shear stress. This phenomenon is called shear thinning and is caused by shear-induced reorganization of the polymer chains to a more stretched conformation.[21,22] This leads to a lower viscosity by a decreased entanglement. Within bioprinting, shear-thinning occurs during dispensing through the nozzle. Directly after removal of the shear stress the temporary network is ideally restored and the plotted filament solidifies. To induce shear-thinning the yield stress must be overcome to initiate a flow.

### 1.1.5 Materials for biofabrication

In biofabrication, cell-loaden hydrogels are commonly used as bioinks. The most essential parameters for a hydrogel that determine its printability are the rheological properties, especially viscosity, shear thinning and yield stress, and the crosslinking mechanism of the hydrogel.[10] Bioinks can be made from natural or synthetic materials, or a combination of both.

#### *1.1.5.1 Natural polymers*

Most hydrogels used as bioinks are based on naturally derived polymers that are extracted from biological systems, for example plants, microorganism, or algae. Naturally derived polymers have

been widely used for decades in the biomedical field since their artificial matrix provides biochemical cues, e.g. signaling, growth factors, proteins, and appropriate biophysical and structural properties to mimic the extracellular matrix of native tissues.[23–27] Due to their biocompatibility these materials improve the cellular attachment and cellular behavior and avoid immunological reactions. Cells benefit from the abundance of chemical signals in these biomaterials resulting in high viability and proliferation rates for the growth of new tissue. Common natural polymers that are used in biofabrication are:

1) polysaccharides
    - alginate[28–30]
    - hyaluronic acid[31,32]
    - citosan[33]
2) proteins
    - collagen[34,35]
    - silk[36–38]
    - gelatin[39,40]
    - fibrin[41–43]
3) bacterial cellulose[44,45]

All the mentioned biopolymers can be modified with functional groups that can undergo crosslinking reactions by e.g. light, enzymes, or ions.[46–48]

Drawbacks of natural materials are a low reproducability due to large batch-to-batch variations and unpredictable compositions which results in mechanical properties and degradation rates that are difficult to control.

### *1.1.5.2 Synthetic polymers*

An alternative to natural materials are synthetic bioinks. Synthetic materials can be tuned to mimic tissue-specific degradation and mechanical properties of the target tissues and organs. Moreover, synthetic materials are used as biomaterial inks. Examples of synthetic materials that have been reported in terms of biofabrication are PCL, polyvinylpyrrolidone, poly(L-lactide) acid

and poly(lactic-*co*-glycolic) acid.[49–52] A very relevant synthetic material in biofabrication is polyethylene glycol.[53,54] Since polyethylene glycol is used in the framework of this thesis, this material will be dealt with in more detail below.

### *1.1.5.3 Polyethylene glycol (PEG)*

Polyethylene glycol (PEG) is synthesized by the ring-opening polymerization of ethylene oxide. First investigations of the polymerization of ethyleneoxide with several catalysts were done by Staudinger in 1929.[55] Today, the common route for the synthesis of PEG is the base-catalyzed anionic ring-opening polymerization due to the good control of the structure and the molecular weight. The mechanism is shown in figure 1.3.[56] Sodium and potassium hydroxides serve as initiators while water, monoethylene glycol or diethylene glycol are usually used as starting molecules. Other possible production routes are the cationic ring-opening polymerization and coordinative strategies.[57] The anionic polymerization leads to a very low polydispersity index below 1.1 for the obtained PEGs due to its controlled character. This ensures an applicable homogenity and reproducibility which is essential in biomedical applications.

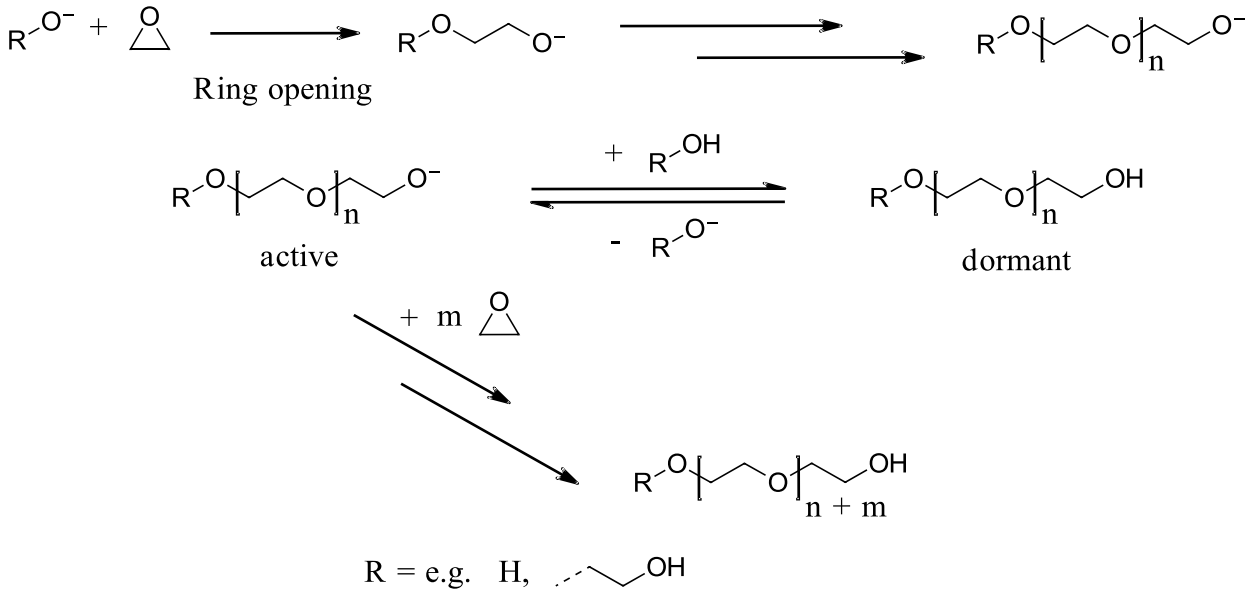


**Figure 1.3:** Scheme of the anionic polymerization of ethylene oxide. The activated alcoxide anion reacts with ethylene oxide by ring opening. Repeating of this reaction steps leads to grow of the polymer chain. The active polymer chain can reversible terminated which leads to a good control of the polymerization. As a result, low polydispersities are obtained for the resulting PEG. Adapted and reproduced with permission (© 2015 American Chemical Society).[56]

The chemical and physical properties of PEG strongly depend on its molecular weight. The melting point of PEG increases with rising molecular weight reaching a value of around 60 °C for high

molecular weight PEGs.[58] Low molecular weight PEGs below 600 g $mol^{-1}$ have a melting area below 22 °C and are a viscous liquid at room temperature. PEGs reveal an excellent water solubility whereby the water solubility slightly decreases with increasing molecular weight.[59] In contrast, polymethylenoxide, polyacetaldehyde, polypropylene glycol, polytrimethylenoxide, and polytetrahydrofuran all having a similar structure to PEG are insoluble in water.[59] The hydrophilicity of PEG results from the appropriate distance between the repeating oxygen units matching with the distance of oxygen atoms in liquid water. This allows the formation of hydrogen bonding networks between the PEG units and water molecules.[60] The formation of the hydrate-shell only occurs below the lower critical solution temperature (LCST).[60] Therefore, PEG becomes insoluble upon heating above the LCST. PEG excellently dissolves in several organic solvents which allows a versatile modification of the hydroxyl end groups.[61] Consequently, PEG can easily linked with other molecule structures and therefore be incorporated in various materials. Moreover, PEG was proven to have a very low intrinsic toxicity.[62]

All the above-mentioned properties result in PEG being one of the most used polymers in biomedical applications and is even named as the “gold standard” in the field of drug delivery.[63] PEG is used in several further applications, e.g. in cosmetics and as non-ionic tensides for the controlled formation of foams.[62,64] Due to its high conductivity PEG and PEG-containing materials are also used in electrolytes of lithium-ion batteries.[65] PEG was found to be thermally stable below 80 °C. At higher temperatures oxidative degradation of PEG can occur at ambient conditions.[66] The thermal stability is enhanced in a nitrogen atmosphere.

### 1.1.6 Biofabrication window

The fabrication of bioinks into complex, tissue-like 3D structures with high resolution causes challenges: On one hand, the physical properties of the applied bioinks need to meet a very narrow physical and mechanical property window. On the other hand, the printed hydrogel structure should facilitate migration, proliferation and differentiation of the embedded and endogenous cells. A look at the biofabrication window (figure 1.4) gives a better understanding of the challenges.[10]

An optimum printing quality of the bioinks with a high shape fidelity can be obtained by increasing the polymer concentration or crosslink density. High crosslinked hydrogels correlate with a high stiffness as shown by the blue marked fabrication window. However, cell migration, growth and differentiation in such a dense polymer network are strongly limited. Cell thrive best in a soft hydrogel with a low extent of crosslinks which is represented by the yellow marked cell culture window [67]. Here, the migration and matrix deposition of cells is not limited. However, hydrogels with low crosslink densities lack the ability to maintain their imposed shape of fabrication. This results in a low shape-fidelity and limited overall mechanical properties. Therefore, as a compromise, most constructs have been fabricated with a medium hydrogel crosslink density. This is shown by the green marked traditional biofabrication window. There is the need to shift the biofabrication window to obtain a high shape fidelity by using hydrogels with maximal cell and tissue compatibility ("novel strategies"). Progress in the design of hydrogels together with the development of new bioprinting strategies has been made in the past years.[68] Nevertheless, the essential materials and parameters for the fabrication of intrinsically hierarchical constructs that truly mimic biologically functional tissue are still largely unknown.

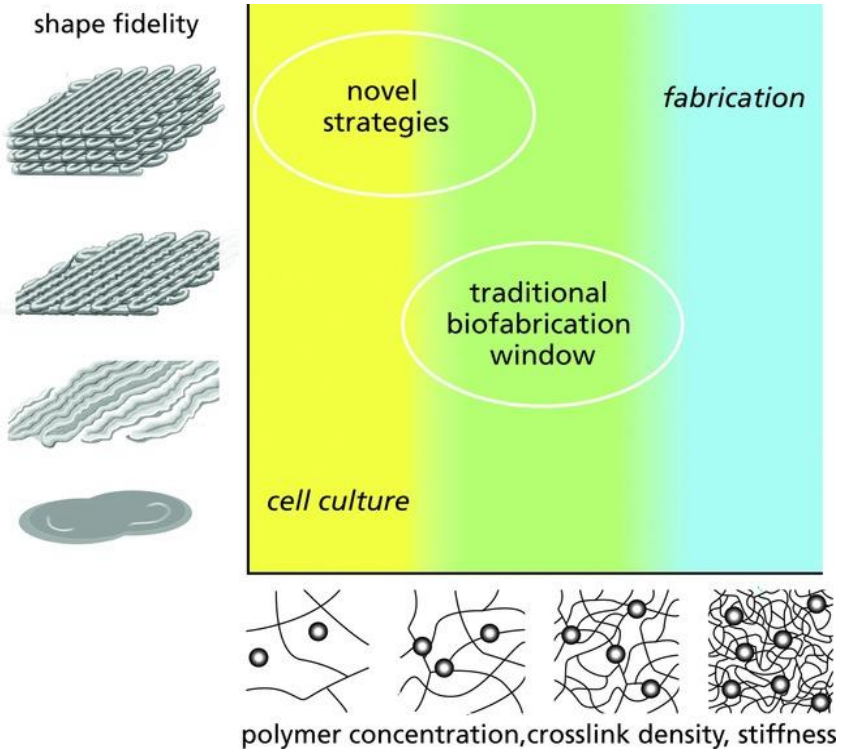


**Figure 1.4:** Schematic representing the traditional and aimed biofabrication window (novel strategie) with regard to the shape fidelity and the stiffness of the applied bioinks. Adapted and reproduced with permission (© 2013 WILEY-VCH Verlag GmbH & Co. KgaA, Weinheim).[10]

## 1.2 $(AB)_n$-segmented copolymers

Copolymers consist of two different monomers (monomer A and monomer B) that can be linked to different structural designs. Depending on the reaction conditions and their reactivity, monomers can polymerize statistically (ABBAABA), in blocks (AAABBB), grafted to each other, or alternating ($(AB)_n$). One specific class are $(AB)_n$-segmented copolymers that are made of two covalently linked segments with different physical properties.[69] The two alternating segments are often termed hard segment and soft segment, and are molecularly incompatible with each other. The soft segments typically have glass transition temperatures below ambient temperature and impart flexibility. Examples of commonly used soft segments are polytetrahydrofuran, polypropylene glycol and polydimethyl siloxane.[70–75] The hard segments undergo intermolecular interactions to form physical crosslinks between polymer chains, e.g. by hydrogen bonding. As a result of their inherent incompatibility combined with the supramolecular interactions, the hard and soft segments undergo micro phase separation. In microphase seperated morphologies the hard segment microdomains are dispersed within the soft polymer matrix. A schematic is shown in figure 1.5.[76] The formation of a microphase-separated morphology is determined by several parameters, such as the overall degree of polymerization, volume fraction of the segments and Flory-Huggins interaction parameters.[77]

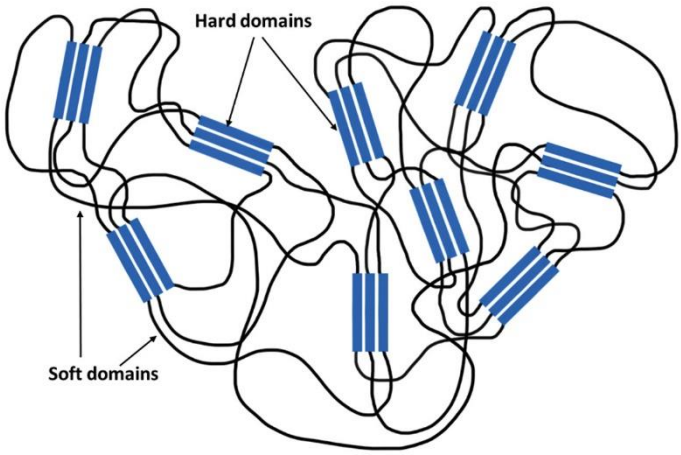


**Figure 1.5:** Illustration of the microphase separation of hard and soft segments in $(AB)_n$-segmented copolymers segments. Adapted and reproduced with permission from reference (© 2021 American Chemical Society).[76]

Two well-known examples of $(AB)_n$-segmented copolymers with a high relevance in industrial applications are polyamides and polyurethanes.[69,78,79] The copolymers are synthesized by step

growth polymerization. For instance, polyurethanes are made by the catalyzed polyaddition of polyhydroxyl compounds, also known as polyols, and isocyanates. Due to their high number of choice the used polyol largely determines the mechanical properties of the polyurethanes. Polyols are commonly based on polyester or polyether but also polycarbonate and polydimethylsiloxane-based polyols are commercially used.[78] By the additional use of chain extenders and additives polyurethanes can be manufactured in an extremely wide range of grades, such as foamed, soft and rigid, with applications in several areas, such as automotive, furniture, construction and thermal insulation. The amide or urethane segments serve as the hard segments and form physical crosslinks via hydrogen bonds (figure 1.6).[80–83] Another polymer class which is assigned to the polyurethanes are polyureas synthesized from amines and isocyanates. The resulting urea groups are crosslinked by bidentate hydrogen bonds (figure 1.6).[72,84,85]

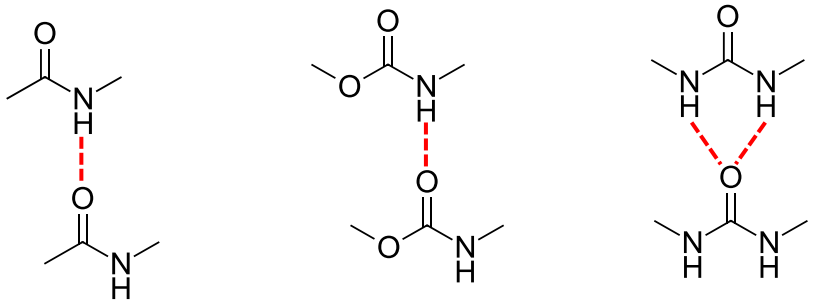

**Figure 1.6:** Hydrogen bonding interactions between amide, urethane, and urea moieties.

Several elastomer resins based on $(AB)_n$-segmented copoymers were reported to be used in additive manufacturing techniques, especially in *vat photopolymerization*.[86]

The supramolecular segments of $(AB)_n$-segmented copolymers are often thermoreversible due to the thermal induced disassembly and reassembly of hydrogen bonds.[73,85,87] The melting temperature range of these hard segments are often far above room temperature. As a result, several polyurethanes and polyureas are thermoplasts or thermoplastic elastomers and can be processed from the melt. For instance, an $(AB)_n$-segmented copolymer consisting of poly(siloxane) soft segments and bisurea hard segments was successfully processed by the additive manufacturing technique *melt electrowriting*.[87]

In the past years intensive research was also done on $(AB)_n$-segmented copolymers with polyethylene glycol segments (PEG) and supramolecular segments. For example, $(AB)_n$-

segmented copolymers with PEG segments and poly(urethane urea) segments were found to undergo microphase separation to obtain several micro- and nanoscale morphologies that can be adjusted by the length of the PEG segments and chemical structure of the poly(urethane urea) segments.[88] Due to the hydrophilic properties of PEG many of these systems have the ability to form hydrogels in aqueous solution which are stabilized by the hydrogen bonding segments. Dankers *et al.* synthesized $(AB)_n$- and (ABA)-segmented copolymers based on PEG segments and ureido-pyrimidone (UPy) segments for intrarenal drug delivery systems after subcapsular implantation.[89] The UPy moieties are able to form four-fold hydrogen bonds. These copolymers form supramolecular hydrogels from mixtures of water and organic solvents. Guo *et al.* expanded this architecture concept with multiblock PEG based copolymers with UPy in the backbone.[90] They realized stimuli-responsive supramolecular hydrogels with 80% weight fraction of water and a microphase separated network. The network is stabilized by the shield of the hydrogen bonding interactions from the PEG segments with short-chain hydrophobic oligo-methylene spacers. The hydrogels exhibit high strength and resilience upon deformation. Obert et al. proved the self-assembly of PEG based (ABA)-segmented polymers with a bisurea segment in the centre in water and organic solvents.[91] The self-assembly results from the hydrogen bonding interactions between the bisurea moieties. The bisurea segment is shielded from the PEG segments by methylene spacers. Wang et al. reported on a PEG-*block*-poly($_L$-phenylalanine) copolymer as fibroblast suppresive hydrogel which is formed by hydrogen bonding and π-π interactions.[92] Pawar *et al.* investigated $(AB)_n$-segmented copolymers with PEG segments and bisurea segments. These polymers were proven to be biocompatible and are able to form injectable hydrogels with shear-thinning behaviour.[93] The properties of the hydrogels can be tailored due to the length of the hydrophilic PEG segments and the length of the alkyl chain between the two bisurea units. An improvement in mechanical and stretchable properties was demonstrated by Cui *et al*. by shorten the length of the PEG segments and using an aliphatic dodecyl instead of a decyl spacer.[94] The hydrophobic decyl or dodecyl spacers shield the urea groups from water. Due to the relatively large spacer the hydrogel is insoluble in water, but can be dissolved in organic solvents, such as methanol, ethanol, and chloroform, and therefore be processed by solution casting or electro-spinning in hydrogel films or nano-fibers.[94] Another PEG-based $(AB)_n$-segmented copolymer with supramolecular segments consisting of several urethane and urea units also revealed excellent

hydrogel properties and was successfully processed by solution elctrospinning and by melt-pressing at 160 °C.[95] It was shown that $(AB)_n$-segmented copolymers with PEG and bisurea segments have poor cell adhesive surface.[96] Recently, PEG-based $(AB)_n$-segmented copolymers with imidazolidinyl urea segments forming four-fold hydrogen bonds were reported by Yu et al.[97] These polymers form stable hydrogels with excellent mechanical and self-healing properties and can be prepared by a much simpler synthesis route as compared to the UPy systems.

The chemical structures of some of the mentioned PEG-based $(AB)_n$-segmented copolymers are shown in figure 1.7. Only one of the presented copolymers that form tough hydrogels in aqueous media has thermal processing from the melt specified, and this is in form of melt-pressing at 160 °C.[95] Thermal analysis was only reported for a few polymers revealing melting of the supramolecular segments above 150 °C.[90,93] This demonstrates that there is still a gap regarding materials that form hydrogels in water and can be thermally processed from the melt at moderate temperatures by using additive manufacturing techniques.

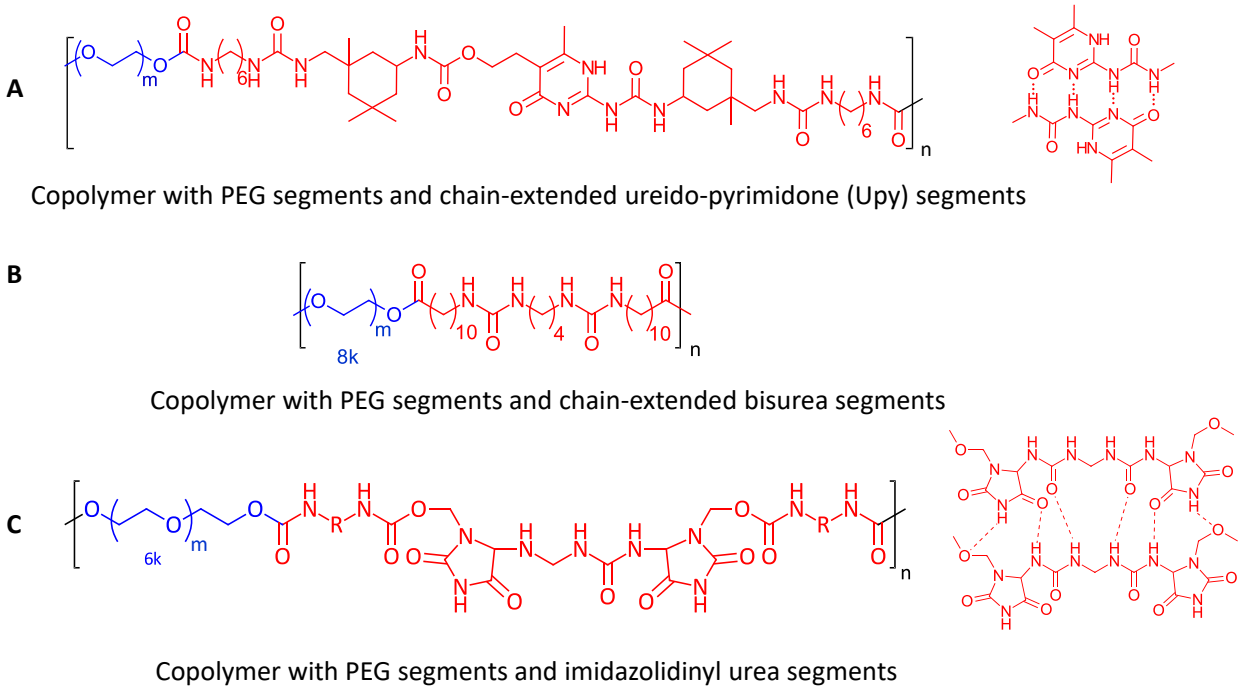


Copolymer with PEG segments and chain-extended ureido-pyrimidone (Upy) segments

Copolymer with PEG segments and chain-extended bisurea segments

Copolymer with PEG segments and imidazolidinyl urea segments

**Figure 1.7:** Chemical structure of selected $(AB)_n$-segmented copolymers based on polyethylene glycol (PEG) and supramolecular segments that are reported in literature. A: Example of a PEG based $(AB)_n$-segmented copolymer with ureido-pyrimidone segments. Adapted and reproduced with permission (© 2012 Elsevier Ltd.).[83] B: Example of an $(AB)_n$-segmented copolymer with PEG segments and bisurea segments that are connected by a decylene spacer. Adapted and reproduced with permission (© 2012 American Chemical Society).[87] C: Example of a PEG-based $(AB)_n$-segmented copolymer with imidazolidinyl urea segments. Adapted and reproduced with permission from reference (© The Royal Society of Chemistry 2020).[91]

## 1.3 Additive manufacturing

### 1.3.1 Definition

Additive manufacturing (AM), also known by synonyms such as 3D printing, rapid prototypig and layered manufacturing, describes a versatile technology platform that produces 3D objects by the deposition of materials by a computer-controlled process. Additive manufacturing was first introduced and commercialized in the 1980s and has experienced very large grow since then.[98]

In a general additive manufacturing process, the object is first created virtually by computer-assisted design (CAD) and then digitally sliced. The coordinates of the virtual object and the digital slices are then transferred to the 3D printing machine which performs the printing of the object.[99] Thereby, the practical implementation of the printing is named as computer-aided additive manufacturing (CAM). In contrast to formative manufacturing techniques that require the use of moulds and substrative manufacturing techniques where machine tools are needed for post-processing, additive manufacturing allows the production of customized parts without tools and fixtures. Instead, the object can be fabricated directly from CAD design which also involves minimal human intervenation. This leads to many advantages in additive manufacturing, e.g. the reduction of tools, elimination of waste and the realization of more complex internal substructures. Moreover, additive manufacturing allows the flexibly designing and fabricating of materials.

On the other hand, additive manufacturing techniques are still facing some challenges. In comparison to conventional manufacturing techniques, such as injection moulding, the production of objects by additive manufacturing requires more time. Another challenge is the adjustment of the mechanical properties since they highly depend on the processed material and the process parameters. Moreover, an insufficient resolution can drastically influence the quality and quantity of the printed objects. Also, the processing of two or more materials with the same print job is complicated due to differences in their properties, reactivity and compatibility. This limits the application in the preparation of objects consiting of different materials. Several research has been done in the past years to overcome these challenges in view of customizing.

In the following, an overview of additive manufactruing techniques will be given.

### 1.3.2 Overview of additive manufacturing techniques

The number of techniques for additive manufacturing is large. The common techniques can be divided in several categories that are briefly presented in the following:

***Vat Photopolymerization***

Vat photopolymerization describes an additive manufacturing technique in which a liquid photomonomer in a vat is selectively cured by light-activation. Thereby, the photomonomer is collected in a tank and treated with either UV or visible light. There are different configurations that can be used for Vat photopolymerization. In the *top down* approach the photomonomer is cured by light above the vat. Afterwards, the built platform is lowered down towards the bottom into the vat. In the *bottom up* approach the curing with light occurs at the bottom of the tank from below. The build platform is then moved upwards out of the resin vat. Several photobased additive manufacturing methods cover the vat polymerization, especially litography-based techniques. Examples are *stereolitography*, *digital light processing*, *Continuous Liquid Interface Production* and *Multiphoton Polymerization*.[100–106]

***Powder Bed Fusion***

Powder bed fusion is a technique in which regions of a powder bed are selectively fused by thermal energy. The thermal energy is provided by e.g. laser or an electron beam. Powder bed fusion can be applied for polymers, metals and ceramics and, thus, allows the use of a large range of materials within this technique. Common powder bed fusion process techniques are *selective laser sintering*, *selective laser melting* and *electron beam machining*.[107–111]

***Material and binder jetting***

Material jetting describes the selectively deposition of droplets of build material which can be e.g. a photopolymer or a thermoplastic material.[112,113] In binder jetting the liquid resin is selectively deposited onto powder materials to fuse them together.[114,115] Both techniques mainly focus on inkjet-printing using resins with low viscosities that are commonly about 10 – 20 mPa s at processing temperature.

***Sheet lamination***

Sheet lamination is an additive manufacturing technique in which thin sheets made from synthetic polymers or paper are laminated, cut and finally bonded together layerwise to form an object. The bonding between the layers can be realized by gluing, thermal bonding, clmping or ultrsonic welding.[116]

***Directed energy deposition***

In directed energy deposition, focused thermal energy is used to fuse materials by melting when they are being deposited. Basically, this process consists of three elements, namely a feedstock unit, a substrate bed having motion controls and a heat source, e.g. laser, electron beam or plasma. The thermal energy is focused on the previous layer while the feedstock with types of wires and powders is fed to the focused region of thermal energy. A molten pool is formed and the previous and new layer fuse together before solidication of the molten pool.[117]

***Material extrusion***

Material extrusion-based additiv manufacturing describes the pressurized layer by layer deposition of molten or semi-molten polymers, polymer solutions and dispersions through a nozzle or orifice.[118] One very important extrusion based additive manufacturing technique is *fused deposition modeling* (FDM)*,* which is also named as *fused filament fabrication*. In FDM thermoplastic polymers are mechanically transfered as thin filaments from a spool into the extrusion print head.[119–121] The printhead is heated to an appropriate process temperature which lays above the melting temperature for semi-crystalline polymers or above the glass temperature for amorphous polymers. FDM is a very robust technology platform and has been the most customized and commonly used additive manufacturing technique worldwide since the early 2000s.[99] Besides FDM extrusion based additive manufacturing can be conducted by 3D dispensing or 3D extrusion. Here, the extrusion printhead comprises a nozzle and a cartridge and is pneumatically controlled by varying the air pressure. The 3D extrusion will be discussed more intensively in chapter 1.2.4. Another extrusion based technique is 3D bioplotting. Additive manufacturing techniques for the processing of bioinks will be presented in more detail in chapter 1.3.3.

### 1.3.3 Additive manufacturing of bioinks

The processing of bioinks with additive manufacturing techniques requires the compatibility of cells with the printing conditions and the simultaneously preservation of mechanically durable and formstable 3D-constructs. The used AM techniques for the hydrogel-based biofabrication are primarily based on laser-induced forward transfer, inkjet printing (either thermal or piezoelectric) and robotic dispensing.[3,10,122–127] All three approaches are schematically shown in figure 1.8. [10]

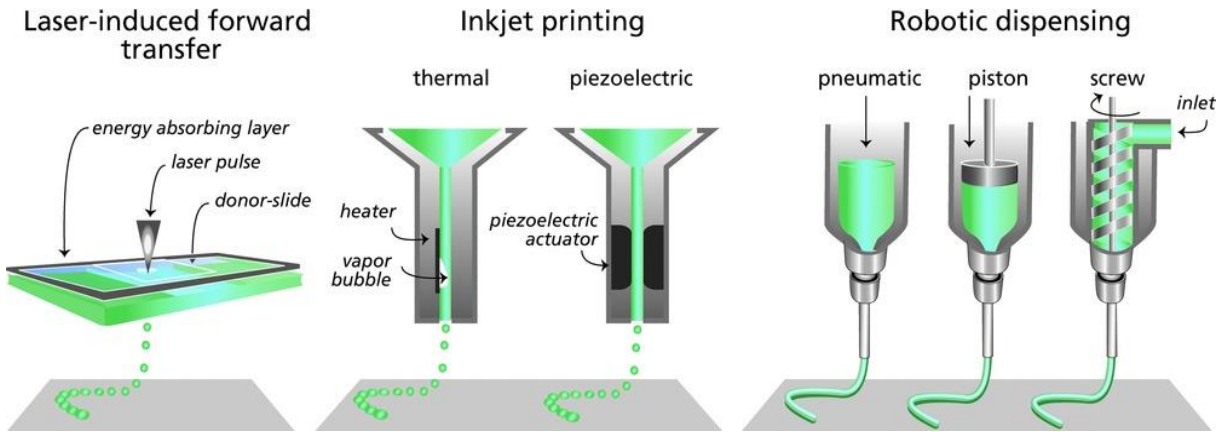


**Figure 1.8:** Overview of selected biofabrication approaches for the additive manufactring of hydrogels in a form of so-called "bioinks". Adapted and reproduced with permission (© 2013 WILEY-VCH Verlag GmbH & Co. KgaA, Weinheim).[10]

In laser-induced forward transfer a donor slide covered with a laser absorbing layer is used. The focused laser pulses result in local evaporaton of the absorbing layer. This generates a high gas pressure that guides the bioink to the collector slide. The technology is nozzle-free, allows a high resolution and can be used for bioinks with a wide range of viscosities up to 300 mPa s. On the other hand, the overall flow rate is very low resulting in long printing times.

Inkjet printing of cells is commonly conducted either thermal or piezo-electric. One retriction of this technology is the low upper limit of viscosity for the ink which is in the order of 100 mPa s. Moreover, the low viscosity facilitates spreading of the droplet on the surface since small droplets are deposited with high velocity. This complicates the printing of 3D constructs.

This work focuses on applications by using robotic dispensing since it is the most promising technique out of the three presented here. In robotic dispensing hydrogels with suspended cells are generally inserted in a disposable syringe and printed by either pneumatic, piston or screw-driven dispensing. A resolution in the order of 200 µm can be achieved with robotic dispensing.

This is lower as compared to laser- and inkjet techniques. On the other hand, the fabrication speed is significantly higher by using robotic dispensing resulting in much lower processing times. Furthermore, a wide range of material viscosities ($30 – 6 \cdot 10^7$ mPa s) can be processed.

Dispersion printing has undergone continuous methodological development over the past years, accompanied by target material developments. Coaxial printing of multilayer strands was enabled by extention of the nozzle by several concentric hollow needles.[128,129] Another novel approach is the processing of bioinks into physical crosslinked hydrogels as supporting bath to mechanically stabilize the printed structures. This technique is named *in-gel printing* and allows the use of less viscous bioinks and extended crosslinking times.[130–134] Additionally, double printing strategies were developed to receive hydrogel constructs with defined porous structures. In *void-free 3D bioprinting* the structure-forming ink and the sacrificial ink are placed next to each other. After printing the structure-forming ink is crosslinked while the sacrificial ink is removed.[135] Also, microfluidic approaches are gaining importance for biofabrication due to higher resolution and the opportunity to simultaneously or alternately print several materials.[136,137]

A strongly emerging trend is the combination of bioprinting with other fabrication technologies. Here, the bioinks are printed in combination with a supporting scaffold made from biomaterial inks. Especially extrusion-based techniques for the printing of the supporting structure are from high interest. For this reason, filament-free melt extrusion based additive manufacturing techniques will be addressed in more detail in the following.

### 1.3.4 Melt Extrusion-based additive manufacturing

In additive manufacturing melt processing is a sustainable approach for the fabrication of scaffolds which avoids the use of solvents. Since this work focuses on extrusion based AM three techniques, namely extrusion-based printing (EBP), melt electrospinning (MES) and melt electrowriting (MEW) will be further presented below.

#### *1.3.4.1 Extrusion-based printing (EBP)*

Extrusion-based printing (EBP) of polymer melts including fused deposition modeling is one of the most cost-effective and readily accessable methods for additive manufacturing.[138] Thereby, the used polymer is heated in a chamber to the melt. The molten polymer is then extruded through a nozzle onto a translating build plate as shown in figure 1.9.[139] Considering the diversity of final applications, the range of available printable materials for melt processing with EBP is still limited. EBP has mainly been investigated with either polylactic acid (PLA) or poly(acrylonitrile-butadiene-styrene) (ABS).[140] Other polymers used for EBP include polypropylene (PP), poly(ε-caprolactone) (PCL), polycarbonate (PC), poly(ether ketone) (PEEK) and nylon. [140–144]

For biofabrication approaches fiber diameters are preferably below 50 µm. However, this technique is limited to maximum fiber sizes above 50 µm. This can be explained by a processing phenomenon called “Barus effect” or “die swell” which predominates at small nozzle diameters of 100 µm and below.[145] Therefore, in EBP the practical lower limit of the processed melt in the printing diameter is difficult to overcome.

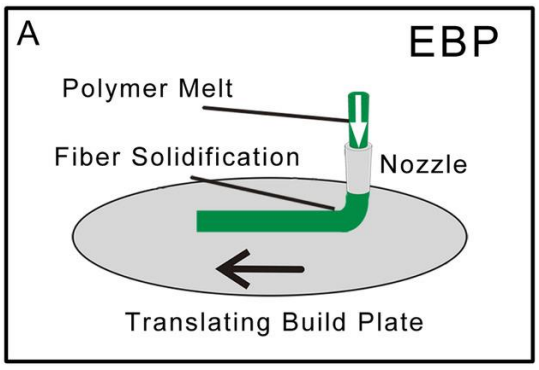


**Figure 1.9:** Schematic of the melt extrusion-based AM technologies *Extrusion based printing* (EBP). EBP is the most common AM technology and involves extrusing onto a build plate”. Adapted and reproduced with permission (© 2020 The Authors. Macromolecular Chemistry and Physics published by WILEY-VCH GmbH).[139]

### *1.3.4.2 Melt Electrospinning (MES)*

As compared to EBP fibers with significantly smaller diameters can be generated using melt electrospinning (MES). The setup of MES is depicted in figure 1.10.[139] In this additive manufacturing technique, there is a several centimetres gap between the spinneret and the moving collector. High voltages are applied to initiate electrical instabilities that result in stretching of the molten jet into smaller dimensions. Fiber diameters from 500 nm up to low-micron have been reported for MES. Common polymers and polymer blends such as PCL, PLA, polypropylene and polyethylene terephthalate with different additives have been processed with MES.[146–149] Moreover, MES of blends of PCL and PLA with polyethylene glycol was reported.[150–153] A significant drawback of MES is, that the fiber placement is much more difficult to control and random, coiled fibers are created as also observed with solution electrospinning.[154] Consequently, this method is not applicable for the production of well-defined scaffolds with optimum fiber placement and controlled layer-by-layer stacking. For this reason, this approach will not be pursued in the course of this work.

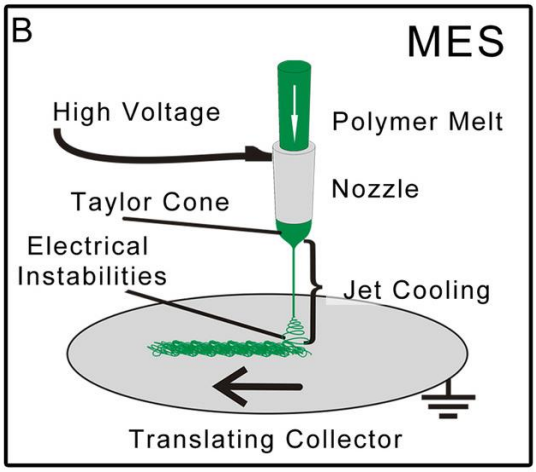


**Figure 1.10:** Schematic of the melt extrusion-based AM technology *Melt electrospinning* (MES). MES involves a larger diameter nozzle that is charged with an applied voltage and is raised above an earthed collector. Adapted and reproduced with permission (© 2020 The Authors. Macromolecular Chemistry and Physics published by WILEY-VCH GmbH).[139]

### *1.3.4.3 Melt Electrowriting (MEW)*

Melt electrowriting (MEW) combines the characteristics of EBP and MES and produces fiber diameters that range between those of EBP and MES. The design, develop and build of a custom MEW printer is described by Eichholz et al.[155] The schematic setup of the MEW technique is illustrated in figure 1.11.[139] A molten jet is electrically stabilized and direct-written onto a moving collector. In more detail, the polymer melt is supplied from a heat chamber through a spinneret by e.g. gas pressure. After emerging from the spinneret the polymer reaches the electric field. Electric charges affect the surface of the polymer meniscus and generate forces that draw the polymer melt towards the collector. Thereby, the electrostatic force is described by the ratio between the applied voltage and the spinneret-collector distance.[156] As charge builds up, the droplet deforms by repulsive coulomb forces. If these repulsive forces exceed the surface tension of the melt which favors spherical shapes the drop deforms into a conical profile termed “Taylor Cone”.[156,157] As a result, the electrically charged polymer jet rapidly elongates away from the droplet and thins towards the collector. This effect enables fiber diameters significantly lower as compared to EBP. The initiation of the polymer jet usually takes place in the order of a few to 10 minutes depending on the flow rate and/or melt viscosity.[158] Ideally, the polymer jet rapidly cools and solidifies on the way from the nozzle to the collector.

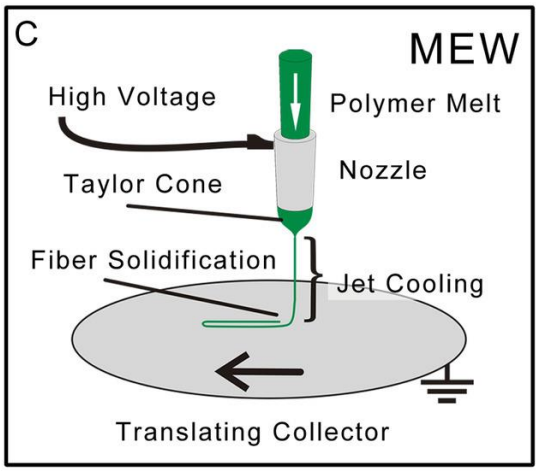


**Figure 1.11:** Schematic of the melt extrusion-based AM technology *Melt Electrowriting* (MEW). MEW does not have electrical instabilities due to lower applied voltage and a higher flow rate as compared to MES. Adapted and reproduced with permission (© 2020 The Authors. Macromolecular Chemistry and Physics published by WILEY-VCH GmbH).[139]

In contrast to MES no electrical instabilities occur due to the lower voltage and a higher flow rate to the nozzle. Therefore, straight fibers are printed if the computer-controlled collector velocity is higher as the velocity of the polymer jet.[159] This speed is named as *critical translation speed* (CTS). Below the CTS jet buckling occurs and non-linear patterns can be observed. These patterns are usually sinusoidal, loop-shaped or have translated coiling.[160] Depending on the flow rate out of the nozzle and the translation speed of the collector fiber diameters in a wide range down to 0.8 µm can be produced.[161,162] Therefore, in contrast to EBP defined constructs with cellular dimensions can be manufactured by the use of MEW. Moreover, other instrumental parameters, such as the applied voltage, the spinneret-collector distance, the spinneret diameter and the temperature in the heat chamber and in the spinneret have influence on the fiber diameter.[156] Especially the temperature plays a key role since it influences the melt viscosity of the applied polymer.

Moreover, the molecular weight of the polymer has a significant impact on the fiber morphology since it correlates with the melt viscosity. It was shown that PCL has a critical molecular weight above which entaglement effects result in a noticeable change in the fiber morphology which allows the printing of well-defined fibers and scaffolds.[163] Below the critical molecular weight, continuous jet break up, buckling and overflow and fuse of neighboring fibers was observed. The range of viscosity that allows successful printing of MEW structures was found to range between 43 and 1455 Pa s. Higher viscosities require high accelerating voltages resulting in dielectric breakdown of the air and formation of an arc between the nozzle and the collector.

MEW has been studied and optimized over the years in view of the stability of the process over the time to realize the preparation of complex structures by accurate fiber placement throughout the entire print. Hochleitner et al found out that an equilibrium between the mass flow through the spinneret and electrostatic forces pulling the material from the nozzle to the collector is essential for reaching stable printing conditions.[160] A force imbalance leads to mass flow oscillation during printing resulting in inhomogeneous fiber diameters and visible offsets in the turning points by variable lag of the jet drawn to the collector. This phenomen is termed *fiber pulsing* and can be characterized by three types. Temporary pulsing describes the initial disequilibrium causing jet oscillation at the beginning of the process and by changes in

instrumental parameters until a stable condition is reached. Continuous pulsing results from excessive flow rate conditions leading to ongoing oscillation of fiber diameters. The jet can be stabilized by an increase of the voltage to generate a stronger electric field. Long bead defects can be characterized as large outliners in the function of fiber diameters resulting in large standard deviations. Long beading occurs at very low voltage or high pressure. The undesired instabilities can be overcome by reducing the feeding pressure or by increasing of the electric field strenght.[160] Another effect that was studied is bridging of close adjacent fibers due to electrostatic attraction. The minimum feasible interfiber distance without bridging was found to increase with larger fiber sizes and with higher number of layers.[164] For instance, with PCL, a minimum interfiber distance of 62 ± 2.7 µm was found for single fibers with a diameter of 15 µm.

The MEW technique has been predominantly developed with ε-Polycaprolactone (PCL).[159,160] The key advantages of PCL are its low melting temperature of 60 °C and rapid solidification as well as its long-term thermal stability.[160,165] Moreover, PCL is approved by the U.S. Food and Drug Administration (FDA) for certain clinical purposes, is used in tissue engineering research and has a slow degradation rate.[166–168] For these reasons, PCL is named as the "gold standard" for MEW. The ability to print highly ordered scaffolds with a height of 8 mm and cut these scaffolds was proven by using PCL.[169] The printing of different designs with MEW was reported in literature, including box-structured scaffolds but also more complicated designs such as tubes, sinusoid structures with horizontal layer stacking and aortic root scaffolds featuring the sinuses of Valsalva.[162,170–173] Moreover fibrillar, porous scaffolds have been prepared for reconstruction of human tissue matrices of human trabelcular meshwork.[174] Examples of a square-box and a tubular scaffold are shown in figure 1.12.[162,170]

Fiber networks of PCL manufactured by MEW have been successfully used for the reinforcement of soft hydrogels to tailor their mechanical properties.[175–178] This approach offers a fundament for the production of tissue constructs with biological and mechanical compatibility. Furthermore, fiber-hydrogel composites that have mechanical properties similar to that of heart valve were manufatcured.[179,180]

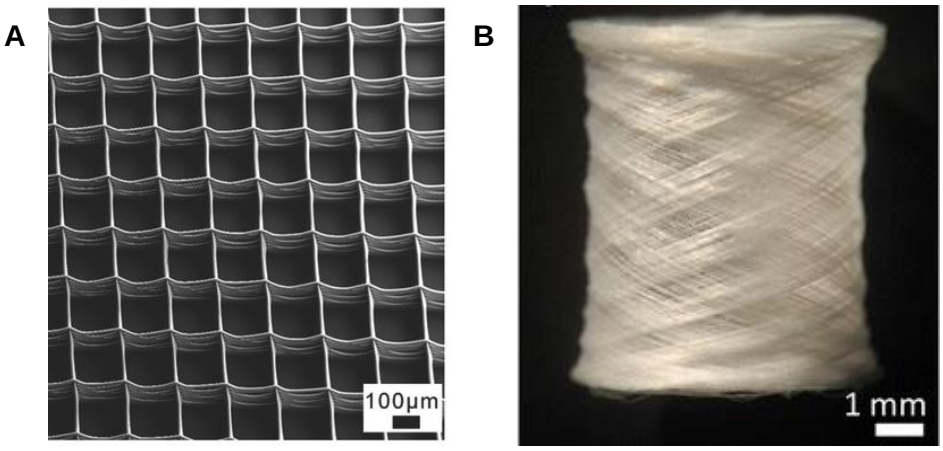


**Figure 1.12:** Examples of A: a square box. Adapted and reproduced with permission (© 2018 The Authors. Published by WILEY-VCH Verlag GmbH & Co. KgaA, Weinheim).[162] B: a tubular-shaped scaffold manufactured by Melt electrowriting (MEW) of PCL. Adapted and reproduced with permission (© The Author(s) 2012. Published with open access at Springerlink.com).[170]

A promising approach in the field of biofabriction is the combination of extrusion-based 3D bioprinting with MEW. One example is inkjet bioprinting of mesenchymal stem cells into box-like MEW scaffolds for the engineering of stratified cartilage tissues.[181] Ruijter et. al. reported the simultaneous printing of PCL MEW fibers and bioinks made of gelantin-methacryloyl embedded with equine-derived mesenchymal stroma cells in a single-step biofabrication process.[182] Porous constructs are printed by MEW followed by the spatial placement of the cell-laden hydrogels inside the scaffold pores to create voluminous and complex hierarchical structures that can resemble the characteristics of functional biological tissues. It was found out that the cells are not influenced by applying high voltages for MEW up to 15 kV and the metabolic activity did not decrease. The strategy of double-printing targets the extension of the biofabrication window as shown in figure 1.13.[182]

Despite its high compatibility with MEW and medical applications PCL has several disadvantages, e.g. its inherent rigidity, opaque properties and high hydrophobicity. PCL fibers do not swell or dissolve in water. Therefore, other materials that can be manufactured by MEW are from great interest to extend the medical application window.

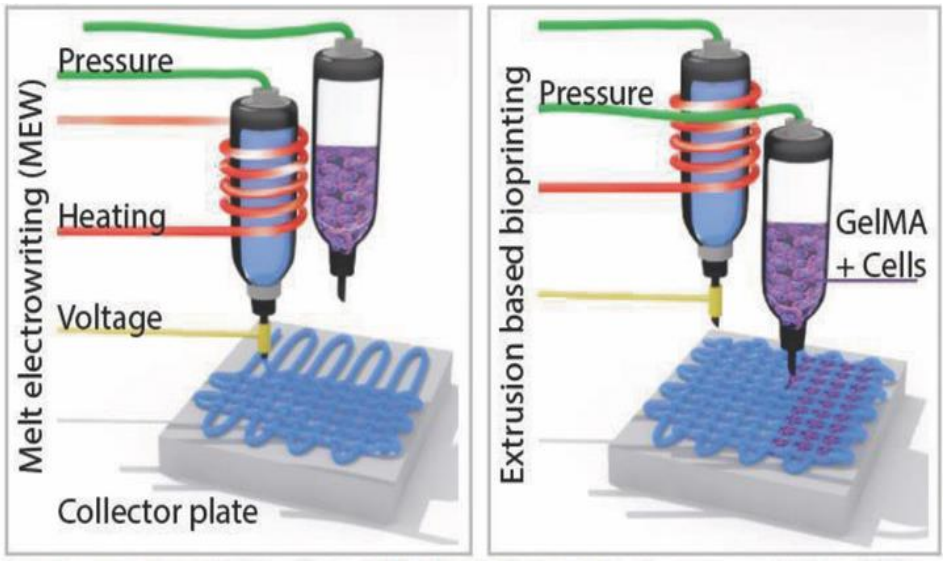


**Figure 1.13**: Setup for simultaneous printing of MEW fibers with PCL and bioinks made of gelantin-methacryloyl (GelMA) and cells. Adapted and reproduced with permission (© 2018 The Authors. Published by WILEY-VCH Verlag GmbH & Co. KgaA, Weinheim).[182]

Several materials besides PCL have been successfully processed via MEW, such as polypropylene, the piezoelectric polymer poly(vinylidene difluoride) (PVDF), polylactide acid (PLA) with incorporated tungsten oxide nanoparticles, poly(lactic-co-glycolic acid), poly-hydroxymetylglycolide-co-ε-caprolactone and poly(dioxanone).[183–188]

With PVDF the collector temperature was varied to adjust the collector temperature. Increasing of the temperature from room temperature to above 100 °C results in improved accuracy and increased fiber bonding allowing the printing of more layers. Further heating leads to fusion and bagging of the fiber layers due to slow solification.[189]

A thermoplastic polycaprolactone-polyurethane elastomer was used for MEW printing in combination with bioprinting of hyaluronic hydrogel for the manufacturing of shape-changing bilayer scaffolds that allow the growth of aligned muscle cells.[190] Another material used in MEW is the water-soluble sugar isomalt. The feasibility to fabricate constructs with perfusable channels with diameters in a wide range between 30 and 200 µm in polydimethylsiloxane moulds by the dissolution of the prepared MEW fibers in aqueous media was shown.[191] Hochleitner et al. reported on MEW of a PLA-PEG-PLA triblock copolymers obtaining a promising polymer/ceramic composite for stimulating bone tissue formation by the addition of 45S5 bioactive glass particles.[192]. This work demonstrated that polymers containing PEG segments are applicable for

MEW. Moreover, the photo-cross-linkable and biodegradable polymer poly(ι-lactide-*co*-ε-caprolactone-*co*-acryloyl carbonate) was processed by MEW.[193] After printing into fibers the material was crosslinked at room temperature by UV irradiation to increase the stiffness of the fibers by factor 10. Stacking behavior properties and lifetime during MEW-printing could be improved by removing the lactide component resulting in poly(ε-caprolactone-*co*-acryloyl carbonate).[194] The polymer was proven to be cytocompatible. Also, liquid crystal elastomers were successfully processed by MEW and croslinked by UV light after printing.[195]

Recently, Nahm et al. reported on melt electrowriting of chemically-crosslinked hydrogels based on hydrophilic poly(ethyl-2-oxazine).[196] Spontaneously, chemical crosslinking of the printed MEW fibers occurs directly after processing by Diels-Alder click chemistry upon cooling. The written scaffolds swell to stable and thermoreversible hydrogels in water with a high water content of 84 %. The crosslinked hydrogels are an appropriate biomaterial class and can be readily functionalized with fluorophores or peptides.

Wu et al. reported on MEW of a hydrophilic supramolecular (ABA)-segmented copolymer consisting of polyethylene glycol with telechelic ureido-pyrimidinone groups that can form quadruple hydrogen bonds.[197] The Upy moieties are shielded by an alkyl spacer from the PEG segment. The printed MEW scaffolds form hydrogels in aqueous solution by showing anisotropic swelling which was assumed to originate from a shear-induced orientation of the crystals.

Another polymer class showing excellent printing behavior in MEW are poly(urea-siloxane) thermoplastic elastomers.[87] Thermoplastic elastomers reveal properties of an elastomer except that chemical crosslinking is replaced by physical crosslinking.[198] Poly(urea-siloxane) is an $(AB)_n$-segmented copolymer consisting of siloxane segments as elastic parts and urea segments as physical crosslinking parts. The hydrogen bonds in the urea segments form a melt upon heating by disassembling and reassemble upon cooling. Therefore, this polymer class is applicable for melt processing. MEW of poly(urea-siloxane) results in highly uniform fibers with diameters of 10 – 20 µm, very excellent fiber stacking capacity and fiber fusion between layers. A drawback of this polymer class is its high hydrophobicity resulting in neither swelling nor dissolving in aqueous and biological media.

# 2 Aim and motivation of the thesis

The hybrid printing of bioinks that contain cells and supporting polymer constructs named as biomaterial inks is a promising approach in the field of biofabrication to achieve structural patterning and enable cell deposition of low viscosity bioinks. Up to now, the reported materials for such supporting constructs are either hydrophobic semicrystalline polymers with opaque properties, such as poly(ε-caprolactone) or materials which are chemically crosslinked after a printing process. There is a need for new polymers that can be processed from the melt via extrusion based 3D printing techniques and have the potential to swell in aqueous media to optically clear hydrogels with adjustable mechanical properties that slowly disintegrate or dissolve after a certain period of time.

In this context, the central goal of this thesis is the development of tailored water-swellable $(AB)_n$-segmented copolymers (figure 2.1) with polyethylene glycol (PEG) segments and bisurea segments as schematically shown. The underlying concept is that the bisurea segments self-assemble by the formation of hydrogen bonds to form physical crosslinks (B) resulting in a mechanically stable polymer at room temperature. The physical crosslinks should disassemble upon heating to obtain processable polymer melts (A). It is the goal to process the materials by melt electrowriting and extrusion based 3D printing techniques to prepare stable 3D constructs. These constructs should have the ability to swell with water and biological media to form hydrogels (C).

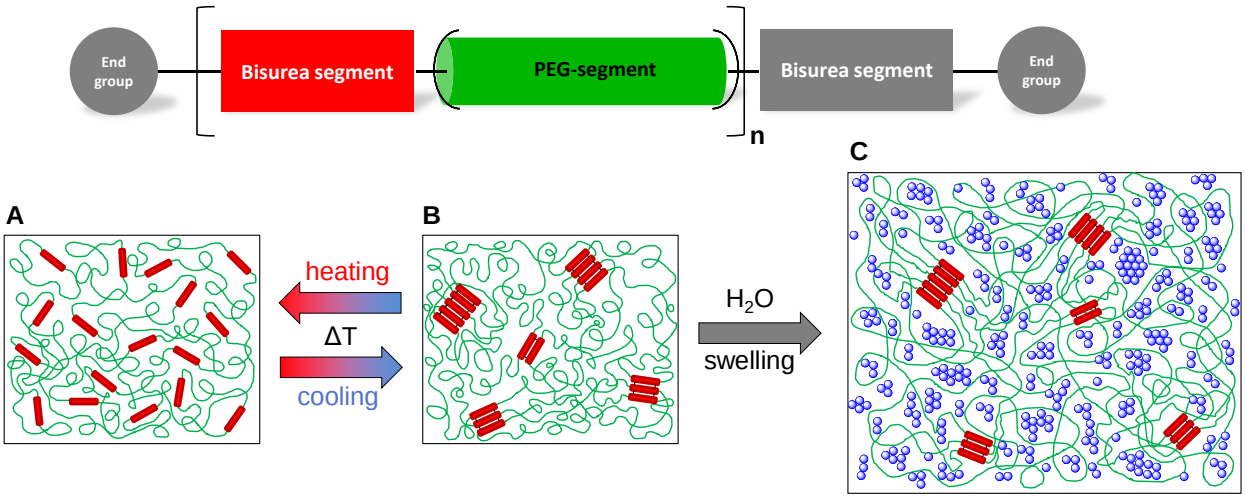


**Figure 2.1:** Schematic representation of $(AB)_n$-segmented copolymers consisting of bisurea segments (red) and polyethylene glycol containing segments (green) with *n* repeating units and end groups (grey). The polymers are illustrated in the melt (**A**), in the solid state (**B**) and in the swollen state as hydrogel (**C**). At elevated temperatures (**A**) the bisurea segments are separated and a processable melt is present. Upon cooling (**B**) the bisurea segments assemble and form physical crosslinks. The $(AB)_n$-segmented copolymers swell with water (blue dots) to a hydrogel (**C**) due to the hydrophilicity of the PEG segments.

Within the class of $(AB)_n$-segmented copolymers there are several possibilities to vary the polymer structure and to tailor the desired polymer properties with respect to processability, stability at printing temperature and swelling ability in aqueous media. The melt viscosity can be adjusted by the degree of polymerization. The chemical structure of the bisurea segments influences the strength of the hydrogen bonds and mainly the reversible transition temperature between elastomer and melt. The length of the PEG segments predominantly determines the mechanical and swelling properties of the hydrogels and the compatibility with bioinks.

The aim of the thesis is to synthesize and characterize new $(AB)_n$-segmented copolymers as biomaterial inks and to reveal structure-property-relations in view of the melt processing temperature, the stability of the polymer melt, the printability, the swelling properties in aqueous solution and the cytotoxicity. Thereby, the desired property spectrum should lead to polymers that form stable hydrogels and also hydrogels that slowly disintegrate or dissolve, in order to broaden the biofabrication window.

In this context, the thesis contains three parts:

1. **$(AB)_n$-segmented copolymers based on polypropylene glycol-b-polyethylene glycol-b-polyethylene glycol (PPG-PEG-PPG) and bisurea segments**

$(AB)_n$-segmented copolymers based on polypropylene glycol-*block*-polyethylene glycol-*block*-polypropylene glycol (PPG-PEG-PPG) segments and bisurea segments should be synthesized and characterized. The preparation of these copolymers can be realized by using commercially available PPG-PEG-PPG diamines which are sold under the trade name Jeffamine®. Structure-property relations should be explored with respect to different lengths of the hydrophilic segments and the chemical structure of the bisurea segments which are responsible for the formation of physical crosslinks. In this series the short hydrophobic polypropylene glycol spacers are expected to support the hydrogen bond formation and to form physical crosslinks in aqueous media.

The main objectives of this chapter are:

- Synthesis of a series of $(AB)_n$-segmented copolymers on a laboratory scale (above 50 g).
- Variation of the melt viscosity by altering the degree of polymerization.
- Investigation of structure-property relations regarding the thermal behavior, mechanical properties and their swelling behavior in aqueous and biological media.
- Investigation of the cytotoxicity of selected $(AB)_n$-segmented copolymers.

## 2. Additive manufacturing of $(AB)_n$-segmented copolymers based on PPG-PEG-PPG and bisurea segments

Extrusion based additive manufacturing techniques are promising methods in the field of biofabrication since they are suitable to print constructs from the melt with different shapes and sizes. Possible extrusion-based additive manufacturing techniques are extrusion based printing (EBP), melt electrospinning (MES) and melt electrowriting (MEW). In the context of this work, MEW was chosen as the focal method. In a cooperation with the *Department of Functional materials in medicine and Densistry, University of Würzburg,* it was given the opportunity to perform the MEW-experiments self. Consequently, the main objectives of this chapter are:

- Selection of suitable $(AB)_n$-segmented copolymers for MEW.
- Determination of the fiber diameter range that can be achieved under reproducible conditions.
- Optimization of the printing parameters with respect to line width, line accuracy and quality of printed structures.
- Preparation of 3D constructs with line widths below 50 µm.
- Investigation of the swelling behavior of the printed 3D constructs.

In addition, initial studies with EBP should be performed by pursuing the following objectives:

- Selection of suitable $(AB)_n$-segmented copolymers for EBP.
- Printing of 3D constructs.
- Investigation of the swelling behavior of the printed 3D constructs.

# 3 Synthesis and characterization of hydrophilic $(AB)_n$-segmented copolymers

## 3.1 Synthesis and molecular characterization

The synthesis of $(AB)_n$-segmented copolymers with bisurea segments is carried out with diamines and diisocyanates as building blocks. Polypropylene glycol terminated polyethylene glycol diamines are used as hydrophilic segments. These diamines are commercially available in different molecular weights under the trade name Jeffamine®. In this thesis Jeffamine® ED-600 with a molecular weight of 600 g mol$^{-1}$ (**1a**), Jeffamine® ED-900 with 900 g mol$^{-1}$ (**1b**) and Jeffamine® ED-2003 with 2000 g mol$^{-1}$ (**1c**) were selected. The polypropylene glycol terminated polyethylene glycol segments are abbreviated as PPG-PEG-PPG in this thesis.

Numerous aliphatic and aromatic diisocyanates are commercially available and in principle applicable as monomers to form the bisurea segments with the above presented Jeffamines®. Since aromatic structures are not preferred for biomedical applications due to their potential toxicity, this work focuses on bisurea segments synthesized from aliphatic and cycloaliphatic diisocyanates. We selected hexamethylene diisocyanate (**2**) as a linear structure, and *trans*-1,4-cyclohexane diisocyanate (**3**) and 4,4'-methylenebis(cyclohexylisocyanate) (**4**) as cycloaliphatic structures. The diisocyanate **4** consists of a mixture of *cis* and *trans* isomers. For the regulation of the degree of polymerization the monofuctional *n*-butylamine (**5**) was used. The chemical structures of the monomers are depicted in figure 3.1.

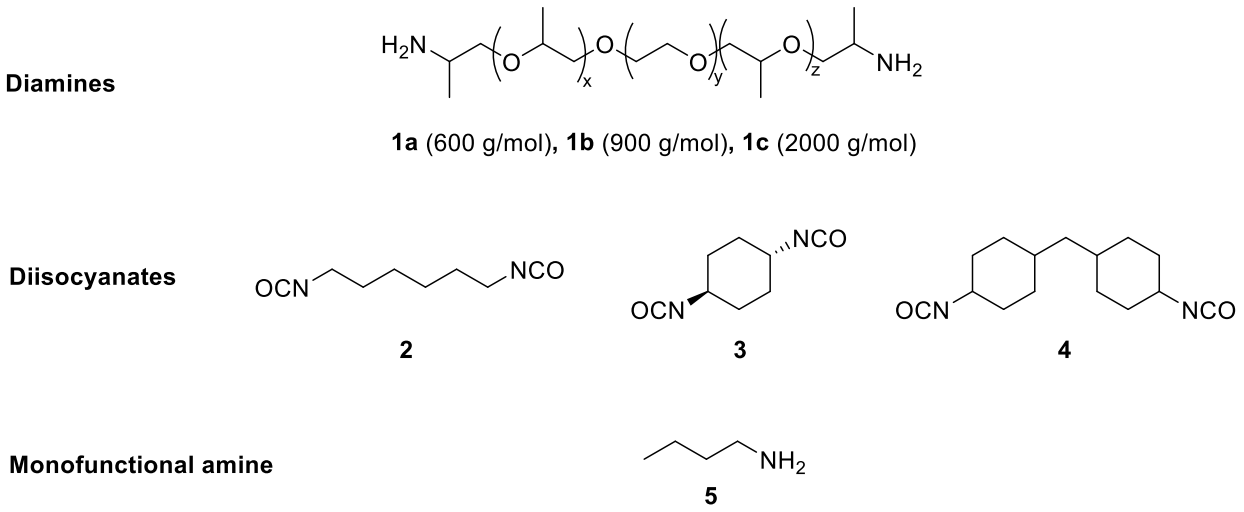


**Figure 3.1**: Chemical structures of diamines **1a** – **1c** and diisocyanates **2** – **4** used for the synthesis of $(AB)_n$-segmented copolymers. The monofunctional amine **5** was used to regulate the degree of polymerization.

The Jeffamines **1a**, **1b** and **1c** were characterized by means of proton NMR and MALDI-TOF mass spectrometry to determine the number of polypropylene glycol (PPG) units. MALDI-TOF spectrum of **1b** is shown in figure 3.2**.** Figure 3.2A reveals a mass distribution with several signals in the range from 500 to 1300 g mol$^{-1}$ with the highest intensities located around 900 g mol$^{-1}$.

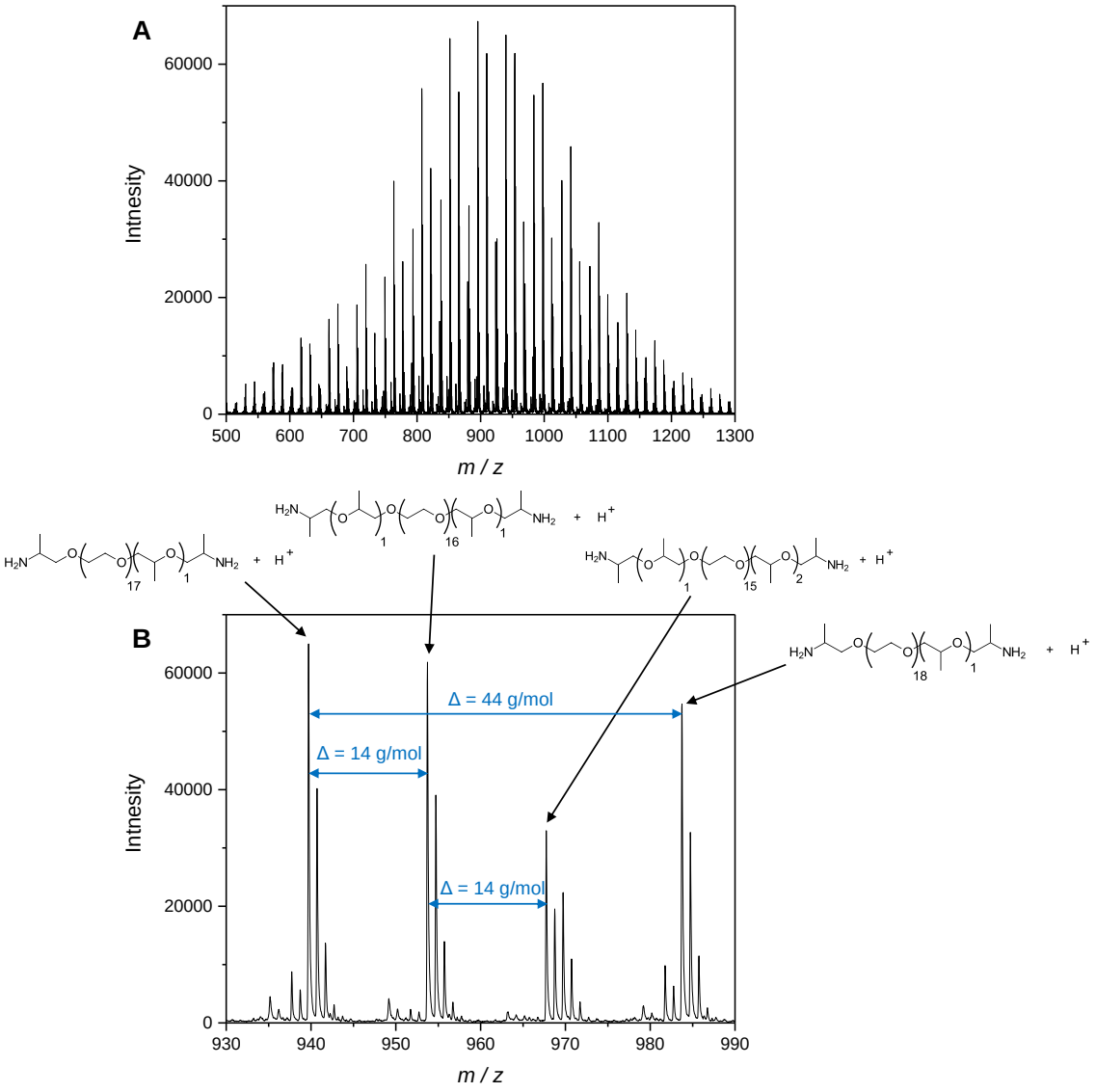


**Figure 3.2. A:** MALDI-TOF of Jeffamine® **1b** revealing the molecular weight distribution. **B:** The Proton series of the Jeffamine® with three, four and five PPO units was verified as shown in a section from 930 to 990 g mol$^{-1}$.

The assignment of the signals to the chemical structure of the Jeffamines was conducted by looking at a section between 930 and 990 g mol$^{-1}$ (figure 3.2B). The section reveals four peak series. Thereby, the first three peak series are separated by a mass of 14 g mol$^{-1}$. This is exactly the mass difference between a PEG and a PPG unit. The distance between the first peak series

with the highest intensities at 939 g mol$^{-1}$ and the fourth series with a peak maximum at 983 g mol$^{-1}$ is 44 g mol$^{-1}$ correlating to one PEG unit. Consequently, the Jeffamine consists of PPG-PEG-PPG oligomers with three different numbers of PPG units. By adding a proton, series with Jeffamines® having three, four and five PPG units could be identified. In the depicted section this correlates with 16 and 17 PEG units.

Proton NMR studies confirmed these results as shown for **1b** in figure 3.7 on page 38. If the integral of the methyl protons is set to 12 which counts for four methyl groups, the PEG and PPG protons show an integral of 80. This correlates with a Jeffamine with averagely four PPG and 16 PEG units resulting in a molecular weight of 938 g mol$^{-1}$. Series with three, four and five methyl groups were also proven in **1a** and **1c** by MALDI-TOF and proton NMR. Consequently, it can be assumed that all three Jeffamines have an average number of about two methylene groups at both ends. Therefore, Jeffamines **1a**, **1b** and **1c** only differ in the number of PEG units, while the number of methylene units is constant with about four in average in each molecule.

Since the stoichiometry is highly relevant in polyaddition reactions the exact average molecular weight was determined by titration with 0.1 M hydrochloric acid in isopropanol solution. The molarity of the hydrochloride acid solution $c$ was proven to be exactly 0.1 mol L$^{-1}$ by titration of dibutyl amine. Every titration was done three times and the molecular mass $M_n$ was determined by using equation (1).

$$M_n = \frac{m_a \cdot z}{V_{eq} \cdot c} \qquad (3.1)$$

The weighted mass of amine and the number of amine end groups is expressed by $m_a$ and $z$, respectively, whereas $V_{eq}$ describes the volume of added 0.1 M hydrochloride acid solution until the equivalent point is reached. The determined molecular weights $M_n$ are depicted in table 3.1. The values match well with the molecular weights $M_n$ given by the supplier. In the following, the experimental determined values (627, 894 and 2018 g mol$^{-1}$) were used to calculate the stoichiometric amounts for the synthesis of the $(AB)_n$-segmented copolymers. For simplicity, the supplier values are used in the further context of this thesis to identify the different Jeffamines.

**Table 3.1**: Characterization of Jeffamines **1a**, **1b** and **1c**: Determined molecular weight $M_n$ by titration compared to the values $M_n$ given by the supplier.

| Sample | 1a | 1b | 1c |
|---|---|---|---|
| $M_n$ (titration) [g mol$^{-1}$] | 627 | 894 | 2018 |
| $M_n$ (supplier) [g mol$^{-1}$] | 600 | 900 | 2000 |

The $(AB)_n$-segmented copolymers based on PPG-PEG-PPG were prepared by a polyaddition reaction following a step growth polymerization mechanism. All syntheses were conducted in tetrahydrofuran as solvent using equimolar amounts of the different Jeffamines® **1a**, **1b** and **1c** and different diisocyanates **2**, **3** and **4** (figure 3.3). The degree of polymerization was regulated by adding monofunctional *n*-butylamine **5** in various ratios $N_{Bu}$ from 0 to 20 mol% prior to the addition of diisocyanate. The influence of the monofuctional monomer on the degree of polymerization can be determined by using the Carothers equation. Assuming a monomer consumption of 100 % the degree of polymerization ***n*** only depends on the stoichiometric imbalance r according to the following equation:[199]

$$\boldsymbol{n} = \frac{1+r}{1-r} \qquad (3.2)$$

Thereby, *r* is influenced by the addition of a monofunctional monomer. With stoichiometric quantity of diamine and diisocyanate *r* only depends on the molar ratio of *n*-butylamine $N_{Bu}$. Assuming the equal reactivity of the diamine and the monofunctional amine the following equation can be applied:

$$r = \frac{1}{1+2\,N_{Bu}} \qquad (3.3)$$

According to equations (3.2) and (3.3) the addition of 5 mol% of **5** ($N_{Bu}$ = 0.05) leads to a calculated degree of polymerization ***n*** of 21 while 10 mol% ($N_{Bu}$ = 0.1) of **5** lowers the degree of polymerization to 11. The addition of **5** strongly influences the degree of polymerization**.** In addition, the end groups of the polymers are predominantly *n*-butyl if **5** is added.

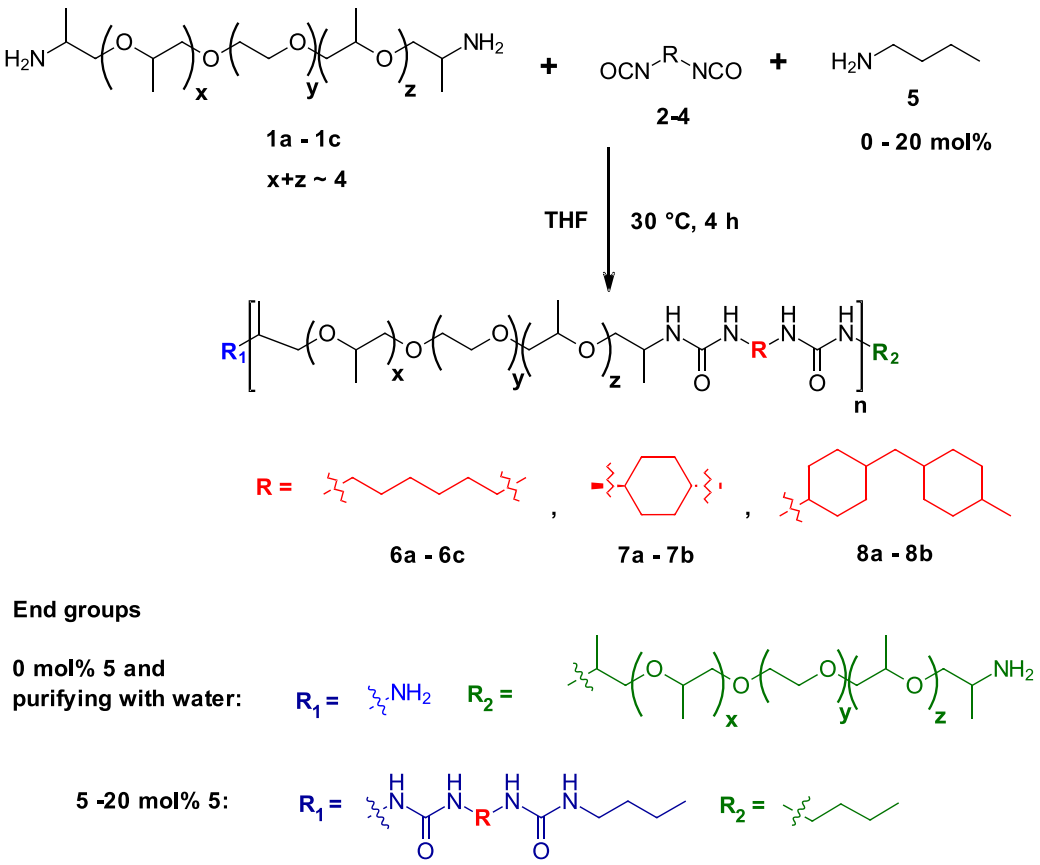


| No. | Amine/Di-isocyanate | $N_{Bu}$ [mol%] | $w_{bydrophil}$ [wt%] | $w_{bisurea}$ [wt%] | No. | Amine/Di-isocyanate | $N_{Bu}$ [mol%] | $w_{hydrophil}$ [wt%] | $w_{bisurea}$ [wt%] |
|---|---|---|---|---|---|---|---|---|---|
| **6a** | **1a / 2** | 0 | 74 | 26 | **7a** | **1b / 3** | 0 | 82 | 18 |
| **6a-1** | **1a /2** | 5 | 74 | 26 | **7b** | **1c / 3** | 0 | 91 | 9 |
| **6a-2** | **1a / 2** | 10 | 74 | 26 | **7b-1** | **1c / 3** | 5 | 91 | 9 |
| **6b** | **1b / 2** | 0 | 82 | 18 | **8a** | **1b / 4** | 0 | 75 | 25 |
| **6b-1** | **1b / 2** | 5 | 82 | 18 | **8a-1** | **1b / 4** | 5 | 75 | 25 |
| **6b-2** | **1b / 2** | 10 | 82 | 18 | **8a-2** | **1b / 4** | 10 | 75 | 25 |
| **6c** | **1c / 2** | 0 | 91 | 9 | **8a-3** | **1b / 4** | 20 | 75 | 25 |
| **6c-1** | **1c / 2** | 5 | 91 | 9 | **8b** | **1c / 4** | 0 | 87 | 13 |
| **6c-2** | **1c / 2** | 10 | 91 | 9 | **8b-2** | **1c / 4** | 10 | 87 | 13 |
| **6c-3** | **1c / 2** | 20 | 91 | 9 | | | | | |

**Figure 3.3**: Synthesis and nomenclature of $(AB)_n$ – segmented copolymers **6 – 8** based on the Jeffamines **1a – 1c** and the diisocyanates **2** – **4**. The molecular weight was controlled by the addition of different amounts $N_{Bu}$ of *n*-butylamine **5**. After purification with water, polymers synthesized without the addition of **5** have amino end groups at both chain ends. With the addition of **5** the end groups are predominantly *n*-butyl. The mass ratios of the hydrophilic PPG-PEG-PPG segments ($w_{hydrophil}$) and the bisurea segments ($w_{bisurea}$) within one repeating unit are listed.

Due to the high reactivity of the isocyanate end groups with water, all syntheses were carried out under dry conditions and an argon atmosphere. In addition, the hygroscopic Jeffamines **1a – 1c** were dried for 16 h at 50 – 65 °C under vacuum to remove water prior to use. Tetrahydrofuran was dried and distilled over potassium hydroxide and potassium. *n*-butylamine **5** was dried and distilled over calcium hydride under argon atmosphere. The Jeffamine and *n*-butylamine were first dissolved in tetrahydrofuran. Afterwards, the diisocyanate was added and the reaction mixture was allowed to stir at 30 °C for 4 h. The reaction mixture turned viscous after a few minutes. The overall polymer concentration in the solution was between 15 and 20 wt%. In the case of copolymers **6a-1**, **6a-2**, and **7a** precipitation or gelation in THF occurred. Therefore, the solvent was changed from THF to anhydrous dichloromethane in these three cases. In dichloromethane no precipitation or gel formation was observed. An overview of 19 synthesized $(AB)_n$-segmented copolymers is given in figure 3.3.

During each polyaddition reaction, a small amount of the reaction solution was withdrawn after 4 h. The solvent was evaporated, and the sample was analyzed by Fourier transformation infrared (FT-IR) spectroscopy to confirm the complete conversion. Except the evaporation of solvent no purification of the copolymers was conducted prior to the measurement. FT-IR spectroscopy revealed the complete conversion of the polyaddition reaction for all synthesized copolymers after 4 h. As an example, figure 3.4 compares the IR spectra of polymer **6b-2** having PPG-PEG-PPG segments with a molecular weight of 900 g $mol^{-1}$ and hexamethylene bisurea segments after 4 h reaction time with the spectra of hexamethylene diisocyanate **3.** The full conversion of the diisocyanate is demonstrated by the disappearance of the diisocyanate vibration signal at 2250 $cm^{-1}$. Additionally, the formation of the urea moieties is visible by the presence of the N-H stretching vibration at 3335 - 3352 $cm^{-1}$, the carbonyl (C=O) stretching vibration at 1620 - 1630 $cm^{-1}$ and the combination of N-H bending and C-N stretching vibration at 1552 - 1569 $cm^{-1}$. Therefore, after a reacting time of 4 h the reaction mixture was cast into Teflon moulds (10 cm x 5 cm x 1 cm). These moulds were covered by a petri dish to prevent dust impurities and the solvent was slowly removed to a large extend by evaporating in the fume hood. Complete removal was done in the vacuum drying oven at 60 °C resulting in films of the $(AB)_n$-segmented copolymers (see experimental).

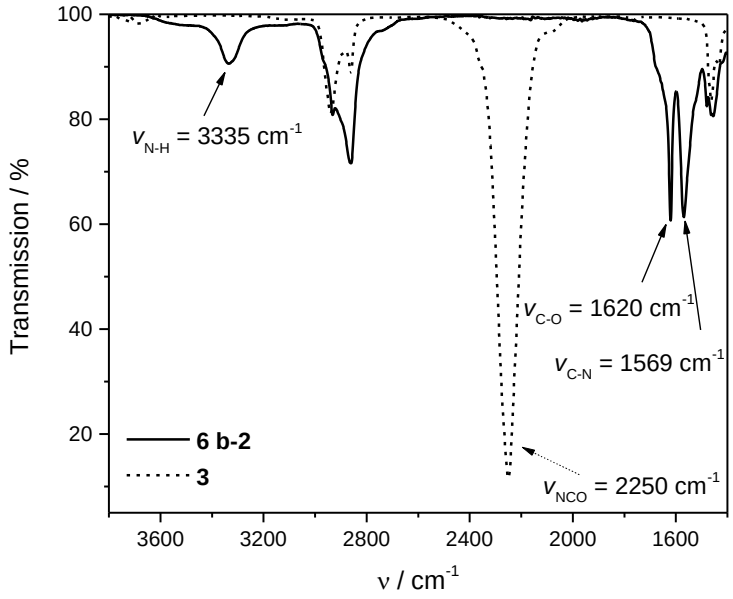


**Figure 3.4**: FT-IR spectra of **6b-2** with PPG-PEG-PPG segments of 900 g mol$^{-1}$ and hexamethylene bisurea segments after 4 h reaction time and hexamethylene diisocyanate **3** for comparison. The spectra reveal the fully conversion of diisocyanate and the formation of the bisurea segments.

Most of the synthesized copolymers are soluble in tetrahydrofuran. Therefore, for the soluble copolymers, size exclusion chromatography (SEC) analysis could be done in the solvent with tetrabutylammoniumbromide (THF-TBAB) in a concentration of 0.25 wt%. In all cases a monomodal peak was found in the high molecular weight range as exemplarily shown for copolymers **6b-2** and **8a-2**. Additionally, a small peak in the low molecular weight range of the diamine was found. Similar observations were made by Meijer group for similar PEG containing $(AB)_n$-segmented copolymers.[90,94] It is most probably that the impurity results from not completely amino group functionalized Jeffamines. Removal of the impurity was first attempted by dissolution of copolymers in dichloromethane and precipitation in diethyl ether followed by washing several times with ether and hexane. However, no purification was observed in SEC analysis.

Successful purification was achieved for all copolymers that disintegrate in aqueous solution by dialysis in water. Here, a membrane with a cut off of approximately 3500 g mol$^{-1}$ was used to remove the low molecular weight impurities. Preparative yields of 70 – 90 % were obtained and SEC analysis after dialysis showed a monomodal distribution with the absence of low-molecular weight peaks as exemplarily shown in figure 3.5A for $(AB)_n$-segmented polymer **6b-2**. Polymers which do not disinegrate in water swell and form a hydrogel. In this case, purification was

achieved by swelling in water and exchanging water for a couple of times. Also in this case, SEC analysis revealed the absence of low molecular weight impurities as exemplarily shown for copolymer **8a-2** in figure 3.5B.[139] The copolymers **6a, 6a-1** and **6a-2** which are not soluble in THF+TBAB were analyzed by SEC in *N*,*N*-dimethylformamide (DMF) with lithium bromide (LiBr) in a concentration of 0,25 wt%.

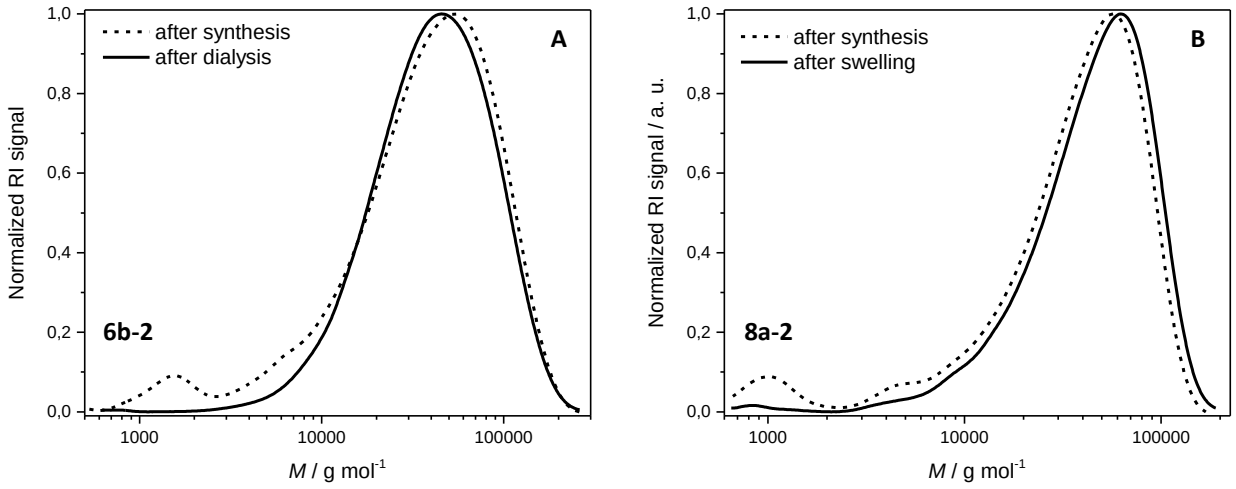


**Figure 3.5. A:** SEC of copolymer **6b-2** with PPG-PEG-PPG segments of 900 g mol$^{-1}$ and hexamethylene bisurea segments after synthesis and after dialysis in water. **B:** SEC of copolymer **8a-2** with PPG-PEG-PPG segments of 900 g mol$^{-1}$ and 4,4'-methylene-bis(cyclohexyl) bisurea segments after synthesis and after swelling and extraction in water. Adapted and reproduced with permission (© 2020 The Authors. Macromolecular Chemistry and Physics published by WILEY-VCH GmbH).[139]

The successful synthesis was also proven by $^1$H-NMR. The spectra of Jeffamine **1b** with a molecular weight of 900 g mol$^{-1}$ and polymer **6b-2** are shown as an example in figure 3.6. The formation of the urea moieties is demonstrated by the broad singlet between 5.6 and 4.8 ppm. Since one $(AB)_n$ unit consists of two urea moieties with 4 protons the integral was calibrated to 4. Two signals appeared at 1.3 and 1.5 ppm, respectively. They can be assigned to the protons **h** and **I** of the hexamethylene unit. The protons **j** located adjacent to the urea groups show up around 3.2 ppm as a broad singlet due to the low resolution of the multiplets. The integral was determined to be around 4 as expected. The multiplet at the spectra of the Jeffamine **1b** in the same range belongs to the protons of the amine end groups. The triplet at 0.9 ppm with an integral of 0.52 can be assigned to the methyl protons **k** of the butyl end groups. Assuming that all end groups are *n*-butyl the integral of single proton belonging to a methyl end group is 0.09. Consequently, the degree of polymerization *n* is 11 which exactly correlates to the theoretical *n*

calculated by equations (3.2) and (3.3). Therefore, the NMR spectrum indicates that *n*-butylamine was incorporated into the polymer. The methylene protons of the butyl end group overlap with protons **h**, **I** and **PPG-Me.** Therefore, the overall integral is higher than 20.

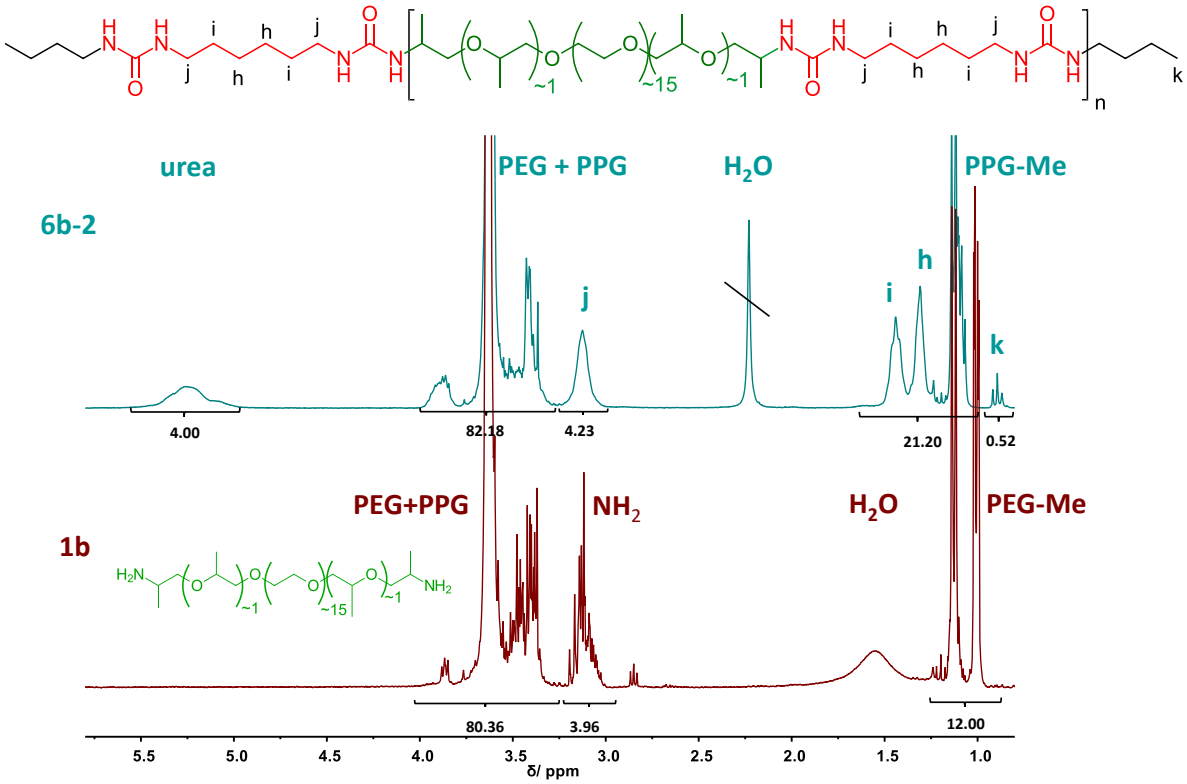


**Figure 3.6:** $^{1}$H-NMR of Jeffamine ED-900 **1b** and copolymer **6b-2** which was successfully synthesized from **1b** with hexamethylene diisocyanate and 10 mol% *n*-butylamine (solvent: $CDCl_3$).

The isocyanate end groups react with water during the purification step. By release of carbon dioxide an amino group is formed in a second step. As result of the purification with water the copolymers not regulated with **5** have amino end groups at both ends.

In the next step the number average molecular weights $M_n$, the mass average molecular weights $M_w$ and the polydispersities were determined from the SEC analysis. The SEC results of all $(AB)_n$-segmented copolymers are summarized in table 3.2. Furthermore, the number average molecular weights $M_n$ were also used to calculate the degree of polymerization $X_n$ by the following equation:

$$X_n = \frac{M_n}{M_{JA}+M_{DI}+x\,M_{Bu}} \qquad (3.4)$$

$M_{JA}$ and $M_{DI}$ and $M_{Bu}$ describe the molecular weights of the Jeffamine, the diisocyanate and *n*-butylamine with $x$ = 0 – 0.2 depending on the amount of *n*-butylamine. The calculated values

were compared with theoretical $X_{n,th}$ by using equation (3.2). The SEC results reveal that $M_n$ and $X_n$ decrease with an increasing amount of added *n*-butylamine in all copolymer series. This is further illustrated in figure 3.7 where the molecular weight distributions of the copolymer series **6c-1** and **6c-3** made from Jeffamine **1c** and **HMDI** and the polymer series (**8a** – **8a-3**) made from Jeffamine **1b** and **m-b-CHDI** (**8a** – **8a-3**) are depicted. For both polymer series the molecular weight distribution is shifted to lower molecular weight with increasing amount of *n*-butylamine ($BuNH_2$). As a result, SEC analysis confirms the regulation of the degree of polymerization by the addition of a monofunctional amine. The calculated values for $X_n$ are higher as compared to the theoretical values determined by the Carothers equations. Moreover, the differences of $X_n$ within a polymer series is lower. This can be explained by the polystyrene calibration resulting in too high molecular weights shown in the SEC. Moreover, the deviations of the polystyrene calibration can vary for different molecular weights. Additionally, the increase of the length of the PPG-PEG-PPG segments from 900 to 2000 g $mol^{-1}$ and maintain of the amount of added monofunctional amine result in higher $M_n$ and $M_w$ values as expected. Polymers with different bisurea segments were not compared due to possible different interactions with the SEC columns. Most of the copolymers have poly dispersities between 1.50 and 2.60 which are typical for step-growth polymerizations. Comparable molecular weight distributions were also obtained for similar $(AB)_n$-segmented copolymers with PEG segments.[93]

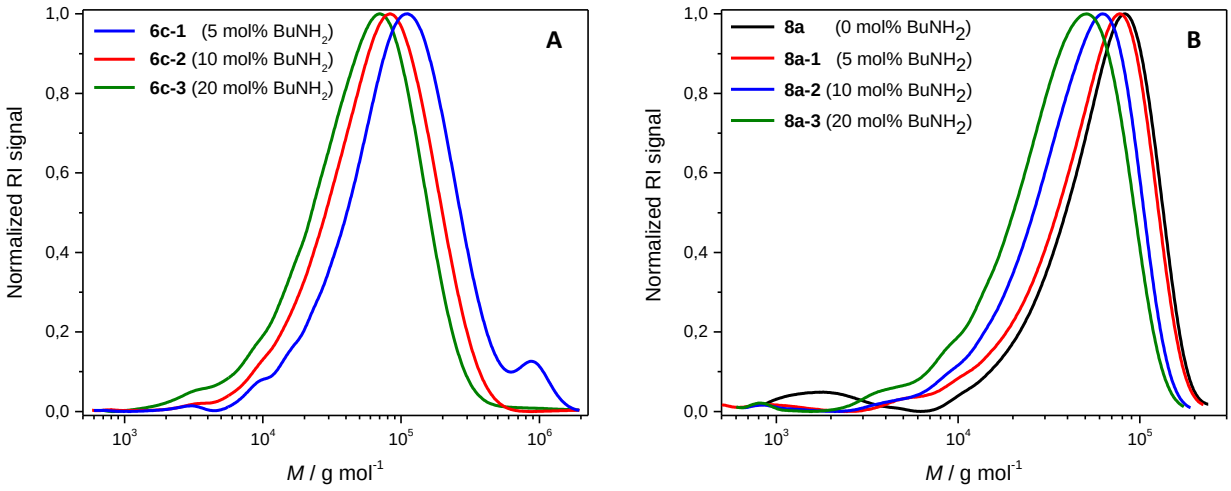


**Figure 3.7. A:** SEC of purified copolymers **6c-1**, **6c-2**, **6c-3** with 91 wt% PPG-PEG-PPG segments and 9 wt% hexamethylene bisurea segments after purification. **B:** SEC of purified polymers **8a**, **8a-1**, **8a-2**, **8a-3** with 75 wt% PPG-PEG-PPG segments and 25 wt% 4,4'-methylene-bis(cyclohexyl) bisurea segments. Adapted and reproduced with permission (© 2020 The Authors. Macromolecular Chemistry and Physics published by WILEY-VCH GmbH).[139]

**Table 3.2**: Overview of all synthesized $(AB)_n$-segmented copolymers with hydrophilic PPG-PEG-PPG segments and bisurea segments together with the number-average molecular weight $M_n$, weight-average molecular weight $M_w$ and poly dispersion index $Đ$ determined by SEC analysis in THF+TBAB solution with polystyrene calibration. The degree of polymerization $X_n$ was calculated from the $M_n$ values and was compared with the theoretical degree of polymerization $X_{n,th}$ In addition, the mass ratios of the hydrophilic PPG-PEG-PPG segments ($w_{hydrophil}$) and the bisurea segments ($w_{bisurea}$) within the repeating unit are listed.

| | Jeffamine ($g\ mol^{-1}$)/ Diisocyanate | $N_{Bu}$ [mol%] | $M_n$ [kg $mol^{-1}$] | $M_w$ [kg $mol^{-1}$] | $Đ$ | $X_n$ | $X_{n,th}$ | $w_{hydrophil}$ [wt%] | $w_{bisurea}$ [wt%] |
|---|---|---|---|---|---|---|---|---|---|
| **6a** | 600 / HMDI | 0 | 59.4[1] | 118[1] | 2.0[1] | 77 | ∞ | 74 | 26 |
| **6a-1** | 600 / HMDI | 5 | 23.6[1] | 43.5[1] | 1.84[1] | 31 | 21 | 74 | 26 |
| **6a-2** | 600 / HMDI | 10 | 18.4[1] | 33.4[1] | 1.81[1] | 24 | 11 | 74 | 26 |
| **6b** | 900 / HMDI | 0 | -[2] | -[2] | -[2] | | ∞ | 82 | 18 |
| **6b-1** | 900 /HMDI | 5 | 41.2 | 61.6 | 1.49 | 39 | 21 | 82 | 18 |
| **6b-2** | 900 / HMDI | 10 | 30.1 | 51.0 | 1.69 | 28 | 11 | 82 | 18 |
| **6c** | 2000 /HMDI | 0 | -[2] | -[2] | -[2] | | ∞ | 91 | 9 |
| **6c-1** | 2000 /HMDI | 5 | 62.8 | 158.6 | 2.51 | 29 | 21 | 91 | 9 |
| **6c-2** | 2000 / HMDI | 10 | 42.1 | 91.9 | 2.17 | 19 | 11 | 91 | 9 |
| **6c-3** | 2000 / HMDI | 20 | 29.1 | 74.5 | 2.56 | 13 | 6 | 91 | 9 |
| **7a** | 900 / CHDI | 0 | 17.7 | 38.4 | 2.17 | 17 | ∞ | 82 | 18 |
| **7b** | 2000 / CHDI | 0 | 50.3 | 100.0 | 1.99 | 23 | ∞ | 91 | 9 |
| **7b-1** | 2000 / CHDI | 5 | 43.1 | 86.2 | 2.00 | 20 | 21 | 91 | 9 |
| **8a** | 900 / mb-CHDI | 0 | 43.8 | 68.7 | 1.57 | 38 | ∞ | 75 | 25 |
| **8a-1** | 900 / mb-CHDI | 5 | 39.6 | 65.2 | 1.64 | 34 | 21 | 75 | 25 |
| **8a-2** | 900 / mb-CHDI | 10 | 37.0 | 59.2 | 1.60 | 31 | 11 | 75 | 25 |
| **8a-3** | 900 / mb-CHDI | 20 | 30.8 | 52.4 | 1.70 | 26 | 6 | 75 | 25 |
| **8b** | 2000 / mb-CHDI | 0 | 63.2 | 110.2 | 1.74 | 29 | ∞ | 87 | 13 |
| **8b-2** | 2000 / mb-CHDI | 10 | 54.2 | 100.9 | 1.77 | 25 | 11 | 87 | 13 |

1: SEC analysis was done in DMF-LiBr instead of THF+TBAB solution with a polystyrene calibration.
2: The polymer was not completely soluble in THF-TBAB solution.

## 3.2 Investigation of hydrogen bonding formation

The existence and strength of the hydrogen bonds between the urea groups was examined by FT-IR spectroscopy for several $(AB)_n$-segmented copolymers. Meijer and Coleman did intensive infrared studies on polyureas and found that the frequencies of the N-H and C=O stretching vibration decrease with increasing hydrogen bonding strength as shown in figure 3.8.[85,200] This corresponds to an increase of the wave number $\tilde{\nu}$. In contrast, the wave number of the combination of N-H bending and C-N stretching vibration (amide II band) decreases with increasing hydrogen bond strength.[85]

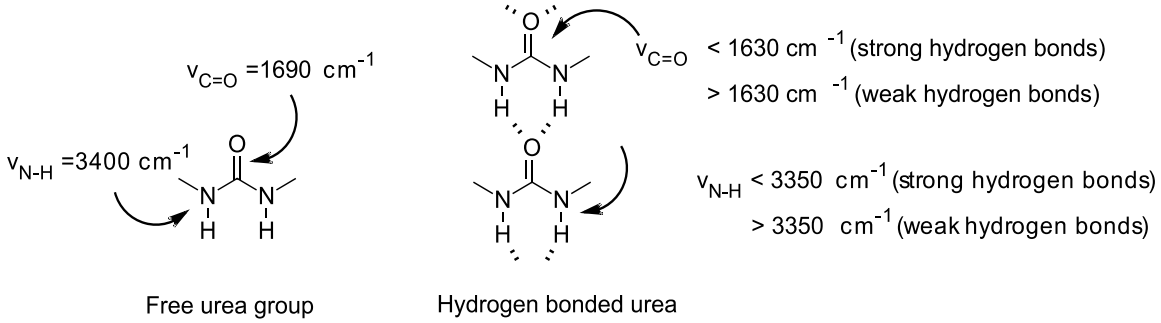


**Figure 3.8:** Infrarot spectroscopy vibrations of polyurea hydrogen bonds (cite Meijer, Coleman). The strength of the hydrogen bonds have influence on both the carbonyl (C=O) and N-H stretching vibrations. Both vibrations are shifted to lower wave with increasing hydrogen bond strength. Adapted and reproduced with permission (© 2005, American Chemical Society).[85]

The influence of the chemical structure of the bisurea segments and the length of the PPG-PEG-PPG segments on the strength of the hydrogen bonds was investigated by FT-IR spectroscopy at room temperature. Solution casted polymer films were used for the measurements. Table 3.3 reveals that hydrogen bonding exists in all investigated copolymers at room temperature due to the N-H and C-O stretching vibrations are far below 3400 and 1690 cm$^{-1}$, respectively. Copolymers with bisurea-hexamethylene, *trans*-1,4-cyclohexane and methylene-(bis-cyclohexyl) segments were compared. Figure 3.9 reveals the FT-IR spectra of copolymers **6b**, **7a** and **8a**. All three copolymers have a PPG-PEG-PPG segments of 900 g mol$^{-1}$ and were synthesized without molecular weight regulation. Therefore, they only differ in the chemical structure of the bisurea segment. FT-IR spectra show that hexamethylene and *trans*-1,4-cyclohexane-based bisurea segments lead to stronger hydrogen bonding as compared to bisurea-4,4'-methylenebis(cyclohexane) segment as proven by the shift of the N-H and carbonyl stretching

vibration to higher wave numbers and the shift of the amide II band to lower wave numbers. Furthermore, signal broadening was higher in polymer **8a**. The same trend was observed for copolymers with extended PPG-PEG-PPG segments of 2000 g mol$^{-1}$. It is assumed that the results can be explained by sterically hindrance of the bulky structure of 4,4'-methylenebis(cyclohexane). Additionally, the bisurea segment exists as isomeric mixture which further lowers the interaction between the urea groups. The other two bisurea segments are isomerically pure.

**Table 3.3:** FT-IR analysis of $(AB)_n$-segmented copolymers.

| | $M_{Jeffamine}$ [g mol$^{-1}$] | Diisocyanate | $\tilde{\nu}_{N-H}$ [cm$^{-1}$] | $\tilde{\nu}_{C=O}$ [cm$^{-1}$] | $\tilde{\nu}_{amideII}$ [cm$^{-1}$] |
|---|---|---|---|---|---|
| **6a** | 600 | HMDI | 3338 | 1622 | 1566 |
| **6b** | 900 | HMDI | 3335 | 1621 | 1569 |
| **6b-1** | 900 | HMDI | 3335 | 1621 | 1569 |
| **6b-2** | 900 | HMDI | 3335 | 1620 | 1569 |
| **6c** | 2000 | HMDI | 3340 | 1624 | 1568 |
| **6c-2** | 2000 | HMDI | 3345 | 1622 | 1573 |
| **7a** | 900 | CHDI | 3321 | 1625 | 1573 |
| **7b** | 2000 | CHDI | 3322 | 1626 | 1573 |
| **8a** | 900 | m-b-CHDI | 3347 | 1629 | 1554 |
| **8a-2** | 900 | m-b-CHDI | 3352 | 1630 | 1552 |
| **8b** | 2000 | m-b-CHDI | 3354 | 1630 | 1552 |
| **8b-2** | 2000 | m-b-CHDI | 3360 | 1635 | 1553 |

Interestingly, the carbonyl vibration is shifted to higher values for copolymers with hexamethylene bisurea segments as compared to copolymers with bisurea-*trans*-1,4-cyclohexane segments whereas the opposite is observed for the N-H stretching vibration. The length of the PPG-PEG-PPG segments and the degree of polymerization have no significant influence on the strength of the hydrogen bonds in the copolymers.

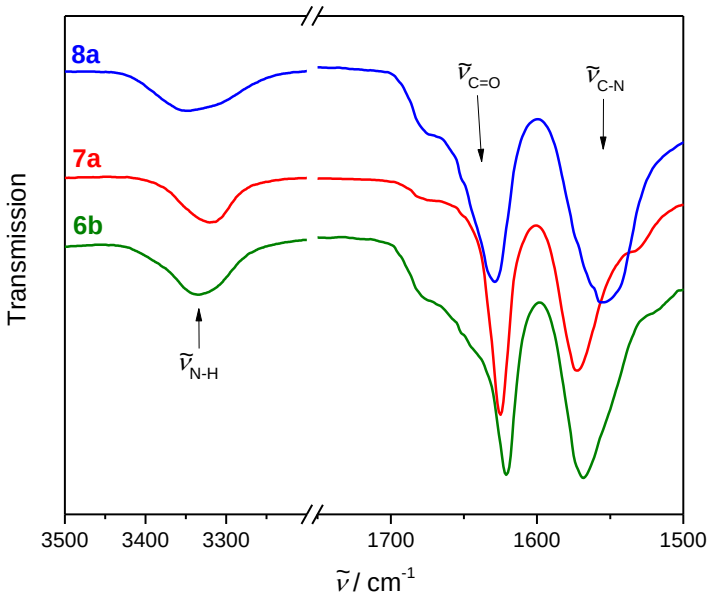


**Figure 3.9:** Influence of the chemical structure in the bisurea segment on the hydrogen bonding strength between the urea units. They can be determined by the N-H stretching vibration, the carbonyl stretching vibration and the combination of N-H bending and C-N stretching vibration. Polymers **6b** having hexamethylene bisurea segments and **7a** having *trans*-1,4-cyclohexane bisurea segments form stronger hydrogen bonds as compared to **8a** with 4,4'-methylene-bis(cyclohexyl) bisurea segments.

## 3.3 Characterization of thermal and rheological properties

The thermal properties of the $(AB)_n$-segmented copolymers were characterized by several manners:

*Differential Scanning Calorimetry (DSC)***:** DSC analysis was conducted to explore the melting and crystallization transitions of the PPG-PEG-PPG segments and the bisurea segments. The samples were placed in an aluminum pan without previous melting. The first *cooling* and second *heating* curves were recorded with a rate of 10 K min$^{-1}$ if not mentioned differently.

*Polarization microscopy:* Temperature dependent polarization microscopy was used to investigate the crystallinity of the PPG-PEG-PPG segments at room temperature. Moreover, the copolymers were heated with a rate of 10 K min$^{-1}$ to study the flow at elevated temperatures which occurs by the transition from the elastic to viscous melt state due to the disassembly of the physical crosslinks.

*Dynamic Mechanical Thermal Analysis (DMTA) – Single cantilever method:* In the single cantilever method the sample is placed as solution-casted film in the sample holder which is bent without previous *heating*. The first *cooling* and the second *heating* curves with a rate of 2 K $min^{-1}$ were recorded. In this experiment, the temperature range of the transition can be determined but not the mechanical properties. The storage and loss moduli are recorded for both the polymer and steel pocket simultaneously. Therefore, only the qualitative variation of the moduli induced by thermal transitions of the copolymer can be determined. This method was used to determine the glass transition temperatures upon *heating* and *cooling* and to investigate if the disassemble of the hydrogen bonds of the bisurea segments upon *heating* and reassemble upon *cooling*. The storage modulus *E*' and the loss factor tan $\delta$ were recorded. Thereby, the loss factor indicates a peak at the glass transition.

*Dynamic mechanical thermal analysis (DMTA) – Tension geometry method:* The tension geometry method additionally allows the quantitative determination of the storage modulus and the loss modulus *E''* and the transition between elastic and viscous behavior by the intersection of the storage and the loss modulus. On the other hand, only the first *heating* curve can be recorded since the sample loses its shape geometry after melting. For tension geometry measurements films which were prepared from the melt in a press were used. The *heating* and *cooling* rate were 2 K $min^{-1}$ for both methods.

*Oscillation shear rheology:* The melt viscosity and the storage and loss modulus can be measured by oscillation rheology. For the storage and loss modulus the first *cooling* and second *heating* curve were recorded to figure out the hysteresis effect. The melt viscosity is an important parameter for extrusion based additive manufacturing. Therefore, the temperature-dependent viscosity of the polymers was measured upon *cooling* from the polymer melt. Rheology and viscosity measurements were conducted by using a melt-pressed polymer sample.

In the following the thermal properties of the $(AB)_n$-segmented copolymers will be discussed for copolymer series with different bisurea segments and increasing length of the PPG-PEG-PPG segments.

### 3.3.1 $(AB)_n$-segmented copolymers with hexamethylene bisurea segments

As first class, $(AB)_n$-segmented copolymers with hexamethylene-bisurea segments will be discussed. Within this class, the thermal properties of 9 different copolymers were characterized. The chemical structure of these copolymers is shown in figure 3.10. Copolymers **6a, 6a-1** and **6a-2** consist of 74 wt% PPG-PEG-PPG segments of a molecular weight of 600 g $mol^{-1}$ and 26 wt% hexamethylene bisurea segments. The average degree of polymerization is 77 for **6a**, 31 for **6a-1** and 24 for **6a-2** as determined from SEC analysis. Copolymers **6b**, **6b-1** and **6b-2** consist of 82 wt% PPG-PEG-PPG segments of a molecular weight of 900 g $mol^{-1}$ and 18 wt% hexamethylene bisurea segments. The average degree of polymerization could not be determined for **6b** since no SEC measurement could be conducted. The reason for this is that the copolymer is not soluble in the solvent that is used as eluent. The degree of polymerization of **6b** is expected to be higher as for **6b-1** with an average degree of polymerization of 39 and **6b-2** of 28. Copolymers **6c**, **6c-1, 6c-2** and **6c-3** consist of PPG-PEG-PPG units with 91 wt% with a molecular weight of 2000 g $mol^{-1}$ and 9 wt% hexamethylene bisurea segments. The determined average degree of polymerization is 29 for **6c-1**, 19 for **6c-2** and 13 for **6c-3**. **6c** is expected to have a higher degree of polymerization, tough, it could not be determined due to insolubility of the copolymer in the SEC eluent.

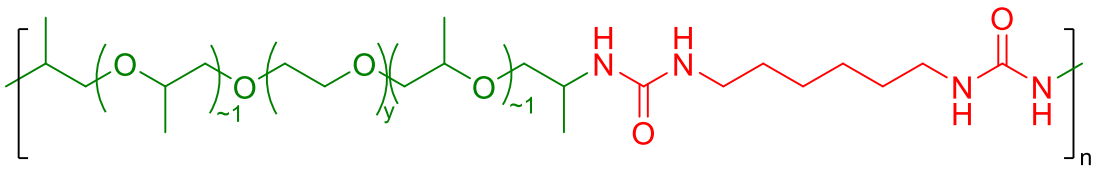


**6a, 6a-1, 6a-2; 6b, 6b-1, 6b-2; 6c, 6c-1, 6c-2, 6c-3**

**Figure 3.10:** Chemical structure of the repeating unit of the series of $(AB)_n$-segmented copolymers with PPG-PEG-PPG segments and hexamethylene bisurea segments.

***Copolymers with a content of 74 wt% hydrophilic segments and 26 wt% bisurea segments***

First, the *Differencial Scanning Calorimetry* measurements of copolymer **6a** are discussed. The molecular weight of **6a** was not regulated. In the DSC measurements the sample was first heated to 180 °C to remove the thermal history. Upon first *cooling* (blue curve) two broad exothermic peaks between 90 and 50 °C are visible as depicted in figure 3.11. The transitions correspond to the assembly of the bisurea segments. It needs to be taken into account that the *cooling* rate is slower than 10 K $min^{-1}$ below -20 °C due to insufficient *cooling* of the instrument in this temperature range. Thus, thermal transitions below -20 °C were not evaluated upon *cooling* for the $(AB)_n$-segmented copolymers in this work. The second *heating curve* (red) shows a glass transition temperature at - 41 °C for the PPG-PEG-PPG segments. Several endothermic peaks correspond to the stepwise disassembly (melting) of the hydrogen bonding segments over a very broad temperature range from 15 to 160 °C. The broad melting transitions with several peaks in the DSC can also be found in thermoplastic polymers as also shown in literature, for example for thermoplastic polyurethane elastomers.[201] Compared to **6a** the DSC curves of molecular weight regulated copolymers **6a-1** and **6a-2** with lower degree of polymerization (see attachment 1) showed no significant differences.

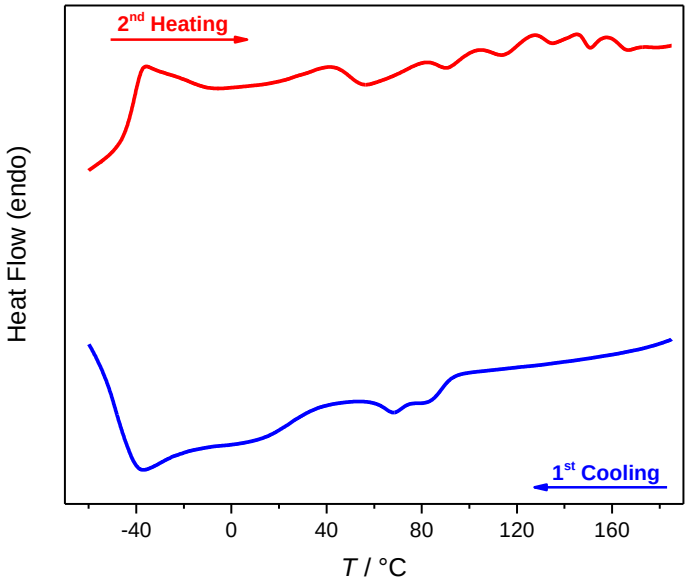


**Figure 3.11:** DSC curves of **6a** with 74 wt% PPG-PEG-PPG segments and 26 wt% hexamethylene bisurea segments. A glass transition of the PPG-PEG-PPG segments at -41 °C and a stepwise melting of the bisurea segments are visible.

The thermal transitions of copolymer **6a** were also characterized by *Dynamic Mechanical Thermal Analysis - Single cantilever method*. The sample was first heated to 150 °C. Then, the first *cooling* and second *heating curves* were recorded. The elastic modulus *E'* (figure 3.12A) and the loss factor tan *δ* (figure 3.12B) were examined. The first *cooling curve* of *E'* reveals a slight increase between 100 and 30 °C indicating the assembly of the bisurea segments. This transition is also visible in the *cooling* curve of tan *δ* as a broad peak. A very steep increase of *E'* below -40 °C results from the glass transition of the PPG-PEG-PPG segments. Tan *δ* results at this temperature in a sharp peak. The peak maximum was used to report the values for the glass transition temperature for all investigated $(AB)_n$-segmented copolymers in this thesis. For **6a** a glass transition temperature ($T_g$) of -42 °C upon *cooling* was determined. The *heating curves* of *E'* and tan *δ* (red) show a glass transition temperature of -39 °C. This value is slightly higher compared to the telechelic PPG-PEG-PPG diamine **1a** which was used for the synthesis of **6a** with a $T_g$ of -49 °C. In the literature a glass transition temperature of -42 °C is reported for polyethylene glycol with a molecular weight of 600 g mol$^{-1}$.[202] The second *heating curve* revealed a broader multistep decrease of *E'* upon *heating* starting around 50 °C. This transition results from the breaking of the hydrogen bonds between the bisurea segments. This disassembly of the bisurea segments is also indicated by a broad peak in the *heating curve* of tan *δ*.

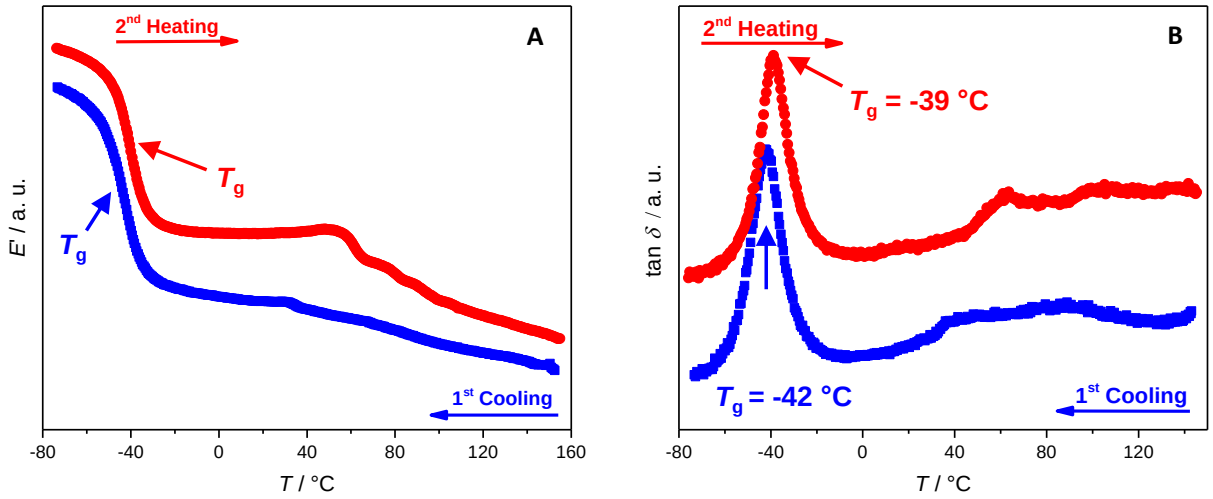


**Figure 3.12:** Dynamic mechanical thermal analysis of **6a** with 74 wt% hydrophilic segments and 26 wt% bisurea segments using the single cantilever method (*cooling* and *heating* rate: 2 K min$^{-1}$, frequency: 0.5 Hz). **A:** The elastic modulus (*E'*) shows a sharp change around -40 °C (*cooling* and *heating*) indicating the glass transition of the PPG-PEG-PPG segments. The decrease of the elastic modulus *E'* starting around 50 °C upon *heating* corresponds to the disassembly of the hydrogen bonds. **B:** The loss factor (tan *δ*) reveals the glass transition of the PPG-PEG-PPG segments at – 39 °C upon *heating* and at -42 °C upon cooling. The assembly and disassembly of the urea hydrogen bonds are shown by the broad peak in the range between 120 and 20 °C upon *cooling* and 50 - 120 °C upon *heating*.

In the *Dynamic Mechanical Thermal Analysis - Tension geometry method* of **6a** the elastic modulus *E'* (blue) reveals a steep decrease by one order of magnitude between -45 and -30 °C upon first *heating* as depicted in figure 3.13. This transition corresponds with the glass transition of the PPG-PEG-PPG segments. Several approaches for the determination of the glass transition temperature ($T_g$) are reported in literature, e.g. by using the maximum of *E''* or the inflection point of *E'*.[203] In this thesis the turning point of *E'* is reported as $T_g$. A glass transition temperature value of -34 °C was determined for **6a**. This value correlates quite well with the glass transition temperature at -39 °C found with the DMTA-single cantilever method. Upon further *heating E'* remains constant at around $10^8$ Pa within a wide range from -30 to 60 °C. A second decrease of E' from $10^8$ to around $5 \cdot 10^4$ Pa can be seen starting at 60 °C. This transition results from the disassembly of the bisurea segments. Both transitions are also visible in the curve of the viscous modulus *E''* (green). *E''* is located below *E'* upon *heating* up to the crossover temperature $T_{cross}$ at 85 °C showing that the copolymer is in the elastic regime below this temperature. The intersection between *E'* and *E''* reveals the transition from elastic to viscous behavior. Above 85 °C *E''* is higher as *E'* and **6a** is in the viscous melt. The copolymer is completely molten above 120 °C when both *E'* and *E''* reach a plateau.

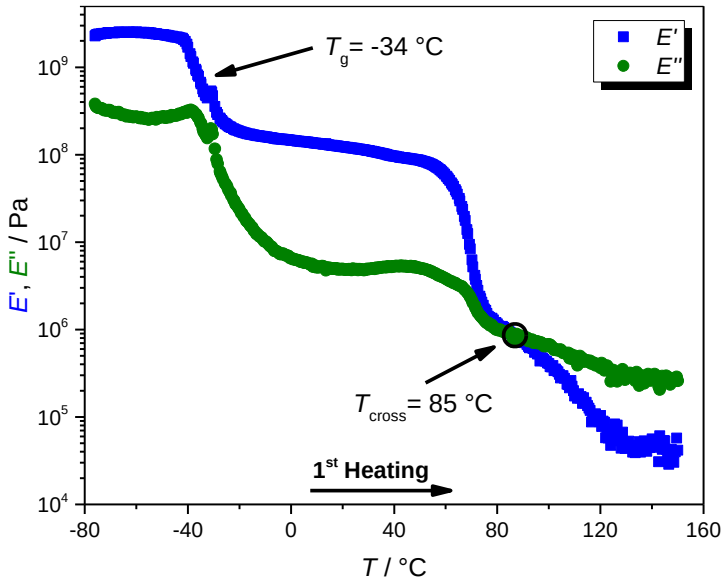


**Figure 3.13:** Dynamic mechanical thermal analysis of **6a** with 74 wt% hydrophilic segments and 26 wt% hexamethylene bisurea segments using the tension geometry method (*heating* rate: 2 K $min^{-1}$, frequency: 1 Hz). The turning point of the elastic modulus (*E'*) at -34 °C corresponds to the glass transition of the PPG-PEG-PPG segments. The transition from elastic to viscous behavior occurs at 85 °C by the intersection of the elastic and viscous module (*E''*).

The elastic (G') modulus and loss modulus (G'') of **6a** were also investigated by *Oscillation shear rheology*. The sample was first heated to 140 °C. Afterwards, the first *cooling* (blue) and second *heating* (red) *curve* of the elastic modulus *G*' and viscous modulus *G*'' were recorded in a temperature range between 20 and 140 °C (figure 3.14). Upon *cooling G*' increases from $5 \cdot 10^3$ to $2 \cdot 10^7$ Pa within the recorded temperature range, whereby a steeper increase is observed from starting around 45 °C. *G*'' increases between 80 and 35 °C less pronounced than *G*'. The intersection between *G*' and *G*'' occurs at 60 °C. Above 60 °C, *G*'' is higher as *G*' and the copolymer is in the viscous state. Below 60 °C, *G*'' is lower as *G*' and the copolymer is in the elastic state.

The second *heating curve* reveals a strong decrease of *G*' between 55 and 65 °C followed by four further small stepwise transitions up to a temperature of 130 °C. *G*'' decreases less pronounced as *G*' between 50 and 100 °C. The transition from elastic to viscous behavior indicated by the intersection of *G*' and *G*'' is found around 85 °C. This value matches with the intersection found in the tension geometry DMTA measurement discussed before. The hysteresis of 25 °C between first *cooling* and second *heating* can be explained by a later formation of strong hydrogen bonding of the bisurea segments upon *cooling*. Strong hydrogen bonding was confirmed in FT-IR analysis as discussed in chapter 3.2.

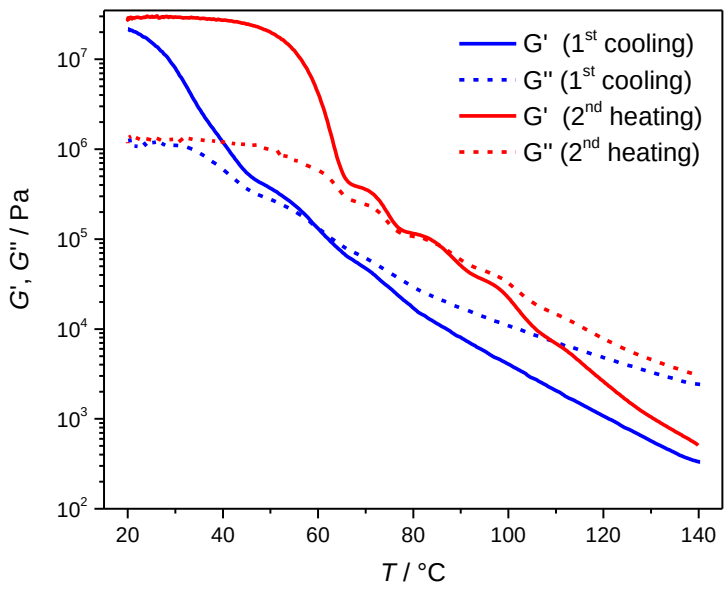


**Figure 3.14:** Oscillation rheology measurement of **6a** with 74 wt% hydrophilic segments and 26 wt% hexamethylene bisurea segments shows the transition between elastic and viscous state at 60 °C upon *cooling* and 85 °C upon *heating* (*cooling* and *heating* rate: 2 K $min^{-1}$, frequency: 1 Hz).

Furthermore, oscillation shear rheology was used to investigate the thermal and rheological properties, especially the melt viscosity. The melt viscosity is an essential parameter for additive manufacturing by *melt electrowriting* (MEW) and *extrusion-based printing* (EBP) since it has to be in the proper range to extrude the polymer through a fine spinneret and to deposit the strands.[99,156] Furthermore, the polymer needs to solidify rapidly during MEW to fix the printed construct. The viscosity $\eta$ of a polymer melt correlates with its molecular mass $M$ which can be explained by using a relationship that was described by Fox and Flory.[204,205]

$$[\eta] \sim M^{3.4} \tag{3.4}$$

It has to be taken into account that the complex melt viscosity $\eta^*$ is measured by oscillation rheology. The complex viscosity and the steady viscosity $\eta$ are connected by the Cox-Merz relation.[206] With equal angular velocity $\omega$ and the sheer velocity $\dot{\gamma}$ the following correlation is valid for $\omega = \dot{\gamma}$:

$$|\eta^*| = \eta \tag{3.5}$$

The melt viscosities were measured for the copolymers **6a**, **6a-1** and **6a-2** with different degree of polymerization. For this the copolymers were heated up to 140 °C and the first *cooling* experiment from the melt down to 20 °C was performed with a *cooling* rate of 2 K min$^{-1}$. As shown in figure 3.15 the viscosity of the molecular weight regulated copolymer **6a-1** sharply increases between 40 and 30 °C and the viscosity of **6a-2** between 50 and 40 °C. These transitions show clearly the self-assembly of the bisurea units via hydrogen bonds. Interestingly, the solidification of **6a** proceeds in a not so clear manner. A multi-step transition in a broad temperature window between 80 and 35 °C is observed. It can be assumed that the assembly speed of the hydrogen bonds depends on the melt viscosity of the polymer. Low molecular polymers with low melt viscosity diffuse through the melt faster due to less chain entanglements.[204] Therefore, a low viscosity increases the migration of polymer chains and, as a consequence, the assembly of the urea hydrogen bonds is more uniform. Another possible reason for the different transition behavior of **6a** as compared to **6a-1** and **6a-2** is the influence of the end groups. Copolymers **6a-1** and **6a-2** consist of mainly *n*-butyl end groups while **6a** has two amino end groups. The amino end groups can lead to additional intermolecular interactions that further limit the migration of

the polymer chains. The viscosity of all three copolymers increases to an equal viscosity range of around $4 \cdot 10^6$ Pa s at room temperature.

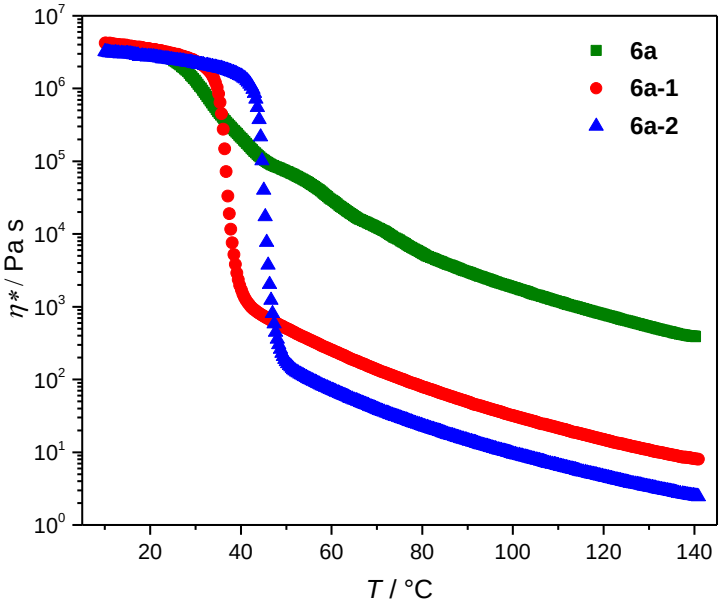


**Figure 3.15:** Complex viscosity curves of **6a, 6a-1** and **6a-2** measured by oscillation rheology upon *cooling* with a rate of 2 K $min^{-1}$ showing the influence of the degree of polymerization on the melt viscosity.

The viscosities of the three copolymers in the melt at 100 °C can be compared. At this temperature melt viscosities of 1770 Pa s for **6a**, 749 Pa s for **6a-1** and 77 Pa s for **6a-2** were determined for **6a**, **6a-1** and **6a-2**. Consequently, the melt viscosity decreases in the order **6a-2** < **6a-1** < **6a** clearly reflecting the decreasing degree of polymerization. The viscosity of **6a** is about factor 100 higher as for **6a-2**. This result demonstrates that the melt viscosity and, therefore, the temperature window of the copolymers for melt processing can be adjusted which is important for the selected extrusion based additive manufacturing technique.

***Copolymers with a content of 82 wt% hydrophilic segments and 18% bisurea segments***

In this section, the thermal properties of $(AB)_n$-segmented copolymers **6b**, **6b-1 and 6b-2** that consist of 82 wt% PPG-PEG-PPG segments of a molecular weight of 900 g mol$^{-1}$ and 18 wt% bisurea segments are discussed. For the *Differencial Scanning Calorimetry* (DSC) measurements the samples were first heated to 180 °C and the first *cooling* and second *heating curves* were recorded. As an example, the DSC curves of polymer **6b-2** with the lowest degree of polymerization within this series are depicted in figure 3.16A. The first *cooling curve* (blue) of **6b-2** reveals the supramolecular assembly of the bisurea segments between 40 and -20 °C with an enthalpy of -14.2 J g$^{-1}$. In the second *heating curve* (red) the glass transition of the PPG-PEG-PPG segments was found at -54 °C. In comparison to the previously discussed copolymer **6a** with only 74 wt% PPG-PEG-PPG segments (-41 °C) the glass transition is shifted to lower temperatures. An increase of the ratio of PPG-PEG-PPG segments leads to a lower glass temperature. This correlates also with the glass transition temperature of -62 °C for PPG-PEG-PPG diamine **1b** used for the synthesis of **6b** which is lower as compared to the glass transition of -46 °C determined for PPG-PEG-PPG diamine **1a** applied in the preparation of **6a**. Upon further *heating* a broad transition with several endothermic peaks in the temperature range between 30 and 120 °C was found. These transitions reveal the disassembly (melting) of the hydrogen bonding segments. A total melting enthalpy of 15.1 J g$^{-1}$ was determined over all peaks and correlates very well with the solidification enthalpy (-14.2 J g$^{-1}$). As a result, the assembly and disassembly of the supramolecular segments upon *cooling* and *heating*, respectively, are reversible. No crystallization or melting of the PPG-PEG-PPG segments was found. Interestingly, the DSC curves of PPG-PEG-PPG diamine **1b** used for the synthesis of **6b-2** show a crystallization and melting peak (Appendix 2). However, in the $(AB)_n$-segmented copolymers the PPG-PEG-PPG segments are not able to crystallize under these conditions.

Non-crystallized PPG-PEG-PPG segments in **6b-2** were confirmed by polarization microscope images after monitoring the polymer for 1 h at 20 °C. Crystallized PEG is birefringent and would cause patterns between crossed polarizers. However, an isotropic phase was observed as shown in figure 3.16B. This demonstrates that no PEG crystals were formed and the broad melting transition in the DSC curve only results from the melting of the supramolecular bisurea segments.

The line in the middle of the polarization microscopy images shows the edge of the polymer. After *heating* the polymer up to 65 °C with a rate of 10 K $min^{-1}$ the edge did not move indicating that the polymer is still in the elastic state. Further *heating* lead to a flow of the polymer indicated by the movement of the edge. At 100 °C the physical crosslinks are broken and the polymer is in a viscous processable melt.

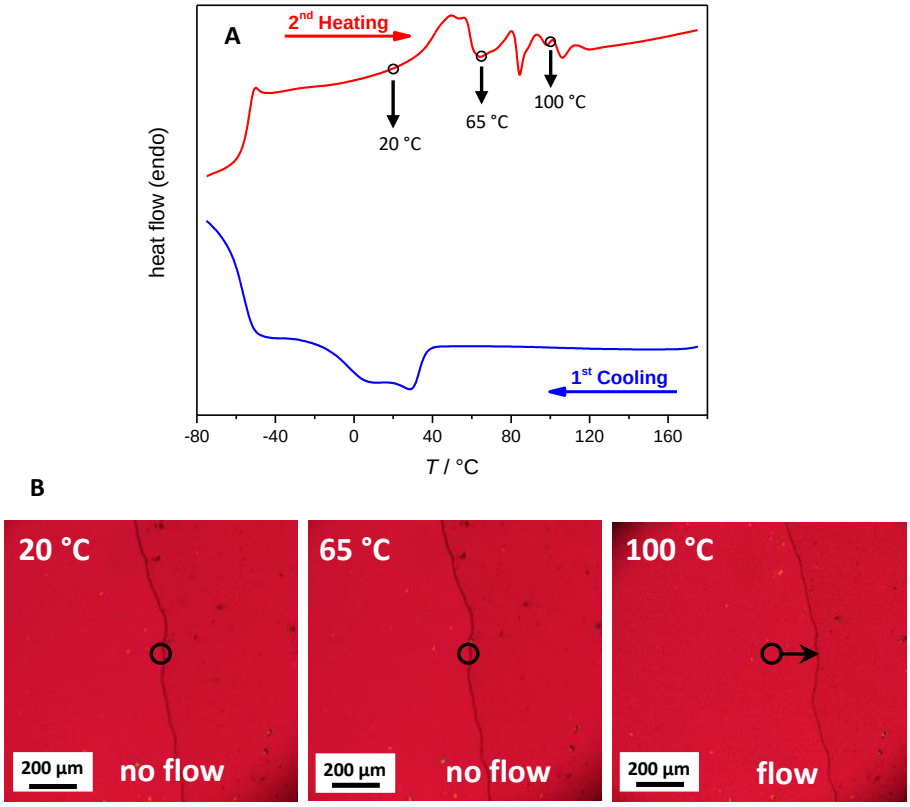


**Figure 3.16. A:** DSC curves of **6b-2** with 82 wt% PPG-PEG-PPG segments and 18 wt% hexamethylene bisurea segments and a low degree of polymerization. DSC curve reveals a glass transition at - 54 °C and a stepwise melting of the bisurea segments. **C:** Polarization microscope images of **6b-2** show no crystallization of the PEG segments. The polymer flows at 100 °C. The images were recorded between crossed polarizers and by using a λ/4 pate.

DSC curves of **6b-1** look equal as of **6b-2**. For **6b** with the highest degree of polymerization, a broader melting transition of the bisurea segments starting at around -15 °C was observed (see attachment 3).

*Dynamic Mechanical Thermal Analysis - Single cantilever method* of **6b-2** confirms the DSC results. The sample was first heated up to 100 °C. The first *cooling* and second *heating curve* for the elastic modulus *E'* and the loss factor tan *δ* were recorded and are shown in figure 3.17. The first *cooling* curve (blue) shows a slight increase of *E'* around 30 °C which can be assigned to the assembly of the bisurea segments. The sharp increase of *E'* between -50 and -70 °C corresponds to the glass transition of the PPG-PEG-PPG segments. Consequently, tan *δ* shows a sharp peak at this temperature. The glass transition temperature was determined by the peak maximum of tan *δ* at -55 °C. Upon second *heating* (red), the glass transition temperature in the curves of E' and tan *δ* was found at -53 °C. Upon further *heating E'* and tan *δ* both remain constant up to 40 °C before a broad decrease of *E'* is visible between 40 and 70 °C reflecting the melting of the bisurea segments. The disassembly of the bisurea hydrogen bonds can also be seen in the *heating curve* of tan *δ* by a peak with a maximum at around 55 °C. Interestingly, the reassembly of the bisurea segments is not visible in the first *cooling curve* of tan *δ*.

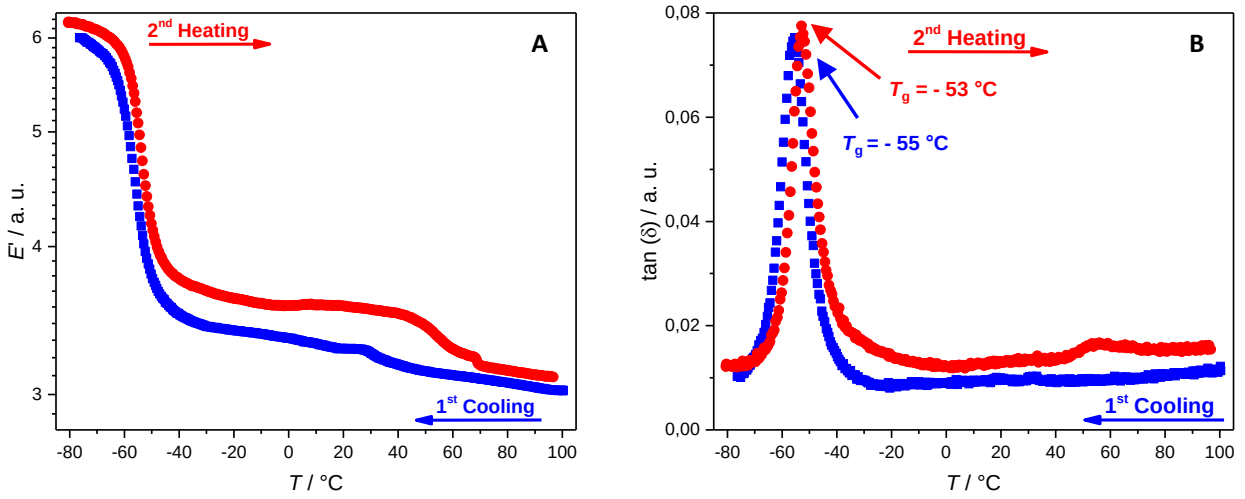


**Figure 3.17:** Dynamic mechanical thermal analysis of **6b-2** with 82 wt% PPG-PEG-PPG segments and 18 wt% hexamethylene bisurea segments using the single cantilever method (*cooling* and *heating* rate: 2 K $min^{-1}$, frequency: 0.5 Hz). **A:** The elastic modulus (*E'*) shows a sharp slope around -55 °C upon *cooling* and *heating* indicating the glass transition of the PPG-PEG-PPG segments. The decrease of *E'* starting around 40 °C upon *heating* corresponds to the disassembly of the bisurea hydrogen bonds; **B**: The loss factor (tan *δ*) reveals a glass transition of the PPG-PEG-PPG segments at -53 °C upon *heating* and -55 °C upon *cooling*. The disassembly of the bisurea hydrogen bonds upon *heating* is shown as a peak between 40 and 70 °C.

The *Dynamic Mechanical Thermal Analysis-tension geometry method* (figure 3.18) of **6b-2** reveals a glass transition temperature of -43 °C upon *heating* at the turning point of the decreasing elastic modulus *E*' (blue curve). At the glass transition a decrease of *E*' by about one order of magnitude from $2 \cdot 10^9$ to $10^8$ Pa is detectable. Further *heating* up to 60 °C results in a constant plateau of *E*'. Here, the copolymer is in the elastic state and the physical crosslinks of the bisurea segments are present. Between 60 and 90 °C *E*' decreases to around $5 \cdot 10^4$ Pa due to the disassembly of the bisurea hydrogen bonds. Both the glass transition of the PPG-PEG-PPG segments and the melting of the bisurea segments are also clearly visible in the curve of the viscous modulus *E*'' (green curve). *E*'' is located below *E*' until *heating* up to 83 °C. In this region the copolymer is in the elastic state due to the presence of physical crosslinks of the bisurea segments. The crossover point at 84 °C reveals the transition from elastic to viscous behavior.

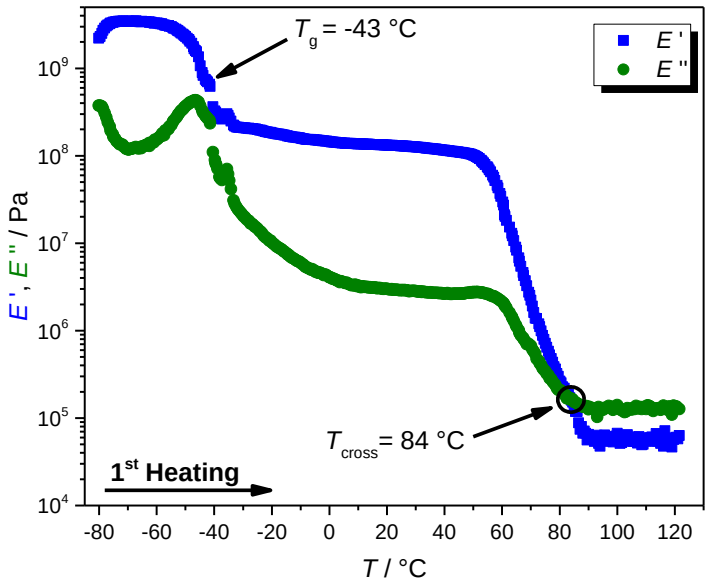


**Figure 3.18:** Dynamic mechanical thermal analysis of **6b-2** with 82 wt% PPG-PEG-PPG segments and 18 wt% hexamethylene bisurea segments using the tension geometry method. The turning point of the elastic modulus (*E*') is at -43 °C and corresponds to the glass transition of the PEG-PEG-PPG segments. The transition from elastic to viscous behavior is indicated by the intersection of the elastic (*E*') and viscous (*E*'') modulus occurring at 84 °C.

DMTA-tension geometry method of **6b** with higher degree of polymerization reveals also a glass transition at -43 °C (see attachment 4). In **6b** the intersection between *E*' and *E*'' is shifted to 132 °C. This shows that within this copolymer class the transition from elastic to viscous behavior occurs at higher temperatures if the number of repeating units is increased.

*Oscillation shear rheology* with *cooling* and *heating* rate of 2 K $min^{-1}$ was also conducted for copolymer **6b-2.** The sample was first heated to 160 °C and the first *cooling* and second *heating curve* were recorded (figure 3.19). The first *cooling curve* (blue) reveals a one-step transition of the elastic modulus *G*' and viscous modulus *G*'' with a sharp increase between 50 and 40 °C. This sharp increase demonstrates the solidification of the copolymer by the reassembly of the bisurea hydrogen bonds. The intersection of *G*' and *G*'' occurs at 49 °C and indicates the transition from viscous to elastic behavior. The second *heating curve* (red) shows a three-step transition for both moduli within the temperature range between 65 and 115 °C. The intersection of G' and G'' was found at 100 °C. The hysteresis can be explained by the time the bisurea units need to assemble.

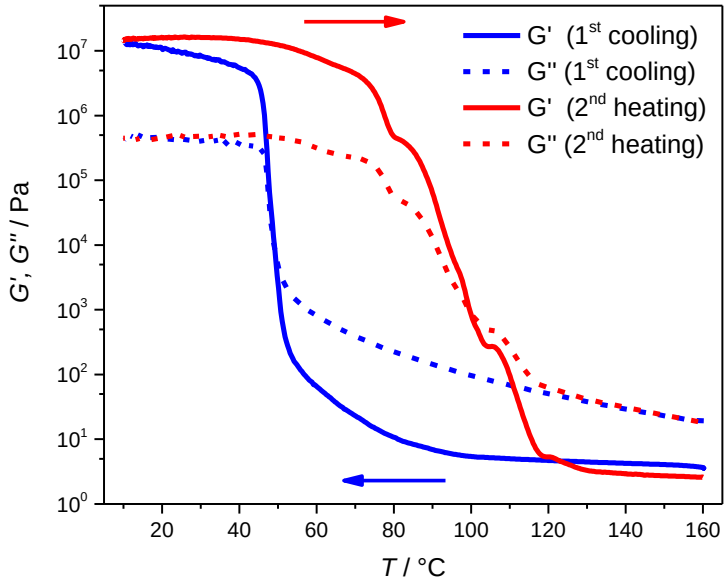


**Figure 3.19:** Oscillation rheology of **6b-2** with 82 wt% PPG-PEG-PPG segments and 18 wt% hexamethylene bisurea segments reveals a single step transition with a crossover temperature between viscous and elastic state of 49 °C upon *cooling* and a three-step transition with a section of elastic and viscous modulus at 100 °C upon *heating* (*cooling* and *heating* rate: 2 K $min^{-1}$, frequency: 1 Hz).

Figure 3.20 compares the complex viscosity for all three copolymers **6b**, **6b-1** and **6b-2** upon *cooling***. 6b-2** with the lowest degree of polymerization shows a steep one-step increase of the viscosity around 45 °C. A broader multi-step increase is observed for copolymers **6b-1** and **6b** with higher molecular weight. The same behavior is observed for the copolymers **6a**, **6a-1** and **6a-2** with 26 wt% hexamethylene bisurea segments as discussed in the previous chapter. For copolymers with higher degree of polymerization the assembly of the bisurea segments starts earlier and more gradual.

The viscosity of all three copolymers at 20 °C was found to be around $10^6$ Pa s which is slightly higher compared to previously discussed copolymers with 26 wt% hexamethylene bisurea segments. Additionally, the viscosities of the three copolymers were compared at 100 °C. The determined melt viscosity at 100 °C is 547 Pa s for **6b**, 73 Pa s for **6b-1** and 15 Pa s for **6b-2**. The melt viscosity decreases in the order **6a-2** < **6a-1** < **6a**. The same trend was observed for polymers **6a**, **6a-1** and **6a-2** with 74 wt% PPG-PEG-PPG segments and 26 wt% hexamethylene bisurea segments.

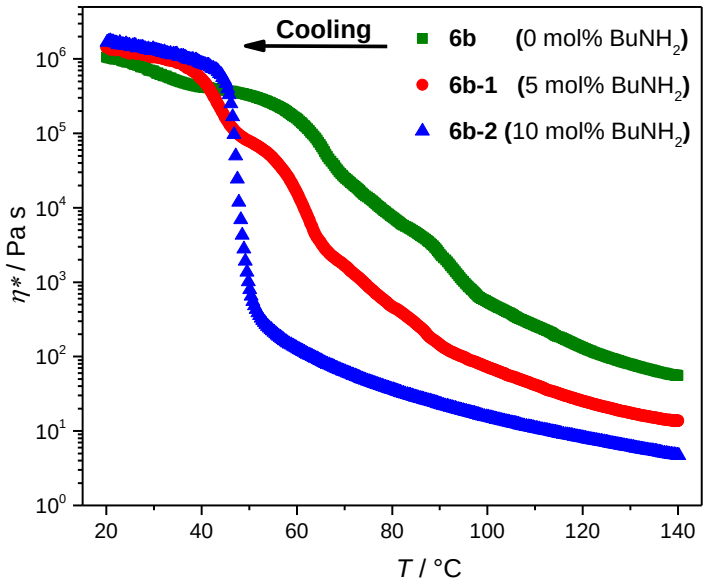


**Figure 3.20:** Complex melt viscosity of **6b**, **6b-1** and **6b-2** with 82 wt% PPG-PEG-PPG segments and 18 wt% hexamethylene bisurea segments upon *cooling* measured by oscillation rheology (*cooling* rate: 2 K $min^{-1}$; frequency: 1 Hz). The copolymers differ in the added amount of *n*-butylamine ($BuNH_2$) upon *cooling* with a rate of 2 K $min^{-1}$ (*cooling* rate: 2 K $min^{-1}$; frequency: 1 Hz).

***Copolymers with a content of 91 wt% hydrophilic segments and 9 wt% bisurea segments***

Copolymers **6c**, **6c-1** and **6c-2** consist of 91 wt% PPG-PEG-PPG segments of a molecular weight of 2000 g/mol and 9 wt% hexamethylene bisurea segments. All three copolymers were characterized by *Differencial Scanning Calorimetry* (DSC). The samples were first heated to 200 °C to remove the thermal history. Then, the first *cooling* and second *heating curve* were recorded. As an example, the DSC curve of **6c-2** is depicted in figure 3.21. Upon first *cooling* (blue curve), a broad small exothermic multistep transition occurs between 95 and 70 °C which is clearly visible in the magnification C. This transition reveals the formation of the hydrogen bonds accompanying with the formulation of physical crosslinks. As compared to the previous discussed copolymer **6b-2** the determined crystallization enthalpy (-1.3 J $g^{-1}$) is significantly lower which can be explained by the lower content of bisurea segments in the copolymer. In contrast to the copolymers with lower PPG-PEG-PPG content a sharp exothermic peak with a peak maximum at 3.2 °C and an enthalpy of -55.2 J $g^{-1}$ was found. A similar transition was also observed in **6c** and **6c-1** and can be explained by the crystallization of the PEG moieties in the PPG-PEG-PPG segments. PEG is semi crystalline at higher molecular weights, while pure PPG is almost amorphous.[56,58,207,208]

Upon *heating*, the glass transition of the PPG-PEG-PPG segments was found at -53 °C. The melting of the PEG units is shown by a sharp endothermic peak with a maximum at 30.7 °C and an enthalpy of 57.3 J $g^{-1}$.

The melting enthalpy $\Delta H_{m,PEG}$ can be used for the determination of the degree of crystallinity of the PEG segments $X_{C,PEG}$ by using the following equation:[207]

$$X_{C,PEG} = \frac{\Delta H_{m,PEG}}{\Delta H^0_{m,PEG} \cdot w_{PEG}} \cdot 100 \qquad (3.6)$$

$\Delta H^0_{m,PEG}$ describes the melting enthalpy for 100% crystalline PEG which is reported in the literature as 196.6 J $g^{-1}$.[207] $w_{PEG}$ is the weight fraction of PEG in the whole polymer. For pure PEG the crystallinity rises with increasing molecular weight up to around 10000 g $mol^{-1}$.[58,208] Assuming a number of four PPG units in the hydrophilic segment as found in the MALDI-TOF and NMR the ratio of PEG units in the copolymer is 80 wt%. As consequence, a degree of crystallinity of 36 % for the PEG units is determined by using equation (3.6). The same calculation can be done

for the diamine **1c** (Jeffamine ED-2003) which was used for the synthesis of **6c-2**. For the diamine **1c** the degree of crystallinity was determined to be 74 %.

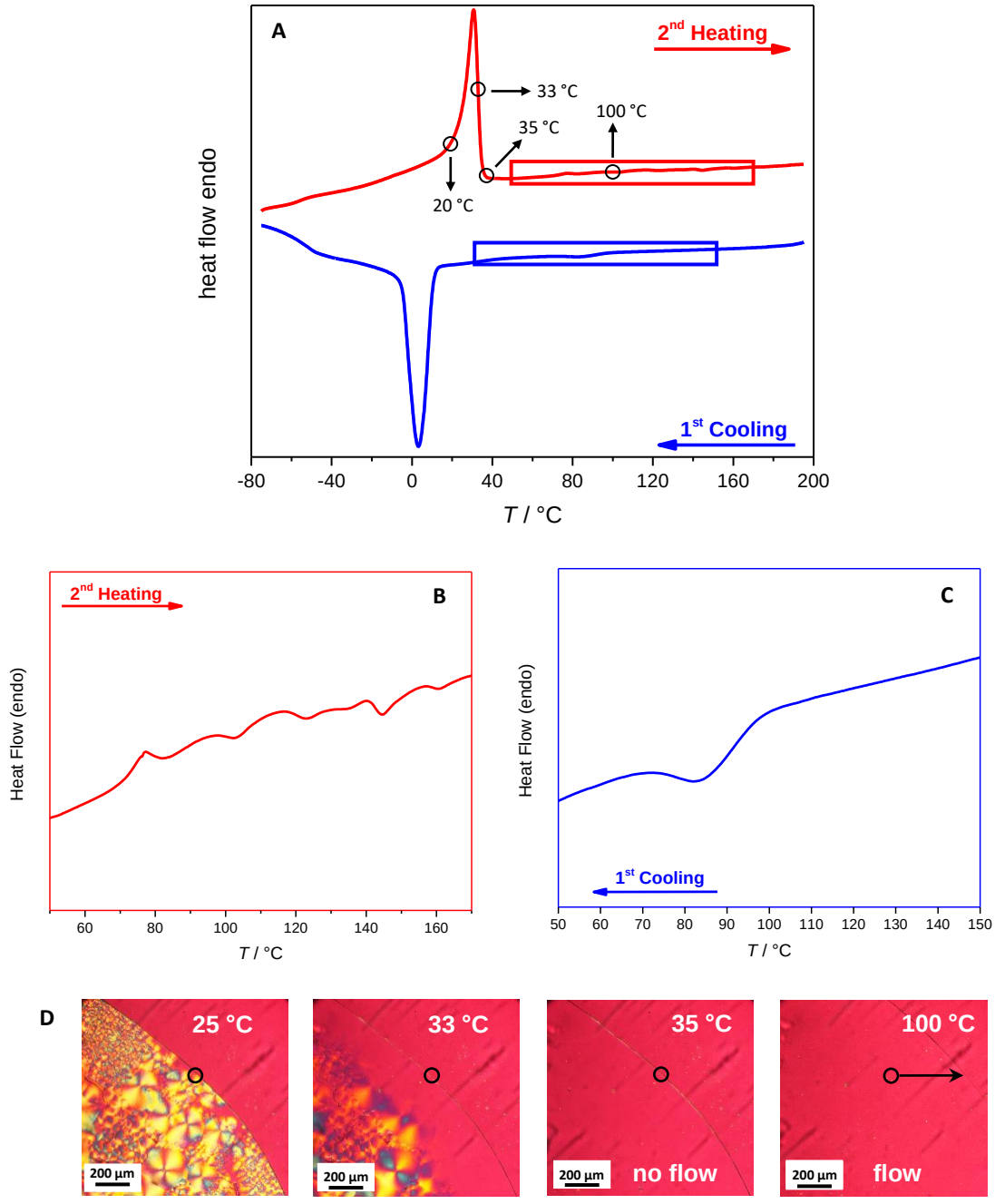


**Figure 3.21:** DSC curve and polarization microscope images of **6c-2** with 91 wt% PPG-PEG-PPG segments and 9 wt% hexamethylene bisurea segments. **A:** Complete DSC curve shows a crystallization peak at 3 °C upon *cooling* and a melting peak at 31 °C upon *heating* correlating with the melting of the PEG crystals. The crystallinity of the PEG segments at 25 °C is confirmed by polarization microscope images. **B** Magnified section of the second *heating* curve revealing the melting of the bisurea segments; **C:** Magnified section of the first *cooling* curve revealing the crystallization of the bisurea segments; **D:** Polarization microscope images of **6b-2** during second *heating* from 25 to 100 °C (*heating* rate: 10 K $min^{-1}$).The images were recorded between crossed polarizers and by using a λ/4 pate.

In conclusion, in case of the (AB)n-segmented copolymers with higher bisurea content, the physical crosslinks of the bisurea segments lower the crystallinity of the PEG moieties.

The crystallinity of the PEG units in **6c-2** is confirmed by polarization microscopy (figure 3.21D). At 25 °C the copolymer reveals birefringent crystals between crossed polarizers which result from the PEG units. These crystals start to melt if the copolymer is heated above 30 °C as shown at a temperature of 33 °C and are completely molten at 35 °C. This is in good accordance with the DSC results. An isotropic phase can be observed indicating that the PEG segments are completely molten. The line in the middle of the sample indicated by a circle reveals the edge of the polymer which does not move up to 35 °C indicating that the copolymer is still in the elastic state and the physical crosslinks prevent the flow. The image at 100 °C proofs a movement of the polymer edge showing that the hydrogen bonds between the urea units disassemble and the polymer starts to flow. In the DSC the melting and disassembly of bisurea segments is not clearly visible in the magnification. Over a broad temperature range between 80 and 150 °C deviations from the baseline are present. The polarization microscopy image (figure 3.21D) at 100 °C already show a flow of this material. The low content of bisurea segments of 9 wt% results in a lower intensity in the melting range as compared to copolymers **6a, 6a-1, 6a-2** and **6b, 6b-1, 6b-2** with higher bisurea segment contents of 26 and 18 wt%, respectively.

The results of the *Dynamic Mechanical Thermal Analysis - Single cantilever method* of **6c-2** are depicted in figure 3.22. The sample was heated to 120 °C. Then, in the first *cooling* and second *heating curve* the elastic modulus *E'* and the loss factor tan δ were recorded. Upon first *cooling* *E'* increases very slightly around 60 °C indicating the assembly of the bisurea segments (figure 3.22A). The formation of the hydrogen bonds is also slightly visible in the curve of tan δ (figure 3.22B) as a broad peak between 100 and 30 °C with a maximum at 75 °C. A steep increase of *E'* and tan δ occurs around 14 °C. This transition corresponds to the crystallization of the PEG units. The strong increase between -10 and -60 °C reveals the glass transition of the PPG-PEG-PPG segments. The glass transition is shown as a peak in the curve of tan *δ*. A glass transition temperature ($T_g$) of -23 °C is determined from the peak maximum.

Upon *heating* the glass transition temperature is found at -17 °C. In comparison to the previous discussed copolymers with 74 and 82 wt% PPG-PEG-PPG segments, the glass transition in **6b-2** is extended to a wider range and its temperature is distinctly lower. E' and tan δ reveal a sharp decrease around 34 °C which corresponds with the melting of the PEG moieties. This value is in good correlation with the melting transition of 30.7 °C in the second *heating curve* of the DSC. The disassembly of the urea hydrogen bonds is barely visible by a slight decrease of *E'* in the range from 50 to 80 °C. This transition is not seen in the curve of tan *δ*.

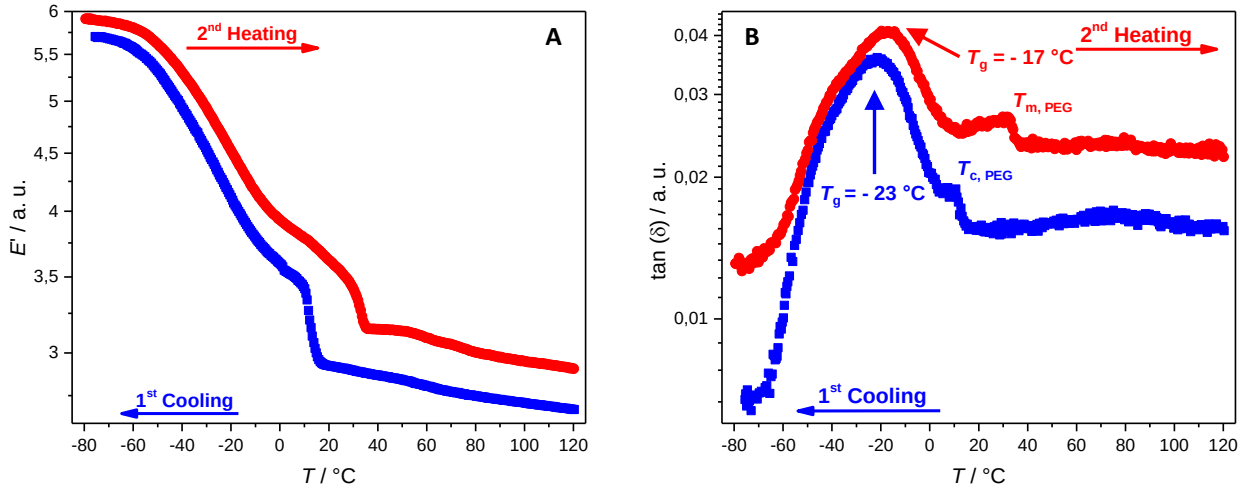


**Figure 3.22:** Dynamic mechanical thermal analysis of **6c-2** with 91 wt% PPG-PEG-PPG segments and 9 wt% hexamethylene bisurea segments (*cooling* and *heating* rate: 2 K $min^{-1}$, frequency: 0.5 Hz); **A:** The elastic modulus (*E'*) shows a sharp slope around -20 °C upon *cooling* and *heating* indicating the glass transition of the PPG-PEG-PPG segments. The sharp decrease of *E'* at around 30 °C upon *heating* corresponds to the melting of the PEG units and the sharp decrease starting from 50 °C reveals the disassembly of the bisurea hydrogen bonds; **B**: The loss factor (tan *δ*) reveals a glass transition of the PPG-PEG-PPG segments at -17 °C upon *heating* and -23 °C upon *cooling*. The melting of the PEG moieties upon *heating* is shown as a sharp peak around 30 °C.

The *Dynamic Mechanical Thermal Analysis - Tension geometry method* measurements of **6c-2** are shown in figure 3.23. Here, the measurement is carried out upon *heating*. The curve for the elastic modulus *E*' reveals a slightly decrease from -60 to 0 °C upon *heating* which corresponds to the glass transition range of the PPG-PEG-PPG segments. This confirms the broad glass transition found in the single cantilever measurement. A glass transition temperature of -45 °C was determined at the turning point of *E*'. The second transition at around 40 °C is very steep and reveals the melting of the PEG units. Thereby, *E*' decreases from $2 \cdot 10^8$ to $3 \cdot 10^7$ Pa. An elastic plateau with constant *E*' maintains constant upon further *heating* up to 60 °C. The copolymer is in the elastic state due to the physical crosslinks of the bisurea segments. Another decrease of *E*' occurs in the range from 60 to 110 °C resulting from the disassembly of the hydrogen bonds in the bisurea segments. The viscous modulus *E*'' also reveals all three transitions found and discussed for *E*'. *E'* and E'' intersect at $T_{cross}$ = 101 °C where transition from elastic behavior to a viscous melt occurs due to the complete disassembly of the bisurea hydrogen bonds.

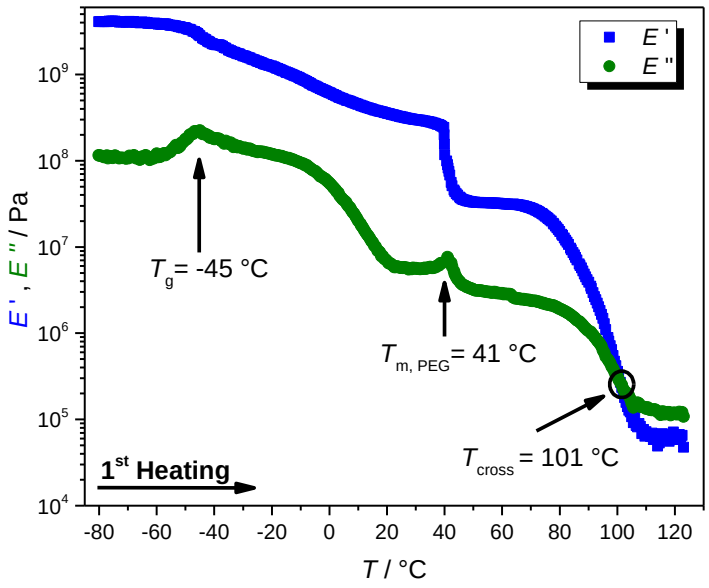


**Figure 3.23:** Dynamic mechanical thermal analysis of **6c-2** with 91 wt% PPG-PEG-PPG segments and 9 wt% hexamethylene bisurea segments using tension geometry experiment (*heating* rate: 2 K $min^{-1}$, frequency: 1 Hz). The turning point of the storage modulus (blue curve) at -25 °C corresponds to $T_g$ of the PEG segments, the transition at 41 °C describes the melting of the PEG units and the transition from elastic to viscous behavior ($T_{cross}$) occurs at 101 °C.

Additionally, *Dynamic Mechanical Thermal Analysis - Tension geometry method* was performed for $(AB)_n$-segmented copolymers **6c-1** and **6c** with higher degree of polymerization (see attachments 5 and 6). As already observed for polymers with PPG-PEG-PPG segments of

900 g mol$^{-1}$ the intersection between the storage and loss modulus is shifted to higher temperatures with increasing molecular weight. Crossover temperatures for the transition from elastic to viscous behavior were determined at 118 °C for **6c-1** and 154 °C for **6c**.

*Oscillation Shear Rheology* was measured for the $(AB)_n$-segmented copolymer **6c-2** to determine the rheological properties and the complex viscosity (figure 3.24). The sample was heated to 160 °C and the first *cooling* and second *heating curve* of the elastic modulus *G*' and the viscous modulus *G*'' were measured.

Upon *cooling* *G*' reveals a strong increase between 120 and 60 °C which demonstrates the assembly of the supramolecular segments. Around 10 °C where the measurement of the *cooling curve* ends, a steep increase starts to become visible. This transition results from the crystallization of the PEG moieties in the PPG-PEG-PPG segments. Similar transitions were observed for *G*''. The crossover point between *G*' and *G*'' was found at 74 °C.

Upon *heating* the steep decrease of *G*' and *G*'' indicates the melting of the PEG units. Both *G*' and *G*'' decrease at around 30 °C indicating the melting of the PEG units. The second decline between 70 and 150 °C reveals the disassembly of the urea hydrogen bonds. The crossover point between *G*' and *G*'' occurs at 112 °C.

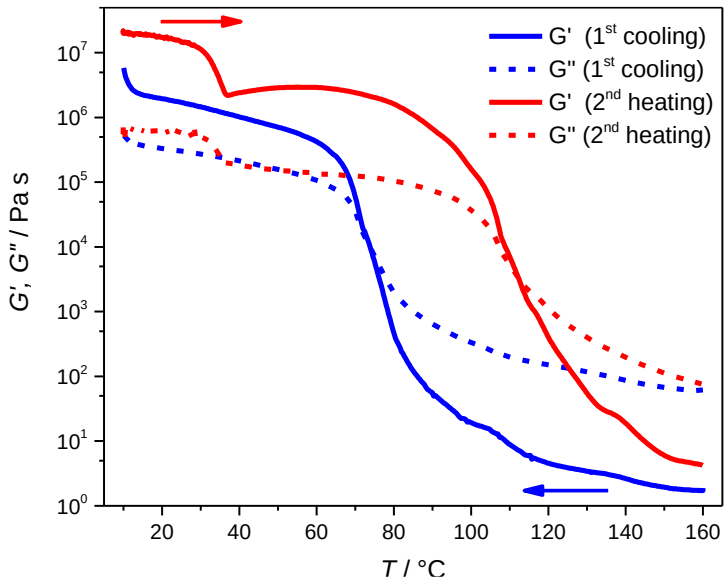


**Figure 3.24:** Oscillation rheology measurement (*cooling* and *heating* rate: 2 K min$^{-1}$, frequency: 1 Hz) of **6c-2** with 91 wt% PPG-PEG-PPG segments and 9 wt% hexamethylene bisurea segments showing the melting and crystallization of the PEG segments and the transition between elastic and viscous state at 74 °C upon *cooling* and 112 °C upon *heating*.

The viscosity curve (figure 3.25) measured upon *cooling* reveals a one-step increase of nearly three orders of magnitudes in a temperature range between 80 and 60 °C. This corresponds to the formation of the physical crosslinks by the urea hydrogen bonds. A further increase starts to become visible close to 10 °C. This transition can be explained by the crystallization of the PEG units. A melt viscosity of 53 Pa s was measured for **6c-2** at 100 °C. This value is in the same order of magnitude as the melt viscosities of **6a-2** (77 mPa s), **6b-1** (73 mPa s) and **6b-2** (15 mPa s) at 100 °C.

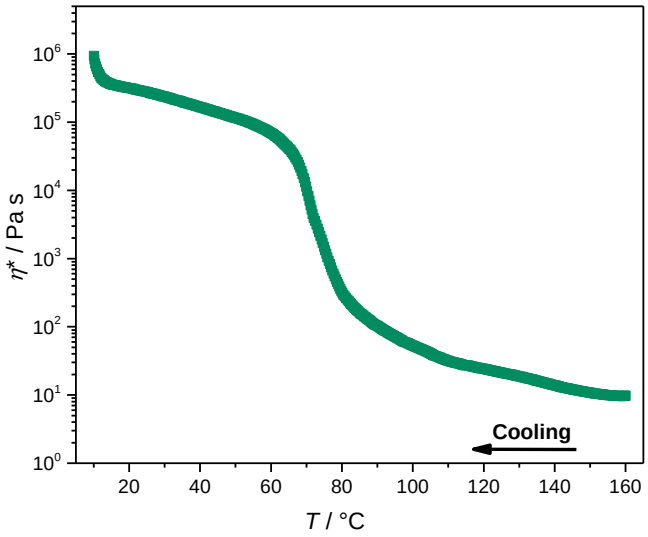


**Figure 3.25:** Complex melt viscosity of **6c-2** with 91 wt% PPG-PEG-PPG segments and 9 wt% hexamethylene bisurea segments upon *cooling* with a *cooling* rate of 2 K $min^{-1}$ revealing the polymer solidification by the assembly of the urea hydrogen bonds and the crystallization of the PEG moieties.

***Summary***

The results of the DSC analysis for the $(AB)_n$-segmented copolymers with hexamethylene bisurea segments are summarized for better comparison in table 3.4. In table 3.5 the results of the dynamic mechanical thermal analysis and oscillation rheology measurements are presented.

In summary, the $(AB)_n$-segmented copolymers with hexamethylene bisurea segments and PPG-PEG-PPG segments of 600, 900 and 2000 g $mol^{-1}$ reveal the thermal property profile that makes them promising candidates for additive manufacturing by melt electrowriting (MEW) and extrusion based printing (EBP).

**Table 3.4:** Summary of the DSC analysis of $(AB)_n$-segmented copolymers (*heating* and *cooling* rate: 10 K $min^{-1}$). The following values were determined: Glass transition of $T_{g,PPG\text{-}PEG,PPG}$ of the PPG-PEG-PPG segments from the second *heating* curve, the crystallization temperature $T_{c,PEG}$ and enthalpy $\Delta H_{c,PEG}$ of the PEG units, the melting temperature $T_{m,PEG}$ and enthalpy $\Delta H_{m,PEG}$ of the PEG units, the degree of crystallization of the PEG units $X_C$ (calculated by equation (3.6), the temperature range for the assembly of the bisurea hydrogen bonds upon *cooling* $T_{c,BU}$ and the temperature range for the disassembly of the bisurea hydrogen bonds upon *heating* $T_{m,BU}$ (n.d. = not detected)

| | $T_{g,PPG\text{-}PEG\text{-}PPG}$ [°C] | $T_{c,PEG}$ [°C] | $\Delta H_{c,PEG}$ [J $g^{-1}$] | $T_{m,PEG}$ [°C] | $\Delta H_{m,PEG}$ [J $g^{-1}$] | $X_{C,PEG}$ [%] | $T_{c,BU}$ [°C] | $T_{m,BU}$ [°C] |
|---|---|---|---|---|---|---|---|---|
| **6a** | -41 | n.d. | n.d. | n.d. | n.d. | n.d. | 90 – 50 | 15 – 160 |
| **6a-1** | -49 | n.d. | n.d. | n.d. | n.d. | n.d. | 85 – 50 | 15 – 160 |
| **6a-2** | -46 | n.d. | n.d. | n.d. | n.d. | n.d. | 135 – 45 | 15 – 170 |
| **6b** | -53 | n.d. | n.d. | n.d. | n.d. | n.d. | 20 – (-25) | -20 – 140 |
| **6b-1** | -55 | n.d. | n.d. | n.d. | n.d. | n.d. | 40 – (-20) | 30 – 120 |
| **6b-2** | -54 | n.d. | n.d. | n.d. | n.d. | n.d. | 40 – (-20) | 30 – 120 |
| **6c** | -54 | 1.4 | -59.9 | 30.6 | 58.6 | 37 | n.d. | 55 – 145 |
| **6c-1** | -53 | 7.2 | -53.7 | 33.7 | 56.7 | 36 | 80 – 45 | 55 – 130 |
| **6c-2** | -53 | 3.2 | -55.2 | 30.7 | 57.3 | 36 | 95 – 70 | 65 – 160 |

**Table 3.5:** Results of *Dynamic mechanical thermal analysis (DMTA) - Single Cantilever method, DMTA- Tension geometry method* and *oscillation shear rheology measurements* of $(AB)_n$-segmented copolymers. In the DMTA cantilever measurements the glass transition temperatures of the PPG-PEG-PPG segments $T_{g,c}$ and $T_{g,h}$ upon *cooling* and *heating* were determined by using the curves of the loss factor tan $\delta$ , the crystallization temperature of the PEG units $T_{c,PEG}$, the bisurea segments $T_{c,BU}$ upon *cooling* and the melting temperature of the PEG units $T_{m,PEG}$ and the bisurea segments $T_{m,BU}$ upon *heating* were determined by using the curves of the elastic modulus $E'$. With the DMTA tension geometry method the glass transition of the PPG-PEG-PPG segments $T_g$, the melting temperature of the PEG units $T_{m,PEG}$ and the temperature $T_{cr}$ where the crossover from elastic to viscous behavior occurs was determined. The crossover temperature between storage and loss modulus $T_{cr,c}$ upon *cooling* and $T_{cr,h}$ upon *heating* and the complex viscosity $\eta^*_{100}$ upon cooling were determined from the oscillation shear rheology measurements.

| | **DMTA - Single cantilever method** | | | | | | **DMTA - Tension geometry method** | | | **Rheology** | | |
|---|---|---|---|---|---|---|---|---|---|---|---|---|
| | $T_{g,c}$ [°C] | $T_{g,h}$ [°C] | $T_{c,PEG}$ [°C] | $T_{m,PEG}$ [°C] | $T_{c,BU}$ [°C] | $T_{m,BU}$ [°C] | $T_g$ [°C] | $T_{m,PEG}$ [°C] | $T_{cr}$ [°C] | $T_{cr,c}$ [°C] | $T_{cr,h}$ [°C] | $\eta^*_{100}$ [Pa s] |
| **6a** | -42 | -39 | n.d. | n.d. | 100 - 30 | 50 - 100 | -34 | n.d. | 85 | 60 | 85 | 1770 |
| **6a-1** | - | - | - | - | - | - | - | - | - | 39 | 90 | 749 |
| **6a-2** | - | - | - | - | - | - | - | - | - | 51 | 100 | 77 |
| **6b** | - | - | - | - | - | - | -46 | n.d. | 132 | 99 | 111 | 547 |
| **6b-1** | -55 | -52 | n.d. | n.d. | 75 - 45 | 55 - 80 | - | - | - | 85 | 96 | 73 |
| **6b-2** | -55 | -53 | n.d. | n.d. | 35 - 25 | 40 - 70 | -43 | n.d. | 84 | 49 | 100 | 15 |
| **6c** | - | - | - | - | - | - | - | 40 | 154 | - | - | - |
| **6c-1** | - | - | - | - | - | - | - | 41 | 118 | - | - | - |
| **6c-2** | -23 | -17 | 14 | 34 | 70 - 50 | 50 - 80 | -45 | 41 | 101 | 74 | 112 | 53 |

n.d.: not detected; - : not measured

### 3.3.2 $(AB)_n$-segmented copolymers with trans-1,4-cyclohexyl bisurea segments

In contrast to the $(AB)_n$-segmented copolymers discussed in the previous chapter (3.3.1), here the bisurea segments are based on the *trans*-1,4-cyclohexane structure. The chemical structure of these copolymers is shown in figure 3.26. Within this class, three different copolymers were synthesized and analyzed: Copolymer **7a** consists of 82 wt% PPG-PEG-PPG segments of a molecular weight of 900 g $mol^{-1}$, resulting in 18 wt% trans-1,4-cyclohexane bisurea segments. The average degree of polymerization of **7a** was determined to be 17. **7b** and **7b-1** are composed of 91 wt% PPG-PEG-PPG segments with a molecular weight of 2000 g $mol^{-1}$ and 9 wt% 1,4-trans-cyclohexane bisurea segments and its degree of polymerization is 19 for **7b** and 13 for **7b-1**.

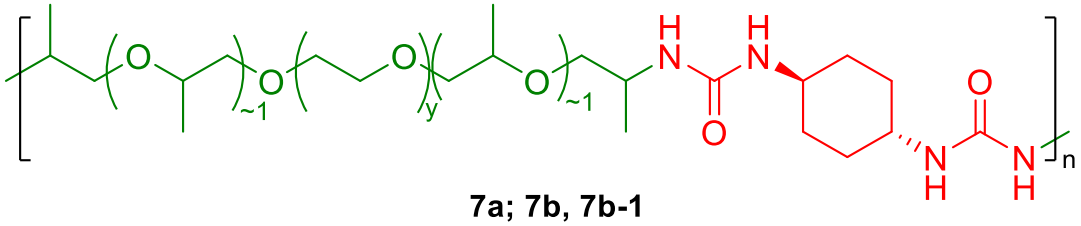


**7a; 7b, 7b-1**

**Figure 3.26:** Chemical structure of the repeating units of the series of the $(AB)_n$-segmented copolymers with PPG-PEG-PPG segments and trans-1,4-cyclohexane bisurea segments.

***Copolymers with a content of 82 wt% hydrophilic segments and 18 wt% bisurea segments***

Copolymer **7a** was characterized by *Differential Scanning Calorimetry* (DSC). The sample was first heated to 250 °C. Afterwards, the first *cooling* and second *heating* curve were recorded (figure 3.27) between -80 and 250 °C. The first *cooling curve* does not indicate a thermal transition within the range between 250 and -20 °C. The exothermic peak between -30 and -70 °C shows the crystallization of the PEG units in the PPG-PEG-PPG segments. In the second *heating curve* two peaks can be observed. Though, a closer look and a comparison with other $(AB)_n$-segmented copolymers within this work leads to the conclusion that a glass transition of the PPG-PEG-PPG segments occurs at -55 °C followed by a recrystallization with a peak maximum at - 33.4 °C and a melting transition with a peak maximum at 3.2 °C. A glass transition of -53 and -55 °C was also observed in $(AB)_n$-segmented copolymers **6b**, **6b-1** and **6b-2** with 82 wt% PPG-PEG-PPG segments and 18 wt% hexamethylene-bisurea segments. Recrystallization and melting enthalpy were determined to be -11.2 and 12.4 J $g^{-1}$, respectively. Therefore, it is assumed that the semi-crystalline PEG units in the PPG-PEG-PPG segments crystallized. A crystallization upon *heating*

below the melting temperature is characteristic for semi-crystalline polymers if the *cooling* below the glass transition temperature occurs faster as the formation of crystals. No endothermic peak that reveals the disassembly of the bisurea hydrogen bonds is visible. In contrast, DSC of previously discussed copolymers **6b**, **6b-1** and **6b-2** with 91 wt% PPG-PEG-PPG segments and 9 wt% hexamethylene bisurea segments indicate the reassembly and disassembly of the bisurea segments. The observations in the DSC were confirmed by *heating* experiments of copolymer **7a** at the hot stage. No melting of the copolymer was observed. Thus, **7a** is considered as not appropriate for extrusion-based melt-processing.

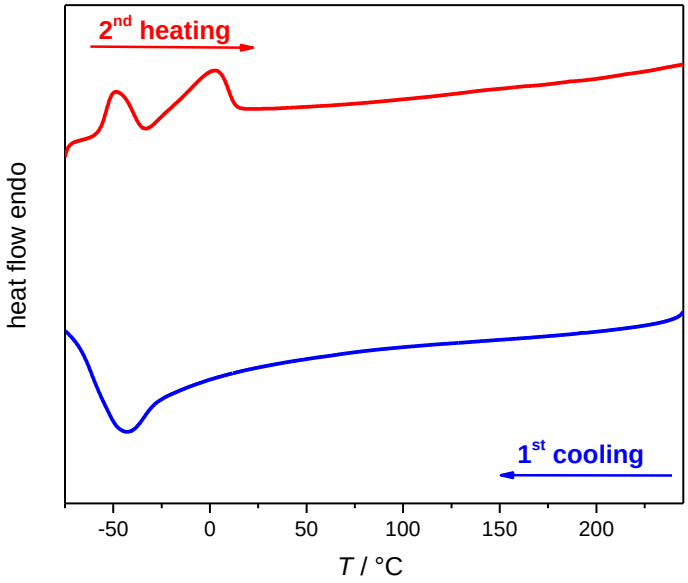


**Figure 3.27:** DSC curves of **7a** with 82 wt% PPG-PEG-PPG segments and 18 wt% *trans*-1,4-cyclohexane bisurea segments. The *heating* curve shows a glass transition of the PPG-PEG-PPG segments at -55 °C and the crystallization and melting of the PEG units.

***Copolymers with a content of 91 wt% hydrophilic segments and 9 wt% bisurea segments***

**7b** consists of 91 wt% PPG-PEG-PPG segments with a molecular weight of 2000 g mol$^{-1}$ and 9 wt% 1,4-trans-cyclohexane bisurea segments and its molecular weight was not regulated. *Differential Scanning Calorimetry* (DSC) was measured between -80 and 180 °C by recording the first *cooling curve* and the second *heating curve* (figure 3.28). Upon first *cooling curve* (blue) an exothermic peak is visible between 130 and 110 °C. The transition indicates the assembly of the bisurea segments by hydrogen bonds. Additionally, a sharp exothermic peak with a peak minimum at -17.9 °C is found revealing the recrystallization of the PEG units in the PPG-PEG-PPG segments. Upon second *heating* a glass transition at -46 °C is visible that can be assigned to the PPG-PEG-

PPG segments. Furthermore, the DSC reveals a sharp peak with a peak maximum at 18.3 °C correlating with the melting of the PEG units. Both the crystallization and melting temperature of the PEG units are 12 – 16 °C lower as compared to previously discussed copolymer **6c-2** with hexamethylene bisurea segments. The crystallization and melting enthalpy of the PEG moieties were found to be -54.4 and 54.1 J $g^{-1}$ resulting in a degree of crystallinity of 34 %. This value is comparable with the crystallinity of 36 % found for polymers with comparable PEG ratio and hexamethylene bisurea segments. Upon further *heating*, a second endothermic peak between 110 and 140 °C is found. This transition can be assigned to the disassembly of the supramolecular bisurea segments. As compared to copolymers with 91 wt% PPG-PEG-PPG segments and 9 wt% hexamethylene bisurea segments the thermal transition of the disassembly and reassembly of the bisurea segments is found at higher temperatures and in a narrow temperature range. Consequently, higher melt-processing temperatures are expected to be required.

DSC curves of **7b-1** which was synthesized by molecular weight regulation with 5 mol% *n*-butylamine reveal equal behavior as **7b.**

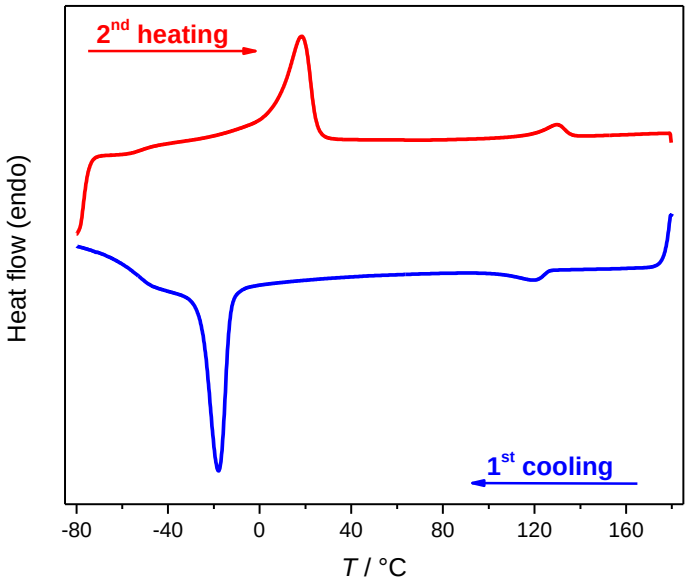


**Figure 3.28:** DSC curves of **7b** with 91 wt% PPG-PEG-PPG segments and 9 wt% *trans*-1,4-cyclohexane bisurea segments by *heating* up to 180 °C. The *heating* curve shows a glass transition at -46 °C, a large melting peak at 18 °C revealing the melting of the PEG moieties and a small melting peak at 130 °C indicating the disassembly of the bisurea segments.

The thermal behavior of **7b** and **7b-1** was further investigated by performing *Dynamic Mechanical Thermal Analysis - Tension geometry method*. Both copolymers revealed similar curves for the

elastic (*E*') and viscous modulus (*E*''). The *DMTA – tension geometry* curve of **7b-1** is exemplary depicted in figure 3.29. Both *E*' (blue curve) and *E*'' (green curve) reveal a decrease in the range between -40 and -10 °C resulting from the glass transition of the PPG-PEG-PPG segments. A glass transition temperature of -30 °C was determined by using the turning point of *E*'. A steep decrease of both the elastic and viscous modulus at around 25 °C reveals the melting of the PEG units in the PPG-PEG-PPG segments whereby *E*' decreases from around $4 \cdot 10^8$ to $3 \cdot 10^7$ Pa. Upon further *heating* *E*' remains constant while *E*'' slightly increases. The copolymer is in the elastic state due to the bisurea hydrogen bonds. A second steep decline of both moduli occurs between 135 and 145 °C indicating the disassembly of the bisurea hydrogen bonds and corresponding well with the transition observed in the DSC. However, no crossover between *E*' and *E*'' was found indicating that the copolymer still remains in the elastic state and does not melt. *Heating* of the copolymer at the hot stage up to 200 °C resulted in softening but not melting of the copolymer.

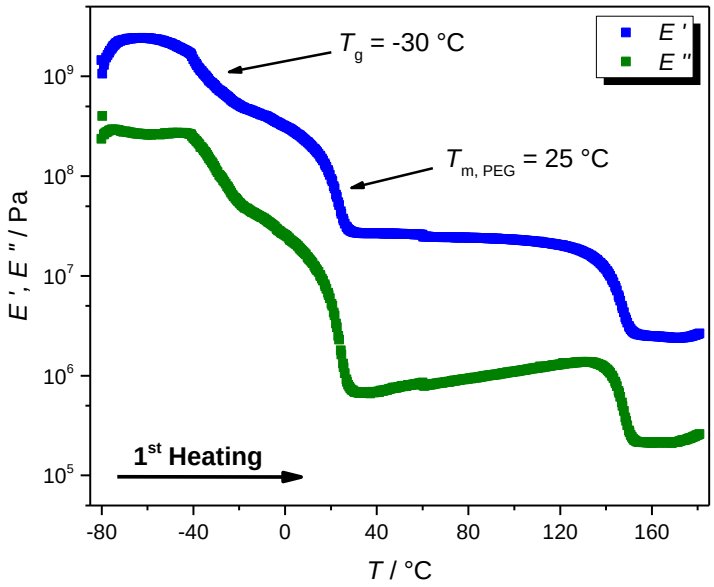


**Figure 3.29:** *Dynamic Mechanical Thermal Analysis – Tension geometry method* of **7b-1** with 91 wt% PPG-PEG-PPG segments and 9 wt% trans-1,4-cyclohexyl bisurea segments (tension geometry experiment, *heating* rate: 2 K $min^{-1}$, frequency: 1 Hz). The turning point of *E*' at -30 °C corresponds to the glass transition of the PPG-PEG-PPG segments, the transition around 20 °C describes the melting of the PEG units and another transition around 140 °C the disassembly of the bisurea segments. No section between *E*' and *E*'' is observed up to 180 °C.

***Summary***

The results of the DSC analysis for the $(AB)_n$-segmented copolymers with *trans*-1,4-cyclohexane bisurea segments are summarized in table 3.6. Table 3.7 summarizes the result from the *Dynamic Mechanical Thermal Analysis* and *Oscillation Shear Rheology measurements*.

In summary, the disassembly and assembly temperatures of the hydrogen bonds in the copolymers with *trans*-1,4-cyclohexane bisurea segments are higher as compared to copolymers with hexamethylene bisurea segments. High melting temperatures may cause difficulties in the desired applications due to a limited upper temperature of 130 °C in *Extrusion based Printing* and thermal decomposition in *Melt Electrowriting*. As a consequence, this polymer class was classified as not appropriate for these two applications within this work.

***Table 3.6:*** Summary of the DSC analysis of $(AB)_n$-segmented copolymers (*heating* and *cooling* rate: 10 K $min^{-1}$). The following values were determined: Glass transition of $T_{g,PPG\text{-}PEG,PPG}$ of the PPG-PEG-PPG segments from the second heating curve, the crystallization temperature $T_{c,PEG}$ and enthalpy $\Delta H_{c,PEG}$ of the PEG units, the melting temperature $T_{m,PEG}$ and enthalpy $\Delta H_{m,PEG}$ of the PEG units, the degree of crystallization of the PEG units $X_C$ (calculated by equation (3.6), the temperature range for the assembly of the bisurea hydrogen bonds upon *cooling* $T_{c,BU}$ and the temperature range for the disassembly of the bisurea hydrogen bonds upon *heating* $T_{m,BU}$ (n.d. = not detected).

| | $T_{g,PPG\text{-}PEG\text{-}PPG}$ [°C] | $T_{c,PEG}$ [°C] | $\Delta H_{c,PEG}$ [J $g^{-1}$] | $T_{m,PEG}$ [°C] | $\Delta H_{m,PEG}$ [J $g^{-1}$] | $X_{C,PEG}$ [%] | $T_{c,BU}$ [°C] | $T_{m,BU}$ [°C] |
|---|---|---|---|---|---|---|---|---|
| **7a** | -55 | n.d. | n.d. | n.d. | n.d. | n.d. | n.d. | n.d. |
| **7b** | -46 | -17.9 | -54.4 | 18.3 | 54.1 | 34 | 130 – 110 | 110 – 140 |
| **7b-1** | -49 | -17.9 | -47.9 | 16.5 | 48.5 | 30 | 130 – 110 | 120 – 140 |

**Table 3.7:** Results of *Dynamic mechanical thermal analysis (DMTA) - Single Cantilever method*, *DMTA- Tension geometry method* and *oscillation shear rheology* measurements of $(AB)_n$-segmented copolymers. In the DMTA cantilever measurements the glass transition temperatures of the PPG-PEG-PPG segments $T_{g,c}$ and $T_{g,h}$ upon *cooling* and *heating* were determined by using the curves of the loss factor tan $\delta$, the crystallization temperature of the PEG units $T_{c,PEG}$ and the bisurea segments $T_{c,BU}$ upon *cooling* and the melting temperature of the PEG units $T_{m,PEG}$ and the bisurea segment $T_{m,BU}$ upon *heating* were determined by using the curves of the elastic modulus E'. With the *DMTA tension geometry method* the glass transition of the PPG-PEG-PPG segments $T_g$, the melting temperature of the PEG units $T_{m,PEG}$ and the temperature $T_{cr}$ where the crossover from elastic to viscous behavior occurs were determined. The crossover temperature between storage and loss modulus $T_{cr,c}$ upon *cooling* and $T_{cr,h}$ upon *heating* and the complex viscosity $\eta^*_{100}$ upon *cooling* were determined from the *oscillation shear rheology measurements*.

| | **DMTA – Single Cantilever method** | | | | | | **DMTA tension Geometry method** | | | **Rheology** | | |
|---|---|---|---|---|---|---|---|---|---|---|---|---|
| | $T_{g,c}$ [°C] | $T_{g,h}$ [°C] | $T_{c,PEG}$ [°C] | $T_{m,PEG}$ [°C] | $T_{c,BU}$ [°C] | $T_{m,BU}$ [°C] | $T_g$ [°C] | $T_{m,PEG}$ [°C] | $T_{cr}$ [°C] | $T_{cr,c}$ [°C] | $T_{cr,h}$ [°C] | $\eta^*_{100}$ [Pa s] |
| **7b** | -48 | -46 | -12 | 12 | 150 – 80 | 105 - 180 | -37 | 22 | n.d. | - | - | - |
| **7b-1** | - | - | - | - | - | - | -30 | 25 | n.d. | - | - | - |

n.d.: not detected; - : not measured

### 3.3.3 $(AB)_n$-segmented copolymers with bisurea-4,4'-methylene-bis(cyclohexyl) segments

The properties of the copolymers with bisurea segments based on 4,4'-methylene-bis(cyclohexyl) structure will be discussed in the following. The chemical structure of this copolymer series is shown in figure 3.30. Copolymers **8a**, **8a-1**, **8a-2** and **8a-3** consist of 75 wt% PPG-PEG-PPG segments of a molecular weight of 900 g $mol^{-1}$ and 25 wt% 4,4'-methylene-bis(cyclohexyl) bisurea segments. **8a** has the highest molecular weight with an average number of repeating units of 38 as determined from SEC analysis. For the other copolymers within this series, the degree of polymerization was lowered with n = 34 for **8a-1**, n = 31 for **8a-2** and n = 26 for **8a-3**. Copolymers **8b** and **8b-1** consist of 87 wt% of the longer PPG-PEG-PPG segments with a molecular weight of 2000 g $mol^{-1}$ and 13 wt% 4,4'-methylene-bis(cyclohexyl) bisurea segments. The determined average degree of polymerization n is 29 for **8b** and 25 for **8b-1**.

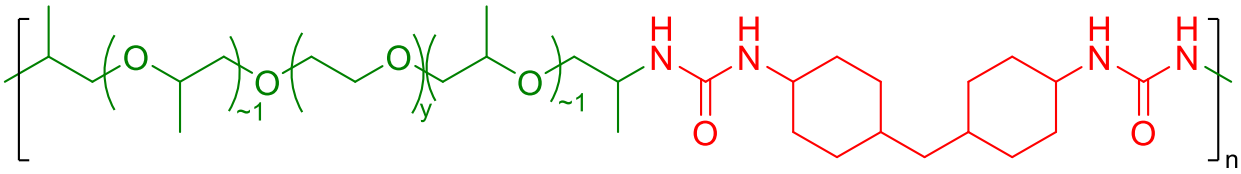


**8a, 8a-1, 8a-2, 8a-3; 8b, 8b-1**

**Figure 3.30:** Chemical structure of the repeating units of the series of the $(AB)_n$-segmented copolymers with PPG-PEG-PPG segments and 4,4'-methylene-bis(cyclohexyl) bisurea segments. Adapted and reproduced with permission (© 2020 The Authors. Macromolecular Chemistry and Physics published by WILEY-VCH GmbH).[139]

***Copolymers with a content of 75 wt% hydrophilic segments and 25 wt% bisurea segments***

Thermal analysis was conducted by means of *Differential Scanning Calorimetry* (DSC). One DSC curve of this copolymer series is exemplarily shown for copolymer **8a-2** in figure 3.31.[139] In the DSC measurements the sample was first heated to 180 °C to remove the thermal history. Upon first *cooling curve* (blue) no exothermic peak is visible above -40 °C. Below -40 °C the glass transition of the PPG-PEG-PPG segments starts. No value was determined due to the cooling rate of -10 K $min^{-1}$ cannot be reached within this temperature range. The second *heating curve* (red) reveals a glass transition at -45 °C resulting from the PPG-PEG-PPG segments. No further transition was found. This demonstrates that the PPG-PEG-PPG segments are completely amorphous. Disassembly and reassembly of the bisurea hydrogen bonds are not detectedable due to the limited sensitivity.

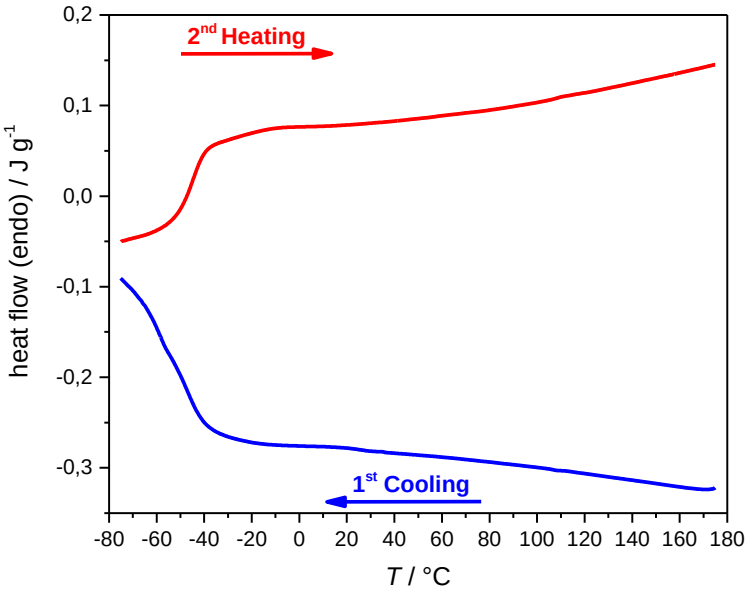


**Figure 3.31.** DSC curves of **8a-2** with 75 wt% PPG-PEG-PPG segments and 25 wt% 4,4'-methylene-bis(cyclohexyl)-bisurea segments. A glass transition of the PPG-PEG-PPG segments at -45 °C is visible upon heating. Adapted and reproduced with permission (© 2020 The Authors. Macromolecular Chemistry and Physics published by WILEY-VCH GmbH).[139]

The thermal transitions of the copolymers were additionally characterized by *Dynamic Mechanical Thermal Analysis - Single cantilever method*. The samples were first heated to 160 °C to remove the thermal history and the first *cooling* and second *heating curve* of the elastic modulus *E'* and the loss factor tan *δ* were recorded. In figure 3.32 the results are shown for copolymer **8a-2**. The first *cooling curve* of *E'* shows a steady increase over a broad temperature range between 140 and 20 °C. However, in the *cooling curve*, tan *δ* has a broad peak with a peak maximum at around 90 °C. This transition can be assigned to the assembly of the bisurea hydrogen bonds. Upon further *cooling* the curve of *E'* shows a steep increase between -35 and - 55 °C and tan *δ* a sharp peak correlating with the glass transition of the PPG-PEG-PPG segments. A glass transition temperature of -44 °C is determined from the peak maximum of tan *δ*. The second *heating curve* reveals a glass transition temperature of the PPG-PEG-PPG segments at - 40 °C. Additionally, *E'* slightly decreases within a broad range between 0 and 135 °C. Tan *δ* shows a broad peak with a peak maximum at around 90 °C. This transition results from the disassembly of the hydrogen bonds in the bisurea segments. Consequently, the disassembly and reassembly of the supramolecular interactions are visible in the DMTA but not in the DSC.

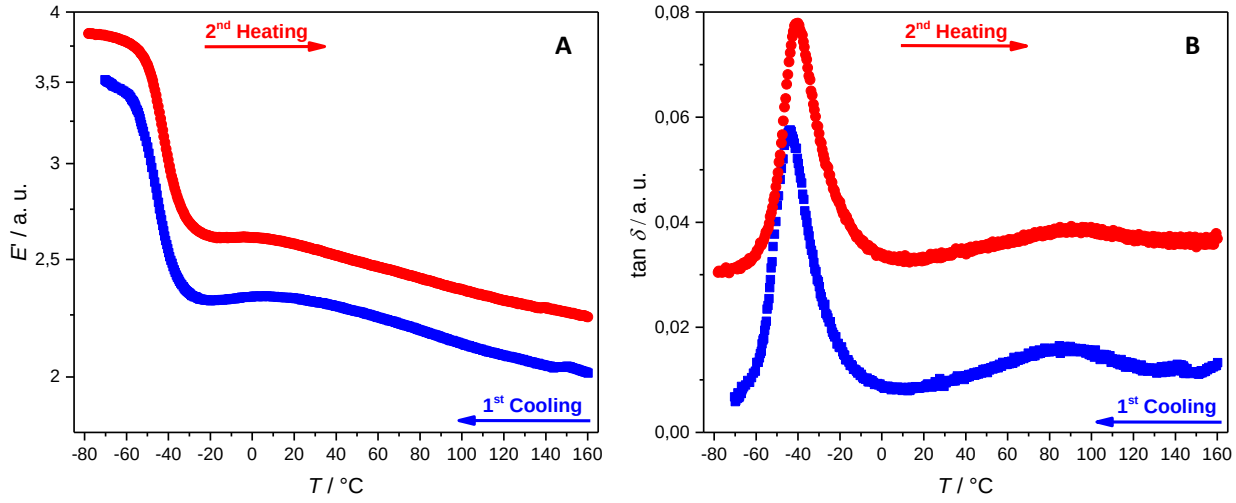


**Figure 3.32.** Dynamic mechanical thermal analysis of **8a-2** with 75 wt% hydrophilic segments and 25 wt% bisurea segments using the single cantilever method (*cooling* and *heating* rate: 2 K $min^{-1}$, frequency: 0.5 Hz). **A:** The elastic modulus (*E'*) shows a sharp change around -40 °C (*cooling* and *heating*) revealing the glass transition of the PPG-PEG-PPG segments. The decrease of the elastic modulus *E'* starting around 0 °C upon *heating* corresponds to the disassembly of the urea hydrogen bonds. **B:** The loss factor (tan *δ*) reveals the glass transition of the PPG-PEG-PPG segments at -40 and -44 °C upon *heating* and *cooling*, respectively. The disassembly and reassembly of the urea hydrogen bonds is shown by the broad peaks with a maximum around 90 °C.

In the *Dynamic Mechanical Thermal Analysis - Tension geometry method* of **8a-2** the elastic modulus *E*' sharply decreases upon *heating* by almost three orders of magnitude from $3 \cdot 10^9$ to less than $5 \cdot 10^6$ Pa between -50 and 10 °C. This reveals the glass transition of the PPG-PEG-PPG segments (figure 3.33).[139] The glass transition temperature, determined by the turning point of the elastic modulus *E*', is located at -41 °C. At 20 °C an elastic modulus of around $3 \cdot 10^6$ was found. As comparison, the elastic modulus of copolymer **6a** with hexamethylene bisurea segments and similar ratio of hydrophilic and supramolecular segments was determined to be around $2 \cdot 10^8$ at 20 °C which is almost two orders of magnitude higher. Consequently, **8a-2** reveals higher softness as **6b**. *E*' is still above *E*'' at 20 °C and the polymer is in the elastic state due to the physical crosslinks. *Heating* above 20 °C results in further decrease of *E*'. The transition from elastic to viscous behavior occurs at the crossing point $T_{cross}$ of *E*' and *E*'' at 53 °C. This is due to the disassembly of the bisurea hydrogen bonds.

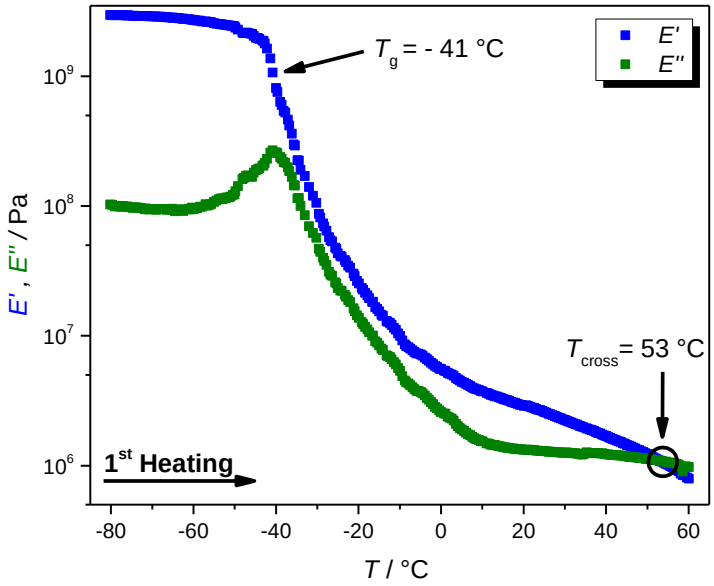


**Figure 3.33:** Dynamic mechanical thermal analysis of **8a-2** with 75 wt% hydrophilic segments and 25 wt% hexamethylene bisurea segments (tension geometry method, *heating* rate: 2 K $min^{-1}$, frequency: 1Hz). The first turning point of the elastic modulus *E*' at -41 corresponds to the glass transition of the PPG-PEG-PPG segments. The transition from elastic to viscous behavior occurs at 53 °C by the intersection of the elastic and viscous module (*E*''). Adapted and reproduced with permission (© 2020 The Authors. Macromolecular Chemistry and Physics published by WILEY-VCH GmbH).[139]

*Oscillation Shear Rheology* (figure 3.34) was measured on **8a-1**, **8a-2** and **8a-3** by heating the samples up to 160 °C and then recording the first *cooling* and second *heating curve*.[139] All three copolymers reveal a continuous increase of the elastic and viscous modulus between 160 and 20 °C upon *cooling*. The intersection between elastic and viscous moduli *G*' and *G*'' was found at 74 °C for **8a-1**, 48 °C for **8a-2** and 34 °C for **8a-3**. As a result of the increasing degree of polymerization, the transition from viscous to elastic behavior is shifted to higher temperatures. The *heating curves* of the three copolymers are almost equal to the *cooling* curves. *G*' and *G*'' slightly increase between 20 and 160 °C revealing the disassembly of the bisurea segments. The intersection between *G*' and *G*'' occurs at 77, 51 and 31 °C for **8a-1**, **8a-2** and **8a-3**, respectively. The crossover temperature of 53 °C for **8a-2** corresponds well with the intersection between *E*' and *E*'' determined in the *DMTA-tension geometry method* of **8a-2**.

In contrast to previously discussed copolymers with hexamethylene bisurea segments no significant hysteresis at *cooling* and *heating* was identified. *Heating* and *cooling curve* almost overlap each other within the entire temperature range. For instance, in copolymer **6a** with 74 wt% PPG-PEG-PPG segments and 26 wt% hexamethylene bisurea segments the intersection between G' and G'' is 25 °C lower upon *cooling* as upon *heating*. It is assumed that the hysteresis effect in the copolymers with hexamethylene segments results in a higher strength of the urea hydrogen bonds due to the linear structure of hexamethylene and the ideal packing.[81,209] Therefore, the thermal response which is necessary to break or assemble the hydrogen bonds is larger in hexamethylene bisurea segments as compared to 4,4'-methylene-bis(cyclohexyl) segments.

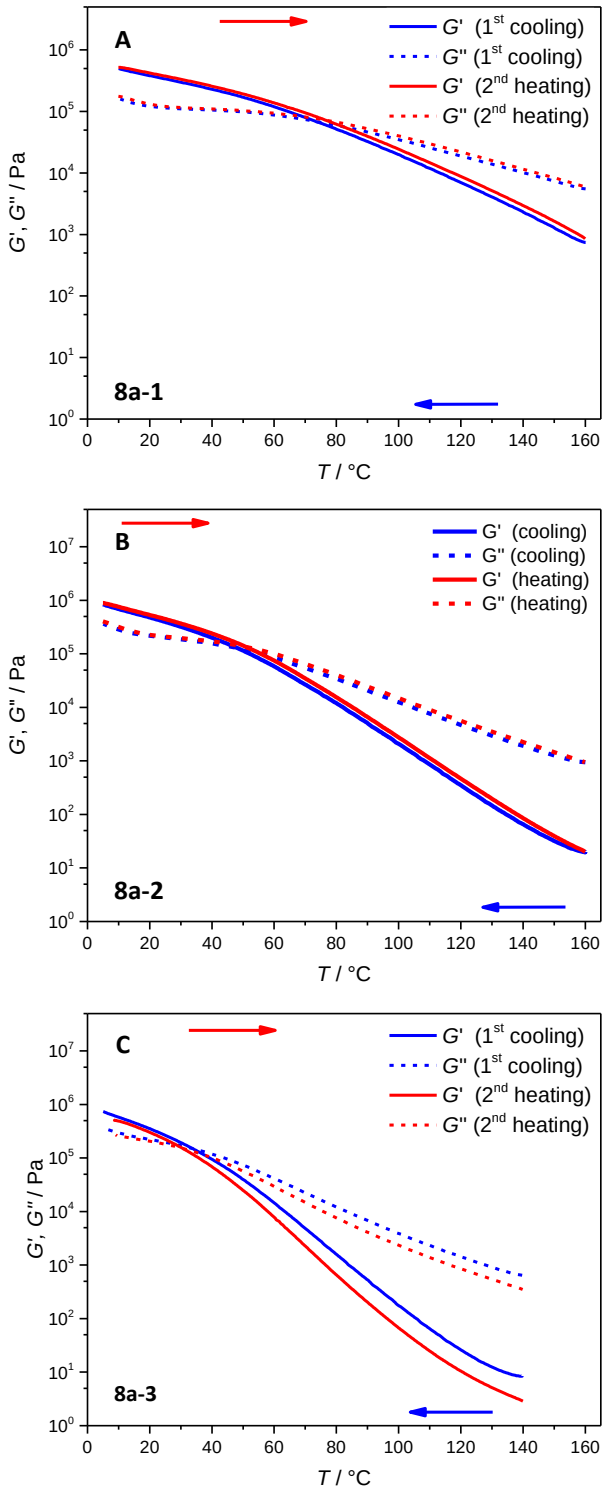


**Figure 3.34:** Oscillation rheology measurement of copolymers with 75 wt% hydrophilic segments and 25 wt% 4,4'-methylene-bis(cyclohexyl) bisurea segments **A**: **8a-1** shows the intersection between the elastic (*G*') and viscous modulus (*G*'') at 74 °C upon *cooling* and 77 °C upon *heating*; **B**: For **8a-2** the transition between elastic and viscous behavior occurs at 48 °C upon *cooling* and 51 °C upon *heating*; **C: 8a-3** shows a transition between elastic and viscous state at 34 °C upon *cooling* and 31 °C upon *heating* (*cooling* and *heating* rate: 2 K $min^{-1}$, frequency: 1 Hz). Adapted and reproduced with permission (© 2020 The Authors. Macromolecular Chemistry and Physics published by WILEY-VCH GmbH).[139]

*Oscillation shear rheology* was also used to measure the viscosity of copolymers **8a-1**, **8a-2** and **8a-3**. Here, the samples were heated to 160 °C. Afterwards, the first *cooling curves* were recorded with a rate of 2 K $min^{-1}$. As shown in figure 3.35 the melt viscosities constantly increase with a continuous transition within the broad temperature window between 140 and 20 °C.[139] The increase can be explained by the assembly of the bisurea hydrogen bonds. Figure 3.35 additionally shows that the viscosity above 40 °C is lower with decreasing degree of polymerization in the order **8a-3** < **8a-2** < **8a-1**. A similar trend was observed for copolymers having hexamethylene bisurea segments. At 100 °C a viscosity of 6390 Pa s for **8a-1**, 2030 Pa s for **8a-2** and 611 Pa s for **8a-3** was determined**.** The viscosity at 100 °C for **8a-1** is more than factor 10 higher as for **8a-3**. This demonstrates the feasibility to adjust the temperature window for melt-processing by the regulation of the degree of polymerization. Interestingly, the measured viscosities of the melt of copolymers with 25 wt% 4,4-methylene-bis(cyclohexyl) bisurea segments are around one order of magnitude higher compared to previous discussed copolymers **6a**, **6a-1** and **6a-2** with 24 wt% hexamethylene-bisurea segments and a similar degree of polymerization. This shows that the chemical structure of the bisurea segments also influences the melt viscosity.

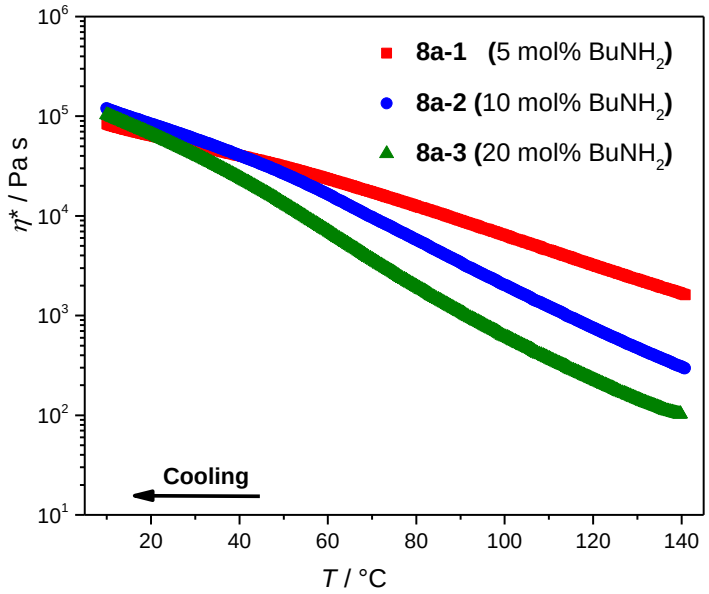


**Figure 3.35:** Melt viscosity of $(AB)_n$-segmented copolymers with 75 wt% hydrophilic segments and 25 wt% 4,4'-methylene-bis(cyclohexyl) bisurea segments measured by oscillation rheology upon *cooling* with a rate of 2 K $min^{-1}$ showing the influence of the degree of polymerization on the melt viscosity. Adapted and reproduced with permission (© 2020 The Authors. Macromolecular Chemistry and Physics published by WILEY-VCH GmbH).[139]

***Copolymers with a content of 87 wt% hydrophilic segments and 13 wt% bisurea segments***

Copolymers **8b** and **8b-1** consist of 87 wt% PPG-PEG-PPG segments of 2000 g mol$^{-1}$ and 13 wt% 4,4'-methylene-bis(cyclohexyl) bisurea segments. *Differencial Scanning Calorimetry* (DSC) was measured for both copolymers by heating the samples up to 240 °C and then recording the first *cooling* and second *heating curve*. The DSC curves of **8b** are shown in figure 3.36. Upon first *cooling* a sharp crystallization peak can be identified at -18.4 °C with a transition enthalpy of 45.6 J g$^{-1}$. The transition results from the crystallization of the PEG units in the PPG-PEG-PPG segments. The crystallization temperatures of **8b** and also **8b-1** are significantly lower as compared to copolymer **6c-2** with 9 wt% hexamethylene bisurea segments demonstrating that the PEG segments crystallize later if the chemical structure of the bisurea segments is changed from hexamethylene to 4,4'-methylene-bis(cyclohexyl). In the second *heating curve* a small glass transition of the PPG-PEG-PPG segments is found at -54 °C. Upon further *heating*, the melting of the PEG units occurs as a sharp endothermic transition with a peak at 31.4 °C which is comparable with **6c-2** having hexamethylene bisurea segments. Furthermore, the melting enthalpy is determined to be 50.9 J g$^{-1}$ resulting in a degree of crystallinity of about 34 % by using equation (3.6). The disassembly and reassembly of the urea hydrogen bonds are not detected in the DSC as it was already the case for the copolymers with 75 wt% PPG-PEG-PPG segments.

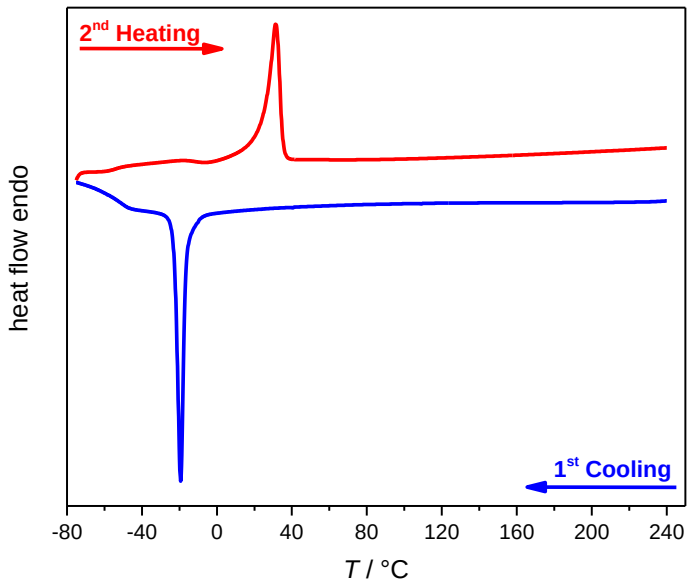


**Figure 3.36:** DSC curve of **8b** with 87 wt% PPG-PEG-PPG segments and 13 wt% 4,4'-methylene-bis(cyclohexyl)-bisurea segments. A glass transition of the PPG-PEG-PPG segments at -54 °C is visible upon *heating*. Additionally, the first *cooling* and second *heating* curve at a rate of 10 K min$^{-1}$ indicate the melting of the PEG moieties at 31 °C upon *heating* and the crystallization at -18 °C upon *cooling*.

Copolymer **8b** was further characterized by *Dynamic Mechanical Thermal Analysis - Tension geometry method* by starting the measurement at ambient temperature (figure 3.37). The curves of both the elastic modulus *E*' and the viscous modulus *E*'' reveal a steep decrease around 40 °C. This transition is caused by the melting of the semi-crystalline PEG moieties in the PPG-PEG-PPG segments. *E*' decreases from around $4 \cdot 10^8$ Pa to $10^6$ Pa. The small steep decrease of *E*' and *E*'' at 55 °C is due to an instrumental error in this measurement. Upon further *heating*, both the elastic and viscous modulus slightly decrease in the temperature range between 80 and 127 °C. The intersection between *E*' and *E*'' occurs at $T_{cross}$= 127 °C indicating the transition from elastic to viscous behavior. A broad transition was also observed for copolymers with 25 wt% 4,4'-methylene-bis(cyclohexyl) bisurea segments and is assumed to result from the slow disassembly of the urea hydrogen bonds.

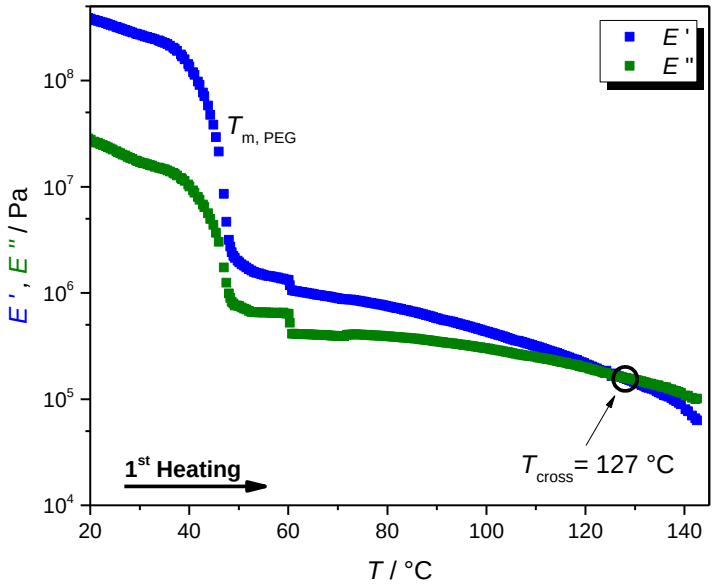


**Figure 3.37:** Dynamic mechanical thermal analysis of **8b** with 87 wt% PPG-PEG-PPG segments and 13 wt% 4,4'-methylene-bis(cyclohexyl)- bisurea segments (tension geometry experiment, *heating* rate: 2 K $min^{-1}$, frequency: 1Hz). The decrease of both the elastic (*E*') and viscous (*E*'') modulus around 45 °C corresponds to the melting of the PEG units. The crossover from elastic to viscous behavior occurs at 127 °C.

For **8b-2** the elastic and loss modulus were measured by *Oscillation shear rheology* (figure 3.38). The sample was first heated to 160 °C. Afterwards, the first *cooling* and second *heating curve* were measured. The first *cooling curve* reveals a broad increase of the storage modulus *G*' and the loss modulus *G*'' in the range between 130 and 40 °C indicating the reassembly of the bisurea hydrogen bonds. The intersection of storage modulus G' and loss modulus G'' occurs at 23 °C. Upon second *heating* G' and G'' intersect at 27 °C. Therefore, nearly no hysteresis occurs in polymers with 4,4'-methylene-bis(cyclohexyl) bisurea segments as already observed for polymers **8a**, **8a-1**, **8a-2** and **8a-3** with lower PPG-PEG-PPG segment ratio of 75 wt%. The crystallization of the PEG units could not be observed upon *cooling* down to 5 °C which is the limit of the rheological equipment used. This result correlates with the DSC curves where the crystallization of the PEG moieties was monitored at -18.3 °C. Consequently, the melting transition of the PEG units is absent in the second *heating* curve as well.

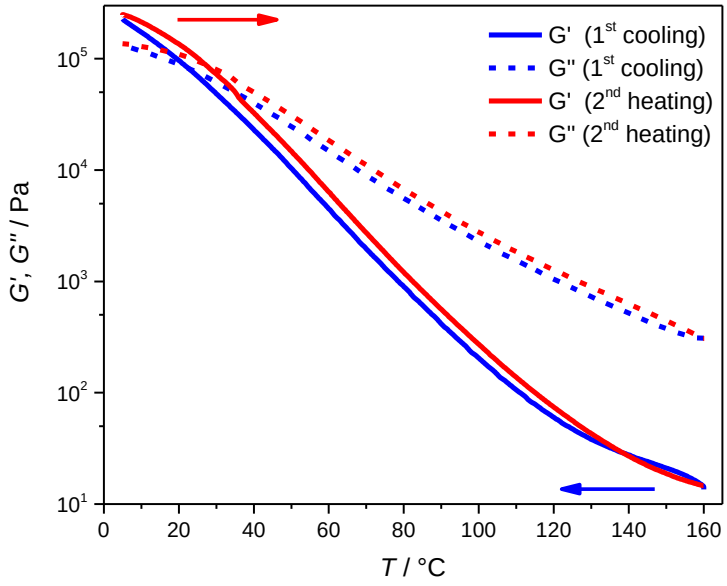


**Figure 3.38:** Oscillation rheology measurement of **8b-2** with 74 wt% hydrophilic segments and 26 wt% hexamethylene bisurea segments showing the transition between elastic and viscous state at 23 °C upon *cooling* and 27 °C upon *heating* (*cooling* and *heating* rate: 2 K $min^{-1}$, frequency: 1 Hz).

Additionally, oscillation shear rheology was used for the measurement of the viscosity for **8b** and **8b-2**. The samples were heated to 160 °C before recording the first *cooling curve*. As shown in figure 3.39 the viscosity steadily increases over the entire measurement range for both copolymers. Here, **8b** is located above **8b-2** within the complete measured temperature range. The viscosity decreases with decreasing degree of polymerization confirming the results received from all other investigated polymer series. At 100 °C melt viscosities of 7900 for **8b** and 378 Pa s for **8b-2** were determined. At 5 °C the viscosities are $1 \cdot 10^5$ Pa for **8b** and $5 \cdot 10^4$ Pa for **8b-2**. These values are in the equal range as the viscosities of copolymers **8a**, **8a-1**, **8a-2** and **8a-3** with a higher bisurea segment content of 25 wt%.

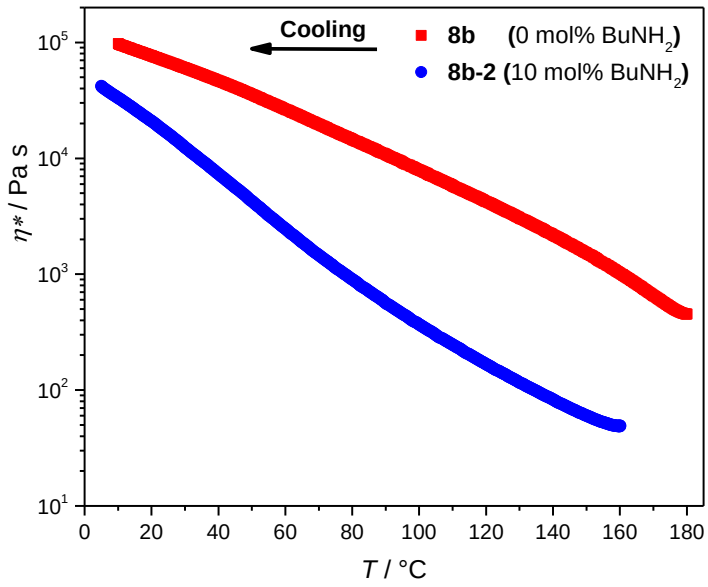


**Figure 3.39:** Complex viscosity of **8b** and **8b-2** with 74 wt% hydrophilic segments and 26 wt% hexamethylene bisurea segments upon *cooling* with a rate of 2 K $min^{-1}$ showing the influence of the degree of polymerization on the melt viscosity.

***Summary***

The results of the DSC analysis for the (AB)n-segmented copolymers with 4,4'-methylenebis(cyclohexyl) bisurea segments are compared in table 3.8. Table 3.9 summarizes the results from the *Dynamic mechanical thermal analysis* and *Oscillation shear rheology* measurements.

In summary, the $(AB)_n$-segmented copolymers with 4,4'-methylenebis(cyclohexyl) bisurea segments and PPG-PEG-PPG segments of 900 and 2000 g mol$^{-1}$ reveal a thermal property profile that is promising for melt electrowriting (MEW) and extrusion based printing (EBP).

**Table 3.8:** Summary of the DSC analysis of $(AB)_n$-segmented copolymers (*heating* and *cooling* rate: 10 K min$^{-1}$). The following values were determined: Glass transition of $T_{g,PPG\text{-}PEG,PPG}$ of the PPG-PEG-PPG segments from the second *heating* curve, the crystallization temperature $T_{c,PEG}$ and enthalpy $\Delta H_{c,PEG}$ of the PEG units, the melting temperature $T_{m,PEG}$ and enthalpy $\Delta H_{m,PEG}$ of the PEG units, the degree of crystallization of the PEG units $X_{C,\ PEG}$ (calculated by equation (3.6), the temperature range for the assembly of the bisurea hydrogen bonds upon *cooling* $T_{c,BU}$ and the temperature range for the disassembly of the bisurea hydrogen bonds upon *heating* $T_{m,BU}$.

| | $T_{g,PPG\text{-}PEG\text{-}PPG}$ [°C] | $T_{c,PEG}$ [°C] | $\Delta H_{c,PEG}$ [J g$^{-1}$] | $T_{m,PEG}$ [°C] | $\Delta H_{m,PEG}$ [J g$^{-1}$] | $X_{C,PEG}$ [%] | $T_{c,BU}$ [°C] | $T_{m,BU}$ [°C] |
|---|---|---|---|---|---|---|---|---|
| **8a** | -42 | n.d. | n.d. | n.d. | n.d. | n.d. | n.d. | n.d. |
| **8a-1** | -45 | n.d. | n.d. | n.d. | n.d. | n.d. | n.d. | n.d. |
| **8a-2** | -45 | n.d. | n.d. | n.d. | n.d. | n.d. | n.d. | n.d. |
| **8a-3** | -45 | n.d. | n.d. | n.d. | n.d. | n.d. | n.d. | n.d. |
| **8b** | -54 | -28.7 | -45.6 | 31.4 | 50.9 | 34 | n.d. | n.d. |
| **8b-1** | -55 | -28.0 | -25.9 | 33.2 | 47.4 | 31 | n.d. | n.d |

n.d.: not detectable

**Table 3.9:** Results of *Dynamic mechanical thermal analysis (DMTA) - Single Cantilever method*, *DMTA - Tension geometry method* and *rheology measurements* of $(AB)_n$-segmented copolymers with PPG-PEG-PPG segments. In the *DMTA - Single cantilever method* the glass transition temperatures of the PPG-PEG-PPG segments $T_{g,c}$ and $T_{g,h}$ upon *cooling* and *heating* were determined by using the curves of the loss factor tan $\delta$, the crystallization temperature of the PEG units $T_{c,PEG}$ and the bisurea segments $T_{c,BU}$ upon *cooling* and the melting temperature of the PEG units $T_{m,PEG}$ and the bisurea segment $T_{m,BU}$ upon *heating* were determined by using the curves of the elastic modulus E'. With the *DMTA tension geometry method* the glass transition of the PPG-PEG-PPG segments $T_g$, the melting temperature of the PEG units $T_{m,PEG}$ and the temperature $T_{cr}$ where the crossover from elastic to viscous behavior occurs were determined. The crossover temperature between storage and loss modulus $T_{cr,c}$ upon *cooling* and $T_{cr,h}$ upon *heating* and the complex viscosity $\eta^*_{100}$ upon *cooling* were determined from the *oscillation shear rheology measurements*.

| | **DMTA – Single cantilever method** | | | | | | **DMTA - Tension geometry method** | | | **Rheology** | | |
|---|---|---|---|---|---|---|---|---|---|---|---|---|
| | $T_{g,c}$ [°C] | $T_{g,h}$ [°C] | $T_{c,PEG}$ [°C] | $T_{m,PEG}$ [°C] | $T_{c,BU}$ [°C] | $T_{m,BU}$ [°C] | $T_g$ [°C] | $T_{m,PEG}$ [°C] | $T_{cr}$ [°C] | $T_{cr,c}$ [°C] | $T_{cr,h}$ [°C] | $\eta^*_{100}$ [Pa s] |
| **8a** | -44 | -41 | n.d. | n.d. | n.d. | n.d. | - | - | - | - | - | - |
| **8a-1** | -42 | -41 | n.d. | n.d. | 140 – 20 | 20 – 130 | - | - | - | 74 | 77 | 6390 |
| **8a-2** | -44 | -40 | n.d. | n.d. | 140 – 20 | 0 – 135 | -41 | n.d. | 53 | 48 | 51 | 2030 |
| **8a-3** | -46 | -37 | n.d. | n.d. | 120 – 5 | 10 – 120 | - | - | - | 34 | 31 | 611 |
| **8b** | - | - | - | - | - | - | - | 46 | 127 | 80 | n.d. | 7900 |
| **8b-1** | -38 | -29 | -8 | 31 | 105 - 0 | 35 – 140 | - | - | - | 23 | 27 | 378 |

n.d.: not detectable; - : not measured

## 3.4 Characterization of mechanical properties

Besides the melt viscosity being essential for the ability to process polymers by extrusion-based additive manufacturing techniques, the mechanical properties are from high interest. On one hand, the copolymers need to be sufficiently strong to prevent that the printed scaffold deforms and flows away. On the other hand, the copolymers should reveal soft properties and sufficiently toughness that it does not break at low strain. As examples, several $(AB)_n$-segmented copolymers were selected and investigated with tensile test experiments. Films of the copolymers were prepared from tetrahydrofuran or water solution. Solutions with a concentration of 20 wt% copolymer were poured into Teflon® moulds (10 cm x 5 cm x 1 cm) and the solvent was evaporated slowly at room temperature and ambient pressure overnight, and subsequently dried under vacuum at 50 °C for 1 – 3 days. Resulting films had a thickness of about 1 mm. Dogbone shaped specimen were punched out of the films and measured. Between four and six measurements were conducted for each copolymer and the average values were calculated and rounded by either the last digit or by two significant digits. The measurements were carried out at room temperature if not otherwise noted. In the following, the influence of the ratio of the bisurea segments, the chemical structure of the bisurea segments and the degree of crystallization of the PEG units in the PPG-PEG-PPG segments on the mechanical properties will be discussed. The results of the tensile tests are summarized in table 3.10 at the end of this chapter.

***Influence of the ratio of the bisurea segments***

$(AB)_n$-segmented copolymers with different content of the *hexamethylene bisurea segments* were compared. The selected copolymers are **6a** with 26 wt% hexamethylene bisurea segments and 74 wt% PPG-PEG-PPG segments, **6b-2** with 18 wt% hexamethylene bisurea segments and 82 wt% PPG-PEG-PPG segments and **6c-2** with 9 wt% hexamethylene bisurea segments and 91 wt% PPG-PEG-PPG segments. It should be noted that these three copolymers were also tested in MEW which will be discussed in chapter 4.1.

The resulting tensile curves are depicted in figure 3.40. First, an elastic deformation, where the stress increases linearly with the strain, occurs followed by a transition to deformation regime at

the yield point. The samples can further be strained until they break. Copolymers **6a** and **6b-2** have amorphous PPG-PEG-PPG segments and are not semi-crystalline at room temperature as already described in chapter 3.3. They reveal a similar Young's modulus of about 170 ± 30 and 140 ± 20 MPa, respectively. Strain at break and strength at break are much higher for **6a,** resulting in a toughness of 11850 ± 380 · $10^4$ J $m^{-3}$, compared to copolymer **6b-2** with 4020 ± 630 · $10^4$ J $m^{-3}$.

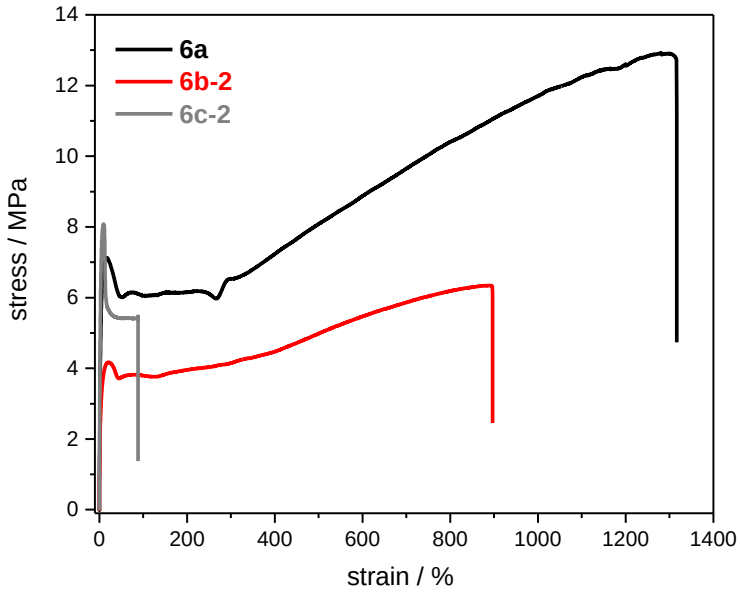


**Figure 3.40:** Comparison of tensile curves of $(AB)_n$-segmented copolymers **6a** with 26 wt% (black), **6b-2** with 18 wt% (red) and **6c-2** with 9 wt% (grey) hexamethylene bisurea segments and PPG-PEG-PPG segments.

Copolymer **6c-2** has only 9 wt% hexamethylene bisurea segments and the PPG-PEG-PPG segments are semicrystalline at room temperature. The highests Young's modulus of 280 ± 20 MPa was determined for **6c-2** compared to the amorphous copolymers **6a** and **6b-2**. The Young's modulus rises with increasing crystallinity of the PEG segments. For comparison semi crystalline PCL, the most commonly used polymer in MEW, has a Young's modulus of about 350 MPa which is comparable to **6c-2**.[210] The semi-crystallinity of **6c-2** results in higher necking and a sharp yield point as compared to **6a** and **6b-2** (figure 3.40). Copolymers **6a** and **6b-2** have a strain at large break with 850 ± 120 % for **6b-2** and even with 1220 ± 110 % for **6a**. In contrast, copolymer **6c-2** can only be deformed until a strain of 150 ± 50 %. As a result, a distinctly lower toughness of 850 ± 260 · $10^4$ J $m^{-3}$ was determined for **6c-2**.

Tensile tests were also carried out for copolymers **8a-2** and **8b-2** with *4,4'-methylene-bis(cyclohexyl) bisurea segments*. Here, the ratio of bisurea segments is 25 wt% for **8a-2** and

13 wt% for **8b-2**. Both copolymers were prepared by adding equal amounts of *n*-butylamine to regulate the molecular weight and reveal comparable degrees of polymerization (31 for **8a-2** and 25 for **8b-2**). The tensile curves are depicted in figure 3.41. Young's modulus for **8a-2** was determined to be 5.8 ± 1.9 MPa which is around a factor of 14 lower than for **8b-2** (81 ± 15 MPa) and even a factor of 300 lower as compared to the previously discussed copolymer **6a** with hexamethylene bisurea segments and with similar ratio of bisurea segments (170 ± 30 MPa). **8a-2** can be deformed up to 195 ± 47 % resulting in a toughness of $21 \pm 5 \cdot 10^4$ J m$^3$ being approximate factor 10 lower as the toughness determined for **8b-2** with only $120 \pm 10 \cdot 10^4$ J m$^3$. The PEG units in **8b-2** are crystallized at room temperature as found by DSC measurements. The crystallinity of the PEG moieties results in a higher Young's modulus and a lower strain at break (46 ± 9 %). The same trend was observed for copolymers with *hexamethylene bisurea segments*. In comparison to **6b-2** the toughness of **8a-2** is around a factor of 200 lower. The softness of these copolymers with *4,4'-methylenebis(cyclohexyl) bisurea segments* can be explained by the weaker hydrogen bonding, as revealed by FT-IR spectroscopy and discussed in chapter 3.2.

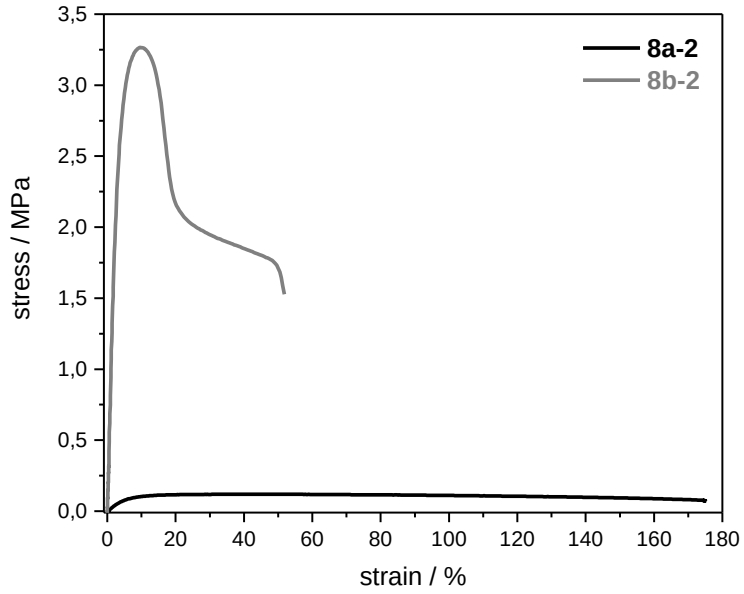


**Figure 3.41:** Comparison of tensile curves of $(AB)_n$-segmented copolymers **8a-2** with 25 wt% (black curve) and **8b-2** with 13 wt% (grey) 4,4'-methylene-bis(cyclohexyl) bisurea segments and 87 wt% PPG-PEG-PPG segments.

### *Influence of the chemical structure of the bisurea segments*

To study the influence of the chemical structure of the bisurea segments, the tensile curves of **6c-2** with *hexamethylene bisurea segments*, **8b-2** with *4,4'-methylenebis(cyclohexyl) bisurea*

*segments* and **7b** with *1,4-trans-cyclohexane bisurea segments* are compared in figure 3.42. All three copolymers have a bisurea segment content in the range of 87 to 91 wt%. Copolymer **8b-2** reveals the lowest Young's modulus of 81 ± 15 MPa. This is more than factor 3 lower as compared to copolymer **6c-2**. This correlates with the rheology and DMTA measurements showing that copolymers with 4,4'-methylenebis(cyclohexyl) bisurea segments have a lower elastic modulus as compared to polymers with hexamethylene bisurea segments. Copolymer **8b-2** reveals a broad yield point indicating its thermoplastic behavior and can be strained until 46 ± 9 %. Consequently, **8b-2** has a low toughness of 120 ± 10 · $10^4$ J $m^{-3}$ which is around factor 7 lower than the toughness determined for **6c-2**. Therefore, the exchange of hexamethylene to 4,4'-methylenebis(cyclohexyl) bisurea segments results in worse mechanical properties. This is caused by the weaker hydrogen bonds between the bisurea-4,4'-methylenebis(cyclohexyl) segments.

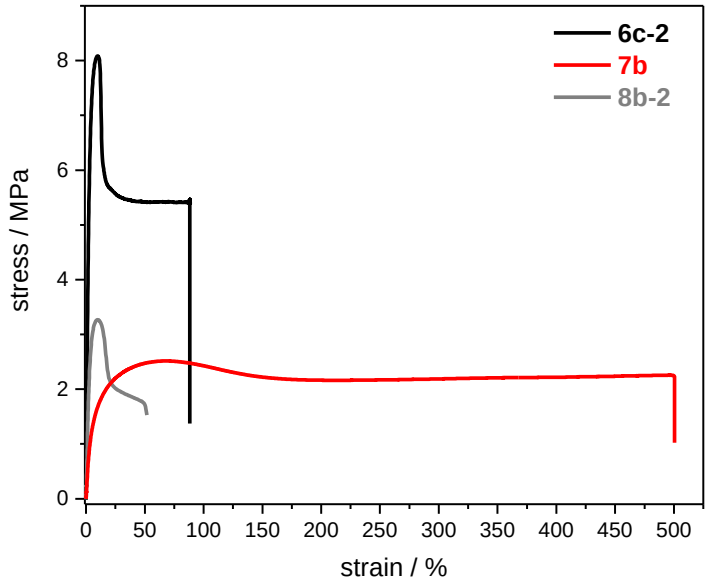


**Figure 3.42:** Comparison of tensile curves of $(AB)_n$-segmented copolymers with 87 – 91 wt% PPG-PEG-PPG segments and hexamethylene bisurea (**6c-2**, black curve), *trans*-1,4-cyclohexane bisurea (**7b**, red) and 4,4'-methylene-bis(cyclohexyl) bisurea (**8b-2**, grey) segments.

The Young's modulus of copolymer **7b** (31 ± 7 MPa) with trans-1,4-cyclohexyl bisurea segments is lower as compared to **8b-2** and **6c-2**. **7b** can be further deformed to 520 ± 160 % resulting in a higher toughness of 1230 ± 370 · $10^4$ J $m^{-3}$. The lower Young's modulus and the higher deformation can be explained by the lower melting point of the PEG units determined to be at about 20 °C by DSC and DMTA.

***Influence of the crystallinity of the PEG units***

Additionally, tensile tests of one copolymer with PEG units in the semi-crystalline state and in the non-crystalline melt state were performed. Copolymer **6c-2** with 9 wt% *hexamethylene bisurea segments* and 91 wt% PPG-PEG-PPG segments was chosen as example. Dogbone films of the copolymer were prepared as described above and then heated to 50 °C for 2 h prior conducting of the tensile test. At 50 °C the copolymer is in the rubbery phase as shown on page in chapter 3.3.1. The tensile test was performed at room temperature directly after taking the sample out of the oven. Experiments with polarization microscope revealed that the crystallization of **6c-2** starts around 20 minutes after the temperature is changed from 50 °C to room temperature. In this case, the PEG units are still in the molten phase during the measurement of the stress-strain curve. Tensile tests of **6c-2** with non-crystallized PEG units result in a Young's modulus of 88 ± 22 MPa which is more than a factor of 3 lower as compared to the sample with crystallized PEG units (figure 3.43). The strain at break increases from 150 ± 50 to 650 ± 80 % and the toughness is enhanced by a factor of 4 to 3150 ± 260 · $10^4$ J $m^{-3}$.

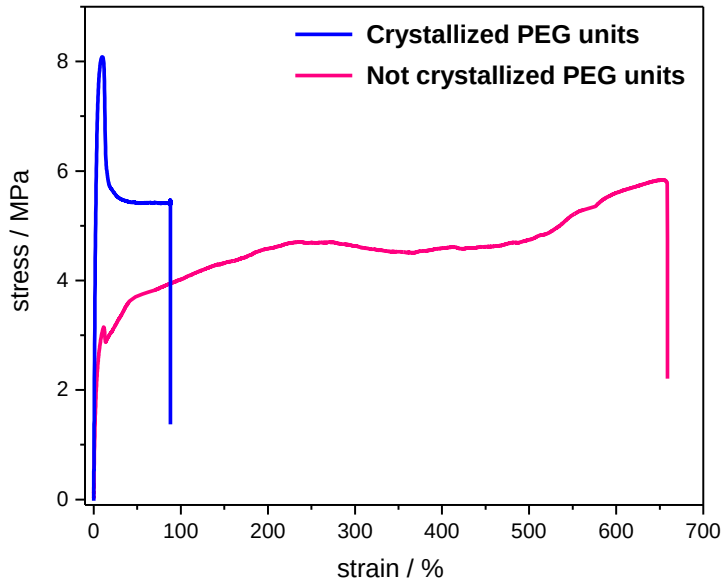


**Figure 3.43. A:** Tensile curves of **6b-2** with 82 wt% PPG-PEG-PPG segments and 18 wt% hexamethylene bisurea segments at room temperature. The blue curve represents a sample in which the PEG units are crystallized. The pink curve shows a sample in which the PEG units are not crystallized.

It is worth to point out, that the maximum deformation, toughness, stress at yield point and stress at break of **6c-2** with PEG units that are not crystallized are similar to **6b-2**. Both copolymers with hexamethylene bisurea segments were in the elastic state during the measurements as a result

of the non-crystallized PEG units. This is the consequence of the physical crosslinks between the bisurea hydrogen bonds demonstrating that the supramolecular interactions lead to elasticity and high toughness.

***Summary***

The tensile tests show that the chemical structure of the bisurea segments and the amount of bisurea segments and PPG-PEG-PPG segments significantly influence the mechanical properties of the (AB)n-segmented copolymers. Copolymers with hexamethylene bisurea segments have the highest toughness. Moreover, the mechanical properties depend on the crystallization of the PEG units as shown by a comparison of a copolymer with crystallized and non-crystallized PEG segments. The strain at break and the toughness of copolymers with crystallized PEG units is much lower if the PPG-PEG-PPG segments are crystallized.

**Table 3.10:** Summarized results of the tensile tests of the investigated $(AB)_n$-segmented copolymers with PPG-PEG-PPG segments. The average value of four to six measurements was determined for each measured copolymer and rounded by either the last digit or two significant digits.

| Polymer | $E$ / MPa[a)] | $\sigma_{yi}$ / MPa[b)] | $\sigma_{br}$ / MPa[c)] | $\varepsilon_{br}$ / %[d)] | $U_T$ / $10^4$ J m$^{-3}$ [e)] |
|---|---|---|---|---|---|
| **6a** | 170 ± 30 | 6.9 ± 0.3 | 12.9 ± 0.2 | 1220 ± 110 | 11850 ± 380 |
| **6b-2** | 140 ± 20 | 3.1 ± 0.2 | 6.1 ± 0.3 | 850 ± 90 | 4020 ± 630 |
| **6c-2** | 280 ± 30 | 8.1 ± 0.2 | 5.5 ± 0.1 | 150 ± 50 | 850 ± 260 |
| **6c-2 (50 °C)** | 88 ± 22 | 3.1 ± 0.2 | 6.1 ± 0.6 | 650 ± 80 | 3150 ± 260 |
| **7b** | 31 ± 7 | 2.6 ± 0.1 | 2.3 ± 0.2 | 520 ± 160 | 1230 ± 370 |
| **8a-2** | 5.8 ± 1.9 | -[1)] | 0.07 ± 0.01 | 195 ± 47 | 12 ± 5 |
| **8b-2** | 81 ± 15 | 3.4 ± 0.3 | 1.7 ± 0.1 | 46 ± 9 | 120 ± 10 |

a) Young's modulus; b) strength at yield; c) strength at break; d) elongation at break; e) toughness; 1) No yield point

## 3.5 Investigation of the hydrogel formation

The properties of the $(AB)_n$-segmented copolymers exposed to aqueous media were investigated by the following procedures:

*Time-dependent behavior of the copolymers in aqueous solution*

The time-dependent behavior of the $(AB)_n$-segmented copolymers in distilled water and phosphate buffered saline (PBS) solution was investigated to evaluate if the copolymers form stable gels or form gels which slowly disintegrate in the aqueous media. Out of a melt-pressed film with a thickness of about 0.5 mm, either square shaped specimen with a size of 0.8 cm x 0.8 cm (if not noted different) or circular specimens with a diameter of 6.0 cm were cut out. The films were placed in a petri dish and immersed either with distilled water or PBS solution. Experiments were done at ambient temperature. Photographs were taken in regular time intervalls. For better visibility a small amount of fluoreszent green was added to some of the copolymers prior to the film preparation.

*Water uptake of $(AB)_n$-segmented copolymers in aqueous solution*

For copolymers that form stable hydrogels that do not disintegrate the time-dependent water uptake was determined by using a humidity balance. In this balance, the weight of the swollen hydrogel was determined. Afterwards, the temperature was increased to 130 °C and the water of the hydrogels was completely removed. The full amount of water is removed if the weight reached a constant value. The water uptake of the copolymers was investigated by swelling for different time periods and then drying in the humidity balance to also determine the speed of water uptake.

*Oszillation rheology of hydrogels*

The viscoelastic properties of selected hydrogels were investigated by using an Anton Paar MCR 302 rheometer. The frequency sweep (0.5 to 5 rad $s^{-1}$) was conducted at ambient temperature and constant strain of 0.2 %.

### *(AB)$_n$-segmented copolymers with hexamethylene bisurea segments*

First, copolymer **6a** consisting of 26 wt% *hexamethylene bisurea segments* was investigated within this copolymer series. For the study of the time-dependent swelling behavior in distilled water and phosphate buffered saline (PBS) solution, square films with 0.8 cm side length were prepared by melt pressing without adding a dye. Experiments were done at ambient temperature. Photographs were taken in regular time intervalls.

Figure 3.44 reveals that the copolymer film of **6a** swells and maintains its shape without dissolving over a period of 120 h. Slight movement of the petri dish had no influence on the film stability. However, the gel was too weak and could not be removed by a pincette. Consequently, the water uptake of **6a** could not be studied since the hydrogel fell apart during the transfer from the water vessel to the humidity balance, thus showing the low mechanical stability of the hydrogel. **6a** first forms a transparent hydrogel which starts to turn opaque after 2 h. After 24 h the copolymer film was completely turbid. Time- or temperature-dependent gel-gel transition from clear to turbid was already reported for other supramolecular hydrogels.[211] A possible reason for such a transition is an altering internal packing arrangement of the swollen polymer.

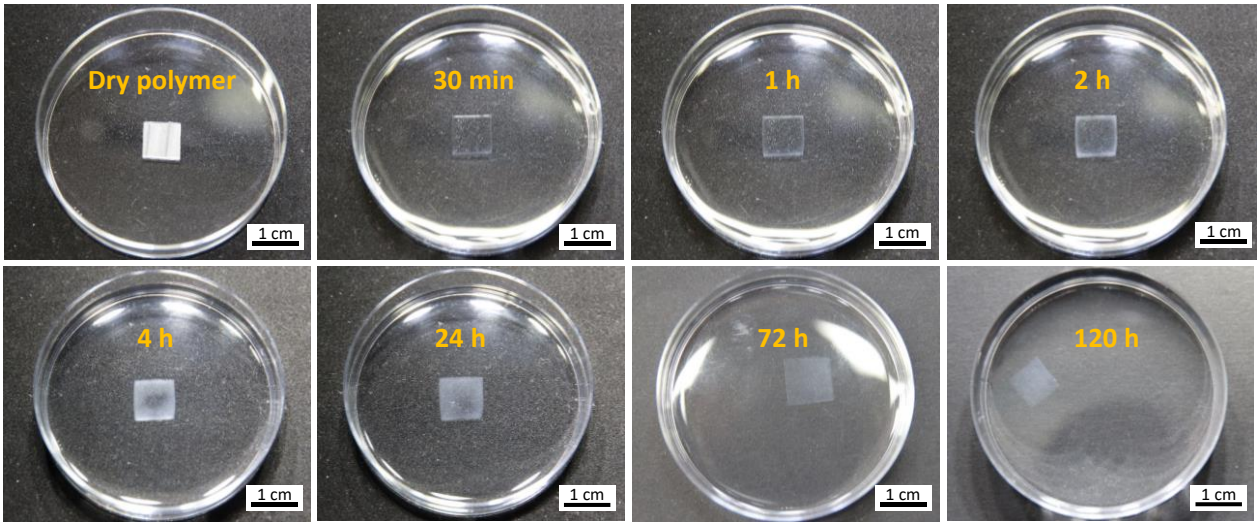


**Figure 3.44:** Photographs representing a film of copolymer **6a** with 74 wt% PPG-PEG-PPG segments and 26 wt% hexamethylene bisurea segments in water. The polymer film maintains its shape within 5 d and starts turning opaque after 2 h.

Similar results as for **6a** were received for molecular weight regulated copolymers **6a-1** and **6a-2.**

The behavior of copolymer **6b-2** with 18 wt% hexamethylene bisurea segments in aqueous solution was also studied. Circular specimens with a diameter of about 6 cm and film thickness of 0.5 mm were prepared. A small amount of a fluoreszent green dye was added prior to the film preparation to achieve a better visibility during the swelling tests. Figure 3.45 reveals that copolymer **6b-2** remains stable up to 1 h in distilled water at room temperature if no mechanical force is applied. Furthermore, the size of the copolymer film slightly increases revealing that the copolymer takes up water. However, if the petri dish was slightly moved the gel fell apart. Mechanical stresses, e.g. by shaking of the dish leads to a further disintegration of the copolymer gel. This demonstrates a very low stability and fragmentation of the formed hydrogel. Conseqently, the hydrogel could not be removed with a pincette and transferred to the humidity balance for evaluating water uptake. Same observations were also made in PBS solution.

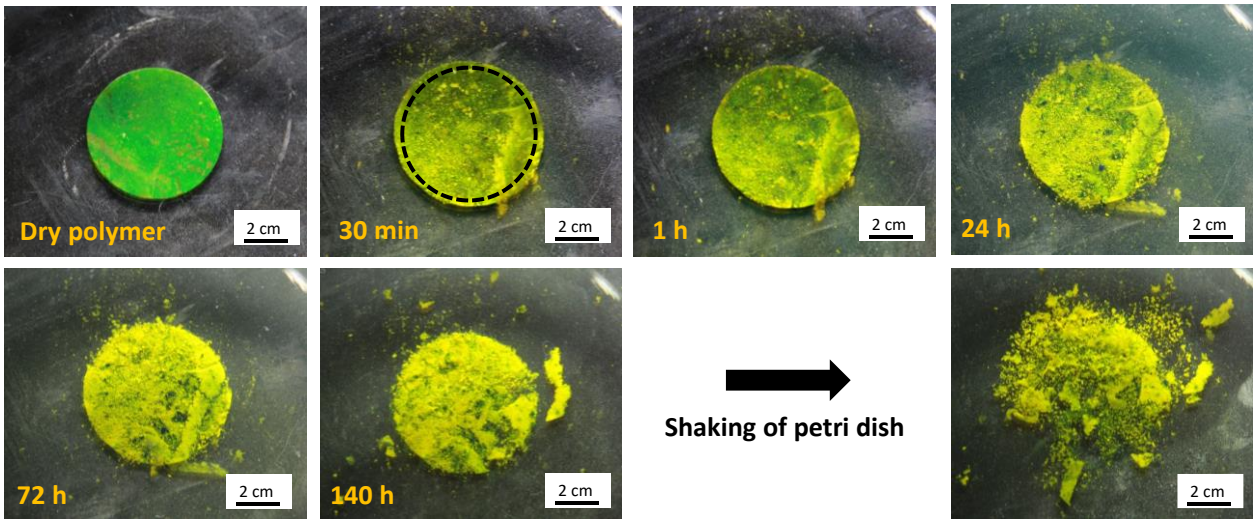


**Figure 3.45:** Photographs showing a film of copolymer **6b-2** with 82 wt% PPG-PEG-PPG segments and 18 wt% hexamethylene bisurea segments covered with fluorescent green dye in water. The polymer film maintains its shape within 140 h without dissolving if no mechanical force is applied. The polymer falls apart if a mechanical force is applied, e.g. by shaking of the petri dish.

The softness and low mechanical stability of the hydrogel of **6b-2** were confirmed by oscillation rheology (figure 3.46). For the measurements, a hydrogel consisting of 30 wt% copolymer and 70 wt% water was prepared. Elastic modulus *G'* was determined to be below 100 Pa within the measured oscillation frequency range between $10^{-1}$ and $10^{2}$ Hz. This is almost two orders of magnitudes lower as compared to similar $(AB)_n$-segmented copolymers reported by Pawar et. al. and Cui et. al. consisting of PEG segments and urea-urethane hard segments which are linked by an alkyl spacer group.[93,94] *G'* was determined to be 65 Pa at oscillation frequency of 1 Hz. Nevertheless, the hydrogel is still in the gel state since *G'* is above the viscous modulus *G''*.

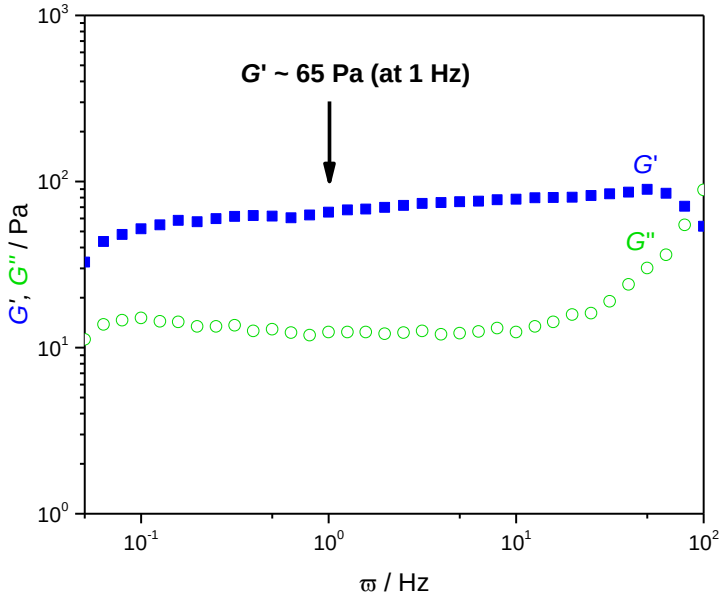


**Figure 3.46:** Oscillation rheology (Frequency sweep) of a gel consisiting of 30 wt% copolymer **6b-2** and 70 wt% water, showing the softness of the hydrogel with a storage modulus of about 65 Pa (temperature: 22 °C,strain: 0.2 %).

In the same way as discussed before the swelling behavior in water of copolymer **6c-2** with 9 wt% hexamethylene bisurea segments was investigated. A small amount of a fluorescent green dye was added for better visibility prior to the film preparation. Figure 3.47 shows that **6c-2** maintains its shape in distilled water for only a few minutes at room temperature. The copolymer starts to disintegrate after 3 minutes which can be seen by the dispersion of the dye particles outside the circle. The circular form is completely vanished after 1 h revealing the fragility. Same observation was made in PBS solution.

As a result, the stability of copolymers with hexamethylene bisurea segments in water decreases with increasing ratio of PPG-PEG-PPG segments. This can be explained by the too high content of the highly hydrophilic PEG moieties and the lower density and size of the physical crosslinks. Copolymers **6c** and **6c-1** and **6c-3** with even high PEG content reveal the same properties if exposed to water.

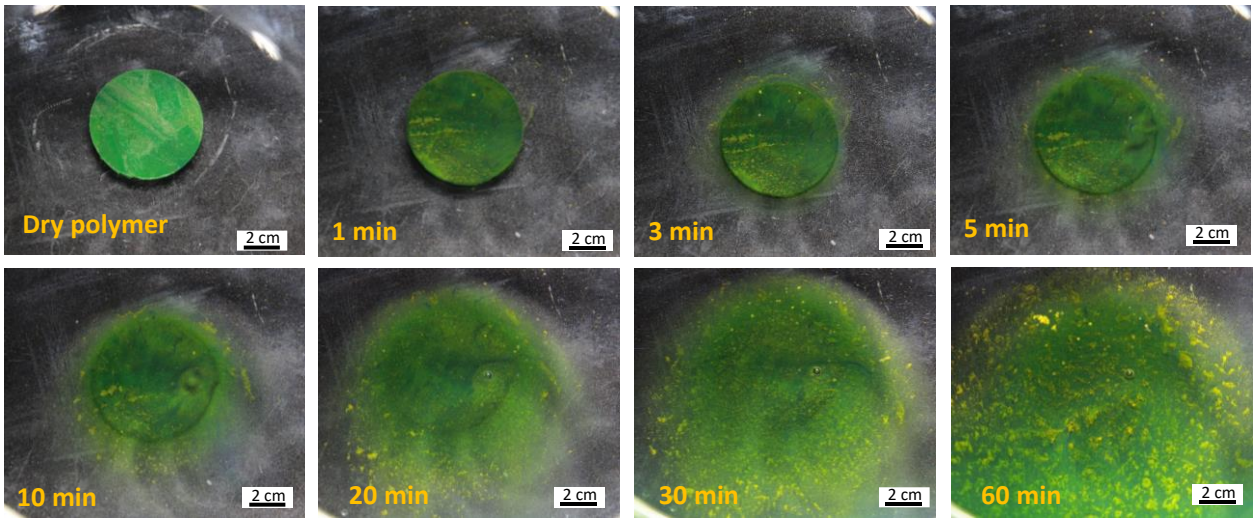


**Figure 3.47:** Images presenting a film of polymer **6c-2** with 91 wt% PPG-PEG-PPG segments and 9 wt% hexamethylene bisurea segments with fluorescent green dye exposed to water. The copolymer film is completely disintegrated in water within 60 min.

### *$(AB)_n$-segmented copolymers with trans-1,4-cyclohexane bisurea segments*

The copolymers **7a**, **7b** and **7b-1** with *trans-1,4-cyclohexane bisurea segments* all disintegrate in aqueous media fast at room temperature regardless of the ratio of the PPG-PEG-PPG and bisurea segments. No swelling of the copolymers prior disintegration was observed. For this reasons these polymer class could not be further investigated regarding their properties in aqueous media.

### *$(AB)_n$-segmented copolymers with 4,4'-methylene-bis(cyclohexyl) bisurea segments*

Copolymers **8a**, **8a-1**, **8a-2** and **8a-3** with 75 wt% PPG-PEG-PPG segments and 25 wt% *4,4'-methylenebis(cyclohexyl) bisurea segments* were studied in aqueous media as circular film with a diameter of 6 cm. In this case no dye was added. All four copolymers were found to swell in aqueous media independent of their degree of polymerization. All hydrogels remain stable in distilled water and PBS solution and do not disintegrate or dissolve. These observations were made at room temperature and also at an elevated temperature of 37 °C.

Swelling tests were performed by placing the polymer film in a dish as exemplarly shown for **8a-2** in figure 3.48. The copolymer films were fully immersed in water. The copolymer increases its size by taking up water and remains stable within 24 h. Additionally, **8a-2** starts getting turbid from the edge after 2 h and is completely opaque after 5 h. This is comparable to the hydrogels of $(AB)_n$-segmented copolymers discussed before with similar amounts of PPG-PEG-PPG segments (74 wt%) and hexamethylene segments (26 wt%) that became opaque after 2 h. The transition from clear to turbid results from the alteration of the internal rearrangement during swelling as also reported for other supramolecular hydrogels in literature.[211] Copolymers **8a**, **8a-1**, **8a-2** and **8a-3** could be transferred to the humidity balance by a pincette. Therefore, the time-dependent water uptake could be studied for this copolymer class.

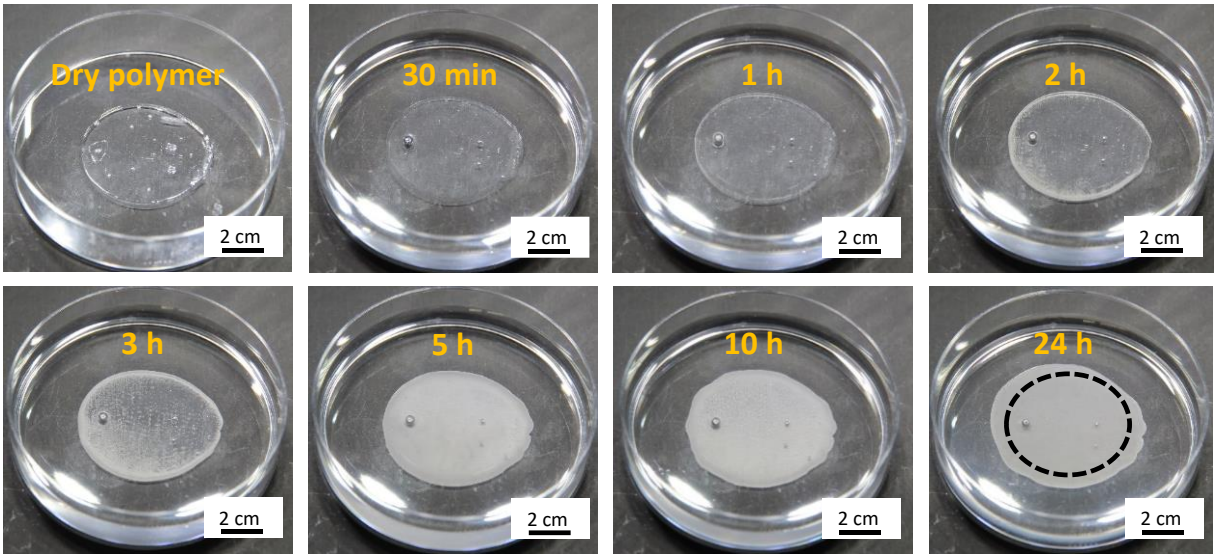


**Figure 3.48:** Images presenting a film of polymer **8a-2** with 75 wt% PPG-PEG-PPG segments of 900 g $mol^{-1}$ and 25 wt% hexamethylene bisurea segments. The copolymer film takes up water by increasing its size within 24 h. The hydrogel gets turbid within 5 h.

The time-dependent water uptake of **8a**, **8a-2** and **8a-3** was determined with a humidity balance (figure 3.49).[139] This series allows to study the influence of the degree of polymerization. The water uptake reached an equilibrium content of about 70 wt% within 1 day of swelling for all three copolymers. The physical crosslinks remain stable in aqueous solution and a stable gel is formed. It is assumed that the hydrophobic PPG spacer together with the bulky methylene-bis(cyclohexyl) structure protect the urea moieties from the hydrophilic PEG units and stabilize the physical crosslinks. The speed of the water uptake of the swollen copolymers slightly decreases in the following order: **8a** > **8a-2** > **8a-3**. **8a** and **8a-2** reach a constant water content after 5 hours whereas the water uptake of **8a-3** is completed after around 10 h. This can be a result of the lower degree of polymerization and increasing amount of n-butyl end groups in copolymers **8a-2** and **8a-3**. It should be pointed out that the determined water contents of about 70 wt% correlate well with several human soft tissues, such as skin, cartilage and muscle which also all consist of around 70 wt% water.

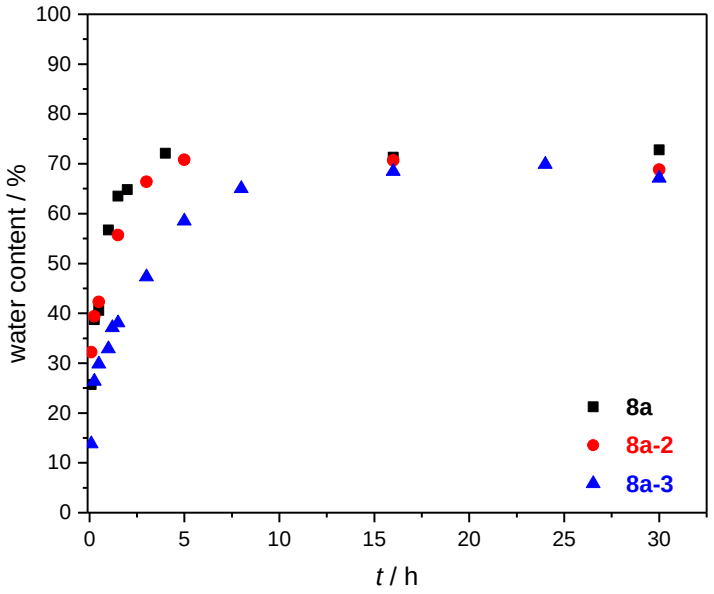


**Figure 3.49:** Time-dependend water uptake of $(AB)_n$-segmented copolymers with 75 wt% PPG-PEG-PPG segments and 25 wt% 4,4'-methylene-bis(cyclohexyl) bisurea segments and a degree of polymerization of 38 (**8a**), 31 (**8a-2**) and 26 (**8a-3**). All three polymers absorb around 70 wt% water. Adapted and reproduced with permission (© 2020 The Authors. Macromolecular Chemistry and Physics published by WILEY-VCH GmbH).[139]

Oscillation rheology was performed for a hydrogel of copolymer **8a-2** to measure the viscoelastic properties. Prior to the measurement the copolymer was swollen in water for 16 h to reach equilibrium water content of around 70 wt%. Figure 3.50 depicts the frequency sweep in the range between 0.5 and 5 rad $s^{-1}$ revealing gel-like behavior below 3 rad $s^{-1}$ due to the fact that the storage modulus *G*' is higher than the loss modulus *G*''. Above 3 rad $s^{-1}$ the material turns into a sol-like behavior with *G*' < *G*''. A low storage modulus of 71 Pa was determined at oscillation frequency of 1 rad $s^{-1}$ showing the high softness of the hydrogel. A similar value of *G*' of 65 Pa was determined for **6b-2** having hexamethylene bisurea segments. Storage and loss modulus are very close to each other showing that the hydrogel is in the gel state at low frequencies.

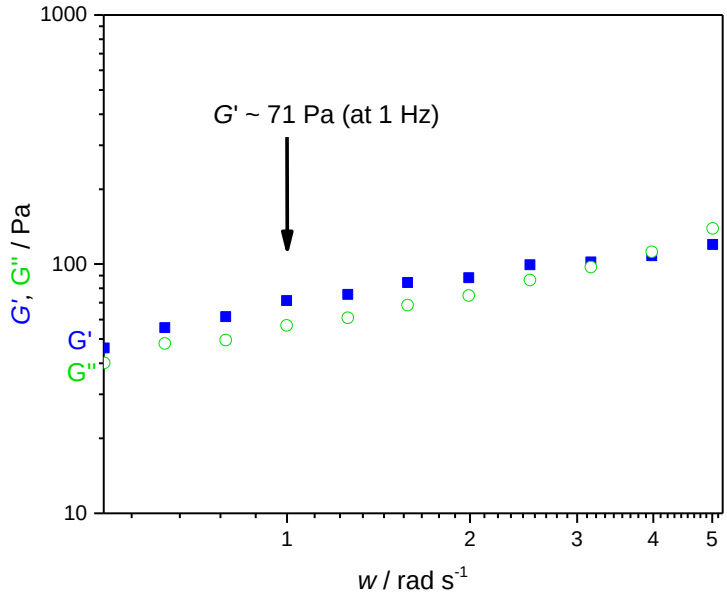


**Figure 3.50:** Oscillation rheology (frequency sweep) of swollen polymer **8a-2** with 75 wt% PPG-PEG-PPG segments and 25 wt% 4,4'-methylene-bis(cyclohexyl) bisurea segments and a degree of polymerization of 31 with 70 wt% water content showing the high softness of the hydrogel with a storage modulus below 100 Pa (temperature: 22 °C,strain: 0.2 %).

Finally, copolymers with a higher content of 87 wt% PPG-PEG-PPG segments and 13 wt% 4,4'-methylene-bis(cyclohexyl) bisurea segments were studied regarding their behavior in aqueous media. For swelling tests a rectangular shape with side lengths of 0.2 and 0.4 cm and a height of 0.05 cm was prepared. The results are exemplary shown for copolymer **8b** which has a degree of polymerization of about 29. **8b** was found to form a stable gel in aqueous solution. The copolymer film expands in all three dimensions upon swelling. As shown in figure 3.51 the longer side increases its length from 0.4 to about 1.1 cm and the shorter side increases from 0.2 to 0.6 cm.

The hydrogel is transparent. In contrast the hydrogel of copolymer **8a-2** with 75 wt% PPG-PEG-PPG segments which was discussed before, here the gel of **8b** remains clear. Water can be removed by drying and the copolymer can be swollen again. A reversible hydrogel formation was demonstrated.

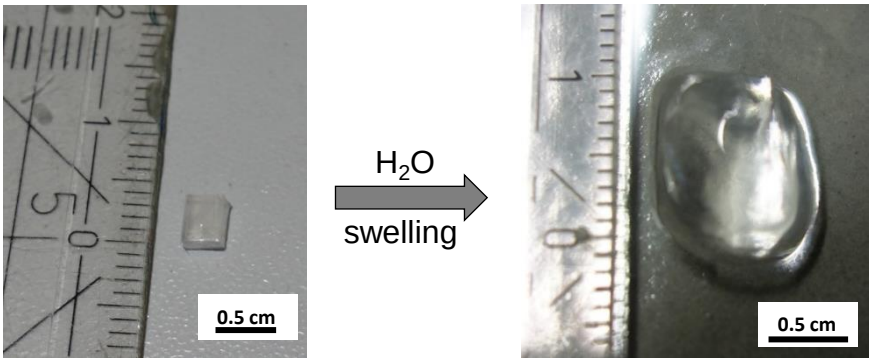


**Figure 3.51:** Size of dry and swollen polymer **8b** with 87 wt% PPG-PEG-PPG segments and 13 wt% 4,4'-methylene-bis(cyclohexyl) bisurea segments.

Copolymer **8b** absorbs a very high amount of water within 8 h as shown in figure 3.52. The water content of the received hydrogel is nearly 95 % resulting in a degree of swelling of almost 20. The increased water content compared to the hydrogels of copolymers **8a**, **8a-2** and **8a-3** with lower PPG-PEG-PPG ratio of 75 % can be explained by the higher ratio of hydrophilic PEG amount in case of the **8b** series.

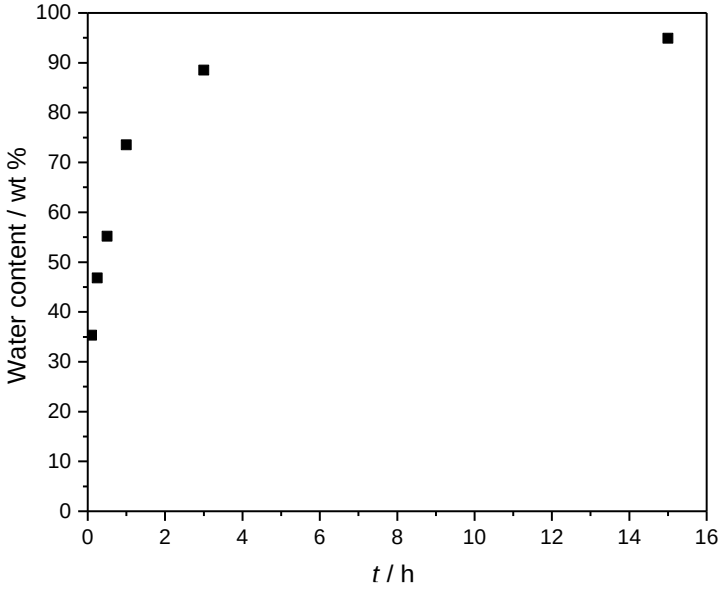


**Figure 3.52:** Time-dependend water uptake of $(AB)_n$-segmented copolymer with with 87 wt% PPG-PEG-PPG segments and 13 wt% 4,4'-methylene-bis(cyclohexyl) bisurea segments. The polymer absorps in its final state almost 95 % water.

The partial crystallinity of the PPG-PEG-PPG segments of copolymer **8a** in the dry form at ambient temperature allows to study the influence of water on the melting point of the PEG segments. A characterization by DSC was conducted by using high pressure pans. Four samples of **8a** with different amount of water ranging from 0 to 48 wt% were prepared. The samples were first heated to 100 °C, then cooled down to -80 °C. The second heating curves were then recorded in a temperature range between – 20 and 100 °C as shown in figure 3.53. The endothermic peaks in the range between 0 and 20 °C reveal the melting of the semi-crystalline PEG segments. An increase of the water content of the copolymer results in a decrease of the peak intensity and the melting enthalpy. Moreover, the maximum of the melting point curve is shifted from 31 °C in the dry state to 7 °C at 22 % of water absorption. At 48 wt% of water absorption the melting peak almost completely vanished. The peak next to this weak transition is an artifact which occurred during the DSC measurement. This results demonstrate that the water absorption occurs at the hydrohphilic PEG segments which turn from semi-crystalline to amorphous by the uptake of water. The same behavior was observed for similar $(AB)_n$-segmented copolymers with bisurea-ureido segments and pure PEGs with several molecular weights in different humidites.[58,90]

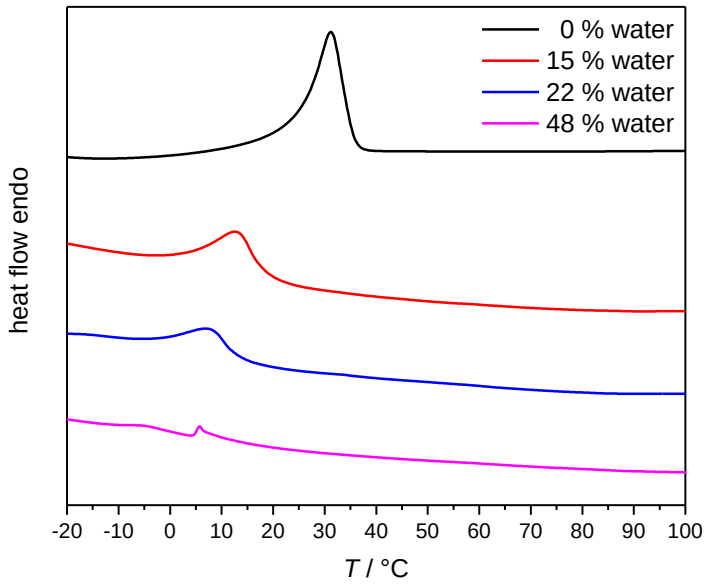


**Figure 3.53:** DSC analysis of **8b** (second *heating* curve) with varied water content showing the diminishing of the melting peak of the PEG segments with increasing water content (*heating* rate: 2 K $min^{-1}$).

Additionally, two oscillation rheology experiments were performed for a hydrogel of **8b** to investigate the viscoelastic properties. The hydrogel was kept in aqueous solution for 16 h prior to the measurement to fully absorb water and reach the equilibrium state. In the first measurement the angular frequency was varied within a range between 0.1 to 100 rad $s^{-1}$ (figure 3.54A) at a strain of 1 %. The elastic modulus G' is continuously located above the viscous modulus G''. Moreover, an elastic modulus of 1300 Pa was determined at 1 Hz. As a result the hydrogel of **8b** indicates a significantly higher strenght as compared to **8a-2** with lower amount of PPG-PEG-PPG segments whose elastic modulus at 1 Hz was only about 71 Pa. The second experiment (figure 3.54) was performed by varying the strain from 0.1 to 10 % at an angular frequency of 1 Hz. Also in this curve, the elastic modulus G' maintains above the viscous modulus G'' over the full investigated range.

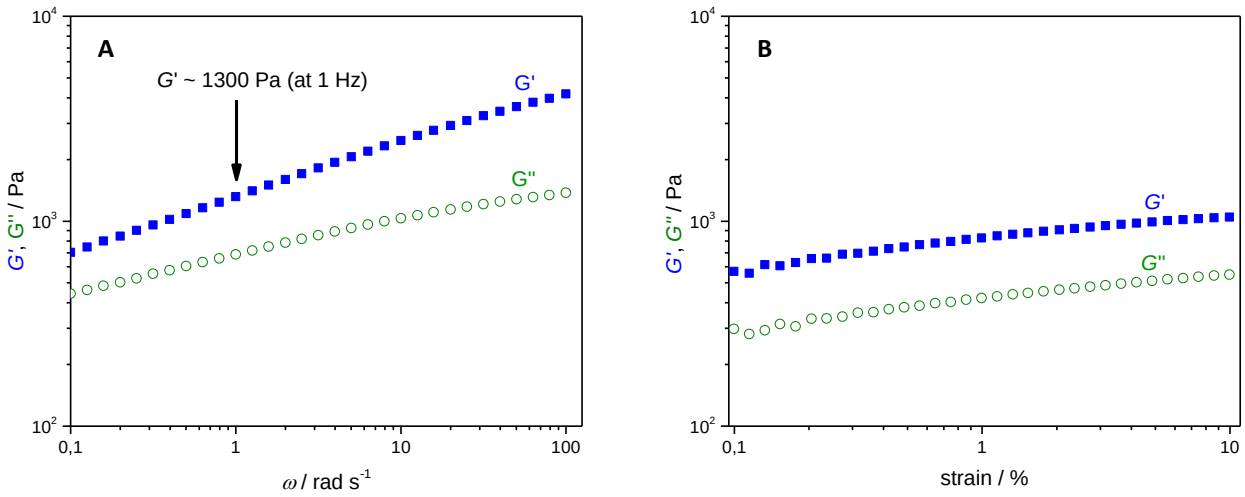


**Figure 3.54.** Oscillation rheology of swollen copolymer **8b** with 87 wt% PPG-PEG-PPG segments and 13 wt% 4,4'-methylene-bis(cyclohexyl) bisurea segments; **A:** Frequency sweep (temperature: 22 °C, strain: 1 %); **B:** strain sweep (temperature: 22 °C, angular frequency: 1 Hz).

To sum up, copolymers with 4,4'-methylene-bis(cyclohexyl) bisurea segments form stable hydrogels in aqueous media that do not disintegrate or dissolve. The strenght of the hydrogels is influenced by the amount of the hydrophilic segments in the copolymer.

## 3.6 Cytotoxicity studies

The cytotoxicity tests were carried out with selected copolymers by the *Department of Functional Materials in Medicine and Dentistry, University of* Würzburg. All cytotoxicity tests were conducted according to ISO Norm 10993-5.

***$(AB)_n$-segmented copolymers with hexamethylene bisurea segments***

The cytotoxicity was determined for copolymer **6b-2** with 82 wt% PPG-PEG-PPG segments and 18 wt% *hexamethylene bisurea segments* and for copolymer **6c-2** with 91 wt% PPG-PEG-PPG segments and 9 wt% hexamethylene bisurea segments. These two copolymers were selected due to their promising melt viscosity properties in view of additive manufacturing by melt electrowriting. To mimic the conditions in extrusion based process, films were melt pressed at 100 °C prior to cell tests. Hereby, the material was already heated to a temperature range in which MEW and EBP will be conducted. Cell culture media containing mouse fibroblast cells were used for the tests. The viability of the mouse fibroblast cells in the presence of copolymers **6b-2** and **6c-2** was studied by WST assay and by cell number counting using a Casy cell counter.[23] Additionally, microscope images of the cells were recorded. The copolymers were inserted into the cell media by using four different concentrations ranging from 50 to 1 g $L^{-1}$. Polymers are regarded to be not cytotoxic if at least 80 % of all cells remain active.

First, copolymer **6b-2** was investigated. Figure 3.55 shows the cell viability in presence of **6b-2.** At concentrations of 1, 5 and 10 g $L^{-1}$ at least 80 % are active in both the WST and cell number measurements. The cell viability distinctly decreases if the concentration of **6b-2** is raised to 50 g $L^{-1}$. The microscope images of the cells confirm this results as indicated in figure 3.56. The density of living cells at 5 and 10 g $mol^{-1}$ do not differ from the reference sample with absent of **6b-2**. In contrast, a lower cell density was found for 50 g $L^{-1}$. Therefore, it can be concluded that **6b-2** is not cytotoxic if the concentration does not exceed 10 g $L^{-1}$.

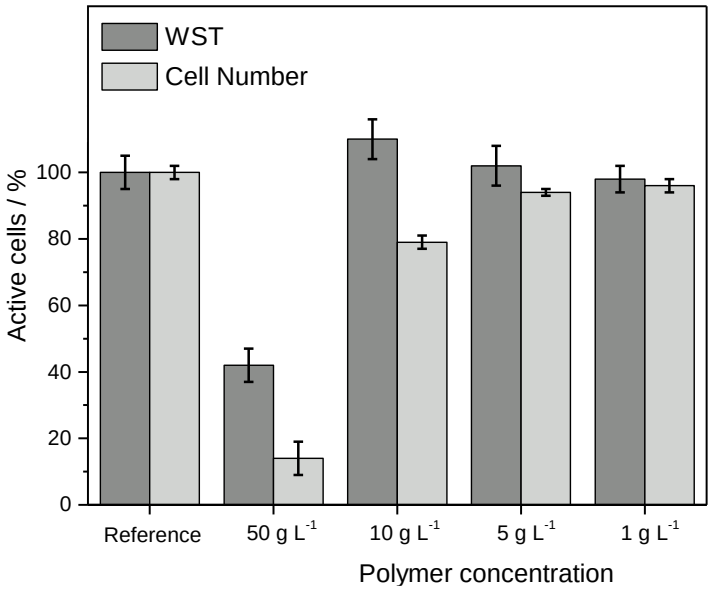


**Figure 3.55:** Viability of mouse fibroblast cells in the presence of **6b-2** with 18 wt% hexamethylene bisurea segments and 82 wt% PPG-PEG-PPG segments and at three different eluate concentrations by performing WST and cell number assay. Four different concentrations of disintegrating copolymers in the eluate were used. The viability reaches or exceeds 80 % at a concentration of 10 g $L^{-1}$ or lower indicating that the copolymer is not cytotoxic at these concentrations.

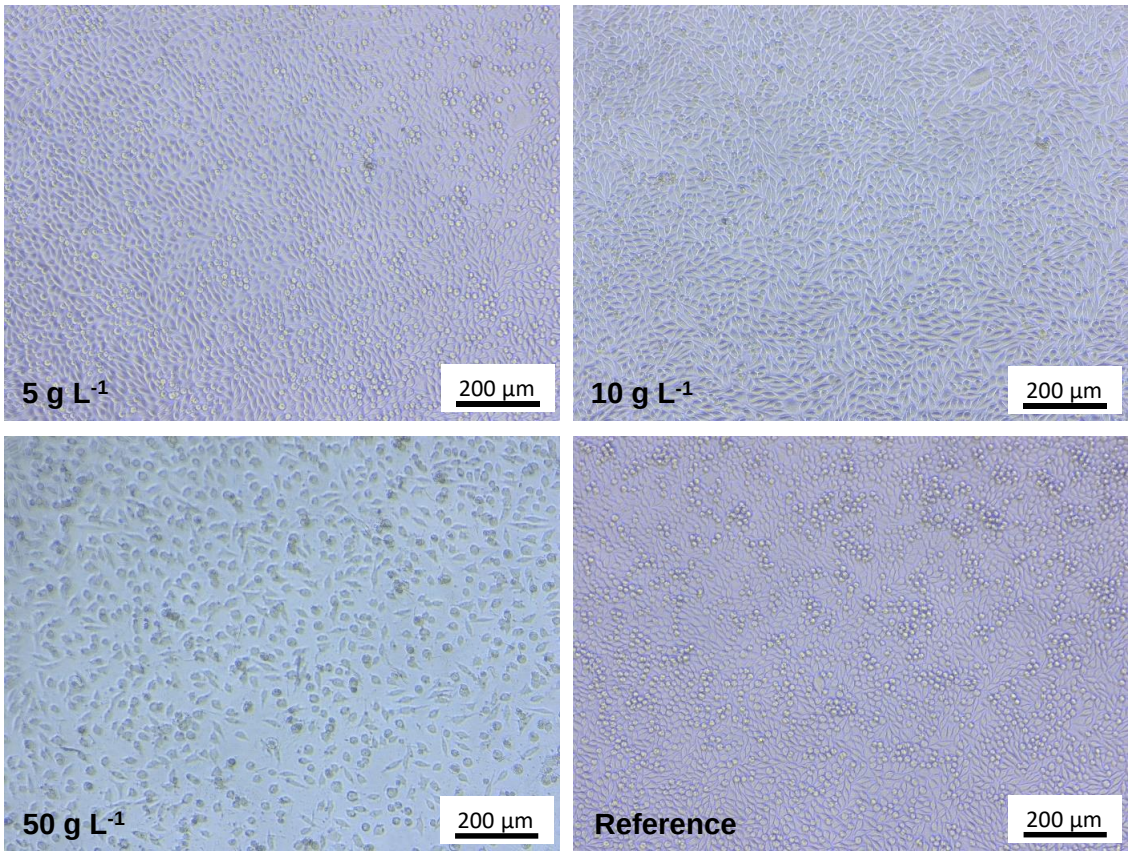


**Figure 3.56:** Microscope images of cells in attendance of **6b-2** with hexamethylene bisurea segment and PPG-PEG-PPG segments of 900 g $mol^{-1}$ in different concentrations (5, 10 and 50 g $L^{-1}$) and in absence of **6b-2**.

For copolymer **6c-2** the number of active cells determined for a copolymer concentration of 1 and 5 g $L^{-1}$ is above 80 % for both the WST and cell number measurements (figure 3.57). The cell number at a copolymer concentration of 10 g $L^{-1}$ was determined to be 71 % whereas the WST measurement revealed a viability of around 100 % as indicated in figure 3.56B. As a consequence, the copolymer shows weak cytotoxicity in one of the tested experiments. At a concentration of 50 g $L^{-1}$ both WST and cell number measurement indicated cell viabilities below 10 %. The microscope images at copolymer concentrations of 1 and 5 g $L^{-1}$ show high cell viability comparable to the reference as depicted in figure 3.58. For a concentration of 10 g $L^{-1}$ lower cell density as compared to **6b-2** was found. At a concentration of 50 g $L^{-1}$ nearly no active cell was found in the image which confirms the results of the WST and cell number measurements. As a consequence, **6c-2** is not cytotoxic at concentrations of 5 g $L^{-1}$ and below. Thus, copolymer **6c-2** with 91 wt% PPG-PEG-PPG segments shows a slightly lower cell viability as **6b-2** at equal concentration. Nevertheless, both copolymers show no cytotoxicity at a concentration of 5 g $L^{-1}$ making them both promising materials for the field of biofabrication.

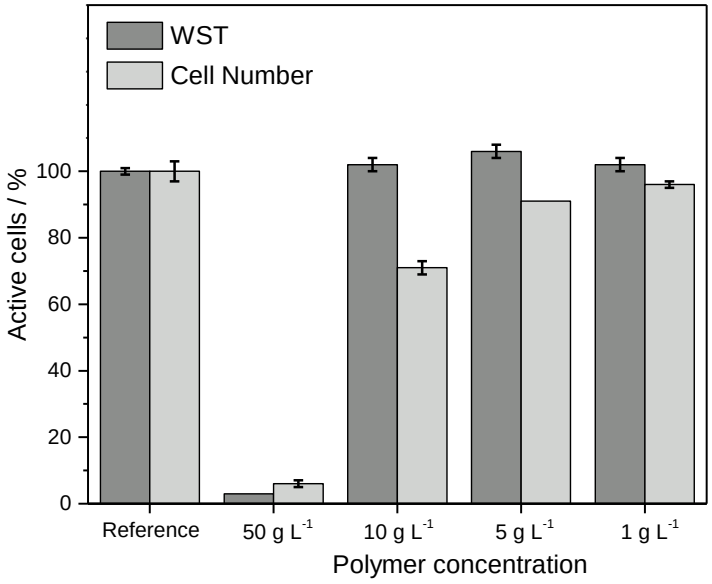


**Figure 3.57.** Viability of mouse fibroblast cells in the presence of **6b-2** with 18 wt% hexamethylene bisurea segments and 82 wt% PPG-PEG-PPG segments and at three different eluate concentrations by performing WST and cell number assay. Four different concentrations of soluble copolymers in the eluate were used. The viability reaches or exceeds 80 % at a concentration of 5 g $L^{-1}$ or lower indicating that the copolymer is not cytotoxic at these concentrations.

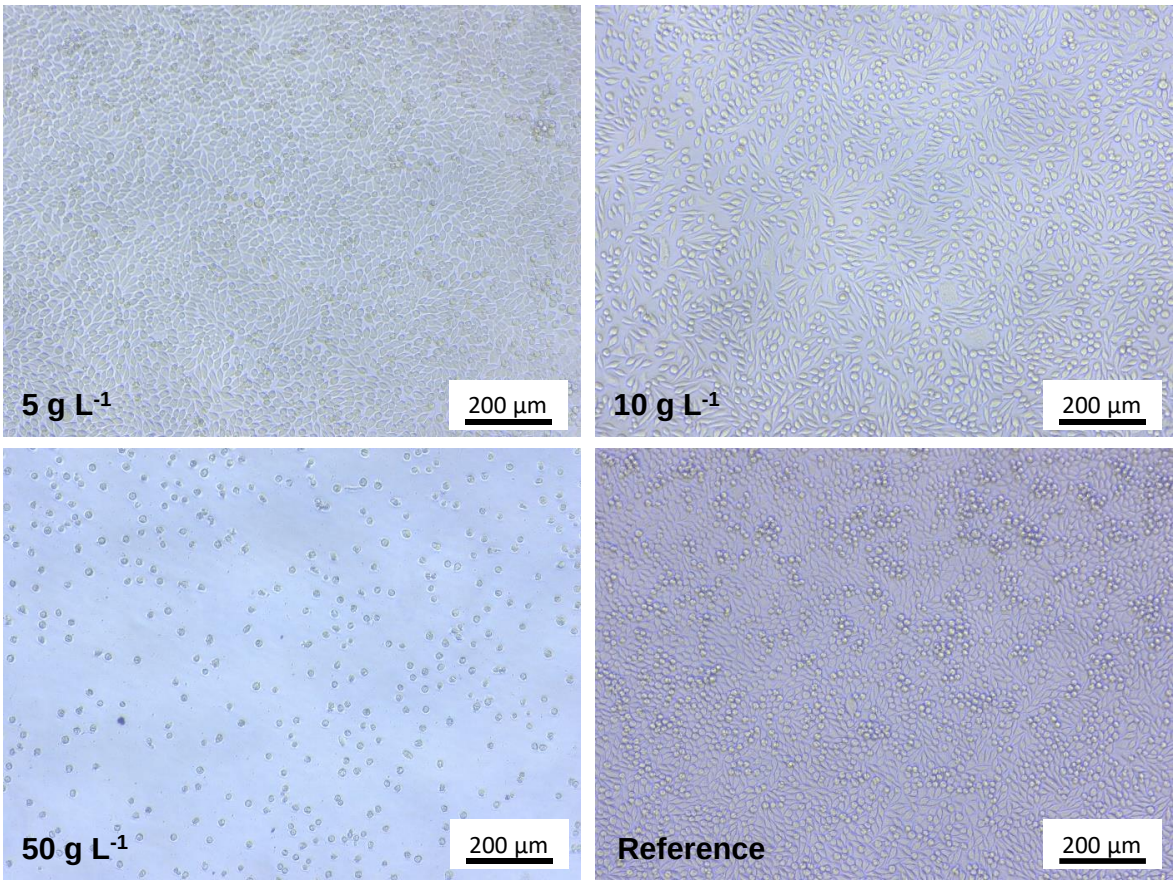


**Figure 3.58:** Microscope images of cells in attendance of polymer **6c-2** with bisurea-hexamethylene hard segment and PPG-PEG-PPG segments of 2000 g $mol^{-1}$ in different concentrations (5, 10 and 50 g $L^{-1}$) and in absence of **6c-2**.

### *$(AB)_n$-segmented copolymers with 4,4'-methylene-bis(cyclohexyl) bisurea segments*

In this copolymer class the cytotoxicity was determined for copolymers **8a-2** and **8a-3** both swelling and forming stable hydrogels in aqueous solution also at 37 °C. Regarding the thermal properties these two copolymers are very promising copolymers that do not disintegrate in aqueous media for additive manufacturing. Polymer samples were prepared as smooth, thin film. More specifically, polymer films were melt pressed at 100 °C. Consequently, the material was already heated to a temperature range were processing by MEW or EBP is typically conducted. The hydrogels were placed in cell media with a concentration of 100 mg/mL. Additionally, diluted samples with 50 and 25% eluate were prepared. The viability of mouse fibroblasts cells in the presence of copolymers **8a-2** and **8a-3** was studied by WST assay, Cell titer Glo luminescent cell viability assay and PicoGreen® dsDNA assay.[212–214] Materials were found to be not cytotoxic if the viability of mouse fibroblast is above 80 %. As shown in figure 3.59 all three assays revealed high cell viability above 80 % for both copolymers and for all eluate concentrations including the

upper end of the error bars.[139] This result demonstrates that these $(AB)_n$-segmented copolymers are not cytotoxic even though they were previously heated to 100 °C. As a result, the materials are very suitable for 3D printing of e.g. supporting scaffolds for biomedical applications.

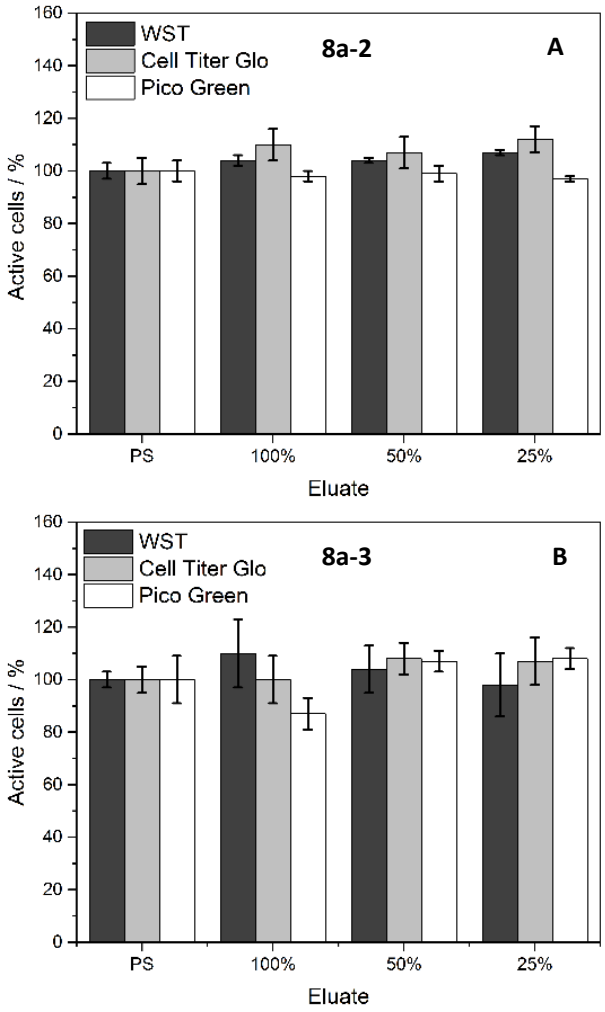


**Figure 3.59. A:** Viability of mouse fibroblast cells in the presence of **8a-2** and **B:** of **8a-3** both having 25 wt% 4,4'-methylene-bis(cyclohexyl) bisurea segments and 75 wt% PPG-PEG-PPG segments at three different eluate concentrations by performing WST, CellTiter Glo and Pico Green assay. Hydrogel concentration in the eluate was 100 mg $mL^{-1}$. The viability is always above 80 % indicating that both polymers are not cytotoxic. Adapted and reproduced with permission (© 2020 The Authors. Macromolecular Chemistry and Physics published by WILEY-VCH GmbH).[139]

## 3.7 Conclusion

A series of 19 $(AB)_n$-segmented copolymers was prepared by polyaddition of telechelic PPG-PEG-PPG diamines (Jeffamines®) with molecular weights of 600, 900 and 2000 g mol$^{-1}$ and three different diisocyanates, namely hexamethylene (HM) diisocyanate, methylene-bis(cyclohexyl isocyanate) (mbCH) and *trans*-1,4-cyclohexyl (CH) diisocyanate, on a laboratory scale up above 50 g. The copolymers were successfully purified from small molecular weight oligomers by extracting in water by swelling or dialysis if water-soluble. The degree of polymerization was controlled by the addition of *n*-butylamine. FT-IR analysis revealed that the strength of the hydrogen bonding depends on the chemical structure of the bisurea segments.

The thermal properties of the copolymers were investigated by *Differential Scanning Calorimetry (DSC), polarization microscopy, dynamic mechanical thermal analysis (DMTA)* (Single cantilever and tension geometry method) and *oscillation shear rheology*. A glass transition temperature of the polypropylene glycol terminated PEG (PPG-PEG-PPG) segments was observed between -55 and -23 °C for all copolymers. Copolymers with high PPG-PEG-PPG segment amounts of 87 and 91 wt% reveal a reversible melting transition between 16 and 34 °C resulting from the semi-crystalline PEG units. The disassembly upon heating and reassembly upon cooling of the bisurea hydrogen bonds was proven for most investigated copolymers. The temperature range is between 10 and 180 °C and is influenced the length of the hydrophilic segments, the structure of the bisurea segments and the degree of polymerization. The copolymers reveal a transition between elastic and viscous behavior within a temperature range between 27 and 154 °C upon *heating* and 99 and 23 °C upon *cooling*. The melt viscosities at 100 °C could be adjusted ranging from 15 to 8000 Pa s. These thermal properties and melt viscosities open opportunities for different additive manufacturing techniques.

Copolymers with HM bisurea segments swell to *hydrogels* in aqueous media that disintegrate over time. The speed of disintegration increases with increasing length of the hydrophilic segments. Copolymers with 25 wt% mb-CH bisurea segments and 75 wt% PPG-PEG-PPG segments swell to hydrogels that do not disintegrate. The hydrogels have a low module < 100 Pa. Much tougher hydrogels with a module > 1000 Pa and water content up to 95 % are formed for copolymers with 87 wt% PPG-PEG-PPG segments. The biocompatibility was demonstrated by cytotoxicity tests for the copolymer series with disintegrating examples up to a concentration of 5 – 10 g L$^{-1}$ and for selected examples which form stable gels. In combination with their adjustable thermal properties these copolymer series are very promising candidates for additive manufacturing by EBP and MEW which will be discussed in the next chapter.

# 4 Additive manufacturing of $(AB)_n$-segmented copolymers

This chapter focuses on additive manufacturing of the hydrophilic $(AB)_n$-segmented copolymers whose synthesis and characterization is described in the previous chapter.

The thermal and mechanical properties of the copolymers reveal that fused deposition modeling is not an appropriate additive manufacturing technique for this material class. The copolymers do either not crystallize or the crystallization is very slow which makes the fabrication of a filament with sufficient mechanical stability very challenging. For this reason extrusion based additive manufacturing processes are seen as much more promising. Possible extrusion-based techniques are extrusion based printing (EBP), melt electrospinning (MES) and melt electrowriting (MEW).

The primarily focus within the context of this thesis is MEW. The experiments were conducted by myself at the *Department of Functional materials in Medicine and Dentistry, University of Würzburg*, in cooperation with the research groups of Paul Dalton and Jürgen Groll. A custom built MEW device as shown in figure 5.7 in the experimental part (page 183) was used. In addition, first studies with EBP were carried in cooperation with Simon Gumbel at the chair of Macromolecular Chemistry I, University of Bayreuth, using a Cellink+ printer. This printer is also shown in the experimental part (figure 5.6 on page 182).

## 4.1 Melt electrowriting (MEW)

Melt electrowriting (MEW) is a hybrid fabrication technology of extrusion-based printing (EBP) and melt electrospinning. The principle is based on a distinct electrohydrodynamic phenomenon supporting the extrusion process. Since MEW allows much smaller printed diameters compared to EBP, it is an interesting technique for the controlled deposition of structures in higher resolution.

In MEW, lower voltages and much smaller distances between spinneret and collector are applied compared to melt electrospinning. This results in a molten jet that remains stable and continuous under the proper processing conditions and parameters. This jet rapidly cools - upon writing on a collector. The collector speed is an important factor to control the straightness of the deposited fibers. At the so-called critical translational speed (CTS), the direct written fiber converts from a sinusoidal to the required linear profile.[24, 26, 29]

In this thesis, the overall goal is to utilize MEW for the first time with the class of hydrophilic $(AB)_n$-segmented copolymers. Based on the thermal and rheological behavior discussed in chapter 3.3, some $(AB)_n$-segmented copolymers were selected as promising candidates for MEW. The selected copolymers are listed in table 4.1 and are based on polypropylene glycol terminated polyethylene glycol (PPG-PEG-PPG) segments of 900 or 2000 g mol$^{-1}$. The bisurea segments of these copolymers are either hexamethylene (HM) or 4,4'-methylene-bis(cyclohexyl) (m-b-CH). The degree of polymerization of these copolymers was varied by the addition of 0 – 20 mol % *n*-butylamine.

In the following, the selected copolymers are presented.

**Table 4.1:** Overview of $(AB)_n$-segmented copolymers with hydrophilic PPG-PEG-PPG segments and bisurea segments tested with MEW. $w_{hydrophil}$ and $w_{bisurea}$ describe the mass ratios of the hydrophilic and bisurea segments within a repeating unit. The degree of polymerization $X_n$ was determined by SEC analysis.

| No. | $W_{hydrophil}$ [wt%] | Bisurea segments | $W_{bisurea}$ [wt%] | $X_n$[1] |
|---|---|---|---|---|
| **6b** | 82 | HM | 18 | -[2] |
| **6b-1** | 82 | HM | 18 | 39 |
| **6b-2** | 82 | HM | 18 | 28 |
| **6c** | 91 | HM | 9 | -[2] |
| **6c-1** | 91 | HM | 9 | 29 |
| **6c-2** | 91 | HM | 9 | 19 |
| **6c-3** | 91 | HM | 9 | 13 |
| **8a** | 75 | m-b-CH | 25 | 38 |
| **8a-1** | 75 | m-b-CH | 25 | 34 |
| **8a-2** | 75 | m-b-CH | 25 | 31 |
| **8a-3** | 75 | m-b-CH | 25 | 26 |
| **8b** | 87 | m-b-CH | 13 | 29 |
| **8b-2** | 87 | m-b-CH | 13 | 25 |

1: SEC analysis was done in THF+TBAB solution with a polystyrene calibration.
2: No SEC analysis was conducted due to the polymer was insoluble in THF-TBAB solution.

### 4.1.1 Determination of MEW-printing window

***MEW-printing temperature window***

For all selected $(AB)_n$-segmented copolymers, the minimal printing temperature $T_{MEW,min}$ and the printing temperature maximum $T_{MEW,max}$ of the MEW processing window were determined. At $T_{MEW,min}$, a stable jet is obtained without interruption for at least ten minutes. Thus, $T_{MEW,min}$ describes the lower temperature limit of the MEW processing window. Above $T_{MEW,max}$ the jet turns inhomogenous and partically drops are formed. This is due to a very high flow rate resulting from a too low viscosity. Depending on the copolymer, the difference between $T_{MEW,min}$ and $T_{MEW,max}$ was found to be 10 up to 20 °C.

In the actual MEW experiments, the copolymers were first heated to a temperature of about 25 - 30 °C above $T_{MEW,min}$ and then cooled down to the actual printing temperature.

***Correlation of MEW-printing temperature window with rheology***

A correlation of the MEW processing window with the rheology properties was performed. The oscillation rheology measurements are described in chapter 3.3. The complex melt viscosities $\eta^*_{MEW,min}$ at $T_{MEW,min}$ and $\eta^*_{MEW,max}$ at $T_{MEW,max}$ were determined from the oscillation rheology curves of each copolymer.

In the following, the determined values of $T_{MEW,min}$, $T_{MEW,max}$, $\eta^*_{MEW,min}$ and $\eta^*_{MEW,max}$ are discussed for all tested copolymers and the results are summarized in table 4.2. Based on these results, the most promising copolymers were selected for more detailed MEW studies. This includes additional measurements of the viscosity over a longer time by rotational rheology to determine the thermal stability of the copolymer melt at the processing temperatures. The thermal stability at the MEW processing temperature is critical with respect to thermal degradation or molecular weight changes of the copolymer during the relative long printing time. Within this work, the typical time window for printing MEW scaffolds was chosen to be maximum 2 h. Over this time period, the melt viscosity should be constant and not change.

#### *4.1.1.1 $(AB)_n$-segmented copolymers with 82 wt% PPG-PEG-PPG segments and 18 wt% hexamethylene bisurea segments*

Within this copolymer series, the influence of the molecular weight on the MEW-processing temperature was investigated for the three copolymers **6b**, **6b-1** and **6b-2** which have a different degree of polymerization. As already discussed in chapter 3.3, the melt viscosity depends on the degree of polymerization. The minimum MEW-processing temperature $T_{MEW,min}$ at which a stable and constant MEW processing with uniform fibers becomes possible was found to significantly drop with decreasing degree of polymerization from 135 °C for **6b** to 75 °C for **6b-2**. The optimal MEW-processing window is highlighted in the viscosity curves shown in figure 4.1 and ranges for **6b** from 75 – 85 °C, for **6b-1** from 110 – 120 °C and for **6b-2** from 135 – 145 °C. The temperature range between $T_{MEW,min}$ and $T_{MEW,max}$ is denoted in the following as $T_{MEW,r}$. $\eta^*_{MEW,r}$ indicates the melt viscosity range between $\eta^*_{MEW,min}$ and $\eta^*_{MEW,max}$. For all three copolymers, $T_{MEW,r}$ is located in a similar viscosity range between 25 – 80 Pa s. Molecular weight regulation is an ideal approach to lower the MEW processing temperature window to more moderate temperatures.

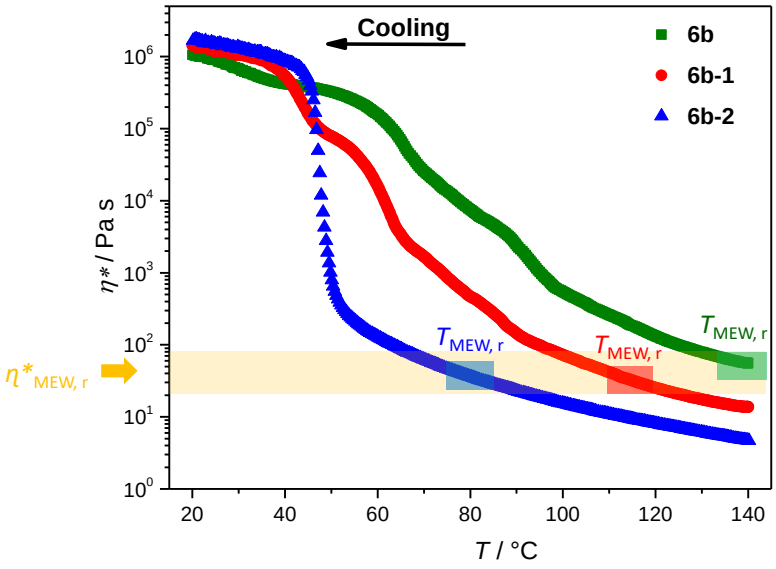


**Figure 4.1:** Melt viscosity of **6b, 6b-1** and **6b-2** with 82 wt% PPG-PEG-PPG segments of 2000 g mol$^{-1}$ and 18 wt% hexamethylene bisurea segments upon *cooling* with a rate of 2 K min$^{-1}$. The optimum MEW processing temperature window $T_{MEW,r}$ and the corresponding optimum range of complex melt viscosity $\eta^*_{MEW,r}$ are highlighted.

Due to the lowest processing temperature window from 75 to 85 °C, copolymer **6b-2** was chosen for more detailed MEW studies. The thermal stability of the melt of **6b-2** was determined by measuring the melt viscosity at a constant temperature for 15 hours using a shear rate of 0.5 $s^{-1}$. A temperature of 100 °C was chosen, which is 25 °C higher as the minimum MEW processing temperature. A constant viscosity of around 17 Pa s was observed over a duration of 15 hours as shown in figure 4.2. Due to the constant viscosity over time, no variations during printing are expected within the determined MEW processing time window for this copolymer. The copolymer remained also colorless after 15 h confirming the thermal stability at 100 °C. As a result, copolymer **6b-2** is a very good candidate for MEW processing within the temperature window between 75 to 85 °C.

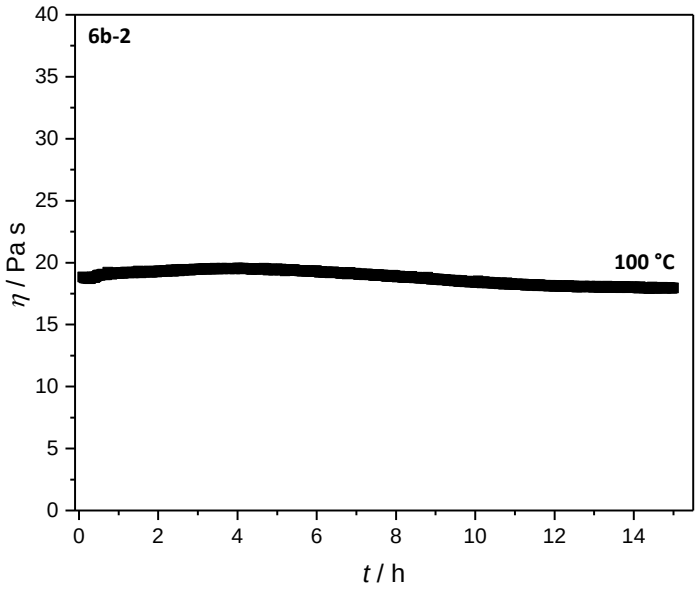


**Figure 4.2:** Time-depending rotational viscosity measurement of **6b-2** at 100 °C and a shear rate of 0.5 $s^{-1}$ for 15 h indicating no significant change in the melt viscosity.

#### *4.1.1.2 $(AB)_n$-segmented copolymers with 91 wt% PPG-PEG-PPG segments and 9 wt% hexamethylene bisurea segments*

The copolymers **6c**, **6c-1**, **6c-2** and **6c-3** with 91 wt% PEG-PPG-PEG segments and 9 wt% bisurea segments have the same trend regarding viscosity as the previously discussed copolymer series with 82 wt% PPG-PEG-PPG segments.

Copolymer **6c** with the highest molecular weight cannot be melt-processed by MEW below 210 °C. The used MEW equipment does not allow higher temperatures. For **6c-1** with a lower molecular weight**,** MEW is possible at 180 °C**.** However, the obtained jet was inhomogeneous and the process was interrupted after some minutes, making a continuous melt-processing by MEW not possible. Copolymer **6c-2** can be melt-processed by MEW at more moderate temperatures between 90 and 110 °C. The optimum MEW-processing window for **6c-3** with a lower molecular weight ranges from 80 to 100 °C.

The melt viscosity as function of the temperature was measured for **6c-2** with rheology upon *cooling* (Figure 4.3). $\eta^*_{MEW,r}$ was determined for the optimum MEW-processing temperature window of 90 to 110 °C ranging from 30 to 105 Pa s. $\eta^*_{MEW,r}$ is slightly higher but comparable to the viscosities at MEW processing temperature observed for the previously discussed copolymers **6b**, **6b-1** and **6b-2** in the previous chapter.

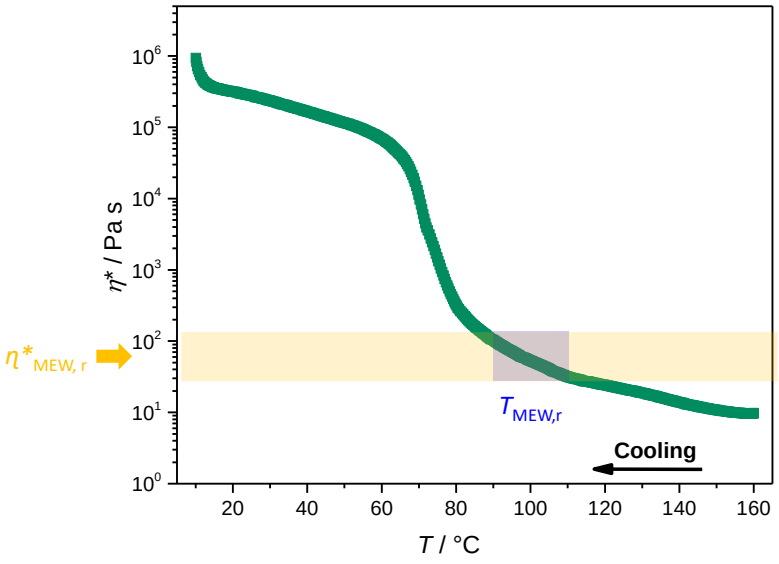


**Figure 4.3:** Complex melt viscosity of **6c-2** with 91 wt% PPG-PEG-PPG segments of 2000 g mol$^{-1}$ and 9 wt% hexamethylene bisurea segments determined by an oscillation experiment with a *cooling* rate of 2 K min$^{-1}$. The optimum MEW processing temperature window and the correlating optimum complex melt viscosity are highlighted.

The thermal melt stability of **6c-2** was determined by rotational rheology at a shear rate of 0.5 $s^{-1}$ at different temperatures of 100, 120, 140, 160 and 180 °C (Figure 4.4). At 100 °C the measurement reveals a constant viscosity of about 180 Pa s over the time period of 4 hours followed by a continuous moderate linear decrease over the following 12 hours. As a result, the material is well suited for MEW at a temperature of 100 °C since a constant viscosity at this temperature within a time frame of 2 h is given. After 2 hours a steady decrease of the viscosity is observed.

Additionally, the rotational rheology was measured at 120, 140, 160 and 180 °C to further analyze the thermal stability at higher temperatures (Figure 4.4). At 120 °C, the viscosity slightly drops from beginning starting at 100 Pa s and decreases to about 55 Pa s within 16 hours. It can be assumed that the slightly decrease of melt viscosity results from the thixotropic effect. The thixotropic effect describes the thinning of the material by shearing or deformation.[215] Remarkably, a viscosity increase occurs after 16 h. At 140 °C, the viscosity at the start of the measurement is lower with about 15 Pa s. The viscosity slightly drops within the first hour and then suddenly increases to more than 100 Pa s. After 2 h the measurement was stopped and the copolymer was received back as a hard yellow material. A melt viscosity below 10 Pa s was measured by further increasing the starting temperature to 160 °C. Here, the viscosity starts to significanty increase already after 35 min. At 180 °C this viscosity increase was observed after only 20 min yielding also a hard yellow material. The sharp viscosity increase also explains the jet interruption during MEW printing of **6c-1** at 180 °C after only a few minutes. It is assumed that the viscosity increase results from back reactions into amines and isocyanates followed by the subsequent cross-linking of the isocyanate moieties with urea groups. A similar behavior was observed for $(AB)_n$-segmented copolymers having polysiloxane segments and hexamethylene segments.[87]

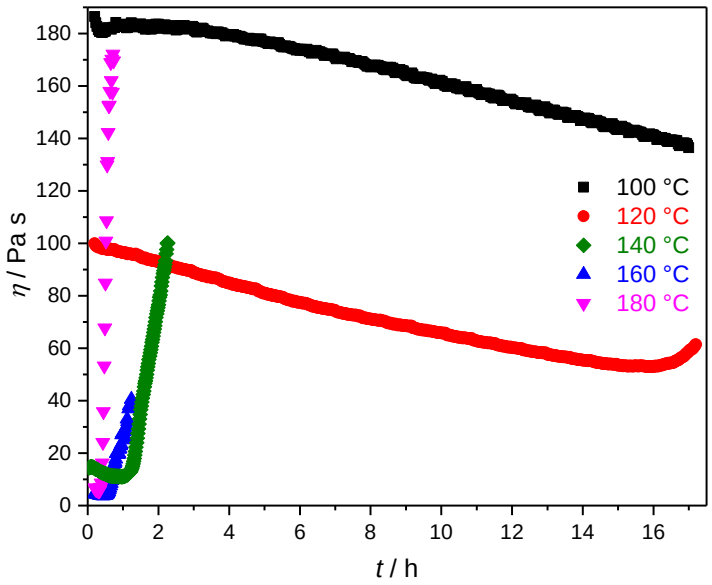


**Figure 4.4:** Time-depending rotational viscosity measurement of **6c-2** with a shear rate of 0.5 $s^{-1}$ at five different temperatures in the range between 100 to 180 °C. At 100 °C the melt viscosity is constant 3.5 h and then slowly decreasing. At 120 °C the melt viscosity first decreases before rising again after 16 h. At 140 °C and higher a significant increase of the melt viscosity can be observed within 2 h.

All in all, the experiment shows that melt-processing with MEW can be performed well at 100 °C but is not possible at temperatures of 140 °C and higher within this copolymer class. Based on these results, copolymer **6c-2** was selcted for more detailed studies with MEW, reported in the following.

#### *4.1.1.3 $(AB)_n$-segmented copolymers with 75 wt% PPG-PEG-PPG segments and 25 wt% 4,4'-methylenebis(cyclohexyl) bisurea segments*

For this copolymer series (**8a-1**, **8a-2** and **8a-3**) the melt viscosity upon *cooling* was measured by oscillation shear rheology as discussed in chapter 3.3.3. All three copolymers and **8a** were tested for MEW. **8a** can not be melt processed by MEW below 210 °C which is the upper temperature limit of the used equipment. For **8a-1** MEW is possible at 150 °C**,** but the obtained jet is inhomogeneous and interrupts after a few minutes. This confirms the results of the previously dicussed copolymer class with 9 wt% hexamethylene bisurea segments in which the viscosity increases after a short time period at temperatures of 140 °C and above. More moderate minimum MEW-processing temperatures of 95 and 85 °C were obtained for **8a-2** and **8a-3**. Figure 4.5 compares the melt viscosities of **8a-1**, **8a-2** and **8a-3** upon *cooling* between 140 and 10 °C.[139] The viscosity decreases with lower molecular weight ($M_n$). The optimum MEW-processing window $T_{MEW,r}$ is highlighted in the viscosity curves and ranges from 95 to 110 °C for **8a-2** and from 85 to 100 °C for **8a-3**. The melt viscosities $\eta^*_{MEW,min}$ at the minimum MEW-processing temperature $T_{MEW,min}$ were determined to be around 2600 and 1450 Pa s for **8a-2** and **8a-3**, respectively.

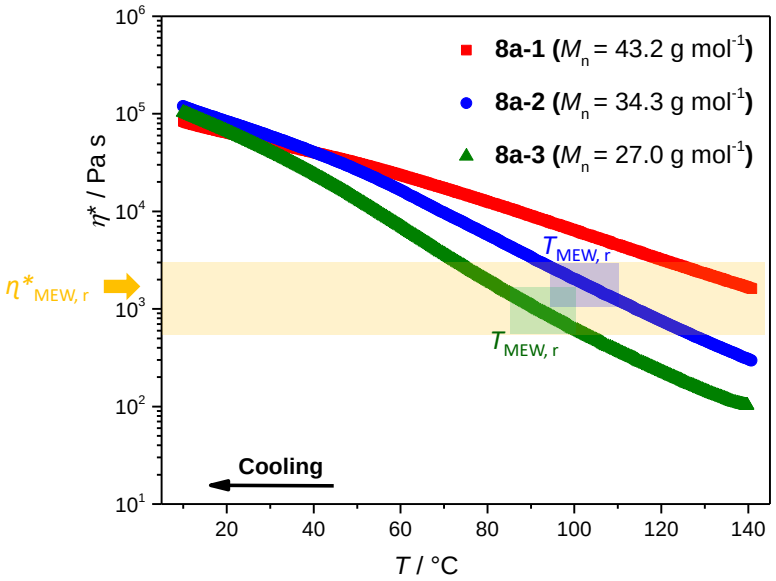


**Figure 4.5:** Complex melt viscosity of **8a-1, 8a-2** and **8a-3** with 75 wt% PPG-PEG-PPG segments of 900 g mol$^{-1}$ and 25 wt% 4,4'-methylene-bis(cyclohexyl) bisurea segments upon *cooling* with a rate of 2 K min$^{-1}$ by conducting oscillation experiment. Additionally, the optimum MEW processing temperature window $T_{MEW,r}$ and the correlating optimum range of complex melt viscosity $\eta^*_{MEW,r}$ are highlighted for **8a-2** and **8a-3**. Adapted and reproduced with permission (© 2020 The Authors. Macromolecular Chemistry and Physics published by WILEY-VCH GmbH).[139]

It should be pointed out that compared to the previously discussed copolymers with hexamethylene bisurea segments, $\eta^*_{MEW,min}$ is more than one order of magnitudes higher. The chemical structure of the bisurea segments influences the chain stiffness and, consequently, the melt viscosity. With 4,4'-methylene-bis(cyclohexyl) segments higher viscosities were found.

Isothermal rotational rheology measurement was performed for **8a-3** at 100 °C and 120 °C to evaluate the thermal stability over time. Figure 4.6 shows that the melt viscosity is constantly around 700 Pa s over an extended period of 20 h at 100 °C.[139] A constant viscosity of around 90 Pa s was also observed at 120 °C. No increase of the viscosity was found within 20 h. In both cases the used time exceeds by far the printing time of maximum 2 h used in this thesis. Over this time period, the fiber diameter and printing quality is not affected.

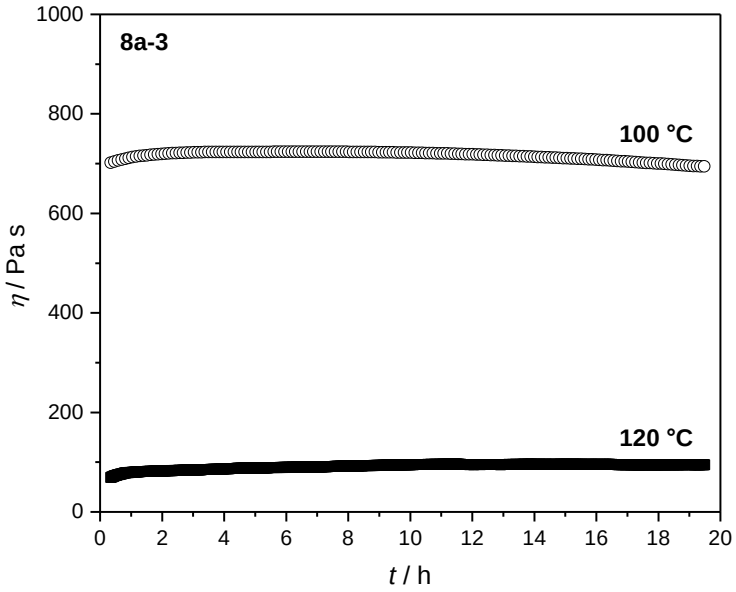


**Figure 4.6:** Time-depending rotational viscosity measurement of **8a-3** at 100 and 120 °C for 20 h indicating no significant change in melt viscosity (adapted and reproduced with permission (© 2020 The Authors. Macromolecular Chemistry and Physics published by WILEY-VCH GmbH).[139]

It was decided to conduct further MEW-experiments with both copolymers **8a-2** and **8a-3** out of this polymer class. Additionally, a more detailed influence of the molecular weight on the MEW printing behaviour and properties of the printed parts can be studied by using these two copolymers with different degree of polymerization within one class for MEW.

#### *4.1.1.4 $(AB)_n$-segmented copolymers with 87 wt% PPG-PEG-PPG segments and 13 wt% 4,4'-methylenebis(cyclohexyl) bisurea segments*

Within this copolymer series **8b** and **8b-1** were tested with respect to MEW-printing.

Copolymer **8b** can be processed by MEW at 180 °C or higher. The obtained jet is first stable and produces homogeneous fibers. However, the jet interrupts after less than 10 minutes and MEW is not possible anymore. Also, the color of the polymer in the syringe turned to yellow. The jet interruption can be explained by an increase of the melt viscosity within only a few minutes by crosslinking reactions. This was observed for copolymer **6c-2** in rotational rheology measurements over time at 180 °C (figure 4.4 on page 113). In conclusion, **8b** is not appropriate for MEW-processing.

However, **8b-1** with a lower degree of polymerization can already be melt processed starting from 80 °C. A stable and homogeneous polymer jet was obtained within the optimum MEW-processing temperature window from 80 to 100 °C. The melt viscosity at the minimum processing temperature $T_{MEW,\ min}$ was determined to be 900 Pa s. This is about a factor of 3 lower as compared to the previously discussed copolymers with 75 wt% PPG-PEG-PPG segments. It looks that for copolymers with 4,4'-methylene-bis(cyclohexyl) bisurea segments the length of the hydrophilic segments even more significantly influences the melt viscosity and MEW becomes possible.

In summary, selected copolymers were tested regarding the applicability for melt electrowriting. In table 4.2 the minimum processing temperature $T_{MEW,min,}$ the maximum processing temperature $T_{MEW,max}$ and the corresponding complex viscosities $\eta^*_{MEW,\ min}$ and $\eta^*_{MEW,\ max}$ of the preselected copolymers are summarized. The viscosity was found to decrease with decreasing degree of polymerization within one copolymer series. The melt viscosity within the MEW processing range varies from 20 to 105 Pa s for copolymers with hexamethylene bisurea segments and from 250 to 2600 Pa s for copolymers with 4,4'-methylenebis(cyclohexyl) bisurea segments. Based on these findings, the four copolymers **6b-2**, **6c-2**, **8a-2** and **8a-3**, were chosen for more detailed MEW printing.

**Table 4.2:** Overview of $(AB)_n$-segmented copolymers with hydrophilic PPG-PEG-PPG or PEG segments and bisurea segments tested for MEW. $w_{hydrophil}$ describes the mass ratio of the hydrophilic segments within a repeating unit. The determined minimum MEW-processing temperature $T_{MEW,\,min}$, the highest temperature within the optimum MEW-processing window $T_{MEW,\,max}$ and the corresponding complex melt viscosities $\eta^*_{MEW,min}$ at $T_{MEW,\,min}$ and $\eta^*_{MEW,max}$ at $T_{MEW,\,max}$ are listed.

| No. | $W_{hydrophil}$ [wt%] | Bisurea segments | $T_{MEW,\,min}$ [°C] | $T_{MEW,\,max}$ [°C] | $\eta^*_{MEW,\,min}$ [Pa s] | $\eta^*_{MEW,\,max}$ [Pa s] |
|---|---|---|---|---|---|---|
| **6b** | 82 | HM | 135 | 145 | 65 | -[4] |
| **6b-1** | 82 | HM | 110 | 120 | 42 | 25 |
| **6b-2** | 82 | HM | 75 | 85 | 47 | 28 |
| **6c** | 91 | HM | -[1] | - | -[4] | -[4] |
| **6c-1** | 91 | HM | -[2] | - | -[4] | -[4] |
| **6c-2** | 91 | HM | 90 | 110 | 101 | 32 |
| **6c-3** | 91 | HM | 80 | 100 | -[4] | -[4] |
| **8a** | 75 | m-b-CH | -[1] | - | -[4] | -[4] |
| **8a-1** | 75 | m-b-CH | -[3] | - | -[4] | -[4] |
| **8a-2** | 75 | m-b-CH | 95 | 110 | 2600 | 1230 |
| **8a-3** | 75 | m-b-CH | 85 | 100 | 1450 | 615 |
| **8b** | 87 | m-b-CH | -[2] | - | -[4] | -[4] |
| **8b-2** | 87 | m-b-CH | 80 | 100 | 899 | 246 |

1: MEW-processing was not possible up to 210 °C.
2: MEW-processing was only possible at 180 °C for a very short period below 10 minutes
3: MEW-processing was only possible at 150 °C for a very short period below 10 minutes
4: Melt viscosity was not measured for this copolymer at this temperature.

### 4.1.2 Influence of MEW-printing parameters

The fiber diameter, uniformity and quality of MEW printed fibers are influenced by the material properties as well as by instrumental parameters. Therefore, the influence of important instrumental parameters was studied. Besides obtaining the desired fiber diameter, the placement of uniform and straight fibers is cruical to prepare well-defined structures, for example as scaffolds in biofabrication.

In this thesis, the overall goal is to utilize MEW for the first time with the class of hydrophilic $(AB)_n$-segmented copolymers and to determine the fiber diameter range which can be reproducably achieved under optimized conditions. In addition, it should be explored under which conditions the thinnest fibers can be printed with MEW.

An important printing parameter is the collector movemement speed. Straight fibers are obtained starting at or above the *critical translation speed* (CTS). At the CTS the collector movement speed is equal to the speed of the polymer jet hitting the collector. If the collector speed is lower than the jet speed coiled fibers are obtained.[159] Additionally, the speed and thickness of the polymer jet out of the nozzle should be stable to prevent fiber pulsing and long bead defects as, for example, described for PCL.[160]

Therefore, the influence of processing parameters on the printing quality and the fiber diameter were investigated. Within this study, single fiber arrays were printed. The printing temperature, the extrusion rate adjusted by the nitrogen pressure, the spinneret diameter, the distance between spinneret and collector, the applied voltage and different collector speeds in the range between 800 and 2150 mm $min^{-1}$ were varied. In addition, two different collector surfaces were used. For each collector velocity, four fibers were printed. The average fiber diameter and its standard deviation were determined from 16 measured fiber diameters (4 measurements per fiber).

#### *4.1.2.1 $(AB)_n$-segmented copolymer with 82 wt% PPG-PEG-PPG segments and 18 wt% hexamethylene bisurea segments*

As already discussed in chapter 4.1.1.1 for copolymer **6b-2** a minimum MEW-processing temperature of 75 °C was determined. These MEW experiments at 75 °C revealed a homogenous, stable jet without interruptions over at least one hour. Therefore, a processing temperature of 75 °C was used for most of the following experiments with this copolymer.

***Influence of the flow rate and collector velocity***

The *flow rate* (extrusion rate) was reported to have the highest influence on the fiber diameter.[156,159] In the used apparatus within this thesis, the flow rate is controlled by nitrogen pressure used to extrude the polymer melt out of the nozzle. Hence, the influence of the *nitrogen pressure* was studied by using several *collector velocities* and the two different collector substrates, namely glass and silicon wafer. The nitrogen pressure can be adusted between 0.1 and 5 bar and was varied in this thesis between between 0.5 and 2.0 bar.

The determined *critical translation speed* (CTS) increases with decreasing nitrogen pressure for both substrates from 200 mm $min^{-1}$ at 2 bar to 1030 mm $min^{-1}$ at 1 bar and further to 2150 mm $min^{-1}$ at 0.5 bar. The increase of the CTS with declining nitrogen pressure is due to a lower resistance of less viscoelastic mass getting out of the nozzle.[159] As consequence, the speed of the polymer jet is higher if the flow rate is reduced and a higher collector speed is required to print straight fibers. The increase of the collector speed reduces the fiber diameter independent of the applied nitrogen pressure and the collector surface since the fibers are more stretched by a further movement of the collector.

Figure 4.7 shows the resulting fiber diameter as a function of the collector speed for different flow rates and applying different nitrogen pressures on a glass and a silicon substrate. All other parameters were kept constant (*extrusion temperature*: 75 °C; *spinneret diameter*: 0.45 mm; *spinneret-collector distance*: 2.2 mm; *voltage*: 2.7 kV). The fiber diameter and its standard deviation were found to become larger with increasing nitrogen pressure, regardless of the collector surface. This effect can be explained by the increased polymer mass being extruded per time resulting in a thicker polymer strand and, consequently, larger fiber diameters. This was also

reported in the literature.[159] Furthermore, forces induced by the electric field can lead to stretching of the polymer jet.[160]

The fiber diameter decreases significantly with increasing collector velocity (Figure 4.7). The fibers are more streched by the faster movement of the collector.

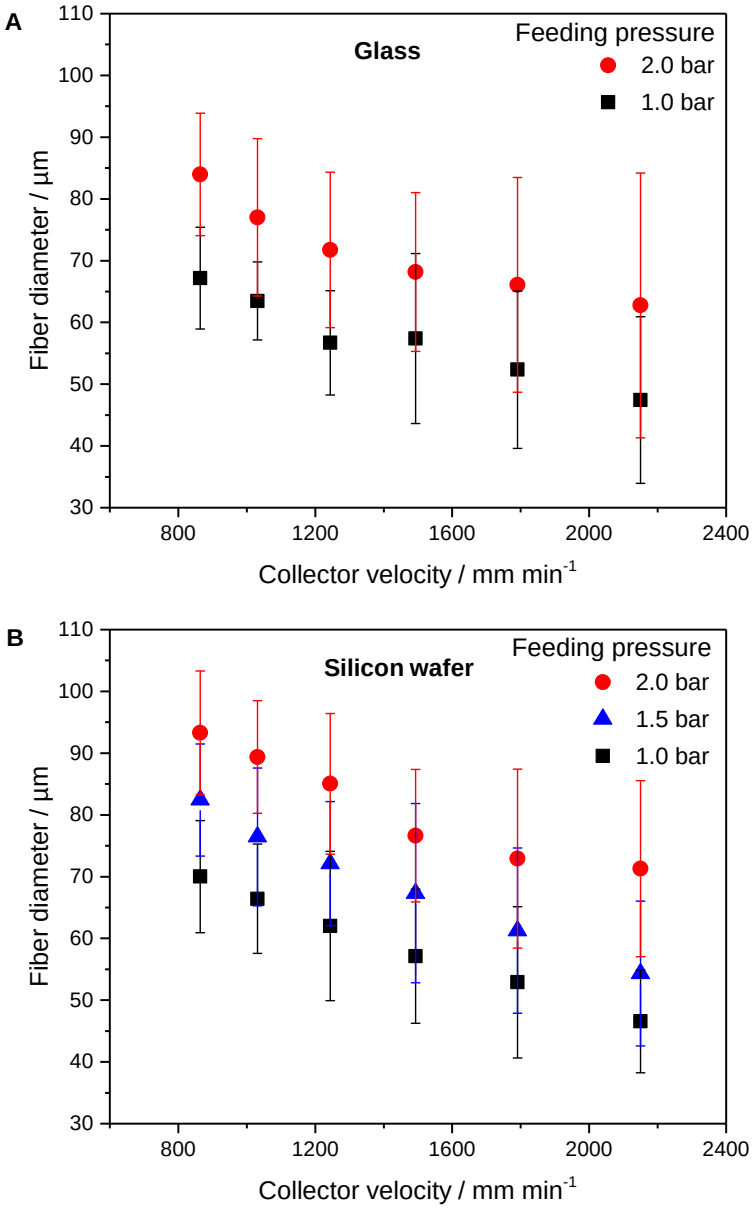


**Figure 4.7:** Influence of the *feeding pressure* and *collector speed* on the fiber diameter during MEW-processing of **6b-2** A) onto glass and B) onto silicon wafer substrate. The fiber diameter decreases significantly with increasing collector velocity and decreasing nitrogen pressure. Higher fiber diameters were observed onto silicon wafer surface. The statistical error decreases with declining pressure. (Constant printing parameters: *extrusion temperature:* 75 °C*; spinneret diameter:* 0.45 mm*; spinneret-collector distance:* 2.2 mm*; voltage:* 2.7 kV).

Interestingly, printing onto a silicon wafer surface tend to result in larger fiber diameters compared to a glass surface at 2 bar by comparing graphs A and B. A possible explanation are stronger interactions between the copolymer and the silicon surface. As a consequence, fibers stretch out more. However, at a pressure of 1.0 bar no significant difference can be seen.

By printing onto glass substrate fiber diameters in the range between 85 and 62 µm are obtained at a nitrogen pressure of 2 bar. The fiber diameter decreases to 67 to 47 µm with a reduced nitrogen pressure of 1 bar. Printing onto silicon substrate results in fiber diameter ranges of 94 to 73 µm at 2 bar, 83 to 55 µm at 1.5 bar and 70 to 47 µm at 1.0 bar, respectively. The thinnest fibers (38 µm) were obtained with a nitrogen pressure of 0.5 bar and a collector speed of 2150 mm $min^{-1}$. With a nitrogen pressure of 0.5 bar a fiber diameter of 38 µm can be achieved at a collector velocity of 2150 mm $min^{-1}$. The determined fiber diameter ranges are also listed in table 4.3.

**Table 4.3:** Influence of the *substrate* and the *nitrogen pressure* on the fiber diameter range at collector velocities between 860 and 2150 mm $min^{-1}$ and the critical translation speed (CTS) during MEW processing. Constant printing parameters: *extrusion temperature*: 75 °C; *spinneret diameter*: 0.45 mm; *spinneret-collector distance*: 2.2 mm; *voltage*: 2.7 kV.

| **Substrate** | **Nitrogen pressure [bar]** | **Fiber diameter range [µm]** | **CTS [mm $min^{-1}$]** |
|---|---|---|---|
| Glass | 1 | 47 – 67 | 1030 |
| Glass | 2 | 62 – 85 | 200 |
| Silicon | 0.5 | 38 – 42[a] | 2150 |
| Silicon | 1.0 | 47 - 70 | 1030 |
| Silicon | 1.5 | 55 – 83 | 350 |
| Silicon | 2 | 71 – 93 | 200 |

*a: The fiber diameter was only measured for collector velocities of 1800 and 2150 mm $min^{-1}$ due to the high CTS.*

The dependence of the fiber diameter on the collector velocity for MEW printing of PCL was intensively studied previously resulting in the following correlation:[162]

$$D_2 = D_1 \cdot \sqrt{\frac{V_1}{V_2}} \quad (4.1)$$

$V_1$ is the starting or reference collector velocity. $D_1$ describes the experimentaly determined fiber diameter at $V_1$. $D_2$ is the calculated fiber diameter at a different chosen collector velocity $V_2$. All other parameters have to be constant. It was investigated if equation (4.1) is also applicable for copolymer **6b-2** by comparing the calculated fiber diameters $D_2$ with the experimental determined fiber diameters at several collector velocities $V_2$.

A collector veleocity of 864 mm min$^{-1}$ was chosen as $V_1$. The other parameters were set as follows: *extrusion temperature*: 75 °C, *nitrogen pressure*: 1 bar, *spinneret diameter*: 0.45 mm, *spinneret-collector distance*: 2.2 mm, *voltage*: 2.7 kV, substrate: silicon wafer (here, a fiber diameter $D_1$ = 70.0 µm was measured). The increase of the collector velocity to $V_2$ = 1031 mm min$^{-1}$ results in a measured fiber diameter of 66.4 µm. This value is close to the calculated fiber diameter $D_2$ of 64.1 µm by using equation (4.1). The comparison of experimental and calculated fiber diameter was also done at four further collector velocities. Figure 4.8 shows that the calculated $D_2$ is always located within the error bars of the experimental determined fiber diameters. As a result, equation (3.7) is also applicable for the $(AB)_n$-segmented copolymer **6b-2** revealing that fiber diameters can be predicted and precisely be adjusted regarding the collctor velocity.

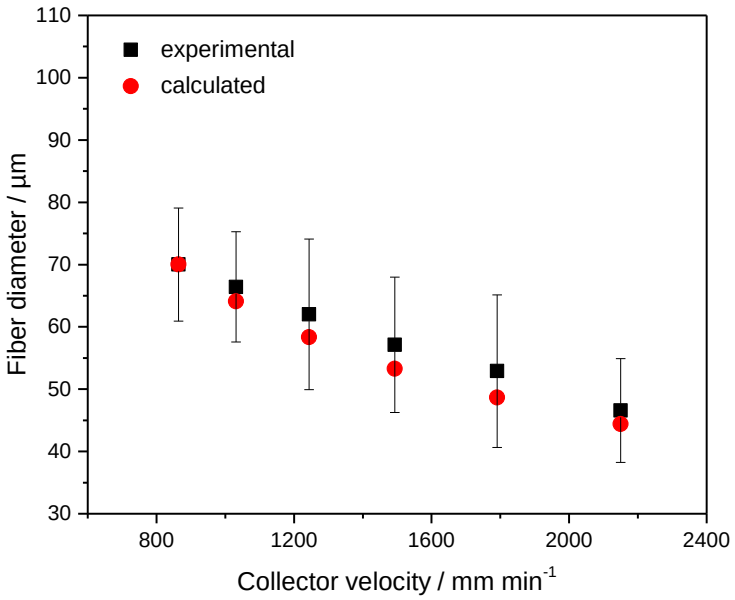


**Figure 4.8:** Comparison of MEW printed fiber diameter (black) of **6b-2** and calculated fiber diameter (red) by using equation (4.1). The experimentally determined fibers diameters correlate well with equation (4.1) which was developed for PCL. Printing parameters: *extrusion temperature*: 75 °C; *nitrogen pressure*: 1 bar; *spinneret diameter*: 0.45 mm; *spinneret-collector distance*: 2.2 mm; *voltage*: 2.7 kV; *substrate*: silicon wafer.

Besides the correlation between the collector velocity and the fiber diameter, an equation was also found for the relation of the nitrogen pressure and the fiber diameter at constant collector velocity:[162]

$$D_2 = D_1 \cdot \sqrt{\frac{P_2}{P_1}} \quad (V_1 = V_2) \quad (4.2)$$

$P_1$ is the applied nitrogen pressure and $D_1$ the resulting fiber diameter. $D_2$ describes the calculated fiber diameter by changing the nitrogen pressure to a different pressure $P_2$. The applicability of equation (4.2) for copolymer **6b-2** was also investigated by comparing the calculated fiber diameter $D_2$ with the experimental determined fiber diameter at several nitrogen pressures $P_2$. At a used pressure $P_1$ of 0.5 bar the determined fiber diameter $D_1$ is 42.3 µm. The other processing parameters were set as follows: *extrusion temperature*: 75 °C, *collector velocity*: 1800 mm min$^{-1}$, *spinneret diameter*: 0.45 mm, *spinneret-collector distance*: 2.2 mm, *voltage*: 2.7 kV, *substrate*: silicon wafer. Figure 4.9 reveals that the fiber diameters calculated from equation (4.2) are always located within the error bars of the experimental determined fiber diameters. However, the variance of experimental and theoretical values slightly increases with rising pressure. Nevertheless, the correlation developed for PCL can be also applied to this polymer and the desired fiber diameter can be predicted and adjusted by the nitrogen pressure.

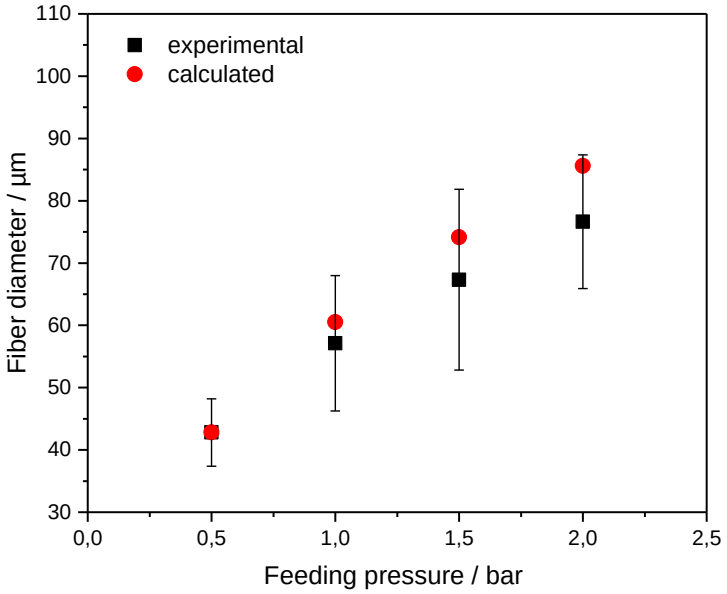


**Figure 4.9:** Comparison of MEW printed fiber diameter (black) of **6b-2** and calculated fiber diameter (red) by using equation (4.2). The experimentally determined fibers diameters correlate well with equation (4.2) which was developed for PCL. Printing parameters: *extrusion temperature*: 75 °C; *collector velocity*: 1800 mm min$^{-1}$ *spinneret diameter*: 0.45 mm; *spinneret-collector distance*: 2.2 mm; *voltage*: 2.7 kV; *surface*: silicon wafer.

***Influence of the spinneret diameter***

Next, the influence of the *spinneret diameter* was studied. By using a processing temperature of 75 °C, a nitrogen pressure of 2 bar, a distance between spinneret and collector of 2.2 mm and a voltage of 2.7 kV the CTS was found to increase with decreasing spinneret diameter from 200 mm $min^{-1}$ with a spinneret diameter of 0.55 mm to 1030 mm $min^{-1}$ if a spinneret diameter of 0.45 mm is used (see also table 4.4). If the nozzle size is reduced to 0.30 mm strong coiling up to the maximum tested collector velocity of 2150 mm $min^{-1}$ was observed. An increase of the spinneret diameter leads to a higher flow rate per time. Consequently, larger fiber diameters and a lower CTS that can be explained by a reduced jet speed are obtained. For this reason, further studies and scaffold printing were conducted only with the nozzle sizes of 0.45 and 0.55 mm and no fiber diameters were measured for a spinneret diameter of 0.30 mm. Spinneret diameters of 0.45 and 0.55 mm were used for printing onto glass and silicon wafer surface.

Figure 4.10 shows the fiber diameter as a function of the collector speed by using different spinneret diameters revealing that the fiber diameters and its standard deviations increase with larger nozzle diameter. The increase of the fiber diameter with increasing spinneret diameter is more significant on a silicon wafer substrate since a fiber diameter range of 141 to 108 µm was obtained with a nozzle size of 0.55 mm and a range of 93 to 71 µm with a size of 0.45 mm. With glass substrate the fiber diameters are located between 94 to 70 µm and 84 and 62 µm by using spinneret diameters of 0.55 and 0.45 µm, respectively.

**Table 4.4:** Influence of *substrate* and *spinneret diameter* on the fiber diameter range at collector velocities between 860 and 2150 mm $min^{-1}$ and the critical translation speed (CTS) during MEW processing. Constant printing parameters: processing *temperature*: 75 °C; *nitrogen pressure*: 2 bar; *spinneret-collector distance*: 2.2 mm; *voltage*: 2.7 kV.

| **Substrate** | **Spinneret Diameter [mm]** | **Fiber diameter range [µm]** | **CTS [mm $min^{-1}$]** |
|---|---|---|---|
| Glass | 0.45 | 47 – 67 | 1030 |
| Glass | 0.55 | 62 – 85 | 200 |
| Silicon | 0.30 | n.d. | > 2150 |
| Silicon | 0.45 | 62 – 84 | 1030 |
| Silicon | 0.55 | 71 – 93 | 200 |

As already previously monitored the fiber diameter decreases with higher collector velocity. Furthermore, larger fiber diameters were obtained on a silicon wafer. This confirms the results from the study of the influence of the flow rate.

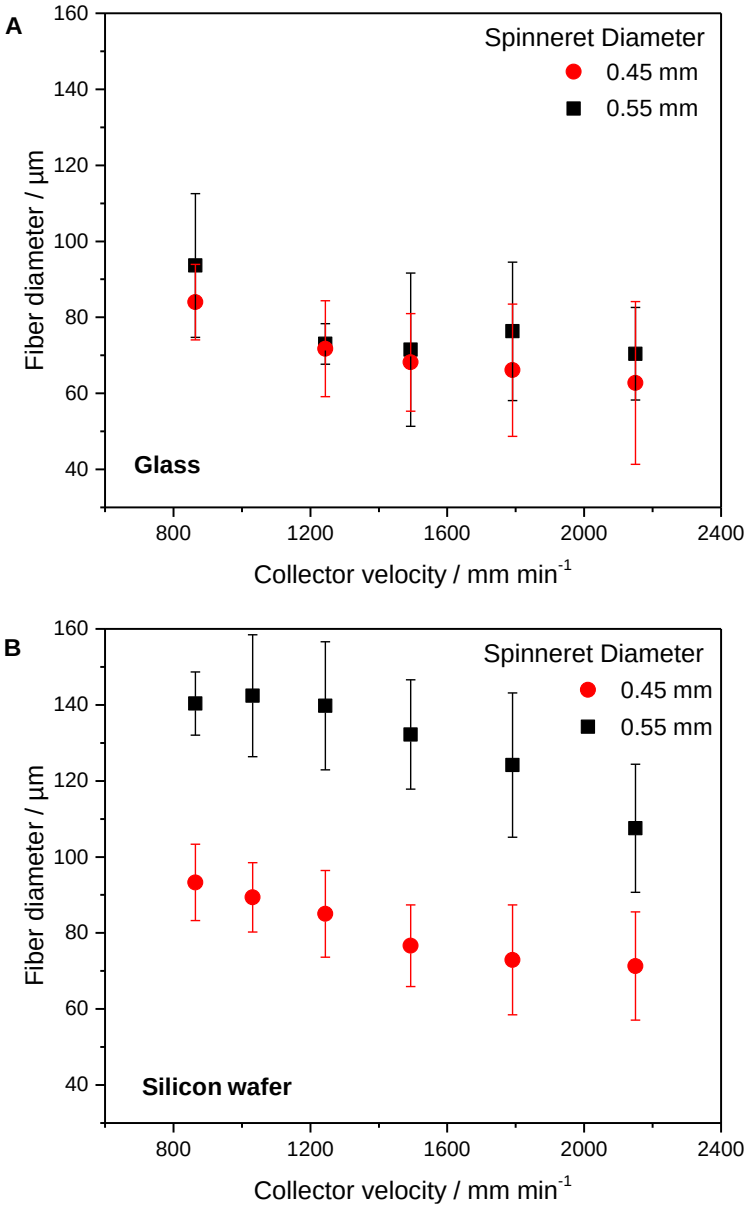


**Figure 4.10:** Influence of the *spinneret diameter* on the fiber diameter during MEW-processing of **6b-2** A) onto glass and B) onto silicon wafer. The fiber diameter and its standard deviation increase with rising spinneret diameter. The effect is more significant if a silicon wafer is used. Constant printing parameters: *extrusion temperature*: 75 °C; *nitrogen pressure*: 2 bar; *spinneret-collector distance*: 2.2 mm; *voltage*: 2.7 kV.

***Influence of the extrusion temperature***

The influence of the *extrusion temperature* on the printing result was studied by MEW processing onto silicon wafer surface. The fiber diameter and its standard deviation were determined for six different collector velocities. The increase of the temperature in the syringe and in the spinneret from 75 to 80 °C results in an increase of the fiber diameter range from 93 to 70 µm to 102 to 71 µm (figure 4.11 and table 4.5). The elevated extrusion temperature results in a lower melt viscosity of the polymer. As a result, the material flow per time out of the nozzle increases and larger fiber diameter are obtained. No significant changes in the standard deviation of the fiber diameter were monitored. Both temperatures result in the same CTS of 200 mm min$^{-1}$.

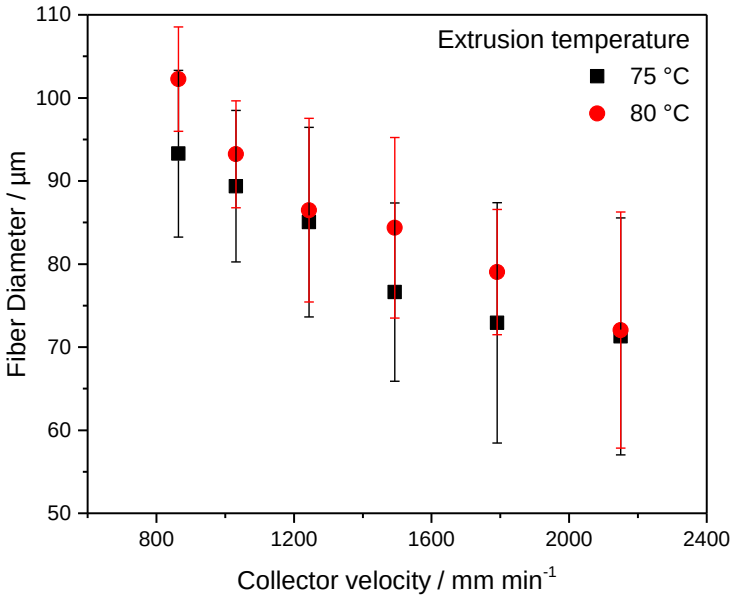


**Figure 4.11:** Influence of the *extrusion temperature* on the fiber diameter during MEW-processing of **6b-2** onto silicon wafer. The fiber diameter increases with rising temperature. Constant printing parameters: *nitrogen pressure*: 2 bar; *spinneret diameter*: 0.45 mm; *spinneret-collector distance*: 2.2 mm; *voltage*: 2.7 kV; *surface*: silicon wafer.

**Table 4.5:** Influence of the *extrusion temperature* on the fiber diameter range at collector velocities between 860 and 2150 mm min$^{-1}$ and the critical translation speed (CTS) during MEW processing. Constant printing parameters: *nitrogen pressure*: 2 bar; *spinneret-diameter*: 0.45 mm; *spinneret-collector distance*: 2.2 mm; *voltage*: 2.7 kV; substrate*:* silicon

| **Extrusion Temperature [°C]** | **Fiber diameter range [µm]** | **CTS [mm min$^{-1}$]** |
|---|---|---|
| 75 | 71 – 93 | 200 |
| 80 | 72 – 103 | 200 |

***Influence of the distance between spinneret and collector***

In this experiment the *distance between spinneret and collector* was varied between 2.2 and 3.3 mm while maintaining the voltage at 3.0 kV. As shown in figure 4.12, no significant change in the fiber diameter was observed. Thereby, the fiber diameter range is located between 84 and 54 µm. However, the standard deviation was higher for a spinneret-collector distance of 3.3 mm. Here, two effects play a role: On the one hand, the stretching of the polymer jet is influenced by the electric force. The electric force correlates with the ratio of the applied voltage and the spinneret-collector distance as previously described in the literature for melt electrospinning of other polymers.[216] Therefore, an increase of the spinneret collector distance is expected to reduce the fiber elongation as a result of the lower electric force which will result in larger fiber diameters. Less elongated fibers also result in wider fiber diameter distributions. On the other hand, the chosen spinneret-collector distances are very low. Former studies revealed that for this case the fiber diameter increases with decreasing spinneret-collector distance since the produced polymer jet has no sufficient time to stretch before reaching the collector.[7] Both effects outweigh each other resulting in comparable fiber diameters. The increase of the spinneret-collector distance from 2.2 to 3.3 mm slightly increases the CTS from 500 to 720 mm $min^{-1}$.

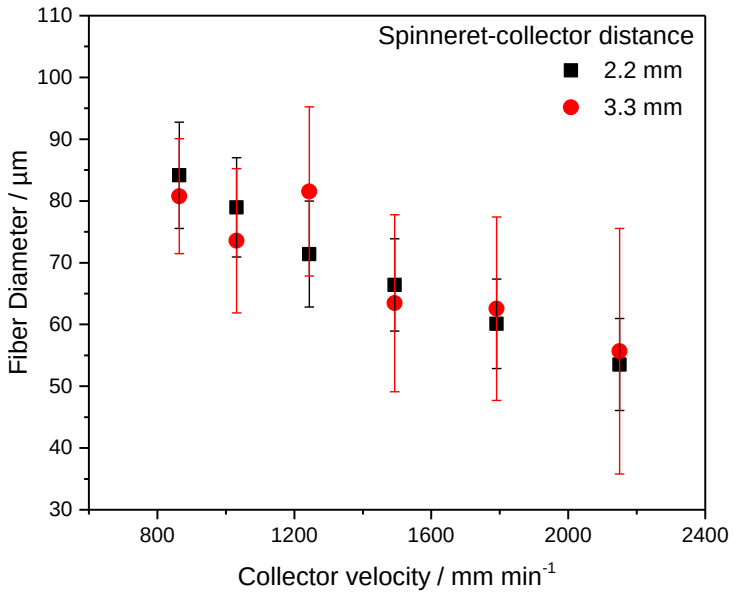


**Figure 4.12:** Influence of the *spinneret-collector distance* on the fiber diameter during MEW-processing of **6b-2** onto silicon wafer. The spinneret-collector distance has no significant influence on the fiber diameter. However, a higher standard deviation was observed for higher spinneret-collector distance. Constant printing parameters: *nitrogen pressure*: 2 bar; *spinneret diameter*: 0.45 mm; *extrusion temperature*: 75 °C; *voltage*: 2.7 kV; *surface*: silicon wafer.

***Influence of the applied voltage***

The influence of the applied *voltage* was also investigated. Figure 4.13 reveals the influence of the voltage on the shape of the fibers. With an extrusion temperature of 75 °C, nitrogen pressure of 2 bar, a spinneret diameter of 0.45 mm, a distance between spinneret and collector of 3.3 mm and a collector velocity of 1500 mm $min^{-1}$ the use of a voltage of 3.0 kV results in defined and straight MEW fibers. If the voltage is increased to 3.6 kV by maintaining all other instrumental parameters including the collector speed constant sinusoidal waves are obtained. Here, the jet speed exceeds the collector speed. The increased voltage results in a significantly enhancement of the jet speed which leads to higher CTS. With an applied voltage of 3.6 kV and a spinneret-collector-distance of 3.3 mm coiling of the fibers is still observed if the collector velocity is increased to 2150 mm $min^{-1}$. With a spinneret-collector distance of 2.2 mm the CTS increases from 200 to 500 mm $min^{-1}$ if the voltage is raised from 2.7 to 3.0 kV (table 4.6).

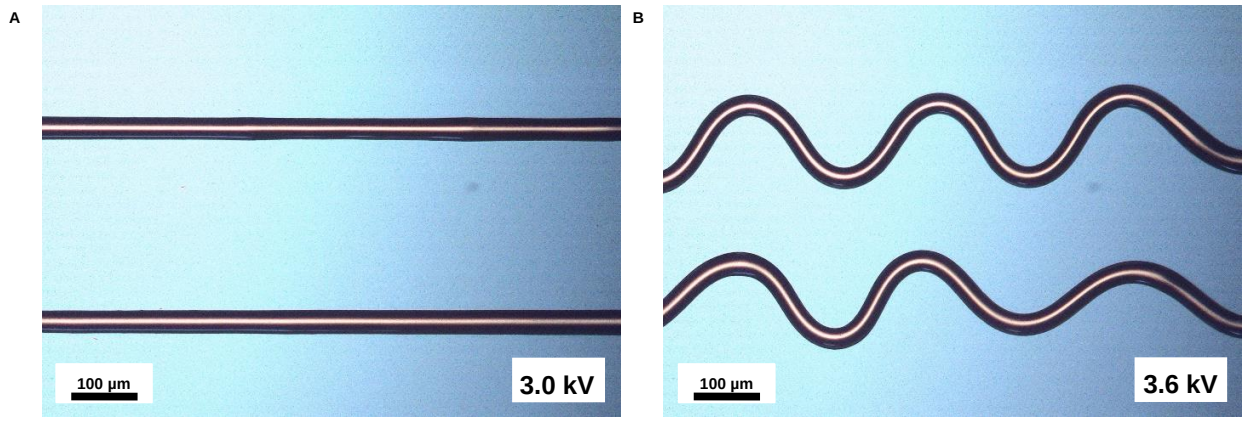


**Figure 4.13:** MEW of **6b-2:** Influence of the applied *voltage* on the critical translation speed. A) Collector speed of 1500 mm $min^{-1}$ results in straight fibers if the voltage is 3.0 kV. B) Coiling of fibers is observed if the voltage is increased to 3.6 kV and the collector speed is hold at 1500 mm $min^{-1}$. Therefore, the velocity of the polymer jet is increased by rising voltage. Printing parameters: *extrusion temperature*: 75 °C; *spinneret diameter*: 0.45 mm; *nitrogen pressure*: 2.0 bar; *spinneret-collector distance*: 3.3 mm; *surface*: silicon wafer.

The increase of the applied voltage from 2.7 to 3.0 kV while maintaining the spinneret collector distance constant at 2.2 mm results in a significantly reduced fiber diameter range from 94 to 73 to 83 to 53 µm (figure 4.14). Here, the electrostatic forces correlates proportional with the applied voltage and is therefore enhanced by increased voltage at constant spinneret-collector distance. As a result, fibers are more elongated, thus resulting in smaller fiber diameters.

Furthermore, elongated fibers have a narrow distribution which is shown by smaller standard deviation at 3.0 kV.

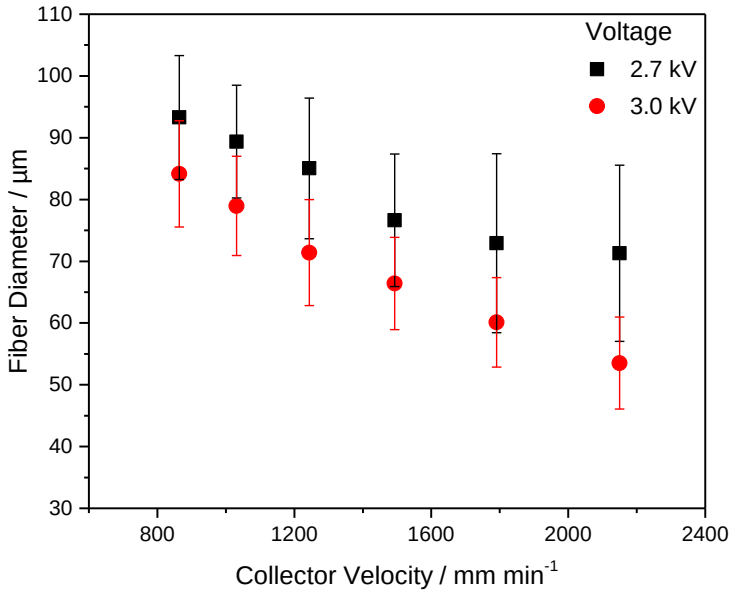


**Figure 4.14:** Influence of the applied *voltage* on the fiber diameter during MEW-processing of **6b-2** onto silicon wafer. The fiber diameter decreases with increasing voltage. The standard deviation increases if the voltage is lower. Constant printing parameters: *nitrogen pressure*: 2 bar; *spinneret diameter*: 0.45 mm; *extrusion temperature*: 75 °C; *spinneret-collector distance*: 2.2 mm; *surface*: silicon wafer.

**Table 4.6:** Influence of the spinneret-collector distance and the applied voltage on the fiber diameter range at collector velocities between 860 and 2150 mm $min^{-1}$ and the critical translation speed (CTS) during MEW processing. Constant printing parameters: *extrusion temperature*: 75 °C; *nitrogen pressure*: 2 bar; *spinneret diameter*: 0.45 mm; *substrate*: silicon

| **Spinneret-collector distance [mm]** | **Voltage [kV]** | **Fiber diameter range [µm]** | **CTS [mm $min^{-1}$]** |
|---|---|---|---|
| 2.2 | 2.7 | 73 – 94 | 200 |
| 2.2 | 3.0 | 53 – 83 | 500 |
| 3.3 | 3.0 | 56 – 81 | 720 |
| 3.3 | 3.6 | n.d. | > 2150 |

In summary, the investigated instrumental parameters, namely *collector velocity*, *flow rate* of the melt *spinneret diameter*, *extrusion temperature*, *spinneret-collector distance*, and applied *voltage* and *collector substrate* influence the MEW processing results and can be optimized for the investigated copolymer **6b-2**.

The nitrogen pressure and the applied voltage were found to have the largest influence on the fiber diameter. The fiber diameter could be varied within a range from about 40 – 140 µm by adjusting certain process parameters. Fiber diameters below 50 µm can be realized with copolymer **6b-2**. The thinnest diameter of 38 µm was realized by printing with the following parameters: *Collector velocity:* 2150 mm $min^{-1}$; *nitrogen pressure*: 0.5 bar; *spinneret diameter*: 0.45 mm; *extrusion temperature:* 75 °C; *spinneret-collector distance*: 2.2 mm; applied *voltage*: 2.7 kV; *substrate*: silicon.

It should be noted that the highest applied collector velocity was 2150 mm $min^{-1}$. A further increase of the collector velocity could result in even lower fiber diameters.

The general influence of the parameters on the printing result are comparable with other copolymers tested for MEW, such as PCL and similar $(AB)_n$- copolymers based on siloxane soft segments.[87,156,162]

#### *4.1.2.2 $(AB)_n$-segmented copolymer with 91 wt% PPG-PEG-PPG segments and 9 wt% hexamethylene bisurea segments*

Similarly to the previously discussed copolymer the influence of instrumental parameters on the fiber diameter, deposition and uniformity of MEW printed fibers was investigated for **6c-2** to find out the fiber diameter range that can achieved with this copolymer.

For copolymer **6c-2** the minimum extrusion temperature where a stable jet can be obtained by MEW was determined to be 90 °C. Therefore, first printing experiments were conducted at this temperature. Figure 4.15A shows three fibers printed one after another onto glass surface at 90 °C using constant instrumental parameters (*spinneret diameter*: 0.45 mm; *nitrogen pressure*: 2.0 bar; *Spinneret-collector distance*: 2.2 mm; *voltage*: 2.7 kV; *collector velocity*: 1800 mm $min^{-1}$). The fibers differ in the diameter and have partly linear and partly sinusoidal character. This can be explained by instabilities during printing leading to inconstant polymer jet speed. As a result, the formation of waves can be observed if the collector speed is higher as the jet speed. Such instabilities were also observed during printing with PCL and are termed *fiber pulsing*.[159]

Increasing the temperature in the spinneret and nozzle to 100 °C by maintaining all other parameters constant resulted in three straight lines with uniform diameter (Figure 4.15B). Therefore, the effect of fiber pulsing can be reduced by an increase of the extrusion temperature. Based on this result, a temperature of 100 °C was used for most of the following experiments.

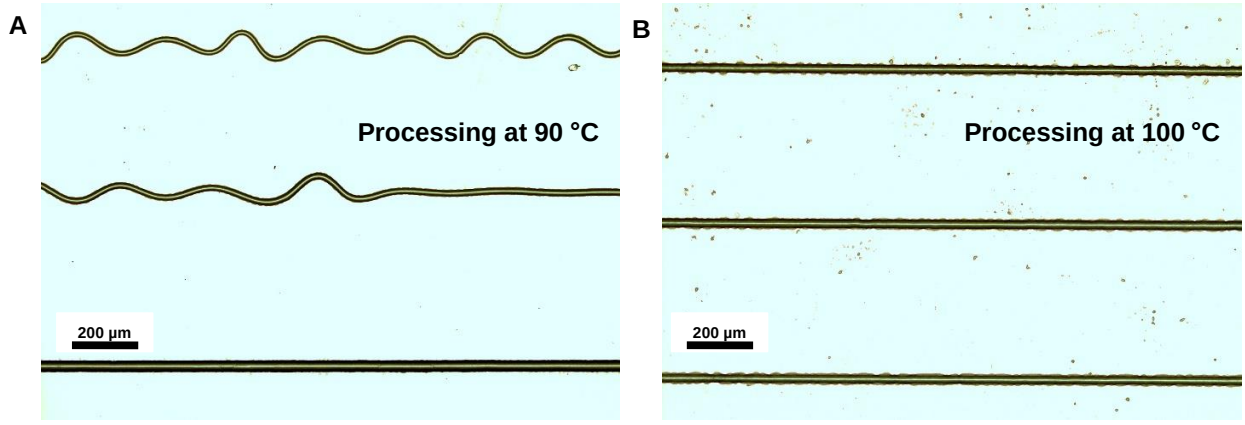


**Figure 4.15:** Microscope image of MEW printed single fibers using **6c-2**. A) MEW processing at 90 °C results in irregularly fiber diameters and partly formation of sinusoidal waves due to fiber pulsing; B) MEW processing at 100 °C leads to straight fibers with constant diameter. Printing parameters: *Spinneret diameter*: 0.45 mm; *nitrogen pressure*: 2.0 bar; *Spinneret-collector distance*: 2.2 mm; *voltage*: 2.7 kV; *collector velocity*: 1800 mm $min^{-1}$; *surface*: glass.

***Influence of the flow rate***

The influence of the *flow rate* (extrusion rate) adjusted by the *nitrogen pressure* on the *critical translation speed* (CTS), the fiber diameter and its standard deviation was determined for seven different collector velocities. The CTS was found as expected to decrease with rising nitrogen pressure. This can be explained by the lower polymer jet speed resulting in higher resistance by the large mass flow. In comparison to the previously discussed copolymer lower CTS were determined for copolymer **6c-2** which allows the use of lower nitrogen pressures to print straight fibers.

The fiber diameter and its standard deviation were measured at nitrogen pressures of 2.0 bar, 1.0 bar and 0.2 bar by printing on glass substrate. All other parameters were kept constant (*temperature*: 75 °C; *spinneret diameter*: 0.45 mm, *distance between spinneret and collector*: 2.2 mm; *voltage*: 2.7 kV). The fiber diameter is presented as function of the collector velocity for different flow rates in figure 4.16. The fiber diameter increases with increasing *nitrogen pressure*. The increased nitrogen pressure leads to a higher flow rate per time unit. Moreover, the fiber diameter decreases with rising *collector velocity*. This tendency was also expected since the polymer fibers are further stretched if the collector is moving faster. Interestingly, the decline is lower at low nitrogen pressures.

The resulting fiber diameter ranges are also listed in table 4.7. With a nitrogen pressure of 2.0 bar fiber diameters in the range between 68 and 42 µm are obtained. The reduction of the nitrogen pressure to 1.0 bar results in fiber diameters of 58 to 28 µm. The thinnest fibers with a diameter of 27 to 18 µm between could be obtained with the lowest applied nitrogen pressure of 0.2 bar.

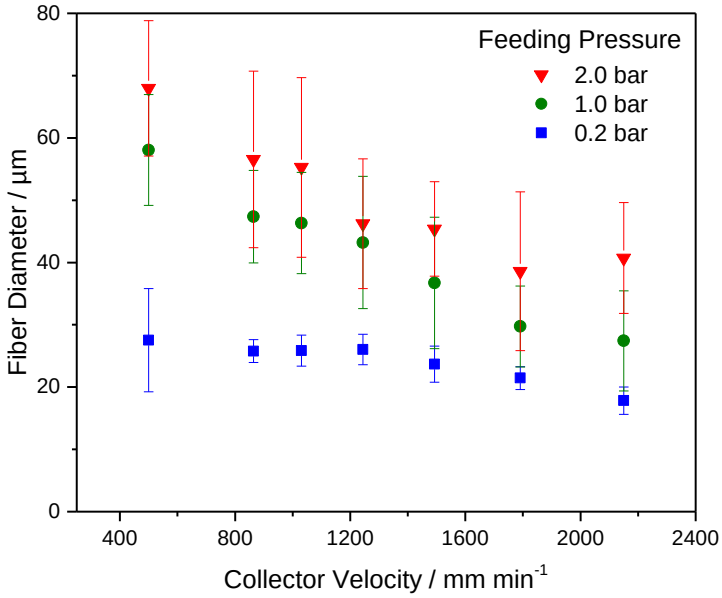


**Figure 4.16:** A) Influence of the *nitrogen pressure* during MEW-processing of **6c-2** on the fiber diameter by using different collector velocities and B) influence of the pressure on the fiber diameter when printing at 1500 mm min$^{-1}$ and on the critical translation speed (CTS). The fiber diameter decreases and has a lower standard deviation if the pressure is lower. Decrease of nitrogen pressure leads to increased CTS. Constant printing parameters: *extrusion temperature*: 100 °C; *spinneret diameter*: 0.45; *spinneret-collector distance*: 2.2 mm; *voltage*: 2.7 kV; *surface*: glass.

**Table 4.7:** Influence of the *nitrogen pressure* on the fiber diameter range at collector velocities between 500 and 2150 mm min$^{-1}$ and the critical translation speed (CTS) during MEW processing. Constant printing parameters: *extrusion temperature*: 100 °C; *spinneret diameter*: 0.45 mm; *spinneret-collector distance*: 2.2 mm; *voltage*: 2.7 kV; *substrate*: glass.

| **Nitrogen pressure [bar]** | **Fiber diameter range [µm]** | **CTS [mm min$^{-1}$]** |
|---|---|---|
| **2.0** | 42 – 68 | 220 |
| **1.0** | 28 – 58 | 290 |
| **0.5** | n.d. | 600 |
| **0.3** | n.d. | 720 |
| **0.2** | 18 – 27 | 860 |

In chapter 4.1.2.1 the validity of equations (4.1) and (4.2) for the correlation of the fiber diameter with the collector speed and the nitrogen pressure was investigated for MEW-processing of copolymer **6b-2**. It was found out that both equations fit the experimental determined fiber diameters for **6b-2** well. The applicability of equations (4.1) and (4.2) was also investigated for **6c-2**. For equation (4.1) the fiber diameter $D_1$ at the reference collector velocity $V_1$ was measured

for the lowest applied collector velocity of 860 mm min$^{-1}$ at a constant nitrogen pressure of 1 bar. The fiber diameters $D_2$ at the other collector velocities $V_2$ were calculated and compared with the experimental determined values. All other instrumental parameters were kept constant. For equation (4.2) the lowest applied pressure of 0.2 bar was used and theoretical values for $p_2$ were calculated for higher pressures. MEW-processing was done onto glass substrate. Figure 4.17 shows that for **6c-2** equation (4.1) can be applied very well. All calculated values lay distinctly within the error bars of the experimental determined fiber diameters for all collector velocities. As a result, the fiber diameter at certain collector velocities can be predicted.

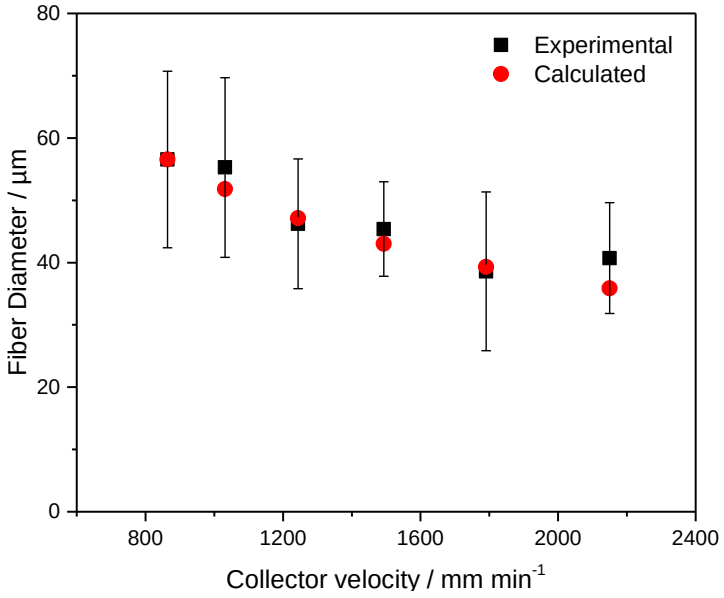


**Figure 4.17:** Comparison of MEW printed fiber diameter of **6c-2** (black) and calculated value (red) by using equation (4.1) for six collector velocities. Printing parameters: *nitrogen pressure*: 1 bar; *extrusion temperature*: 75 °C; *spinneret diameter*: 0.45 mm; *spinneret-collector distance*: 2.2 mm; *voltage*: 2.7 kV; *substrate*: glass.

The applicability of equation (4.2) was done by using a nitrogen pressure of 0.2 bar as reference for $P_1$ and the fiber diameter measured from it as value for $D_1$. Figure 4.18 reveals that the calculated values for the fiber diameter ($D_2$) in relation to the nitrogen pressure are higher as the experimental determined diameters. The deviation becomes larger with increasing flow rate. Consequently, in contrast to **6b-2** equation (4.2) cannot be applied for this copolymer**.**

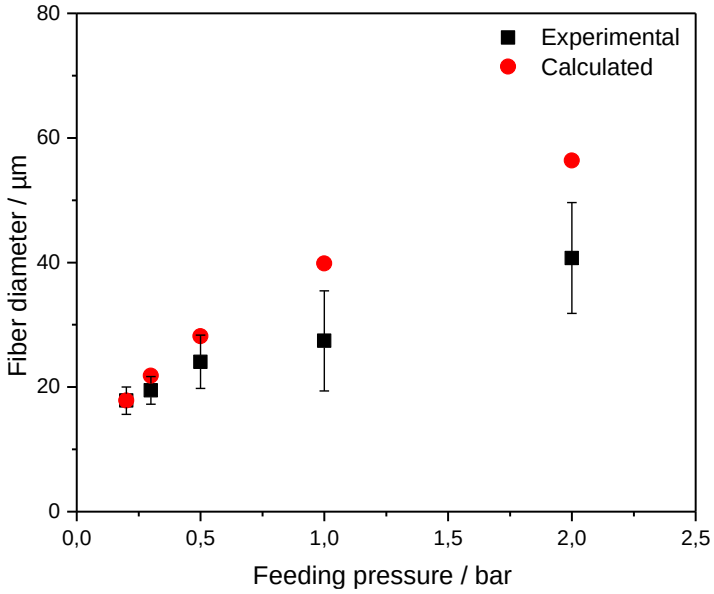


**Figure 4.18:** Comparison of MEW printed fiber diameter of **6c-2** (black) and calculated value (red) by using equation (4.2) for five nitrogen pressures. Printing parameters: *collector velocity*: 1800 mm $min^{-1}$; *extrusion temperature*: 75 °C; *spinneret diameter*: 0.45 mm; *spinneret-collector distance*: 2.2 mm; *voltage*: 2.7 kV; *surface*: glass.

### *Influence of the spinneret diameter*

Next, the influence of the *spinneret diameter* was investigated. Four different spinneret diameters, 0.30, 0.45, 0.60 and 0.70 mm were tested. The CTS decreases with increasing spinneret diameter as shown in table 4.8. This is due to the higher mass flow per time resulting in resistance. Consequently, the jet speed decreases and straight fibers can be printed at lower velocities. On the other hand, the speed of the polymer jet is higher by the use of low spinneret diameters and a higher collector speed is required for the writing of linear fibers. The use of a fiber diameter of 0.7 mm leads to fiber pulsing with instabilities in the polymer jet. The copolymer is partly released from the nozzle by formating big drops. For this reason the fiber diameters were not determined for a nozzle diameter of 0.7 mm.

Figure 4.19 shows the fiber diameter as a function of the collector velocity using different spinneret diameters. The fiber diameter increases with the spinneret diameter. Additionally, the standard deviation increases if a larger size of the nozzle is used. This can be explained by an increasing polymer amount per time flowing out of the spinneret. Furthermore, forces and instabilities induced by the electric field seem to have higher influence on a thicker polymer jet resulting in a broader distribution of fiber diameter. The fiber diameter decreases from

96 – 52 µm to 68 – 37 µm and further to 46 – 23 µm if the spinneret diameter is reduced from 0.60 to 0.45 and 0.30 mm, respectively.

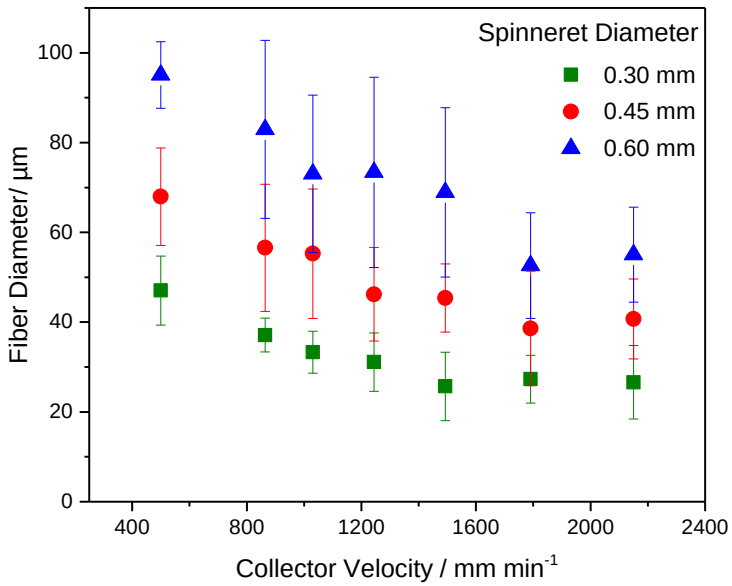


**Figure 4.19:** A) Influence of the *spinneret diameter* during MEW-processing of **6c-2** on the fiber diameter by using different *collector velocities* and B) influence of the spinneret diameter on the fiber diameter when printing at 1500 mm $min^{-1}$ and on the critical translation speed (CTS). The fiber diameter decreases and has a lower standard deviation if the spinneret diameter is lower. Decrease of nozzle size leads to increased CTS. Constant printing parameters: *extrusion temperature*: 100 °C; *nitrogen pressure*: 2.0 bar; *spinneret-collector distance*: 2.2 mm; *voltage*: 2.7 kV; *surface*: glass.

**Table 4.8:** Influence of the spinneret diameter on the fiber diameter range at collector velocities between 500 and 2150 mm $min^{-1}$ and the critical translation speed (CTS) during MEW processing. Constant printing parameters: *extrusion temperature*: 100 °C; *nitrogen pressure*: 2 bar; *spinneret-collector distance*: 2.2 mm; *voltage*: 2.7 kV; *substrate:* glass

| **Spinneret Diameter [mm]** | **Fiber diameter range [µm]** | **CTS [mm $min^{-1}$]** |
|---|---|---|
| 0.70 | n. d. | 160 |
| 0.60 | 52 – 96 | 180 |
| 0.45 | 37 – 68 | 220 |
| 0.30 | 23 – 46 | 500 |

***Influence of the extrusion temperature***

The influence of the processing temperature was determined for six different collector velocities at 100, 110 and 120 °C. Figure 4.20 and table 4.9 show that the fiber diameter range increases from 103 to 41 µm at 100 °C to 126 – 57 µm at 110 °C and to 162 – 82 µm at 120 °C. This can be explained by the lower melt viscosity at elevated temperatures leading to higher material flow per time. Forces induced by the electric field can partly stretch the polymer jet. This effect is larger with increasing mass flow and results in higher fiber deviation at higher extrusion temperatures. No notable influence of the temperature on the CTS was observed.

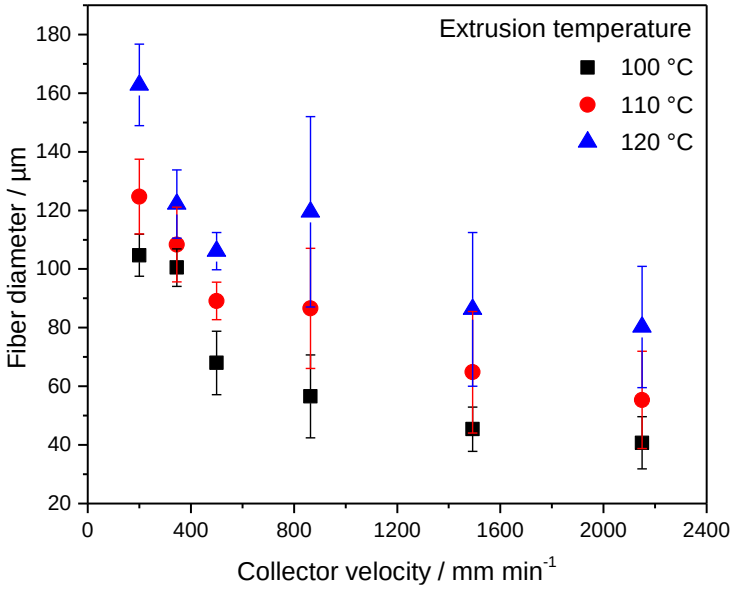


**Figure 4.20:** Influence of the extrusion temperature on the fiber diameter during MEW-processing of **6c-2**. The fiber diameter increases with rising printing temperature and decreases with increasing collector speed. The standard deviation decreases if the temperature is lower. Constant printing parameters: *nitrogen pressure*: 2.0 bar; *spinneret diameter*: 0.45 mm; spinneret-collector distance: 2.2 mm; voltage: 2.7 kV; surface: glass.

**Table 4.9:** Influence of the spinneret diameter on the fiber diameter range at collector velocities between 500 and 2150 mm min$^{-1}$ and the critical translation speed (CTS) during MEW processing. Constant printing parameters: *nitrogen pressure*: 2 bar; *spinneret-diameter*: 0.45 mm; *spinneret-collector distance*: 2.2 mm; *voltage*: 2.7 kV; *substrate:* glass

| **Extrusion Temperature [°C]** | **Fiber diameter range [µm]** | **CTS [mm min$^{-1}$]** |
|---|---|---|
| 100 | 41 – 103 | 220 |
| 110 | 57 – 126 | 220 |
| 120 | 82 – 162 | 200 |

***Influenence of the applied voltage***

As already observed for **6b-2** the applied *voltage* has a high influence on the fiber diameter and on the CTS. For **6c-2** the effect on the CTS is shown in figure 4.21 and summarized in table 4.10. If a voltage of 2.7 kV is applied in combination with a temperature of 100 °C, a nitrogen pressure of 0.2 bar and a spinneret collector distance of 2.2 mm straight fibers can be printed if the collector velocity is minimum 900 mm $min^{-1}$. The CTS rises to 2150 mm $min^{-1}$ if the voltage is increased to 3.0 kV. Further increase of the voltage to 3.3 kV resulted in coiled fibers up to the upper investigated collector speed of 3150 mm $min^{-1}$. As shown in figure 4.21 straight fibers are draw at a collector velocity of 1800 mm $min^{-1}$ for an applied voltage of 2.7 kV. If the voltage is increased to 3.0 kV by maintaining the collector velocity constant sinusoidal fibers are obtained. A further increase of the applied voltage leads to an increase of the velocity of the polymer jet. At 3.3 kV the jet is further accelerated and loop-form shape fibers were observed. The polymer jet speed is now far above the collector velocity. Loop-form shape fibers were also reported for PCL at polymer jet speeds far above the collector speed.[2]

In conclusion, a moderate voltage of 2.7 kV is most applicable for this copolymer and the fiber diameter was not determined for other voltages.

**Table 4.10:** Influence of the applied voltage on the *critical translation speed* (CTS) during MEW processing of **6c-2** onto glass substrate. The CTS significantly increases with increasing voltage. Printing parameters*: extrusion temperature:* 100 °C*; spinneret diameter:* 0.45 mm*; nitrogen pressure:* 0.2 bar; *spinneret-collector distance:* 2.2 mm*;* collector velocity*:* 1800 mm $min^{-1}$*; surface:* glass*.*

| **Applied Voltage [kV]** | **CTS [mm $min^{-1}$]** |
|---|---|
| **2.7** | 860 |
| **3.0** | 2150 |
| **3.3** | > 3150 |

The increase of the distance between the spinneret and collector leads to strong instabilities of the jet. For this reason, the spinneret-collector distance was maintained at 2.2 mm for this copolymer.

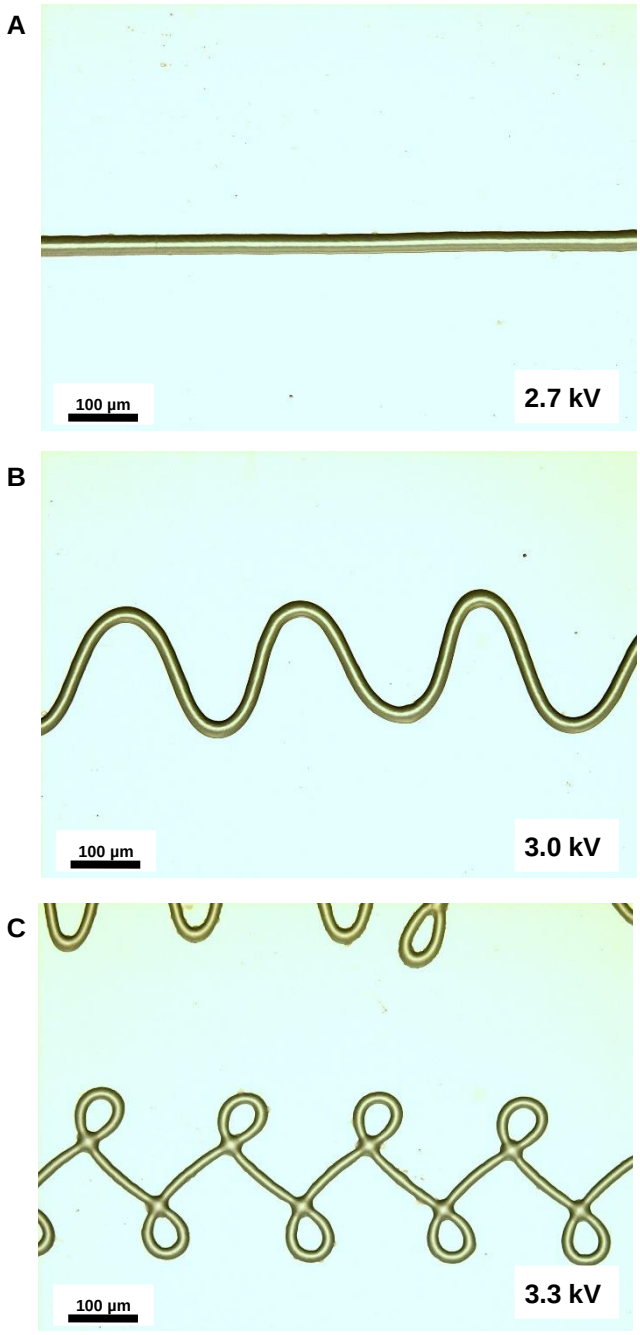


**Figure 4.21***:* MEW of **6c-2**: Influence of the applied *voltage* on the CTS by altering jet speed. A) Straight fibers are received if a voltage of 2.7 kV is applied, B) Increased voltage of 3.0 kV leads to coiling and the formation of sinusoidal fibers, C) further increase to 3.3 kV results in eight-shape fibers. Printing parameters: *extrusion temperature*: 100 °C; *spinneret diameter*: 0.45; *nitrogen pressure*: 0.2 bar; *spinneret-collector distance*: 2.2 mm; *collector velocity*: 1800 mm $min^{-1}$; surface: glass.

***Influence of the collector substrate***

Finally, the influence of the collector *substrate* was investigated by using glass slides and silicon wafer. The following printing parameters were applied: *extrusion temperature*: 75 °C; *nitrogen pressure*: 0.2 bar; *spinneret diameter*: 0.45 mm, *distance between spinneret and collector*: 2.2 mm; *voltage*: 2.7 kV. On a glass surface, thin fibers with a diameter range of 18 to 27 µm were achieved, while on a silicon substrate higher fiber diameters of 28 to 48 µm resulted. The standard deviation did not significantly alter as depicted in figure 4.22. The interaction of printed MEW fibers with the silicon wafer surface is higher leading to increased flattening.

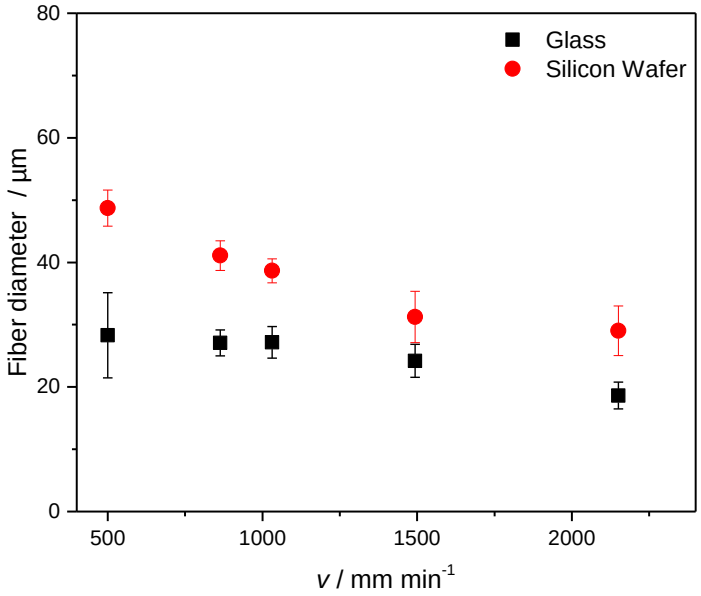


**Figure 4.22:** Influence of different *substrates* on the fiber diameter of **6c-2** by comparing glass and silicon wafer. Fiber diameter is higher if silicon wafer is used as surface. The standard deviation is comparable for both surfaces. MEW-printing parameters: *extrusion temperature*: 75 °C; *nitrogen pressure*: 0.2 bar; *spinneret diameter*: 0.45 mm; *spinneret-collector distance*: 2.2 mm; *voltage*: 2.7 kV.

As shown in chapter 3.3.1 on page 58 the PEG units in copolymer **6c-2** are semi-crystalline at room temperature and melt around 35 °C. Therefore, the MEW-processed fibers were studied by optical light microscopy at 25 °C and 40 °C with crossed polarizations and also with addition of a λ/4 plate. The results are shown in figure 4.23. With crossed polarizers birefringent fibers were observed at room temperature. Here, the birefringence results from the semi-crystal PEG segments and are visible in the polarized microscope. If the fibers are heated to 40 °C the birefringence completely disappears. This is due to the melting of the PEG segments. If the fiber is cooled down to 25 °C the birefringence of the crystals appears again showing the reversibility

of the melting of the PEG segments. A phase shift of the polarized light by the use of the λ/4 plate shows the fiber with the crystals at 25 °C. The crystals disappear upon *heating* to 40 °C. It should be pointed out that the printed fiber maintains its shape and diameter showing that the polymer is still not fluid due to the physical crosslinks between the bisurea segments.

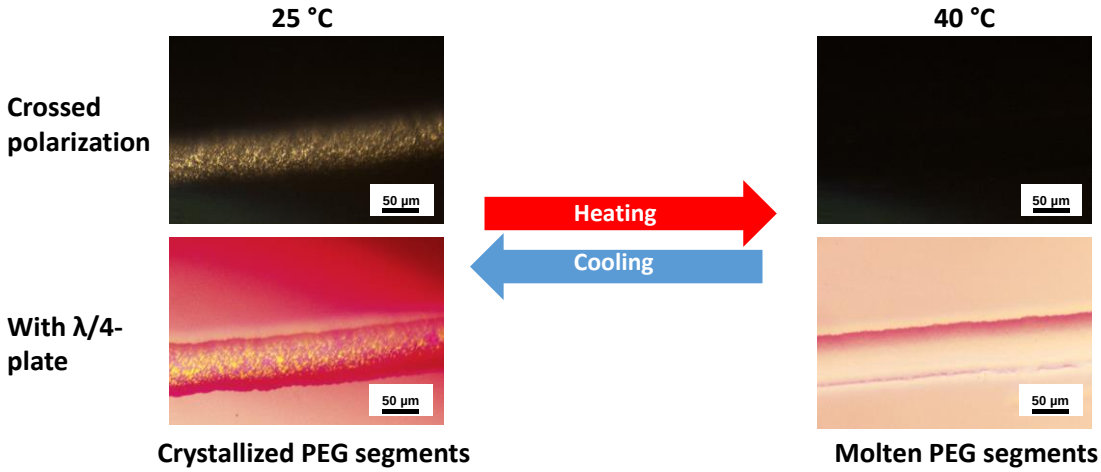


**Figure 4.23:** Polarization light microscopy images of a MEW printed fiber of **6c-2** at 25 °C and 40 °C with and without crossed polarizers. Crystals result from semi-crystalline PEG segments and reversibly melt upon *heating* to 40 °C. The MEW fiber maintains its shape and diameter and does not melt away due to bonding of the bisurea segments.

To sum up, all investigated instrumental parameters, namely *collector velocity*, *flow rate, spinneret diameter*, *extrusion temperature*, *voltage* and *collector substrate* influence the MEW processing results of copolymer **6c-2** and can be optimized with respect to the fiber diameter. The nitrogen pressure was found to have the strongest influence on the fiber diameter. On the other hand, the *critical translation speed* (CTS) is strongly influenced by the applied voltage. The fiber diameter could be varied within a range between about 20 and 160 µm in dependence of the selected parameters. Fiber diameters below 20 µm can be realized with copolymer **6c-2**. The thinnest diameter of 18 µm was realized by printing with the following parameters: *Collector velocity:* 2150 mm $min^{-1}$; *nitrogen pressure*: 0.2 bar; *extrusion temperature:* 75 °C; *spinneret diameter*: 0.45 mm; *spinneret-collector distance*: 2.2 mm; *applied voltage*: 2.7 kV; *substrate*: glass. As a result, lower fiber diameters could be achieved as compared to the previously discussed copolymer **6b-2.** It should be noted that the highest applied collector velocity was 2150 mm $min^{-1}$. A further increase of the collector velocity is expected to result in even lower fiber diameters.

#### *4.1.2.3 $(AB)_n$-segmented copolymer with 75 wt% PPG-PEG-PPG segments and 25 wt% 4,4-methylene-bis(cyclohexyl) bisurea segments*

In the same manner as for $(AB)_n$-segmented copolymers **6b-2** and **6c-2** with hexamethylene bisurea segments the influence of several instrumental parameters for the printing of single fibers by MEW was investigated for copolymers **8a-2** and **8a-3** with 4,4'-methylene-bis(cyclohexyl) segments. Both copolymers have 75 wt% PPG-PEG-PPG segments and a 25 wt% 4,4'-methylene-bis(cyclohexyl) bisurea segments and differ in the degree of polymerization. More studies were conducted with copolymer **8a-2** whose average degree of polymerization was determined to be 31 by SEC analysis. Copolymer **8a-3** has an average degree of polymerization of 26. The collector velocity was varied between 500 and 2150 mm $min^{-1}$. All printing experiments were conducted on glass substrates. For most of the experiments, a temperature of 100 °C was used.

***Influence of the flow rate***

The influence of the *flow rate* on the fiber diameter and the fiber diameter distribution was investigated for both copolymers using different nitrogen pressures of 0.2, 0.5 and 1 bar and keeping all other parameters constant (*extrusion temperature:* 100 °C*; spinneret diameter:* 0.30 mm*; spinneret-collector distance:* 2.2 mm*; voltage:* 3.3 kV). With both copolymers no coiling of the fibers was observed for all applied nitrogen pressures and collector velocities above 200 mm $min^{-1}$.

Figure 4.24 shows that the fiber diameter increases if the *nitrogen pressure* is increased from 0.2 to 0.5 bar for both copolymers.[139] Interestingly, a further increase of the nitrogen pressure from 0.5 to 1 bar does not result in higher fiber diameters with **8a-2** as shown in table 4.11. With copolymer **8a-3** an increase of the fiber diameter was observed at low collector velocities. With a nitrogen pressure of 0.2 bar, fiber diameters in the range of 10 – 6 µm for **8a-2** and 12 – 8 µm for **8a-3** were obtained. At 0.5 bar the fiber diameters are within 21 and 12 µm for **8a-2** and within 14 and 12 µm for **8a-3**. This increase of the fiber diameters can be explained by a higher material flow out of the nozzle per time. The standard deviation of the fiber diameter becomes larger with increasing nitrogen pressure as expected and also observed for the other previously investigated materials **6b-2** and **6c-2**. As already observed with copolymer **6c-2** and with PCL, the reduction of

the fiber diameter with increased collector velocities is much less pronounced at low nitrogen pressures below 1 bar.

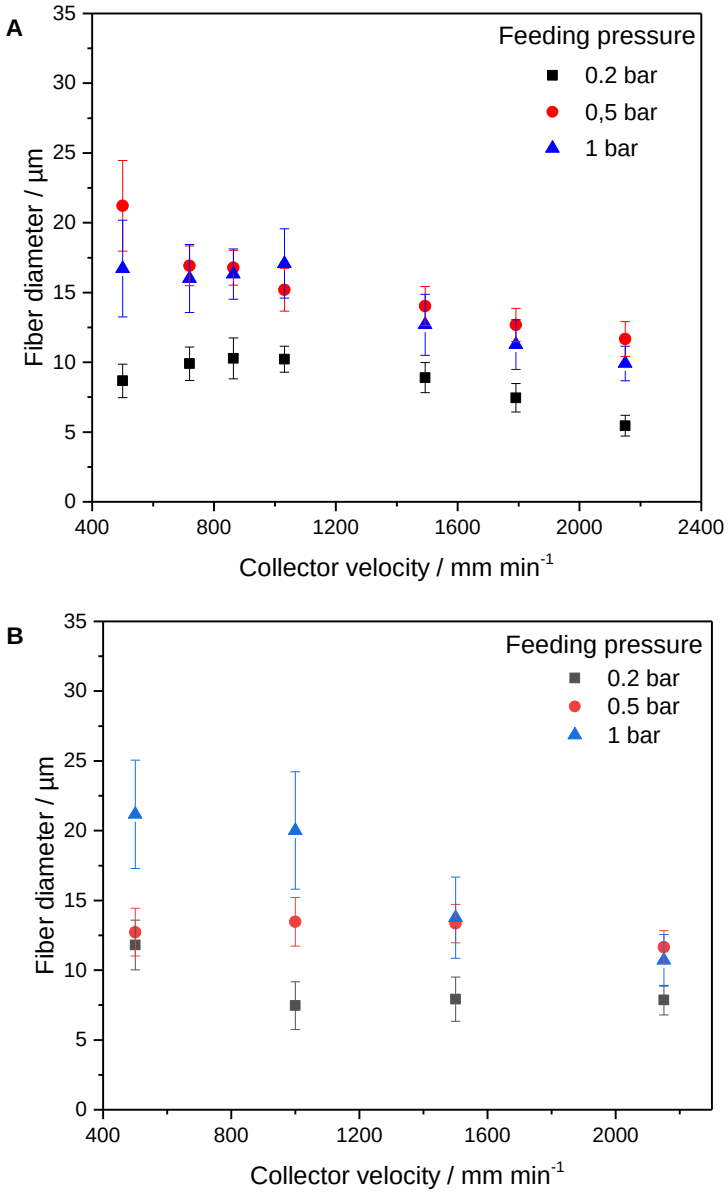


**Figure 4.24:** Influence of the *nitrogen pressure* on the fiber diameter during MEW-processing of **A: 8a-2** and **B: 8a-3** onto glass as surface. The fiber diameter increases with rising pressure below 0.5 bar. The fiber diameters at 0.5 and 1.0 bar are comparable. The fiber size distribution increase with increasing pressure. Printing parameters: *extrusion temperature*: 100 °C; *spinneret-collector distance*: 2.2 mm; *voltage*: 3.3 kV; *spinneret diameter*: 0.30 mm; *substrate*: glass. Adapted and reproduced with permission (© 2020 The Authors. Macromolecular Chemistry and Physics published by WILEY-VCH GmbH).[139]

**Table 4.11:** Influence of the *nitrogen pressure* on the fiber diameter range at collector velocities between 500 and 2150 mm $min^{-1}$ and the critical translation speed (CTS) during MEW processing. Constant printing parameters: *extrusion temperature*: 100 °C; *spinneret diameter*: 0.30 mm; *spinneret-collector distance*: 2.2 mm; *voltage*: 3.3 kV; *substrate*: glass.

| Copolymer | Nitrogen pressure [bar] | Fiber diameter range [µm] | CTS [mm $min^{-1}$] |
|---|---|---|---|
| **8a-2** | 1.0 | 11 – 17 | < 200 |
| **8a-2** | 0.5 | 12 – 21 | < 200 |
| **8a-2** | 0.2 | 6 – 10 | < 200 |
| **8a-3** | 1.0 | 11 – 22 | < 200 |
| **8a-3** | 0.5 | 12 – 14 | < 200 |
| **8a-3** | 0.2 | 8 - 12 | < 200 |

***Influence of the extrusion temperature***

For the investigation of the influence of the extrusion temperature on the fiber diameter three different extrusion temperatures were tested for each copolymer. Figure 4.25 shows that the fiber diameter and its standard deviation increase with rising extrusion temperature for both copolymers.[139] This trend was also for copolymers **6b-2** and **6c-2** with hexamethylene bisurea segments. This can be explained by the reduced viscosity at elevated temperatures leading to a rising material flow per time out of the nozzle. The increase of the fiber diameter with increasing extrusion temperature is less pronounced with copolymer **8a-3**.

At a constant nitrogen pressure of 1 bar the fiber diameter range increases from 23 to 9 µm at 85 °C to 25 – 13 µm at 100 °C as shown in table 4.12. For copolymer **8a-2** the difference in the fiber diameter is higher. At 95 °C fiber diameters are located within 17 and 9 µm. At 95 °C fiber diameters of 23 to 14 µm were obtained. No coiling of the fibers was observed and the CTS is below 200 mm $min^{-1}$ for both copolymers at all applied temperatures.

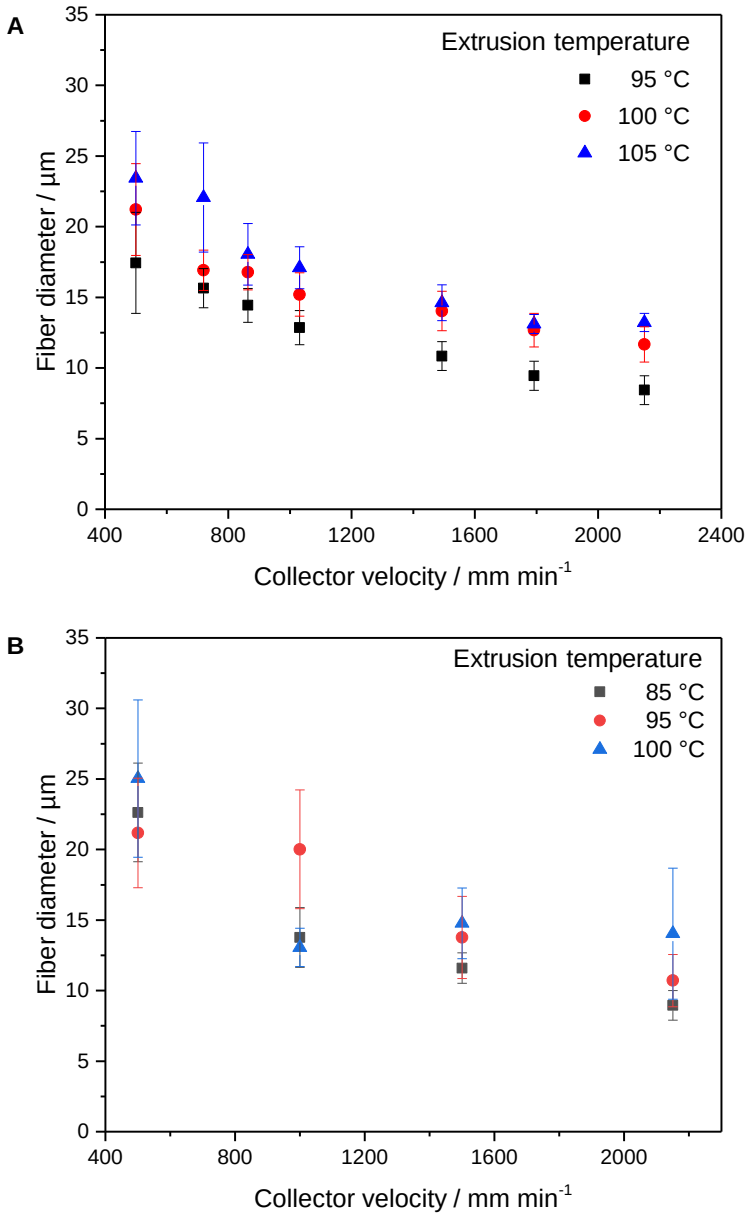


**Figure 4.25:** Influence of the *extrusion temperature* on the fiber diameter during MEW-processing of **A**: **8a-2** and **B: 8a-3** onto glass surface. The fiber diameter and its standard deviation increase with increasing temperature. Printing parameters: *nitrogen pressure*: 0.5 bar; *spinneret-collector distance*: 2.2 mm; *voltage*: 3.3 kV; *spinneret diameter*: 0.30 mm; *substrate*: glass. Adapted and reproduced with permission (© 2020 The Authors. Macromolecular Chemistry and Physics published by WILEY-VCH GmbH).[139]

**Table 4.12:** Influence of the *nitrogen pressure* on the fiber diameter range at collector velocities between 500 and 2150 mm $min^{-1}$ and the critical translation speed (CTS) during MEW processing. Constant printing parameters: *nitrogen pressuree*: 0.5 bar; *spinneret diameter*: 0.30 mm; *spinneret-collector distance*: 2.2 mm; *voltage*: 3.3 kV; *substrate*: glass.

| Copolymer | Extrusion Temperature [°C] | Fiber diameter range [µm] | CTS [mm $min^{-1}$] |
|---|---|---|---|
| **8a-2** | 95 | 8 – 17 | < 200 |
| **8a-2** | 100 | 12 – 21 | < 200 |
| **8a-2** | 105 | 14 – 23 | < 200 |
| **8a-3** | 85 | 10 – 23 | < 200 |
| **8a-3** | 95 | 11 – 21 | < 200 |
| **8a-3** | 100 | 13 – 25 | < 200 |

### *Influence of the applied voltage*

For copolymer **8a-2** the influence of the applied voltage was additionally studied. Figure 4.26 reveals that the fiber diameter decreases with increasing *voltage*.[139] With an *extrusion temperature* of 100 °C, *nitrogen pressure* of 0.5 bar, *spinneret diameter* of 0.30 mm and *distance between spinneret and collector* of 2.2 mm the fiber diameter range decreases from 27 to 12 µm to 17 to 8 µm if the voltage is increased from 2.7 to 3.6 kV. The achieved fiber diameter ranges are also listed in table 4.13. A rising voltage results in a higher electric force. Consequently, the fibers are further stretched and the fiber diameter is reduced. The standard deviation decreases with increased voltage. More elongation of the fibers results in narrow fiber size distribution. No coiling of fibers was observed for all three applied voltages in the investigated collector velocity range between 500 and 2150 mm $min^{-1}$.

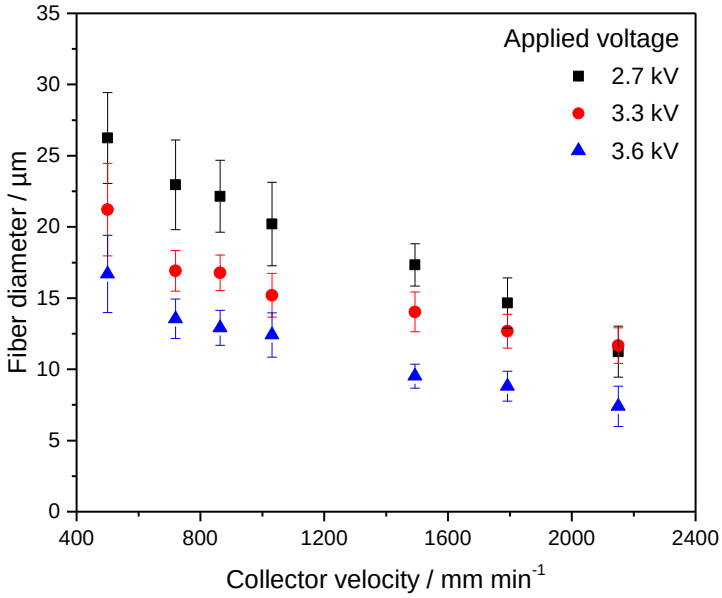


**Figure 4.26:** Influence of the applied *voltage* on the fiber diameter during MEW-processing of **8a-2** onto glass surface. The fiber diameter and its standard deviation decreases with increasing voltage. Printing parameters: *extrusion temperature*: 100 °C; *nitrogen pressure*: 0.5 bar; *spinneret-collector distance*: 2.2 mm; *spinneret diameter*: 0.30 mm; *substrate*: glass. Adapted and reproduced with permission (© 2020 The Authors. Macromolecular Chemistry and Physics published by WILEY-VCH GmbH).[139]

**Table 4.13:** Influence of the *spinneret diameter* on the fiber diameter range at collector velocities between 500 and 2150 mm min$^{-1}$ and the critical translation speed (CTS) during MEW processing. Constant printing parameters: *extrusion temperature*: 100 °C; *nitrogen pressure*: 0.5 bar; *spinneret-collector distance*: 2.2 mm; *spinneret diameter*: 0.30 mm; *substrate*: glass.

| **Applied Voltage [kV]** | **Fiber diameter range [µm]** | **CTS [mm min$^{-1}$]** |
|---|---|---|
| 100 | 12 – 27 | < 500 |
| 110 | 13 – 21 | < 500 |
| 120 | 8 – 17 | < 500 |

### *Influence of the distance between spinneret and collector*

Also, the influence of simultaneous alteration of the applied *voltage* from 3.3 to 5.0 kV and a *spinneret-collector-distance* from 2.2 to 3.3 mm was investigated for copolymer **8a-2**. Consequently, the electric force which is defined as the ratio between the voltage and spinneret collector distance was maintained constant.

The CTS was found to be below 500 mm $min^{-1}$ if the spinneret-collector distance and the applied voltage are 2.2 mm and 3.3 kV. The increase of these parameters to 3.3 mm and 5.0 kV leads to a CTS of 860 mm $min^{-1}$. It is assumed that an increase of the electrostatic force accelerates the polymer jet out of the nozzle.

Figure 4.27 and table 4.14 reveal that the fiber diameter is a little bit lower if the applied voltage and spinneret-collector-distance are increased from 2.2 mm and 3.3 kV to 5.0 kV and 3.3 mm. This can be explained by the increased time for the polymer jet to be stretched prior to reaching the collector as compared to the lower distance of 2.2 mm. In contrast, the size distribution is significantly higher at the larger voltage and larger spinneret-collector distance leading to a higher standard deviation. Equal results were obtained for copolymer **6b-2** with hexamethylene bisurea segments. As a result, the fiber size is better controlled with a spinneret-collector distance of 2.2 mm and an applied voltage of 3.3 kV.

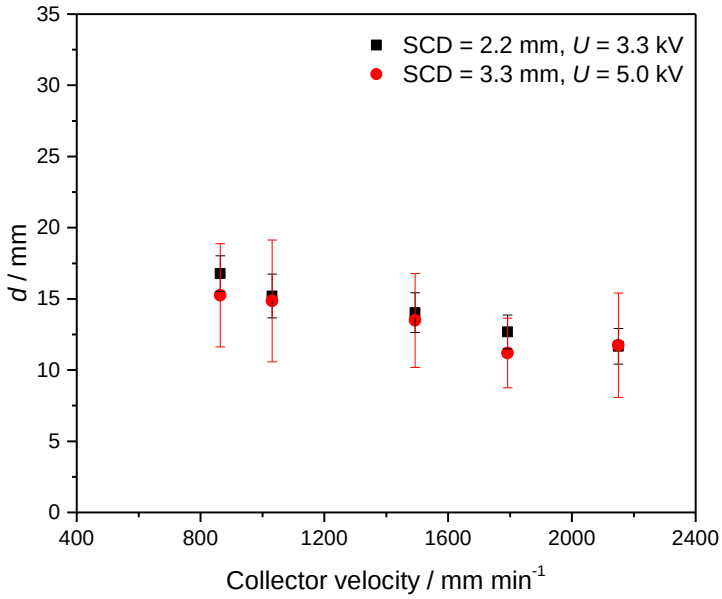


**Figure 4.27**: Influence of the simultaneous alteration of the applied *voltage* (*U*) and the *spinneret-collector distance* on the fiber diameter during MEW-processing of **8a-2** onto glass while maintaining the electric force constant. The fiber diameter is slightly higher with and its standard deviation is lower with decreased voltage and spinneret collector-distance. Constant printing parameters: *extrusion temperature*: 100 °C; *nitrogen pressure*: 0.5 bar; *spinneret diameter*: 0.3 mm; *substrate*: glass.

**Table 4.14:** Influence of the spinneret diameter on the fiber diameter range at collector velocities between 500 and 2150 mm $min^{-1}$ and the critical translation speed (CTS) during MEW processing. Constant printing parameters: *nitrogen pressure*: 2 bar; *spinneret-diameter*: 0.45 mm; *extrusion temperature*: 100 °C; *substrate:* glass

| Distance between spinneret and collector [mm] | Applied Voltage [kV] | Fiber diameter range [µm] | CTS [mm $min^{-1}$] |
|---|---|---|---|
| 2.2 | 3.3 | 12 – 17 | < 500 |
| 3.3 | 5.0 | 12 – 15 | 860 |

***Infuence of the spinneret diameter***

Furthermore, two different *spinneret diameters*, 0.30 and 0.45 mm, were tested at five different collector velocities. The spinneret-collector distance was 3.3 mm and voltage, temperature and nitrogen pressure were set to 5.0 kV, 100 °C and 0.5 bar, respectively.

With a spinneret diameter of 0.30 mm coiling a CTS of 860 mm $min^{-1}$ was determined. In contrast no coiling was observed with a nozzle size of 0.45 mm in the complete used collector speed range. Therefore, the CTS is below 500 mm $min^{-1}$.

Figure 4.28 shows the fiber diameter as a function of the collector velocity between 860 and 2150 mm $min^{-1}$ with the use of two different spinneret diameters. An increase of the spinneret diameter from 0.30 to 0.45 mm results in a significantly increase of the fiber diameter range from 15 to 12 µm to 48 to 20 µm as shown in table 4.15. Additionally, a significantly higher standard deviation was obtained for the higher spinneret diameter of 0.45 mm. An increase of the spinneret diameter leads to a higher flow rate per time. These effects can be explained by a higher mass flow per time at higher nozzle sizes resulting in a thicker polymer jet and larger fiber diameter. Furthermore, forces induced by the electric field can lead to partly stretching of the polymer jet. Consequently, the deviation in the fiber diameter is larger. Interestingly, the decrease of the fiber diameter with rising collector speed is more significant with a spinneret diameter of 0.45 mm.

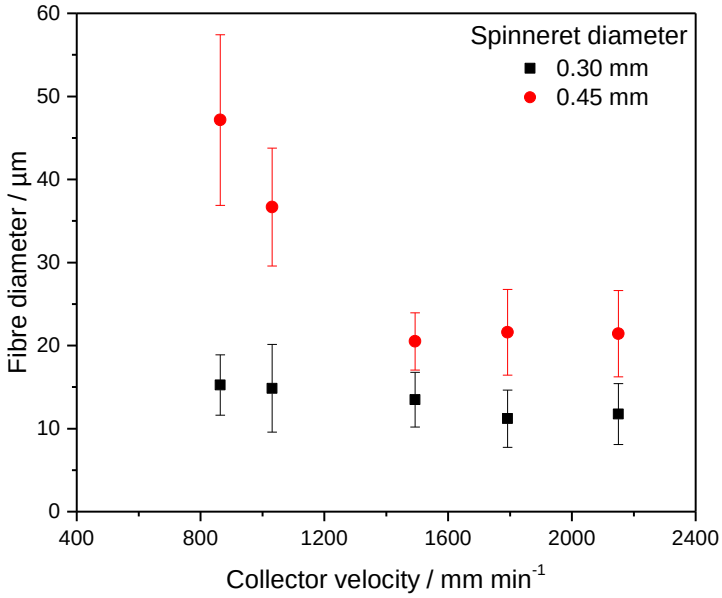


**Figure 4.28:** Influence of the *spinneret diameter* on the fiber diameter during MEW-processing of **8a-2** onto glass surface. The fiber diameter and its standard deviation increase with rising spinneret diameter. Constant printing parameters: *extrusion temperature*: 100 °C; *nitrogen pressure*: 0.5 bar; *spinneret-collector distance*: 3.3 mm; *voltage*: 5.0 kV; *substrate*: glass.

**Table 4.15:** Influence of the spinneret diameter on the fiber diameter range at collector velocities between 500 and 2150 mm min$^{-1}$ and the critical translation speed (CTS) during MEW processing. Constant printing parameters: *extrusion temperature*: 100 °C; *nitrogen pressure*: 0.5 bar; *spinneret-collector distance*: 3.3 mm; *voltage*: 5.0 kV; *substrate*: glass.

| **Spinneret diameter [mm]** | **Fiber diameter range [µm]** | **CTS [mm min$^{-1}$]** |
|---|---|---|
| 0.3 | 12 – 15 | < 500 |
| 0.45 | 20 – 48 | 860 |

In summary, as compared to copolymers **6b-2** and **6c-2** with hexamethylene bisurea segments, it is notable that no coiling of fibers at collector speeds of 500 mm min$^{-1}$ and higher were monitored in all MEW printing experiments that were conducted with a spinneret-collector distance of 2.2 mm, a nozzle diameter of 0.3 mm, nitrogen pressures down to 0.2 bar and voltages up to 3.6 kV. In contrast, no straight fibers could be printed with a spinneret diameter of 0.3 mm up to a collector speed of 2150 mm min$^{-1}$ by using copolymer **6b-2**. With copolymer **6c-2** MEW processing with a spinneret diameter of 0.3 mm was only feasible with nitrogen pressures above

1 bar and voltages of 2.7 kV or lower. It is assumed that the differences in the CTS result from the significantly higher viscosities of **8a-2** and **8a-3** at optimum processing temperatures as compared to **6b-2** and **6c-2**. The higher viscosities possibly leads to a lower flow rate out of the nozzle, thus decreasing the velocity of the jet out of the nozzle. Consequently, the jet speed is lower as the collector speed and straight fibers are printed onto the surface.

The lower flow rate and the opportunity to use higher voltages, lower flow rates and low spinneret-diameter to allow the processing of straight fibers results in the printing of fiber diameters in the range between 6 and 50 µm for this copolymer class. The thinnest fiber diameter of 6 µm was achieved with copolymer **8a-2** with the following parameters: *Collector velocity:* 2150 mm $min^{-1}$; *extrusion temperature:* 100 °C; *nitrogen pressure*: 0.2 bar; *spinneret diameter*: 0.30 mm; *spinneret-collector distance*: 2.2 mm; *voltage*: 3.3 kV; *substrate*: glass. With **8a-3** the lowest realized fiber diameter was 8 µm with the same parameters. In comparison, with copolymers **6b-2** and **6c-2** the thinnest straight fibers achieved were 38 and 18 µm, respectively. Another possible explanation for the different ranges in the fiber diameter are different interactions of the copolymers with the surface. The realized fiber diameters with **8a-2** and **8a-3** are already close to fiber diameters of around 800 nm obtained with PCL.[161]

### 4.1.3 Preparation of MEW constructs

On the basis of optimum printing parameters and the critical translation speed (CTS) as well as the achieved lowest diameters of single fibers the next target is printing of 3D structures. For this, the four copolymers, namely **6b-2**, **6c-2**, **8a-2** and **8a-3**, were selected. In this context, layer-by-layer stacking and crossing of fibers was studied and optimized with the aim to reproducible print defined constructs that have constant fiber diameters below 50 µm.

The quality of the printed scaffolds was analyzed with scanning electron microscopy (SEM) in a low vacuum mode at 40 Pa. The fiber diameters were determined from the SEM images by using the software *imagej*. Optical light microscopy was used for the determination of the height of the scaffolds.

*Copolymer **6b-2**: 82 wt% PPG-PEG-PPG segments and 18 wt% hexamethylene bisurea segments*

In a first experiment, square type scaffolds with 5 layers in x- and 5 layers in y-direction were printed onto a silicon wafer surface. The best printing results were obtained by using the printing parameters listed in table 4.16.

**Table 4.16:** Overview of printing parameters used for MEW-Printing of scaffolds with copolymer **6b-2**.

| Parameter | Value |
|---|---|
| Extrusion temperature | 75 °C |
| Spinneret diameter | 0.45 mm |
| Nitrogen pressure | 2.0 bar |
| Spinneret-collector distance | 2.2 mm |
| Voltage | 2.7 kV |
| Collector velocity | 1500 mm $min^{-1}$ |

The scaffold printed with the above listed parameters is shown in figure 4.29. No interruption of the polymer jet, including at the crossing points was observed during printing of the construct. Image A shows a section of the scaffold from above which is further magnificated in image B. The scaffold has a uniform structure with straight fibers. An average fiber diameter of 48.5 (± 5.6) µm was determined confirming the high printing quality. In pictures C and D the framework is tilted

sideways with an angle of 20°. These images also show the good stacking accuracy of the different layers. The final scaffold has a defined box-like structure with openings of 500 x 500 µm.

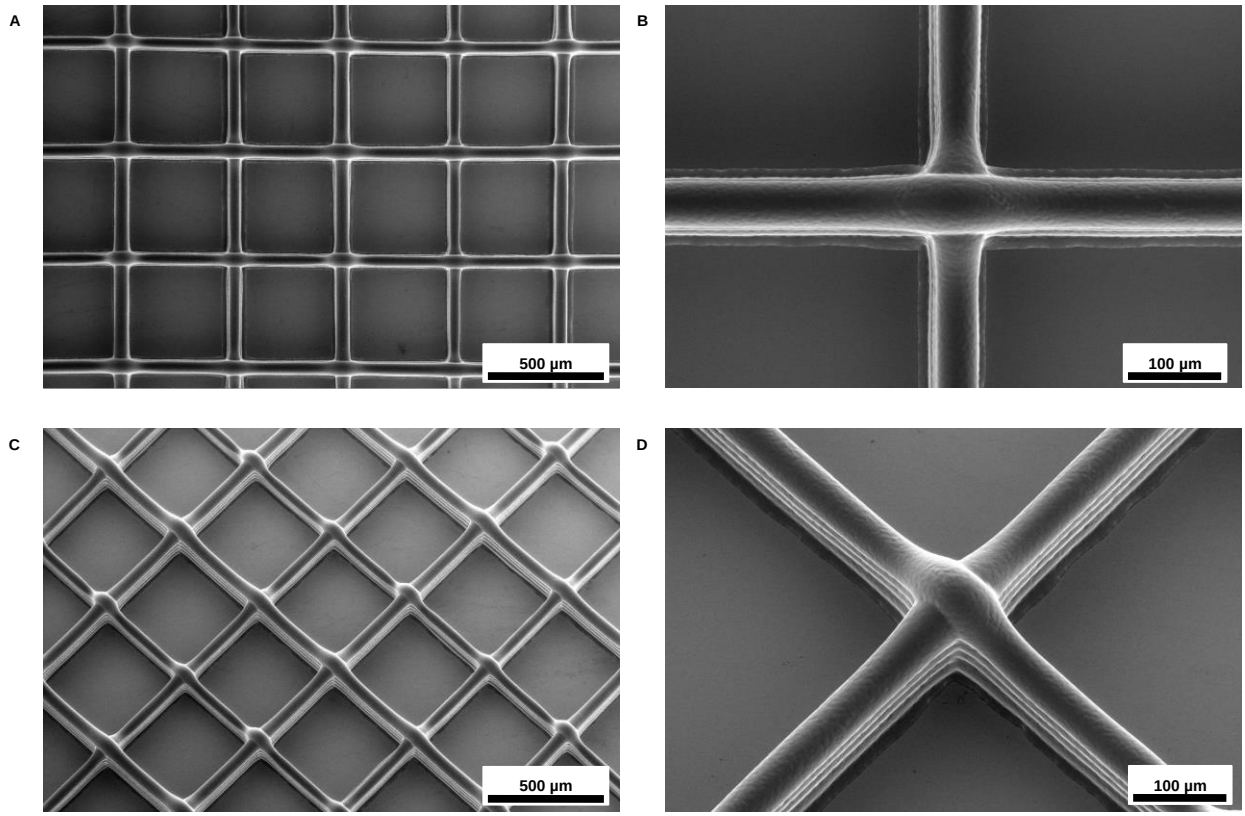


**Figure 4.29:** SEM images of MEW printed scaffolds (5 layers in x and 5 in y-direction) of **6b-2** onto a silicon wafer substrate with A) 50 fold magnification, B) 200 fold magnification, C) 50 fold magnification and tilt of 20°, D) 200 fold magnification and tilt of 20°. Straight fibers with constant diameters and precise stacking accuracy on top of each other with excellent fiber bonding at the crossing points can be observed. The printing parameters are listed in table 4.16.

The optical light microscope image in figure 4.30 shows the scaffold turned by an 90° angle visualizing the stacking in the z-axis. The image shows that fibers of different layers bond to each other. The bonding between the layers is due to the self-healing properties resulting from the hydrogen bonds of the bisurea segments. This image can also be used to determine the scaffold height at crossing points and layers between the crossing points resulting in values of 195 (± 5) µm and 144 (± 4) µm, respectively. The flattening of the single layers is higher at the crossing points where 10 layers are on top of each other.

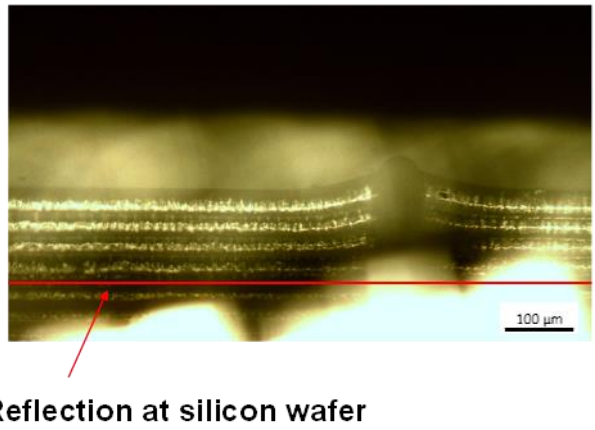


**Figure 4.30:** Optical microscope image of MEW printed scaffolds (5 layers in x and 5 in y-direction) of **6b-2** onto a silicon wafer substrate. The sample was turned by 90° angle to visualize the stacking in the z-axis. The used printing parameters are listed in table 4.16.

To investigate the ability to print higher constructs the scaffold height was increased by printing 10 layers on top of each other in x- and in y-direction (10 x 10 layers) resulting in a total of 20 fibers at the crossing points. The same printing parameters (listed in table 4.16) were applied as for the previous discussed scaffold of 5 x 5 layers. A 10 x 10 layer scaffold of **6b-2** is shown in figure 4.31, whereby 4.31A – C have different magnifications at a tilt of 20°. The fibers are precisely stacked upon each other, and all the ten layers are visible. Figure 4.31C shows a defect where the seventh layer is separated from the layer below, resulting in a gap. The fibers above are mechanically stabilized by strong hydrogen bonding interactions of the copolymer at the crossing points.

The average fiber diameter in the 10 x 10 layer scaffold was determined to be 46.3 (± 4.4) µm which is in the same range as oberved in the 5 x 5 layer construct demonstrating the reproducability. A scaffold height of 317 (± 23) µm between the crossing points was determined. The average scaffold height at the crossing points was found out to be 366 (± 26) µm.

Figure 4.31D shows the edge of the scaffold from above. High accuracy of the fibers upon each other are present. Only the fibers at the loops are not stacked upon each other showing that the lower fibers influence the turning point of the overlying fiber particulary at the high collector speed of 1500 mm $min^{-1}$.

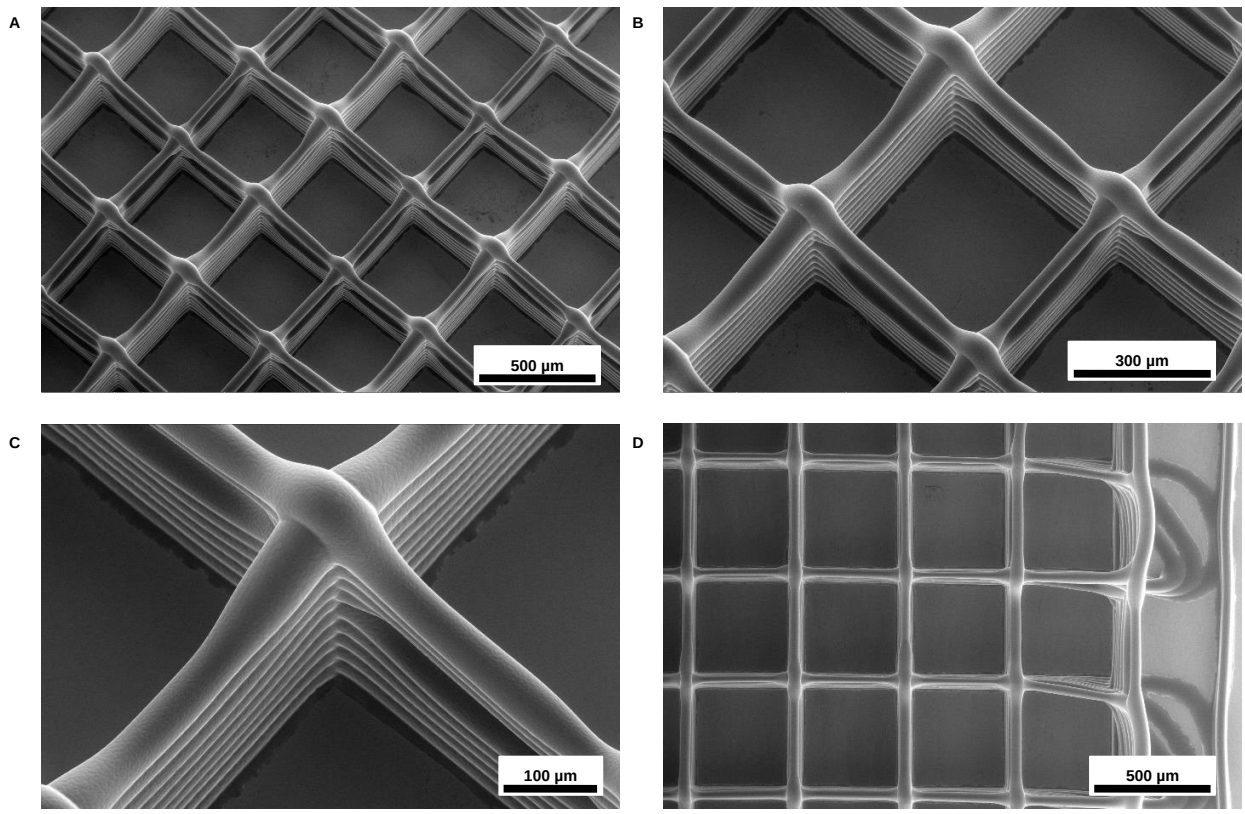


**Figure 4.31:** SEM images of MEW printed scaffolds (10 layers in x and 10 in y-direction) of **6b-2** onto a silicon wafer substrate. A) 50 fold, B) 100 fold, C) 200 fold magnification with a tilt of 20°. The images reveal a precise stacking accuracy and fiber bonding. However, some gaps are visible. D) 50 fold magnification, image shows an edge of the scaffold. The used printing parameters are listed in table 4.16.

*Copolymer **6c-2**: 91 wt% PPG-PEG-PPG segments and 9 wt% hexamethylene bisurea segments*

After optimizing the instrumental parameters for the processing of single fibers the layer-by-layer stacking of MEW processed fibers on top of each other was also studied for copolymer **6c-2**. Here, also square-like constructs with 5 layers in x- and 5 layers in y-direction (5 x 5 scaffold) were manufactured. This results in a total of 10 layers at the crossing points. The used printing parameters for the MEW-printing are listed in table 4.17. Figure 4.32 shows the SEM image (high vacuum mode) of such a MEW-printed scaffold on top of a silicon waver from top view and at a tilt of 20°. The fibers are stacked accurately upon each other and have a smooth surface. The average fiber diameter was determined to be 17.6 (± 1.1) µm. In this example, very uniform fiber diameters far below the targeted limit of 50 µm were achieved with this copolymer. Only four of the five layers are visible by tilting the scaffold about 20° (Figure 4.32B) and two of the five fiber layers are completely merged together. One possible reason for this is the extended MEW-

processing temperature of 100 °C as compared to 75 °C for the previously discussed copolymer **6b-2**. This results in a longer solidification time at the collector and a larger time window for merging of the fibers. The influence of the difference between the processing temperature and the collector temperature was already investigated previously with PVDF.[189]

The final scaffold has a defined box-like structure with openings of 1000 x 1000 µm. The scaffold height was found out to be 27.1 (± 2.7) µm at the fusing points and 16.7 (± 0.9) µm between the fusing points.

**Table 4.17:** Overview of printing parameters used for MEW-printing of scaffolds with copolymer **6c-2**.

| Parameter | Value |
|---|---|
| Extrusion temperature | 100 °C |
| Spinneret diameter | 0.45 mm |
| Nitrogen pressure | 2.0 bar |
| Spinneret-collector distance | 2.2 mm |
| Voltage | 2.7 kV |
| Collector velocity | 1000 mm $min^{-1}$ |

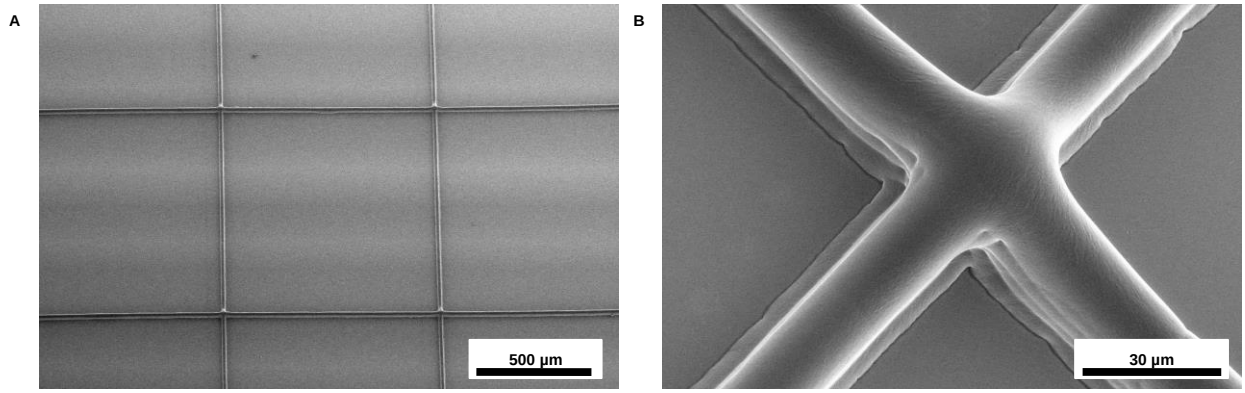


**Figure 4.32:** SEM images of MEW printed scaffold (5 layers in x and 5 layers in y-direction) using **6c-2** onto silicon wafer substrate, A) with 250 fold magnification and B) 50 fold magnification. Images reveal uniform fibers with diameter below 20 µm and highly precise stacking behavior. The fibers are slightly fused together. The printing parameters are listed in table 4.17.

*Copolymers **8a-2** and **8a-3**: 75 wt% PPG-PEG-PPG segments and 25 wt% 4,4-methylene-bis(cyclohexyl) bisurea segments*

After studying the MEW-processing of singe fibers by adjusting the instrumental parameters square-shaped patterns of copolymers **8a-2** and **8a-3** were also printed. First, scaffolds with 5 layers in x- and 5 layers in y-direction were produced with **8a-2** onto a glass substrate resulting in a total of 10 layers at the crossing points. The printing parameters are listed in table 4.18. Figure 4.33 shows the scaffold at two different magnifications from above. The construct has uniform fibers with constant diameters. The average fiber diameter of these layers was determined to be about 21.9 (± 1.5) µm which is below the targeted diameter of maximum 50 µm. Interestingly, the scaffold has a flat height and only one layer in x- and one layer in y-direction can be seen. This demonstrates that the stacked fibers merge together. In contrast, scaffolds printed with **6c-2** at the same temperature of 100 °C have several fiber layers upon each other. The reason for the merging of the fibers printed with **8a-2** can be explained by the viscosity curve shown in figure 4.5 at page 114. The viscosity increases steadily over a wide temperature range upon *cooling*. As a result, the solidification of the polymer occurs more slowly. As revealed by the rheology measurements, **6b-2** and **6c-2** with hexamethylene bisurea segments solidify rapidly which is shown by a sharp increase of the viscosity upon *cooling*. The fusion of the different fiber layers is due to the self-healing behavior by the hyrogen bond formation between the bisurea segments, also across the layers.

**Table 4.18:** Overview of printing parameters used for MEW-Printing of scaffolds with copolymer **8a-2**.

| Parameter | Value |
|---|---|
| Extrusion temperature | 95 °C |
| Spinneret diameter | 0.30 mm |
| Nitrogen pressure | 0.5 bar |
| Spinneret-collector distance | 3.3 mm |
| Voltage | 4.5 kV |
| Collector velocity | 1500 mm $min^{-1}$ |

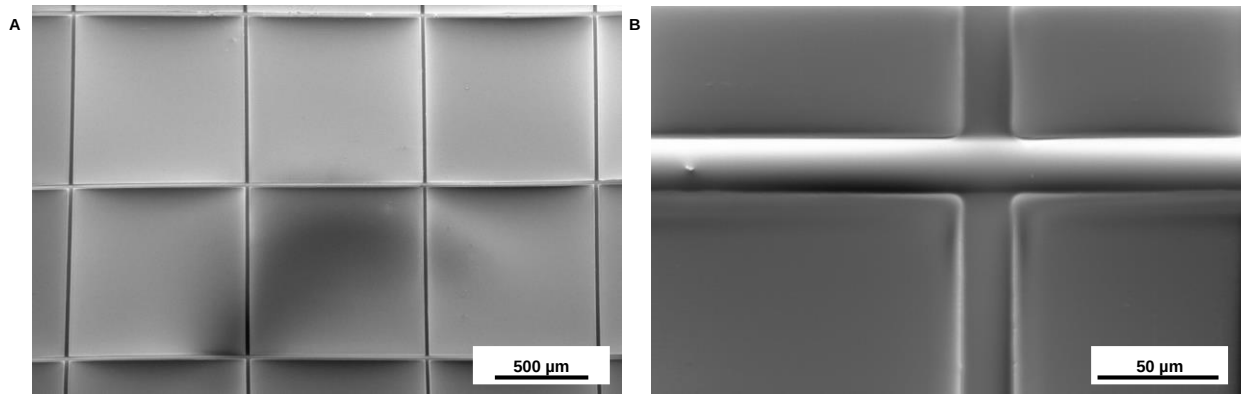


**Figure 4.33:** SEM images of MEW prints onto glass substrate using polymer **8a-2** with 40 fold (A) and 500 fold (B) magnification. 10 layer (5 layers in x- and 5 layers in y-direction) were printed on top of each other. The print has uniform fibers with constant fiber diameters and is flatten by slow solidification and self-healing property of this polymer class. The printing parameters are listed in table 4.18.

In similar manner as before, square-like constructs with 10 layers in x- and 10 layers in y-direction (total of 20 layers) were produced onto glass substrate by using copolymer **8a-3** at 85 °C as shown in figure 4.34C**.**[139] A fiber diameter of about 66 (± 6) µm was determined

Additionally, **8a-3** was melt elctrowritten as a tubular structure by using a cylindrical mandrel (figure 4.34A – B).[139] The manufacture of tubular structures by MEW of PCL was previously reported.[170] The MEW-processing temperature of 85 °C is lower as compared to **8a-2**. Here, the fibers also merge together confirming the self-healing behavior of this polymer class. Defined constructs with uniform fibers and without any defects are obtained. The MEW-processing temperature of 85 °C is lower as compared to **8a-2**. A by 15 °C lower extrusion temperature does not hinder the fusion of the polymer fibers. For the tubular scaffolds a fiber diameter of 140 (± 23) µm was determined. The printing parameters are listed in table 4.19.

**Table 4.19:** Overview of printing parameters used for MEW-Printing of scaffolds with copolymer **8a-3**.

| Parameter | Value for plain print | Value for tubular print |
|---|---|---|
| Extrusion temperature | 85 °C | 85 °C |
| Spinneret diameter | 0.45 mm | 0.41 mm |
| Nitrogen pressure | 1.0 bar | 1.2 bar |
| Spinneret-collector distance | 2.2 mm | 2.55 mm |
| Voltage | 4.0 kV | 3.3 kV |
| Collector velocity | 1000 mm $min^{-1}$ | 307.58 mm $min^{-1}$ |

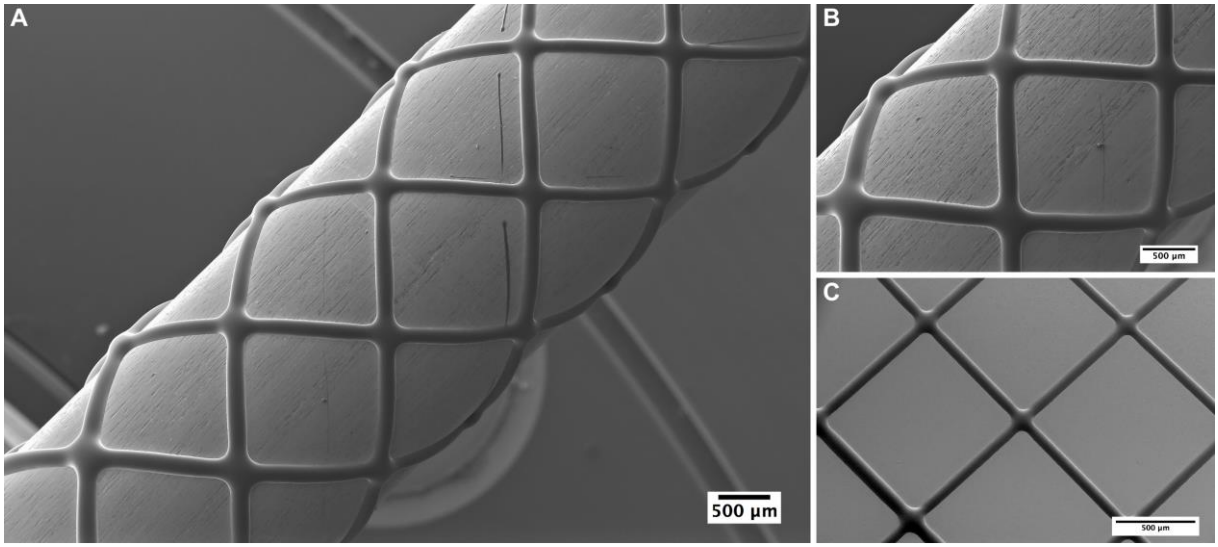


**Figure 4.34:** SEM images of MEW tubes on a (A-B) cylindrical metal mandrel and (C) glass surface using **8a-3**.[139] A, B: 10 layer tubular print. The prints have uniform fibers with constant diameters that are flatten by self-healing property of this polymer class. C: 20 layers (10 layers in x- and 10 layers in y-direction) were printed onto a plain glass slide on top of each other. The printing parameters are listed in table 4.19. Adapted and reproduced with permission (© 2020 The Authors. Macromolecular Chemistry and Physics published by WILEY-VCH GmbH).[139]

In summary, the printing of constructs with copolymers **8a-2** and **8a-3** by MEW onto glass surface was successful and resulted in straight fibers with accurate deposition. The fibers fuse together. Diameters from about 20 – 66 µm were obtained depending on the processing conditions. The strong fusion between the layers can be explained by the slow solidification and the formation of hydrogen bonds between the layers.

### 4.1.4 Swelling of MEW constructs

The swelling behavior of a MEW printed scaffold was investigated on structures printed with copolymer **6b-2** with openings of 500 µm x 500 µm and with 10 layers in x- and 10 in y-direction resulting in overall 20 layers at the crossing points. The used printing parameters are listed in table 4.16 at page 152. The swelling experiments were conducted at 100 % humidity by using environmental scanning electron microscopy (eSEM). Images were first taken at 54 % humidity. Afterwards, the humidity in the chamber was increased to 100 % and then maintained at 100 % humidity for 2 h.

Figure 4.35 reveals that the fiber diameter of the scaffold highly increases within swelling for 2 h. The average fiber diameter was found out to be 46.3 (± 4.4) µm prior and 100.5 (± 23) µm after swelling, respectively. The fiber diameters increased by more than a factor of 2 during the water uptake of the PEG units. The scaffold remained stable after swelling. All fiber layers can still be identified revealing that the construct did not flow away.
After swelling the water content in the eSEM chamber was reduced to 47.5 %. As seen in figure 4.35C the fiber diameter decreased by about 23 % to 87.8 (± 9.5) µm. The swelling of MEW fibers is partly reversible.

Additionally, the fiber height of the scaffold after swelling and drying was determined to be 154 (± 12) µm. Compared with the height of the construct of 317 µm prior to swelling the scaffold reduces its height by more than factor 2 during the swelling and drying process.

Additionally, scaffolds with openings of 200 µm x 200 µm and a total of 8 layers (4 layers in x- and 4 in y-direction) were fabricated by MEW. Fibers are well stacked upon each other as shown in figure 4.36. Swelling of the scaffold results in almost complete filling of the openings by the swollen material. This result shows that fiber distances of at least 200 µm are required to maintain openings within the scaffold after swelling.

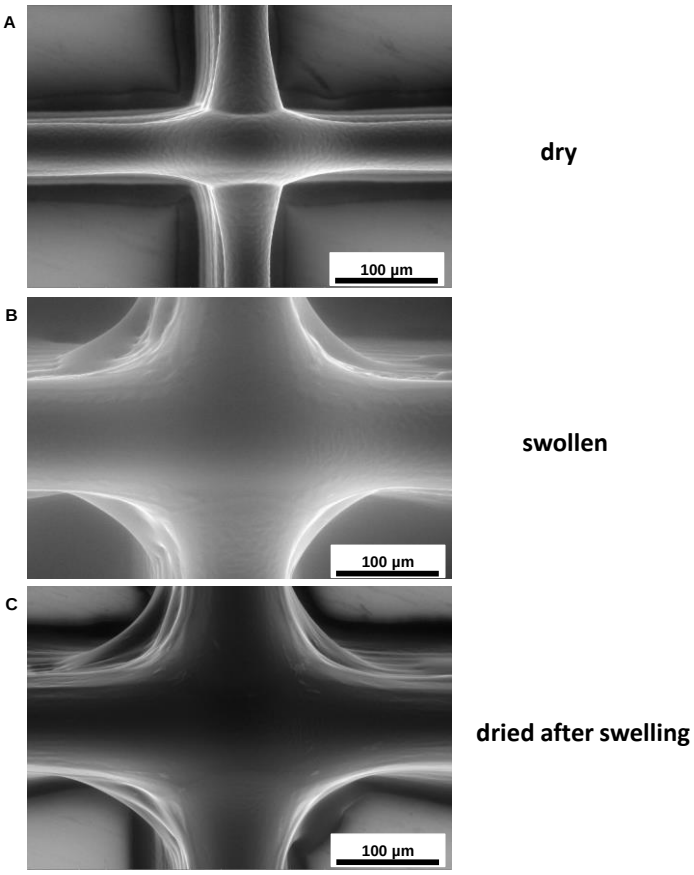


**Figure 4.35:** Environmental scanning electron microscopy (eSEM) images of MEW printed scaffold (10 layers in x and 10 in y-direction) of **6b-2** with 250 fold magnification A) at 54 % humidity, B) after 2 h swelling at 100 % humidity and C) after drying up at a humidity of 47.5 %. Fiber diameter increases by more than a factor of two by taking up water. The scaffold does not fall apart and stacked fibers do not merge together since every single layer is still visible. Printing parameters*: extrusion temperature*: 75 °C; *spinneret diameter*: 0.45 mm; *nitrogen pressure*: 2.0 bar; *spinneret-collector distance*: 2.2 mm*; voltage*: 2.7 kV*; collector velocity*: 1500 mm $min^{-1}$.

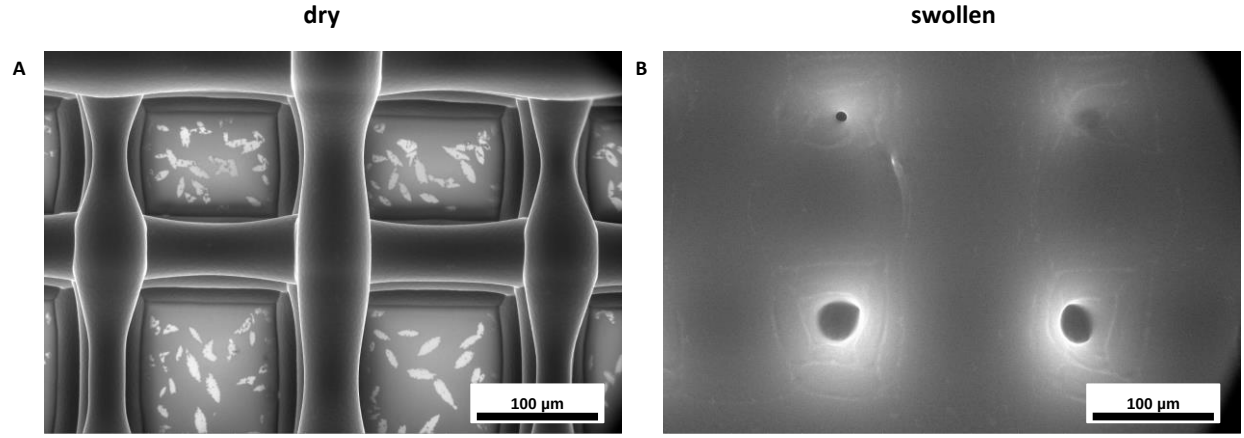


**Figure 4.36**: Environmental scanning electron microscopy (eSEM) images of MEW printed scaffold (4 layers in x and 4 in y-direction) of **6b-2** with 250 fold magnification A) at 54 % humidity and B) after 2 h swelling at 100 % humidity. Distance between two lines is 200 µm. Pores of the scaffold almost disappear by taking up water. Printing parameters: *extrusion temperature*: 75 °C; *spinneret diameter*: 0.45 mm; *nitrogen pressure*: 2.0 bar; *spinneret-collector distance*: 2.2 mm; *voltage*: 2.7 kV; *collector velocity*: 1500 mm $min^{-1}$.

## 4.2 Extrusion-based printing (EBP)

Besides melt electrowriting, preliminary studies for the application of the $(AB)_n$-segmented copolymers in extrusion-based printing (EBP) were conducted.

Extrusion-based printing (EBP) is the extrusion of materials by a pneumatic, piston or a screw driven system. This technique enables the fabrication of continuous fibers from polymer melts, hydrogel systems or bioinks for the creation of three-dimensional constructs. Typically, the fiber size is larger compared to MEW. The diameter of the fibers depends on the nozzle diameter, the applied printing pressure, the melt viscosity of the polymer and the motion speed of print. Finding the right combination of these parameters allows the control of the fiber dimensions and writing of three-dimensional constructs.

The previously discussed thermal properties and results from melt electrowriting (MEW) experiments were used for the selection of $(AB)_n$-segmented copolymers for EBP. It was decided to use the three copolymers **6b**, **6b-1** and **6b-2** with 82 wt% PPG-PEG-PPG segments and 18 wt% hexamethylene bisurea segments which slowly disintegrate in aqueous media and the three copolymers **8a-1**, **8a-2** and **8a-3** with 75 wt% PPG-PEG-PPG segments and 25 wt% 4,4'-methylene-bis(cyclohexyl) bisurea segments which remain stable in aqueous media and form hydrogels.

First, the minimum temperature $T_{EBP,min}$ where a melt flow is possible for at least 1 minute was determined. The limit of the upper temperature of the used 3D printer is 130 °C. This is significantly lower as compared to the upper limit for the used MEW printer which is 210 °C.

The printing parameters for EBP were optimized by varying the extrusion pressure, temperature and motion soeed of print. The nozzle diameter was kept constant at 0.40 mm. Furthermore, the distance between nozzle and substrate was varied. Two-layer grids with openings of 2 mm x 2 mm were printed. In contrast to MEW, in case of EBP the spinneret instead of the collector was moved. The determined best parameters were used for the printing of 3D scaffolds shown in the following in this thesis.

The extrusion based printing experiments were performed on a *cellink+ printer* in cooperation with Simon Gumbel from Macromolecular Chemistry I, University of Bayreuth.

### 4.2.1 Extrusion based printing of copolymers with hexamethylene-bisurea segments

Within this polymer series, the three copolymers **6b**, **6b-1** and **6b-2** with different molecular weights were tested to study the influence of the molecular weight on the processing conditions for extrusion based printing (EBP). The minimum extrusion based printing temperature $T_{EBP,\,min}$ and the temperature maximum $T_{EBP,\,max}$ of the EBP processing window were determined. Within this temperature window processing from the melt using EBP is possible. A correlation of the EBP processing window with the rheology properties is shown in figure 4.37. The underlying oscillation rheology measurements are described in chapter 3.3.1. The complex melt viscosities $\eta^*_{EBP,min}$ at $T_{EBP,min}$ and $\eta^*_{EBP,max}$ at $T_{EBP,max}$ were determined from the oscillation rheology curves of each copolymer and are summarized in table 4.20.

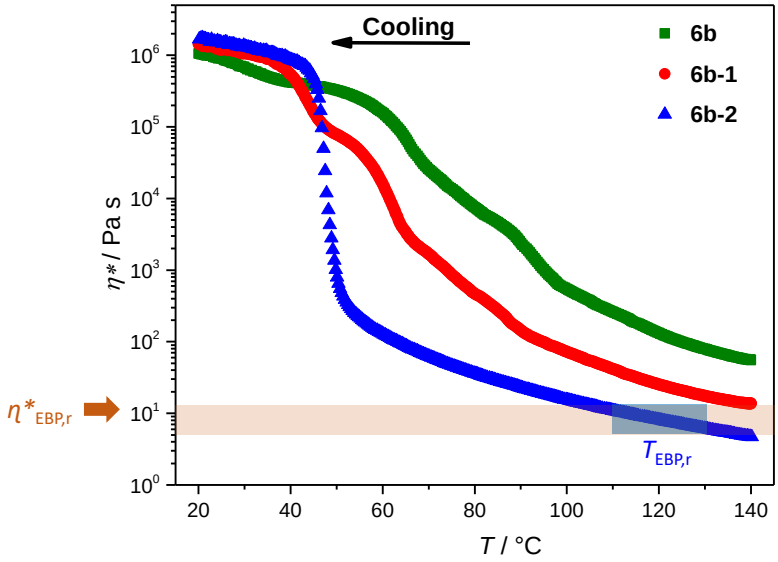


**Figure 4.37:** Melt viscosity of **6b, 6b-1** and **6b-2** with 82 wt% PPG-PEG-PPG segments and hexamethylene bisurea segments upon *cooling* with a rate of 2 K min$^{-1}$. Additionally, the optimum EBP processing temperature window $T_{EBP,r}$ and the correlating optimum range of the complex melt viscosity $\eta^*_{EBP,r}$ are presented.

**6b** and **6b-1** with higher degree of polymerization cannot be melt-processed with the used 3D printer below 130 °C. However, **6b-2** was found out to be melt-processable by EBP at 110 °C.

**Table 4.20:** Overview of $(AB)_n$-segmented copolymers with hydrophilic PPG-PEG-PPG segments and hexamethylene bisurea segments tested for EBP. The degree of polymerization $X_n$ was determined by SEC analysis. The determined minimum EBP-processing temperature $T_{EBP,\,min}$, the highest temperature within the optimum EBP-processing window $T_{EBP,\,max}$ and the corresponding complex melt viscosities $\eta^*_{EBP,min}$ at $T_{EBP,min}$ and $\eta^*_{EBP,max}$ at $T_{EBP,max}$ are listed.

| No. | $X_n$[1] | $T_{EBP,\,min}$ [°C] | $T_{EBP,\,max}$ [°C] | $\eta^*_{EBP,\,min}$ [Pa s] | $\eta^*_{EBP,\,max}$ [Pa s] |
|---|---|---|---|---|---|
| **6b** | -[2] | -[3] | -[3] | -[3] | -[3] |
| **6b-1** | 39 | -[3] | -[3] | -[3] | -[3] |
| **6b-2** | 28 | 110 | 130 | 11 | 6 |

1: SEC analysis was done in THF+TBAB solution with a polystyrene calibration.
2: No SEC analysis was conducted due to the polymer was insoluble in THF-TBAB solution.
3: EBP-processing is not possible up to 130 °C.

The optimum melt viscosity of **6b-2** for EBP is marked in the viscosity curve shown in figure 4.37**.** $\eta^*_{EBP,r}$ describes the melt viscosity range within the optimum temperature window $T_{EBP,\,r}$ and was determined to be located between 6 and 11 Pa s. The printing time within this work is maximum 2 h. Since the melt viscosity was found out to be constant over a period of at least 15 h at 100 °C as shown in figure 4.2 on page 110) it is expected that no thermal degradation of **6b-2** occurs during the melt-processing at 110 °C. In the following, **6b-2** was used for further printing experiments with EBP.

The optimum printing parameters found for **6b-2** are listed in table 4.21. A square scaffold with edge lengths of 10 x 10 mm was printed onto a polystyrene surface as shown in figure 4.38A. 8 layers were printed upon each other resulting in a scaffold height of 1.68 mm. A well-defined scaffold with accurate layer-by layer stacking was obtained. No defects are visible at this magnification.

The stabilization of soft hydrogels by using the produced scaffold in combination with oxidized argarose as hydrogel was investigated.[217] Argarose solutions with different degree of oxidation were filled into the scaffold square and the samples were allowed to gel overnight at 4 °C. A food dye was added for a better visualization. Figure 4.38B shows the swelling and a deformation of the scaffold. A strong swelling was also observed in the MEW scaffolds prepared from **6b-2** by MEW as shown in figures 4.35 and 4.36 on page 161) The strong swelling behavior of **6b-2** results from the hydrophilic PEG units in the copolymer.

The scaffold shows a strong absorption of the color from the food dye. This shows that nutrients can diffuse through the polymer scaffold and an exchange of substances can take place. In combination with the low cytotoxicity of **6b-2** (chapter 3.7) this makes the material promising for biofabrication applications to supply cells with required nutrients.

**Table 4.21:** Overview of printing parameters used for EBP-Printing of scaffolds with copolymer **6b-2**.

| Parameter | Value |
|---|---|
| Extrusion temperature | 120 °C |
| Nozzle diameter | 0.40 mm |
| Nitrogen pressure | 2.5 bar |
| Layer height | 0.1 mm, increase by 0.1 mm for every additional layer |
| Motion speed of print | 150 mm $min^{-1}$ |

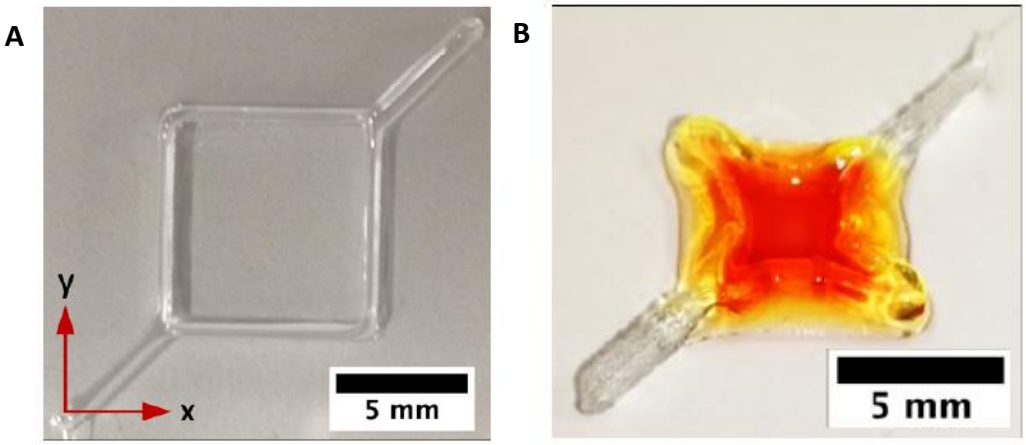


**Figure 4.38:** Photograph of a square grid of copolymer **6b-2** with eight layers produced by Extrusion based Printing onto a polystyrene bowl, **A**: empty and **B:** after filling with hydrogel (argarose with 2 % OA75) and gelation at 4 °C overnight. A food dye was added for visualization. The printing parameters are listed in table 4.21. Adapted and reproduced with permission (© Simon Gumbel).[217]

To sum up, the processability of copolymer **6b-2** by means of melt electrowriting and extrusion-based printing was successfully proven. This allows the manufacturing of filaments in a broad fiber size window ranging from 40 to 450 µm. The constructs of **6b-2** swell in aqueous media to hydrogels. Due to the biocompatibility at concentrations below 10 g $L^{-1}$ and permeability for nutrients this material is a very promising candidate for applications in the field of biofabrication, e.g. for the creation of perfusable channels between bioinks.

### 4.2.2 Extrusion based printing (EBP) of copolymers with 4,4'-methylene-bis(cyclohexyl) bisurea segments

Within this copolymer series, **8a-1**, **8a-2** and **8a-3** were tested with respect to its suitability for extrusion based printing (EBP) and the optimum processing temperature window. The minimum and maximum processing temperature $T_{EBP,min}$ and $T_{EBP,max}$ as well as their corresponding complex melt viscosities $\eta^*_{EBP,min}$ and $\eta^*_{EBP,max}$ are determined from the oscillation rheology curves and are illustrated in figure 4.39.

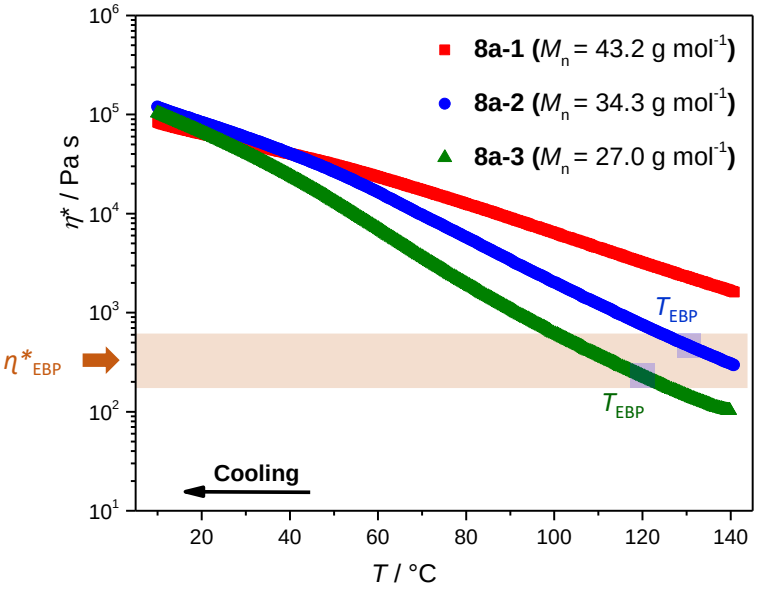


**Figure 4.39:** Complex melt viscosity of **8a-1, 8a-2** and **8a-3** with 75 wt% PPG-PEG-PPG segments and 25 wt% bisurea-4,4'-methylene-bis(cyclohexyl) segments upon *cooling* with a rate of 2 K min$^{-1}$ by conducting oscillation experiment. Additionally, the minimum EBP processing temperature window $T_{EBP,r}$ and the correlating range of complex melt viscosity $\eta^*_{MEW,r}$ are presented for **8a-2** and **8a-3**. Adapted and reproduced with permission (© 2020 The Authors. Macromolecular Chemistry and Physics published by WILEY-VCH GmbH).[139]

Copolymer **8a-1** cannot be processed with EBP. This was expected since $T_{MEW,min}$ is already 150 °C. **8a-2** was tested at 130 °C and 3.5 kPa which are the limits for the used 3D printer. However, poor printing results with undefined fiber diameters were obtained. Only **8a-3** can be constantly processed with EBP within the temperature range between 120 and 130 °C (see table 4.22).

The complex melt viscosity range $\eta^*_{EBP,r}$ of **8a-3** within the temperature window $T_{EBP,r}$ of 130 and 120 °C is in the range from 230 to 140 Pa s. For **8a-2** the melt viscosity at 130 °C is 560 Pa s. Thus, the viscosity of **8a-2** was higher at the tested printing conditions. The increased viscosity of **8a-2** results in a poorer flow behavior of the material and the copolymer is extruded discontinuously.

As a result, only **8a-3** is appropriate for EBP experiments with this printer. Isothermal viscosity measurement of **8a-3** at 120 °C revealed a constant melt viscosity without degradation within a period of 20 h (figure 4.6 on page 115).

**Table 4.22:** Overview of $(AB)_n$-segmented copolymers with hydrophilic PPG-PEG-PPG segments and 4,4'-methylene-bis(cyclohexyl) bisurea segments tested for EBP. The degree of polymerization $X_n$ was determined by SEC analysis. The determined minimum EBP-processing temperature $T_{EBP,\,min}$, the highest temperature within the optimum EBP-processing window $T_{EBP,\,max}$ and the corresponding complex melt viscosities $\eta^*_{EBP,min}$ at $T_{EBP,\,min}$ and $\eta^*_{EBP,max}$ at $T_{EBP,\,max}$ are listed.

| No. | $X_n$[1] | $T_{EBP,\,min}$ [°C] | $T_{EBP,\,max}$ [°C] | $\eta^*_{EBP,\,min}$ [Pa s] | $\eta^*_{EBP,\,max}$ [Pa s] |
|---|---|---|---|---|---|
| **8a-1** | 34 | -[3] | -[3] | -[3] | -[3] |
| **8a-2** | 31 | 130[2] | -[3] | 560[2] | -[3] |
| **8a-3** | 26 | 120 | 130 | 230 | 140 |

1: SEC analysis was done in THF+TBAB solution with a polystyrene calibration.
2: EBP possible at 130 °C, but poor printing result
3: EBP-processing is not possible up to 130 °C.

The printing of scaffolds with EBP was done with copolymer **8a-3**. First, the printing parameters were optimized. The found optimum printing parameters for **8a-3** are listed in table 4.23. The spinneret to collector distance was set to 0.1 mm for the first layer and then increased by 0.1 mm for each additional layer. Different spinneret velocities were tested. The best results were obtained by using 200 mm $min^{-1}$. Higher velocities resulted in undefined scaffolds.

A layer-on-layer stacking of processed fibers was investigated by depositing 10 straight layers on top of each other in a square construct. The size of the square is 1 x 1 cm. A photograph of the construct in Figure 4.40A reveals a well-defined scaffold with accurate layer-by-layer stacking. Additionally, square-patterned prints with varied number of layers were produced. Figure 4.40B shows a construct with 2 layers in x- and 2 layers in y-direction onto a glass surface and figure 4.40C a scaffold with 5 layers in x- and 5 layers in y-direction onto silicon wafer substrate. Both scaffolds are stable and the layers are visible. All three scaffolds were stored at room temperature and were found to be stable. No significant alteration of the scaffolds was observed.

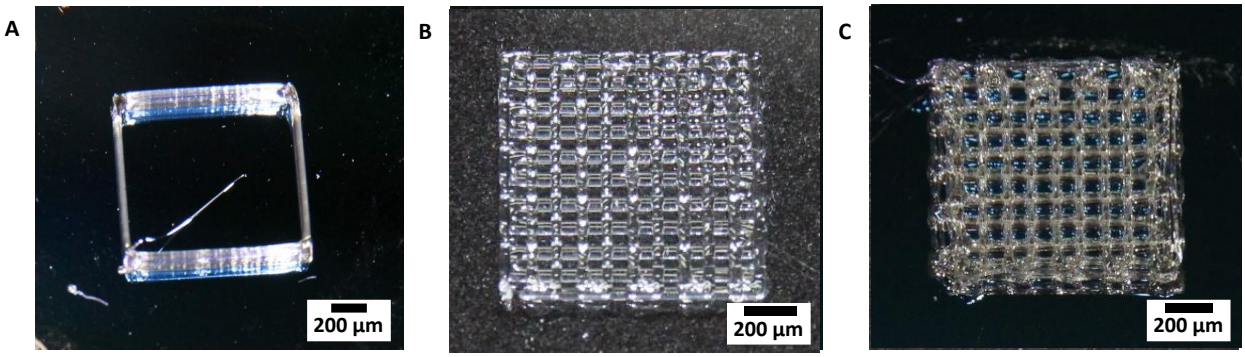


**Figure 4.40:** Photographs of printed scaffolds by EBP using copolymer **8a-3**; **A:** Square construct with 10 layers height on a silicon wafer surface; **B:** Square-shaped patterns with 2 layers in x- and 2 layers in y-direction onto glass surface; **C:** Square-shaped patterns with 5 layers in x-and 5 layers in y-direction onto silicon wafer surface. The printing parameters are listed in table 4.23.

**Table 4.23:** Overview of printing parameters used for EBP-Printing of scaffolds with copolymer **8a-3**.

| Parameter | Value |
|---|---|
| Extrusion temperature | 120 °C |
| Nozzle diameter | 0.40 mm |
| Nitrogen pressure | 2.5 bar |
| Layer height | 0.1 mm, increase by 0.1 mm for every additional layer |
| Motion speed of print | 200 mm $min^{-1}$ |

All three scaffolds were also studied with SEM. An SEM of the one side of the construct with 10 layers upon each other is shown in figure 4.41A.[139] The grid consists of straight and well positioned layers with high accuracy, a smooth surface and no defects. The construct with 2 layers in x- and 2 in y-direction reveals excellent placing of fibers with an average diameter of 260 ± 10 µm (Figure 4.41B). Furthermore, the fibers are fixed at the crossing points and do not sag between them. Figures 4.41C and D show the print with 5 layers in x- and 5 in y-direction and openings of 1 mm x 1 mm resulting in a total of 10 layers at the junction points. The average fiber diameter was determined to be 265 ± 6 µm demonstrating the print quality independent from the number of layers and the used surface. The height of the scaffold at the junction points was determined to be about 1.91 mm. The hydrogen bonds of the bisurea segments result in the bonding at the junction points by self-healing. Consequently, the filaments slightly flatten. Between the junction points a scaffold height is 1.64 (± 0.11) mm. This shows that the filaments

are fixed at the crossing points and do not significantly fall down, but are not in contct between the crossing points. The scaffold was studied again by SEM after storage at ambient conditions for one week. No merging of the fiber layers was monitored.

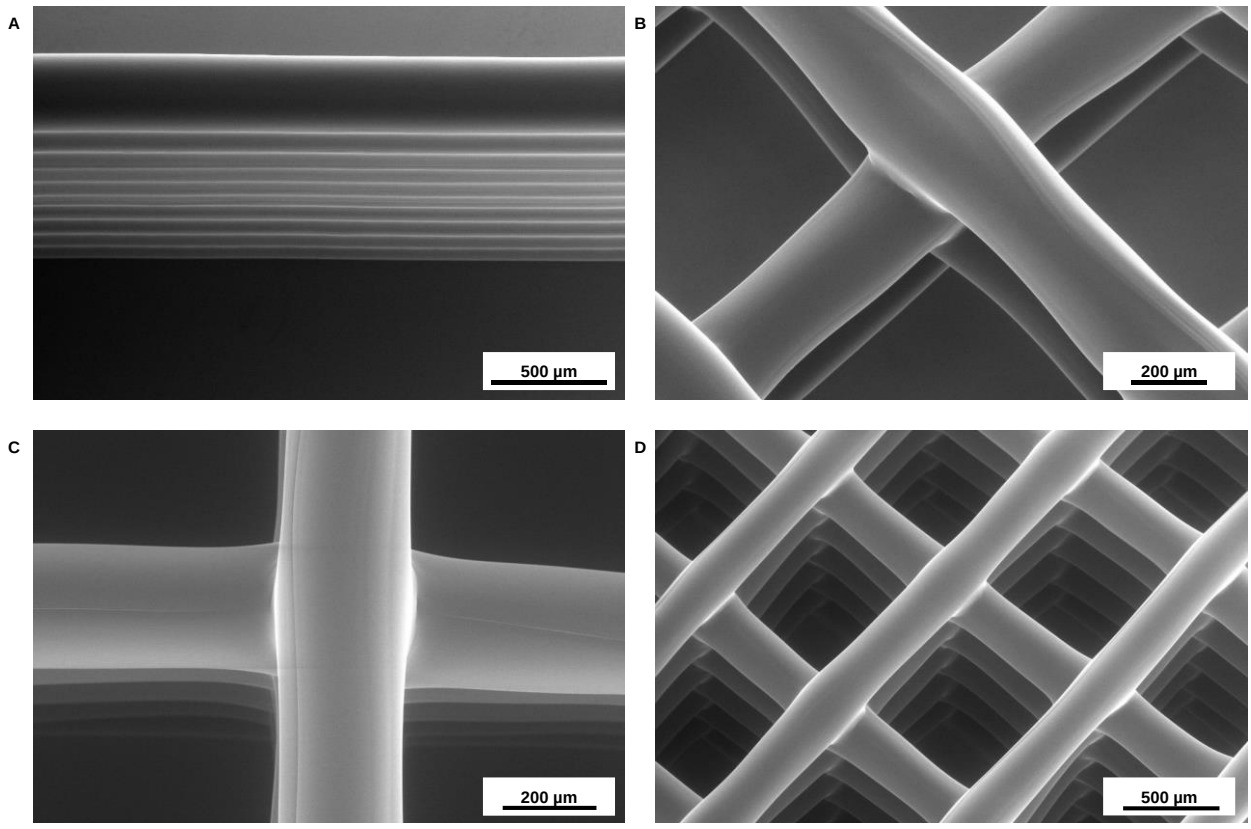


**Figure 4.41:** SEM images of EBP prints with polymer **8a-3. A:** 10 layers printed upon each other presenting the accurate stacking of polymer fibers (50 fold magnification and tilt of 20°). Silicon wafer was used as substrate; **B:** Square-shaped scaffold with 2 layers in x- and 2 layers in y-direction onto glass surface (80 fold magnification and tilt of 20°); **C, D:** Square-shaped scaffold with 5 layers in x- and 5 layers in y-direction onto silicon wafer surface (C: 100 fold magnification; D: 40 fold magnification and tilt of 20°) . All scaffolds demonstrate the high printing accuracy, excellent stacking behavior, constant fiber diameter, smooth surface and fiber bonding at the intersection points (printing parameters: *extrusion temperature*: 120 °C; *pressure*: 250 kPa; *spinneret-collector distance*: 0.1 mm, increase by 0.1 mm for every additional layer; *spinneret velocity*: 200 mm $min^{-1}$). Adapted and reproduced with permission (© 2020 The Authors. Macromolecular Chemistry and Physics published by WILEY-VCH GmbH).[139]

***Swelling in water***

Additionally, the time-dependent swelling behavior of the EBP processed 10-layer print from Figure 4.41C and D was studied by taking photographs of the construct placed in water fully covered. Figure 4.42 reveals that the fibers of the printed copolymer expand by taking up water and, consequently, reducing the opening size.[139] After 80 min the pores are completely closed by the hydrogel while the geometry of the whole print remains stable. The swollen construct was monitored for 2 weeks. The scaffold remained stable in water and did not dissolve. During swelling the filament layers merge together and the height of the scaffold is reduced. Moreover, the swollen scaffold is very soft and cannot be removed from the silicon wafer without causing defects demonstrating the very low module of the hydrogel of **8a-3**. For the hydrogel **8a-2** an elastic module below 100 Pa was determined by rheology measurements.

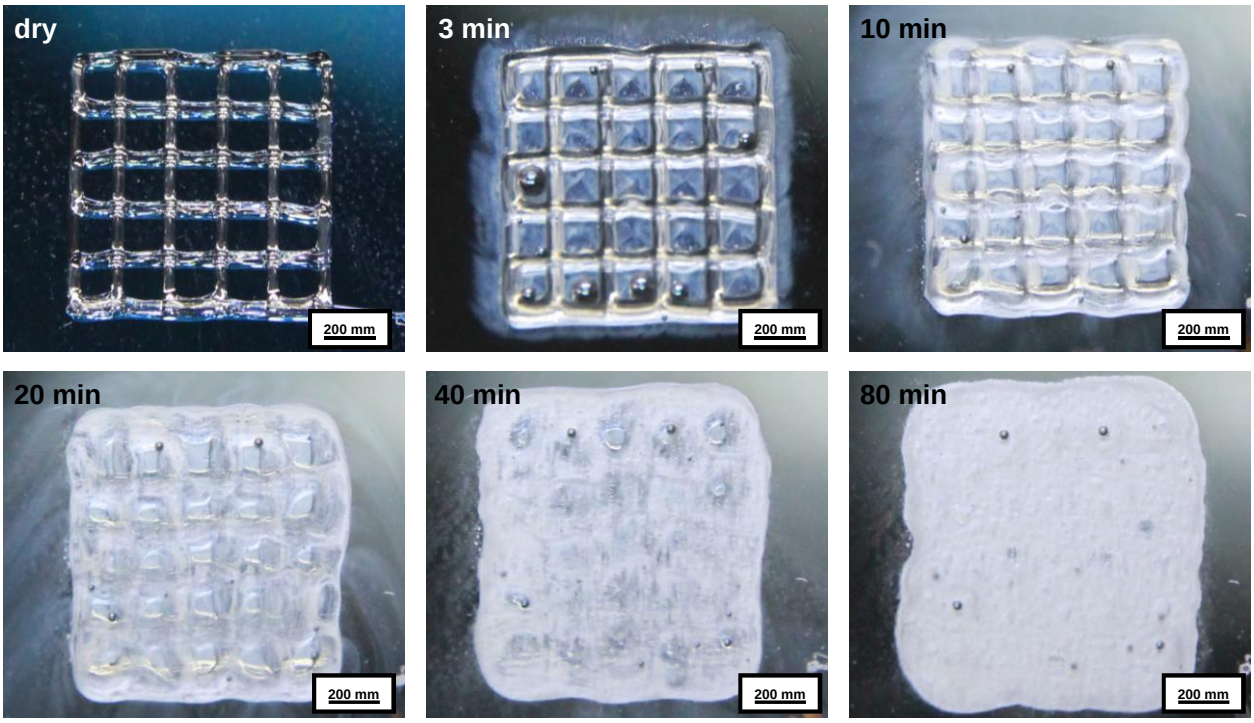


**Figure 4.42:** Photographs presenting the time-phased swelling behavior of the extrusion-based printed scaffold onto silicon wafer surface with 2 layers in x- and 2 layers in y-direction and a mesh wide of 2 mm using copolymer **8a-3**. The copolymer scaffold distinctly spreads by taking up water. As a result, the pores diminish over time and are fully covered by polymer after 80 minutes. Adapted and reproduced with permission (© 2020 The Authors. Macromolecular Chemistry and Physics published by WILEY-VCH GmbH).[139]

To sum up, copolymer **8a-3** with was successfully printed by means of EBP. EBP printing of **8a-3** resulted in fiber diameters of 260 – 265 µm and well-defined constructs with excellent layer by

layer stacking and without the merging of fibers. Besides MEW and EBP, melt electrospinning was conducted with **8a-3** as third processing method. MES fabricates random oriented fibers by applying a voltage which is significantly higher as compared to MEW. For the processing of **8a-3** a voltage of 18.5 kV was applied. Fiber diameters in a range between 0.8 and 15 µm were received.[139] Therefore, the melt processability of **8a-3** with three different methods allows the adjustment of the desired fiber diameter and precision of the printed filaments. This widens the application window in the field of biofabrication. Furthermore, the swelling of the printed scaffolds in aqueous solution without dissolving was proven. The high biocompatibility, the thermal stability at processing temperatures and the ability to be permeable for nutrients makes this material appropriate for biomedical applications.

## 4.3 Conclusion

This chapter deals with the additive manufacturing of selected $(AB)_n$-segmented copolymers. Melt electrowriting (MEW) was used as the focal method in a cooperation with the *Department of Functional materials in medicine and Densistry, University of Würzburg.* The temperature window for MEW was determined for several copolymers that were preselected based on the material properties described in chapter 3. The following copolymers with degree of polymerization $X_n$ and minimum MEW-processing temperatures $T_{MEW,min}$ were found to be most promising:

- **6b-2** with 82 wt% PPG-PEG-PPG segments and 18 wt% hexamethylene-bisurea segments that slowly disintegrates in aqueous solution ($X_n$ = 28; $T_{MEW,min}$ = 75 °C)
- **6c-2** with 91 wt% PPG-PEG-PPG segments and 9 wt% hexamethylene-bisurea segments that disintegrates fast in aqueous solution ($X_n$ = 19; $T_{MEW,min}$ = 90 °C)
- **8a-2** and **8a-3** with 75 wt% PPG-PEG-PPG segments and 25 wt% 4,4'-methylene-bis(cyclo-hexyl) bisurea segments that swell to hydrogels ($X_n$ = 31; $T_{MEW,min}$ = 95 °C and $X_n$ = 26; $T_{MEW,min}$ = 85 °C)

Isothermal rheology measurements of these copolymers at 100 and 120 °C revealed no notable degradation within several hours demonstrating their long-term thermal stability at these temperatures. The MEW printing parameters were optimized by the variation of extrusion temperature, applied voltage, nitrogen pressure, collector speed, spinneret-collector distance, spinneret diameter and printed surface to adjust the jet stability and fiber diameter. With **6b-2** fiber diameters of 45 – 50 µm were realized. The printed scaffolds have straight, uniform fibers, smooth fiber surface and accurate layer by layer stacking. The fiber layers bond to each other due to the hydrogen bonds of the bisurea segments without fusing together. The MEW scaffolds were swollen in 100 % humidity to a twofold fiber diameter by using environmental scanning electron microscopy. No degradation of the wet scaffold was observed. Well-defined scaffolds with accurate layer-by-layer stacking and fiber diameters about 20 µm can be printed by using **6c-2**. The fibers slightly fuse together. MEW-processing of **8a-2** and **8a-3** results in fiber diameters in the range of 5 – 50 µm. Square-line and tubular constructs with uniform line width and fused layers were printed whereby the fusion results from the strong self-healing behavior of these

copolymers. The fusion of the fibers in MEW can possibly be reduced by cooling the collector and more precise optimization of the process parameters, e.g. the voltage.

In addition, preliminary studies with extrusion based printing (EBP) were performed in cooperation with Simon Gumbel from *Macromolecular Chemistry, University of Bayreuth* using a *Cellink+ printer*. The required temperature range for melt-processing with EBP was found to be higher as for MEW. EBP can be conducted well with copolymer **6b-2** having 82 wt% PPG-PEG-PPG segments and 18 wt% hexamethylene-bisurea segments at 110 °C. Additionally, **8a-3** 75 wt% PPG-PEG-PPG segments and 25 wt% 4,4'-methylene-bis(cyclo-hexyl) bisurea segments was successfully EBP-processed at 120 °C. Well-defined scaffolds with high stacking accuracy and well positioned fibers with diameters of 250 – 450 µm were prepared with both copolymers. No merging of the fibers was observed. The addition of a soft hydrogel to a scaffold of **6b-2** results in strong swelling. Nutrients were proven to diffuse through the scaffolds which enables the creation of perfusable channels. A scaffold of **8a-3** was shown to swell in aqueous solution without dissolving.

The hybrid printing of the MEW and EBP processed scaffolds with bioinks is the next step. Moreover, there is room for further tuning of the $(AB)_n$-segmented copolymers, e.g. by combine PPG-PEG-PPG segments of 600 g $mol^{-1}$ and 4,4'-methylene-bis(cyclohexyl) bisurea segments and by adding cell-attaching groups. For instance, amino acid sequences can be incorporated within the segments or in the end groups.

After successful printing of hydrophobic and hydrophilic $(AB)_n$-segmented copolymers by MEW the melt-processing of amphiphilic $(AB)_n$-segmented copolymers with both hydrophobic and hydrophilic segments is from high interest. In a subsequent work, $(ABAC)_n$-segmented copolymers with bisurea segments in combination with hydrophobic poly(dimethyl siloxane) and hydrophilic PPG-PEG-PPG segments were successfully processed by MEW.[218]

All in all, this work shows that the new class of melt-processable hydrophilic $(AB)_n$-segmented copolymers with tunable mechanical properties extends the biofabrication window.

# 5 Experimental

*Materials*

Amino-terminated polypropylene glycol-*block*-polyethylene glycol-*block*-polypropylene glycols (JEFFAMINE® ED-600, batch BCBQ8219, JEFFAMINE® ED-900, batch BCBT5619 and JEFFAMINE® ED-2003, batch BCBQ5628V), hexamethylene diisocyanate, 4,4'-methylene-bis(cyclohexylisocyanate), *n*-butylamine and anhydrous dichloromethane were purchased from Sigma Aldrich. *Trans*-1,4-Cyclohexane diisocyanate was purchased from Alfa Aesar. The Jeffamines were dried under high vacuum at 50 – 65 °C for at least 16 h to remove water prior to use for synthesis. The average molecular weight of the diamines used for the polyaddition reactions within this work was determined by titration of the amino end groups against 0.1 M hydrochloric acid in *iso*-propanol (Merck). Thereby, a Metrohm Titrando 809 electrode was used. *n*-Butylamine was distilled from calcium hydride and stored under an argon atmosphere prior to use. Tetrahydrofuran (THF) was distilled from potassium hydroxide and potassium prior to use. All other chemicals were used as received.

*Synthesis of $(AB)_n$-segmented copolymers with bisurea segments*

Syntheses were carried out on a 50 g-scale at approx. 20 wt% solid content in dry THF or dichloromethane under an argon atmosphere. Jeffamine® **1a, 1b** or **1c** (1.0 eq) was dissolved in either THF or dichloromethane (20 wt%) followed by the addition of *n*-butylamine **5** (0 to 0.2 eq.). Afterwards, either hexamethylene diisocyanate **2**, trans-1,4-cyclohexyl diisocyanate **3** or 4,4'-methylene-bis(cyclohexyl isocyanate) **4** (1.0 eq) was added under vigorous stirring. The reaction mixture was stirred at 30 °C for 4h. After 4 h a small amount of the reaction solution was withdrawn. The solvent was evaporated and the sample was analyzed by FT-IR spectroscopy to confirm the complete conversion of the monomers into the copolymer. Then, the polymer solution was poured into Teflon® moulds (10 x 5 x 1 $cm^3$) and the solvent was removed at room temperature overnight and then at 60 °C under vacuum in the vacuum dring oven. A solution-casted copolymer film is shown in figure 5.1. The copolymers that disintegrate in aqueous solution were purified by dialysis (3.5 kD membrane) in water (Millipore grade) for 6 d by changing the water three times (figure 5.2A). Copolymers were yielded by evaporation of water at ambient conditions for 1 – 3 d and afterwards under vacuum at 60 °C for 1 d. The copolymer sheets forming

a stable hydrogel in aqueous solution were swollen in water (Millipore grade) for 6 d by changing the water 3 times to remove water-soluble impurities (figure 5.2B). The copolymer gels were dried at room temperature for 1 – 3 d and subsequently under vacuum at 60 °C for 1 d.

**Figure 5.1:** Solution-casted polymer film into a Teflon mould after synthesis and evaporation of the solvent.

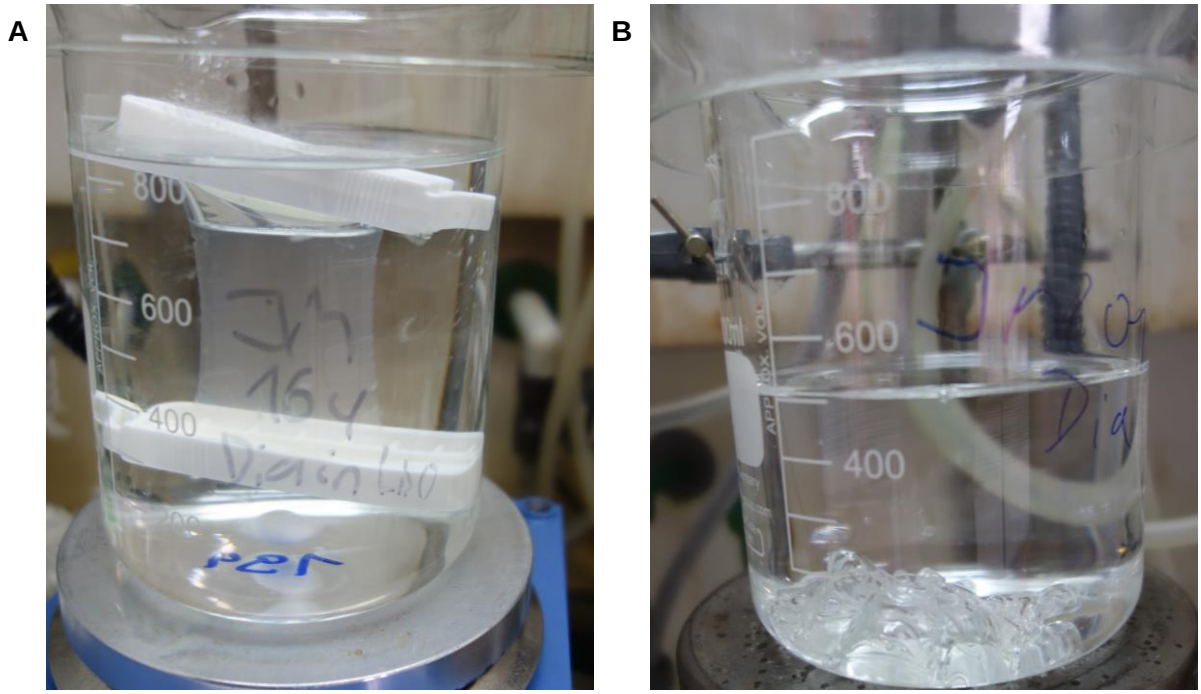


**Figure 5.2. A:** Purification of water-soluble copolymers by dialysis in water (Millipore grade); **B:** purification of copolymers that swell and do not disintegrate in water (Millipore grade).

*Nuclear Magnetic Resonance (NMR)*

NMR measurements were conducted using a Bruker Avance 300 ($^1$H, 300 MHz) spectrometer. The chemical shift $\delta$ is denoted in ppm against tetramethylsilane. Chloroform-$d_1$ was used as solvent. Around 10 mg of sample was dissolved in 0.5 mL chloroform-$d_1$.

*Mass spectrometry*

Jeffamines **1a**, **1b**, **1c** were analysed by *matrix assisted laser desorption ionization* (MALDI) using a Bruker Reflex mass spectrometer in the positive reflectron ion mode by use of a laser with 40 % intensity and a *time of flight* (TOF) analyser. Dithranol was used as matrix material. The matrix to polymer ratio was 100:1.

*Size Exclusion Chromatography (SEC)*

SEC was performed using a Waters 515 HPLC pump and THF with 0.25 wt% tetrabutylammonium bromide (TBAB) as eluent at a flow rate of 0.5 mL min$^{-1}$. A volume of 100 µL of polymer solution (2 mg mL$^{-1}$) was injected with a 707 Waters auto-sampler into a column setup comprising a guard column (Agilent PLgel MIXED-C, 30 x 0.75 cm, particle size 5 µm) and two separation columns (Agilent PLgel MIXED-C, 30 x 0.75 cm, particle size 5 µm). Polymer size distributions with a cut-off of 2000 kg mol$^{-1}$ were monitored with a Waters 414 refractive index detector. Polystyrene standards (PSS, Mainz) were used for calibration and 1,2-dichlorobenzene was employed as internal reference.

SEC of copolymers not soluble in THF-TBAB solution was conducted by using an Agilent 1200 Infinity pump and Dimethyl form amide (DMF) with Lithium bromide (5 g L$^{-1}$) as eluent at a flow rate of 0.5 mL min$^{-1}$. GRAM columns (300 x 8 mm, 10 µm particle size, PSS Mainz) with 100 and 3000 Å pore sizes were used. Polystyrene standards (PSS, Mainz) were used for calibration and toluene (HPLC grade) was employed as internal standard.

*Fourier Transform Infrared Spectroscopy (FT-IR)*

FTIR measurements were conducted using a Perkin Elmer Spectrum 100 FT IT on an ATR crystal. 16 scans in the range between 4000 and 650 cm$^{-1}$ were recorded under ambient atmosphere at a resolution of 4 cm$^{-1}$.

*Film preparation*

Copolymer films of 0.5 – 1 mm thickness were either prepared by casting from solution or by compression moulding. For solution casting the copolymer (20 wt%) was dissolved in methanol. The solution was poured into Teflon® molds (10 x 5 x 1 $cm^3$) and the solvent was removed at room temperature overnight and then at 50 °C under vacuum. The received polymer films were used for tensile test. Compression moulding was conducted in a Carver 25-12-2HC hot press. The films were heated to temperatures between 100 and 110 °C for 5 min and melt pressed between NOWOFLON PFA films by applying a pressure of 6 bar. Then, the films were subsequently transferred into a Hi-Force cold press and pressed at 6 bar upon *cooling* to room temperature. Required geometries were punched out of the polymer films and used for dynamical mechanical thermal analysis, rheology measurements, water absorption experiments, and biocompatibility tests. The experimental setup is shown in figure 5.3.

*Differential Scanning Calorimetry (DSC)*

DSC measurements of the dry copolymers were performed on a Mettler Toledo DS2 device by using a sealed aluminium pan between -80 and 200 °C and under nitrogen atmosphere (50 mL $min^{-1}$). Heating and cooling rates were 10 K/min. First cooling and second heating curves were recorded. DSC measurements of the swollen copolymers were conducted using a high pressure pan between -80 and 100 °C under nitrogen atmosphere.

*Polarization Microscope*

Polarization microscope images were recorded by a NIKON JAPAN DIAPHOT 300 microscope with a DS-Ri2 camera. Heating of the samples was conducted by a METTLER TOLEDO HS82 hot stage and a HS1 hot stage controller using a heating rate of 10 K $min^{-1}$. The second heating cycle was recorded.

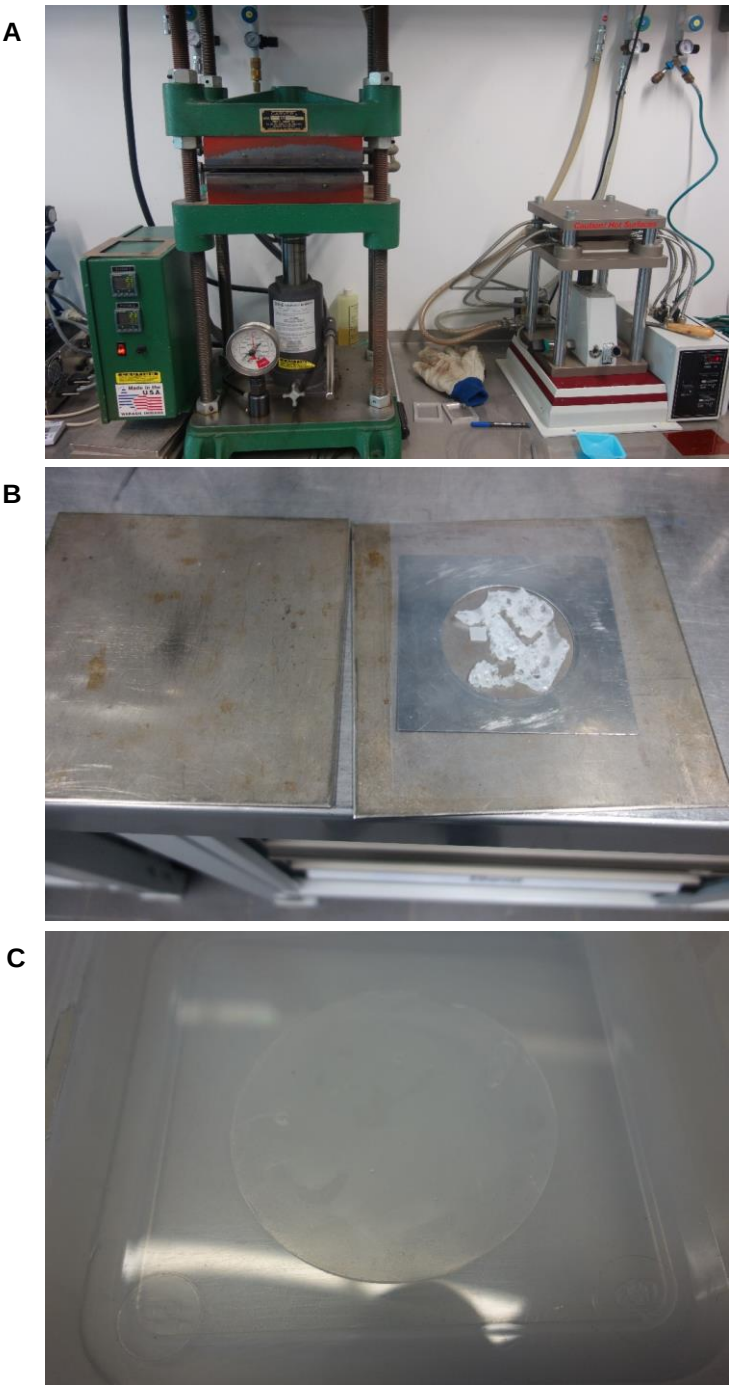


**Figure 5.3. A:** Carver 25-12-2HC hot press (left) and Hi-Force cold press for the preparation of polymer films; **B:** Compression moulding metal form with polymer material prior to melt pressing and NOWPFLON PFA films above and below the polymer; **C:** Obtained melt-pressed film.

*Dynamical Thermal Mechanical Analysis (DMTA)*

Two different DMTA experiments were conducted. *Tension geometry* DMTA measurements were performed on a Rheometric Scientific DMTA IV at a heating rate of 2 K/min and a frequency of 1 Hz (figure 5.4A). Samples with a thickness between 0.5 and 1 mm and a length of around 17 mm were used.

In the *single cantilever* method, a Mettler Toledo device was used and the polymer was clamped into an aluminium pocket (figure 5.4B). Measurements were performed in a temperature range from -80 to 200 °C with heating and cooling rate of 2 K/min and a frequency of 0.5 $s^{-1}$. The first cooling and second heating curves were evaluated.

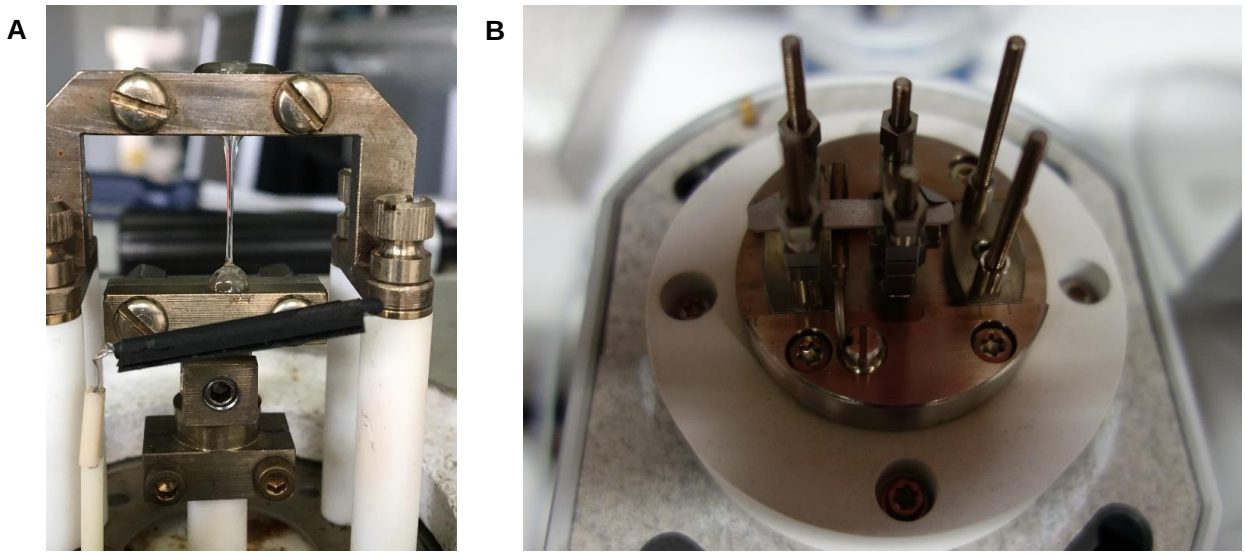


**Figure 5.4. A:** DMTA analysis using the tensile geometry method at the end of the measurement and **B:** the single cantilever method where the polymer is clamped into an aluminium pocket which is bent during the measurement.

*Melt rheology*

Oscillation and rotational rheology of the copolymers were conducted on a Kinexus lab+ rheometer at a heating and cooling rate of 2 K/min and a frequency of 1 Hz. Samples with a thickness around 1 mm were investigated in a plate-plate geometry (25 mm). First cooling and second heating cycle were recorded.

*Hydrogel rheology*

Oscillation rheology measurements for hydrogel were performed by Anton Paar Modular Compact Rheometer (type MCR 302). A Frequency sweep (0.5 to 5 rad $s^{-1}$) with a strain at 0.2 % at 22 °C was conducted in a plate-plate geometry (25 mm).

*Swelling tests*

Copolymer films or scaffolds were placed into a bowl. Then, they were covered with water and regular optical images were recorded to observe the swelling or disintegration behaviour.

Some experiments were conducted by adding 0.1 wt% fluorescence green dye (Kremer Pigmente) to the copolymer prior to film pressing. Thereby, the copolymer and the dye were both dissolved in ethanol and the solvent was evaporated in the fume hood overnight and then at 50 °C in the vacuum drying oven overnight. The dry containing copolymer was then melt-pressed into a film as described above. The obtained film was used for the swelling tests.

*Water uptake*

Copolymers were dried under vacuum at 100 °C prior to water absorption experiments. For the determination of the percentage of water in the hydrogels, the dry copolymer was partitioned into several pieces of comparable size. For copolymers that dissolve in aqueous solution or are mechanical instable, the water uptake of the dry polymer pieces was determined by using a climate chamber with constant temperature and relative humidity.

Additionally, all not water-soluble copolymers pieces were swollen in the equal amount of water for various duration ranging from 6 min to 24 h. After transferring the swollen samples into a humidity balance the hydrogels were dried at 120 °C until constant weight was reached (figure 5.5). The water content of the swollen hydrogel $w$ was then calculated from the mass of the swollen copolymer $m_s$ and the dried polymer $m_d$ by using equation (6.1):

$$w = \frac{m_s - m_d}{m_d} \qquad (6.1)$$

**Figure 5.5.** Humidity balance for measuring the water content of the copolymer or hydrogel.

*Tensile tests*

Tensile tests of $(AB)_n$-segmented polymers at ambient conditions were performed on an INSTRON 5565 universal tester using a 1 kN load cell. Dog-bone shape samples with a thickness of around 1 mm were punched out from a polymer film which was prepared from solution casting. Exact thickness of the samples was determined by a digital micrometer (Mitutoyo 293-831, digimatic MDC Lite). The E-moduli were investigated at a strain rate of 0.5 mm $min^{-1}$ and calculated between 0.1 and 0.3 % strain. Afterwards, a strain rate of 2 – 40 mm $min^{-1}$ was applied depending on the softness of the polymer.

*Biocompatibility/Cytotoxicity*

Cytotoxicity tests were conducted according to ISO 10993-5 applying L 929 CC1 mouse fibroblasts cells. Polymer films were swollen in cell culture media consisting of DMEM GlutaMax, 1% 1M HEPES, 1% Penicillin-Steptomycin and 10% FCS. For copolymers not disintegrating in aqueous solution the hydrogel concentration was 100 g $L^{-1}$. For copolymers that disintegrate in cell culture media different polymer concentrations ranging from 1 to 50 g $L^{-1}$ were prepared. PVC platelets were used for positive control. Pure elution medium served as negative control. Eluates were incubated for 48h at 37°C. Then, suspended sediments were centrifuged, and 100% eluate was prepared using the supernatant. Additionally, for stable hydrogels 50 and 25 % eluates were prepared by dilution with cell culture media. For stable hydrogels WST, Pico Green and Cell Titer Glo Luminescent Cell Viability assays were performed to determine the number of active cells.

For water-soluble polymers the WST assay was performed and the cell number was determined by a Casy Cell Counter.

*Extrusion-based printing (EBP)*

A Cellink+ printer (AB Cellink) as shown in figure 5.6 was used for the fabrication of 3D printed constructs. The device was controlled and programmed by Heartware software (AB Cellink). The printer was equipped with an alumina cartridge and a flat tipped cannula with a diameter of 0.40 mm. Only the cartridge is heated. Hence, the cannula has been shortened to avoid thermal loss and thus a clogging of the nozzle. The cartridge was filled with the $(AB)_n$-segmented copolymer and heated to 120 °C. The printing pressure was generated by an external compressor (Wiltec AF18-2). The pressure was adjusted to 250 kPa. The vertical position (z axis) was calibrated to the height of a silicon wafer slice. The constructs were printed on the surface of the silicon wafer with a motion speed of 200 mm/min.

**Figure 5.6:** Extrusion-based printing device used in this work.

*Melt Electrowriting (MEW)*

A custom-built MEW device as shown in figure 5.7 was used. MEW experiments were performed at 21 ± 3 °C and a relative humidity of 30 ± 5 %. A flat tipped cannula printing nozzle (diameter: 0.30 – 0.70 mm) was positioned above either a glass microscope slide, a silicon wafer slice, an aluminum surface or a cylindrical metal mandrel. The surface was moved under the charged

nozzle using two computer-controlled linear axes (x and y). The collector velocity, flow rate which is adjusted by the nitrogen pressure, temperature, spinneret-collector distance, voltage and collector substrate were varied to investigate the influence on a single fiber diameter. The average fiber diameter and its standard deviation was determined from 16 measured fiber diameters. Box-structure scaffolds were melt electrospun by altering layer deposition in horizontal (x) and vertical (y) direction (20 x 20 $mm^2$) with turning loops. Tubular prints were melt-electrowritten on cylindrical metal mandrels using 45° winding angle. Fibers were electrospun by programming in G-code and controlled by using Mach3 motion control software (Artsoft, USA).

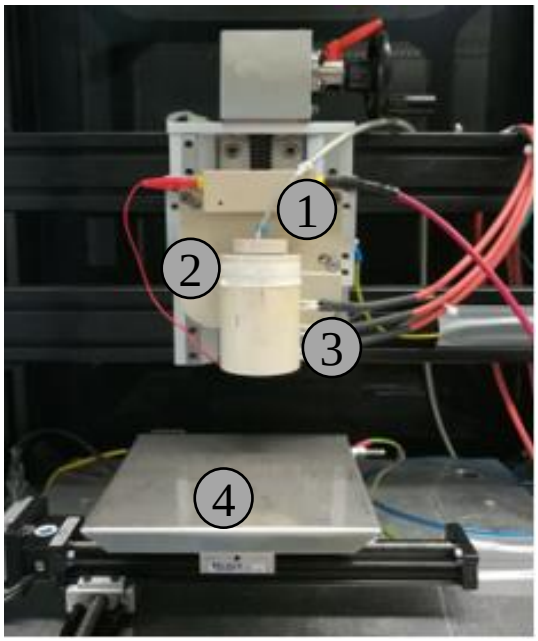


**Figure 5.7:** Melt-Electrowriting device used in this work. 1: Nitrogen gas pressure supply; 2: Electrical heater for syringe with polymer melt; 3: Heated high voltage source; 4: Collector plate.

*Optical Microscopy*

The average fiber diameter and deviation and the average scaffold height of the scaffolds were measured by using an optical microscope (Standard Microscope Olympus BX60) or the stereomicroscope (Discovery V20, Carl Zeiss Microscopy GmbH, Göttingen, Germany) in the reflected light modus and calculated by using the software “imagej”. The experimental setup for the determination of the height of the MEW scaffolds is depicted in figure 5.8.

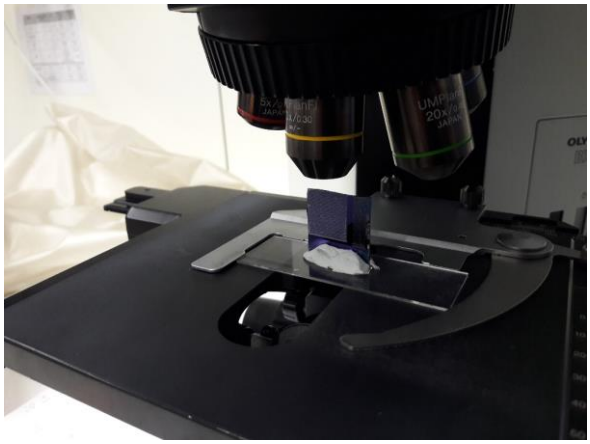

**Figure 5.8:** Experimental setup for the determination of the height of MEW scaffolds

*Environmental scanning electron microscopy*

A Crossbeam 340 scanning electron microscope equipped with GEMINI e-Beam column (Carl Zeiss Microscopy, Göttingen, Germany) was used for measurement of fiber diameter of MES samples and imaging of printed materials. The untreated 3 D printed constructs were placed in the sample chamber of a scanning electron microscope (FEI Quanta FEG 250, ThermoFisher Scientific). The measurements of the scaffolds were conducted in the low vacuum mode by applying a chamber pressure of 40 Pa. Swelling experiments of the scaffolds were performed in the environmental scanning electron microscopy (ESEM) mode. The sample holder was cooled to 2 °C and the chamber was purged twice with water vapour. Subsequently, the chamber was stabilized for 30 minutes at a pressure of 730 Pa, which corresponds to a relative humidity of about 100%. Under these conditions, the swollen state of the scaffold was maintained for 4 h. Scaffolds were dried by changing the pressure to 320 Pa to reduce the relative moisture in the chamber.

# 6 Acknowledgement

At this point, I would like to express my special thanks to my PhD supervisor Prof. Dr. Hans-Werner Schmidt for the opportunity to write my dissertation on a very interesting, interdisciplinary topic in his department, as well as for the great relationship of trust. I especially appreciate the first-class equipment of the workplace and the laboratories, the many profitable discussions and the support in writing the dissertation, which I completed parallel to my full-time job in my free time.

I highly acknowledge Prof. Dr. Paul Dalton and Prof. Dr. Jürgen Groll for the opportunity to conduct experiments in their MEW laboratory at the *Department of Functional Materials in Medicine and Dentistry* in Würzburg as part of a cooperation within the *Transregio SFB Biofabrication*. I would also like to thank Prof. Dr. Paul Dalton for his on-site support and the many beneficial discussions. Additionally, I would like to thank Christoph Böhm for the introduction into the MEW apparatus and Ezgi Bacirzi for the great collaboration in the joint project within the *Transregio SFB Biofabrication*. Further thanks go to Simone Werner for performing the cytotoxicity tests.

Many thanks to Dr. Reiner Giesa for conducting the measurements of *Oscillation shear rheology* and *Dynamic mechanical thermal analysis – tension geometry method* and also for many constructive discussions. I would also like to acknowledge Dr. Christian Neuber, who helped me with scientific questions.

I would like to thank Andreas Frank for the excellent teamwork within the Transregio SFB Biofabrication, for performing several SEM and eSEM measurements and for many fruitful discussions. I would also like to thank Simon Gumbel for carrying out the extrusion based printing experiments together with me.

Further thanks go to Dr. Beate Förster and Martina Heider for taking some SEM images, to Philip Schmode and the MC II department for carrying out the SEC measurements and to Alexander Krimalowski for measuring MALDI-TOF.

Another big thank you goes to my laboratory colleagues Andreas Bernet, Andreas Erhardt, Eva Fürsattel, Tanja Feller, David Heinrich, Patrick Hofmann, Paul Reichstein and Andreas Schedl for the excellent working atmosphere and for the many fruitful discussions.

Several students supported me in the lab by doing their bachelor thesis or their practical training. I am very greatful to all of them. Here, I would like to particularly emphasize Jakob Denk, Matthias Elfinger, Anna Dlugaj and Metecan Erdi who came for an intership with the IAESTE program from USA.

A highly appreciate the great and realiable support of our secretaries Petra Weiß and Christina Wunderlich in organizational matters.

Finally, a big thank you goes to all staff members of the Lehrstuhl MC I for the fantastic working atmosphere with great collegues. I really enjoyed my time there!

I highly acknowledge the University of Bayreuth graduate school for financial support and for very-well organized soft skill seminars and lectures.

I am very grateful for being involved in the organizations *Technik ohne Grenzen e.V.*, *IAESTE* and *JCF Bayreuth* where I met and worked with exciting people of different backgrounds from all over the world. It was an honor to take responsibility as regional group and project leader at *Technik ohne Grenzen e.V.*.

On the personal, I would like to express my special thanks to my family, especially my parents, for their great support in every life situation and being open to my needs.

# 7 References


[1] Derby, B. Printing and prototyping of tissues and scaffolds. *Science (New York, N.Y.)* **2012**, *338*, 921–926. DOI: 10.1126/science.1226340.

[2] Melchels, F. P.; Domingos, M. A.; Klein, T. J.; Malda, J.; Bartolo, P. J.; Hutmacher, D. W. Additive manufacturing of tissues and organs. Progress in Polymer Science, 37(8), 1079-1104. *Progress in Polymer Science* **2012**, *37*, 1079–1104. DOI: 10.1016/J.PROGPOLYMSCI.2011.11.007.

[3] Murphy, S. V.; Atala, A. 3D bioprinting of tissues and organs. *Nature biotechnology* **2014**, *32*, 773–785. DOI: 10.1038/nbt.2958.

[4] Groll, J.; Boland, T.; Blunk, T.; Burdick, J. A.; Cho, D.-W.; Dalton, P. D.; Derby, B.; Forgacs, G.; Li, Q.; Mironov, V. A.*; et al.* Biofabrication: reappraising the definition of an evolving field. *Biofabrication* **2016**, *8*, 13001. DOI: 10.1088/1758-5090/8/1/013001.

[5] Groll, J.; Burdick, J. A.; Cho, D.-W.; Derby, B.; Gelinsky, M.; Heilshorn, S. C.; Jüngst, T.; Malda, J.; Mironov, V. A.; Nakayama, K.*; et al.* A definition of bioinks and their distinction from biomaterial inks. *Biofabrication* **2018**, *11*, 13001. DOI: 10.1088/1758-5090/aaec52.

[6] Langer, R.; Vacati, J. P. Tissue Engineering. *Science* **1993**, *260*, 920–926.

[7] Fedorovich, N. E.; Alblas, J.; Wijn, J. R. de; Hennink, W. E.; Verbout, A. J.; Dhert, W. J. A. Hydrogels as extracellular matrices for skeletal tissue engineering: state-of-the-art and novel application in organ printing. *Tissue engineering* **2007**, *13*, 1905–1925. DOI: 10.1089/ten.2006.0175.

[8] Miller, J. S.; Stevens, K. R.; Yang, M. T.; Baker, B. M.; Nguyen, D.-H. T.; Cohen, D. M.; Toro, E.; Chen, A. A.; Galie, P. A.; Yu, X.*; et al.* Rapid casting of patterned vascular networks for perfusable engineered three-dimensional tissues. *Nature materials* **2012**, *11*, 768–774. DOI: 10.1038/nmat3357.

[9] Shim, J.-H.; Kim, J. Y.; Park, M.; Park, J.; Cho, D.-W. Development of a hybrid scaffold with synthetic biomaterials and hydrogel using solid freeform fabrication technology. *Biofabrication* **2011**, *3*, 34102. DOI: 10.1088/1758-5082/3/3/034102.

[10] Malda, J.; Visser, J.; Melchels, F. P.; Jüngst, T.; Hennink, W. E.; Dhert, W. J. A.; Groll, J.; Hutmacher, D. W. 25th anniversary article: Engineering hydrogels for biofabrication. *Advanced materials (Deerfield Beach, Fla.)* **2013**, *25*, 5011–5028. DOI: 10.1002/adma.201302042.

[11] WICHTERLE, O.; LÍM, D. Hydrophilic Gels for Biological Use. *Nature* **1960**, *185*, 117–118. DOI: 10.1038/185117a0.

[12] Hennink, W. E.; van Nostrum, C. F. Novel crosslinking methods to design hydrogels. *Advanced Drug Delivery Reviews* **2002**, 13–36.

[13] Haider, M. S.; Ahmad, T.; Yang, M.; Hu, C.; Hahn, L.; Stahlhut, P.; Groll, J.; Luxenhofer, R. Tuning the Thermogelation and Rheology of Poly(2-Oxazoline)/Poly(2-Oxazine)s Based Thermosensitive Hydrogels for 3D Bioprinting. *Gels (Basel, Switzerland)* **2021**, *7.* DOI: 10.3390/gels7030078.

[14] Hu, W.; Wang, Z.; Xiao, Y.; Zhang, S.; Wang, J. Advances in crosslinking strategies of biomedical hydrogels. *Biomaterials science* **2019**, *7*, 843–855. DOI: 10.1039/c8bm01246f.

[15] Paidikondala, M.; Wang, S.; Hilborn, J.; Larsson, S.; Varghese, O. P. Impact of Hydrogel Cross-Linking Chemistry on the in Vitro and in Vivo Bioactivity of Recombinant Human Bone Morphogenetic Protein-2. *ACS applied bio materials* **2019**, *2*, 2006–2012. DOI: 10.1021/acsabm.9b00060.

[16] Abasalizadeh, F.; Moghaddam, S. V.; Alizadeh, E.; Akbari, E.; Kashani, E.; Fazljou, S. M. B.; Torbati, M.; Akbarzadeh, A. Alginate-based hydrogels as drug delivery vehicles in cancer treatment and their applications in wound dressing and 3D bioprinting. *Journal of biological engineering* **2020**, *14*, 8. DOI: 10.1186/s13036-020-0227-7.

[17] Anthamatten, M. Hydrogen Bonding in Supramolecular Polymer Networks: Glasses, Melts, and Elastomers. In *Supramolecular Polymer Networks and Gels*; Seiffert, S., Ed.; Springer International Publishing: Cham, 2015; pp 47–99.

[18] Dong, R.; Pang, Y.; Su, Y.; Zhu, X. Supramolecular hydrogels: synthesis, properties and their biomedical applications. *Biomaterials science* **2015**, *3*, 937–954. DOI: 10.1039/c4bm00448e.

[19] Du, X.; Zhou, J.; Shi, J.; Xu, B. Supramolecular Hydrogelators and Hydrogels: From Soft Matter to Molecular Biomaterials. *Chemical reviews* **2015**, *115*, 13165–13307. DOI: 10.1021/acs.chemrev.5b00299.

[20] Li, Y.; Rodrigues, J.; Tomás, H. Injectable and biodegradable hydrogels: gelation, biodegradation and biomedical applications. *Chemical Society reviews* **2012**, *41*, 2193–2221. DOI: 10.1039/c1cs15203c.

[21] Guvendiren, M.; Lu, H. D.; Burdick, J. A. Shear-thinning hydrogels for biomedical applications. *Soft matter* **2012**, *8*, 260–272. DOI: 10.1039/C1SM06513K.

[22] Uman, S.; Dhand, A.; Burdick, J. A. Recent advances in shear-thinning and self-healing hydrogels for biomedical applications. *J Appl Polym Sci* **2020**, *137*, 48668. DOI: 10.1002/app.48668.

[23] Asadi, N.; Del Bakhshayesh, A. R.; Davaran, S.; Akbarzadeh, A. Common biocompatible polymeric materials for tissue engineering and regenerative medicine. *Materials Chemistry and Physics* **2020**, *242*, 122528. DOI: 10.1016/j.matchemphys.2019.122528.

[24] Mora-Boza, A.; Puertas-Bartolomé, M.; Vázquez-Lasa, B.; San Román, J.; Pérez-Caballer, A.; Olmeda-Lozano, M. Contribution of bioactive hyaluronic acid and gelatin to regenerative medicine. Methodologies of gels preparation and advanced applications. *European Polymer Journal* **2017**, *95*, 11–26. DOI: 10.1016/j.eurpolymj.2017.07.039.

[25] Nolan, K.; Millet, Y.; Ricordi, C.; Stabler, C. L. Tissue engineering and biomaterials in regenerative medicine. *Cell transplantation* **2008**, *17*, 241–243. DOI: 10.3727/096368908784153931.

[26] Puertas-Bartolomé, M.; Mora-Boza, A.; García-Fernández, L. Emerging Biofabrication Techniques: A Review on Natural Polymers for Biomedical Applications. *Polymers* **2021**, *13.* DOI: 10.3390/polym13081209.

[27] Tutar, R.; Motealleh, A.; Khademhosseini, A.; Kehr, N. S. Functional Nanomaterials on 2D Surfaces and in 3D Nanocomposite Hydrogels for Biomedical Applications. *Adv Funct Materials* **2019**, *29*, 1904344. DOI: 10.1002/adfm.201904344.

[28] Abka-khajouei, R.; Tounsi, L.; Shahabi, N.; Patel, A. K.; Abdelkafi, S.; Michaud, P. Structures, Properties and Applications of Alginates. *Marine Drugs* **2022**, *20*, 364. DOI: 10.3390/md20060364.

[29] Murab, S.; Gupta, A.; Włodarczyk-Biegun, M. K.; Kumar, A.; van Rijn, P.; Whitlock, P.; Han, S. S.; Agrawal, G. Alginate based hydrogel inks for 3D bioprinting of engineered orthopedic tissues. *Carbohydrate Polymers* **2022**, *296*, 119964. DOI: 10.1016/j.carbpol.2022.119964.

[30] Varaprasad, K.; Karthikeyan, C.; Yallapu, M. M.; Sadiku, R. The significance of biomacromolecule alginate for the 3D printing of hydrogels for biomedical applications. *International Journal of Biological Macromolecules* **2022**, *212*, 561–578. DOI: 10.1016/j.ijbiomac.2022.05.157.

[31] Di Mola, A.; Landi, M. R.; Massa, A.; D'Amora, U.; Guarino, V. Hyaluronic Acid in Biomedical Fields: New Trends from Chemistry to Biomaterial Applications. *International journal of molecular sciences* **2022**, *23*, 14372. DOI: 10.3390/ijms232214372.

[32] Petta, D.; D'Amora, U.; Ambrosio, L.; Grijpma, D. W.; Eglin, D.; D'Este, M. Hyaluronic acid as a bioink for extrusion-based 3D printing. *Biofabrication* **2020**, *12*, 32001. DOI: 10.1088/1758-5090/ab8752.

[33] Taghizadeh, M.; Taghizadeh, A.; Yazdi, M. K.; Zarrintaj, P.; Stadler, F. J.; Ramsey, J. D.; Habibzadeh, S.; Hosseini Rad, S.; Naderi, G.; Saeb, M. R.*; et al.* Chitosan-based inks for 3D printing and bioprinting. *Green Chem.* **2022**, *24*, 62–101. DOI: 10.1039/D1GC01799C.

[34] Redmond, J.; McCarthy, H.; Buchanan, P.; Levingstone, T. J.; Dunne, N. J. Advances in biofabrication techniques for collagen-based 3D in vitro culture models for breast cancer research. *Materials science & engineering. C, Materials for biological applications* **2021**, *122*, 111944. DOI: 10.1016/j.msec.2021.111944.

[35] Bosch-Rué, È.; Díez-Tercero, L.; Delgado, L. M.; Pérez, R. A. Biofabrication of Collagen Tissue-Engineered Blood Vessels with Direct Co-Axial Extrusion. *International journal of molecular sciences* **2022**, *23.* DOI: 10.3390/ijms23105618.

[36] Gupta, S.; Alrabaiah, H.; Christophe, M.; Rahimi-Gorji, M.; Nadeem, S.; Bit, A. Evaluation of silk-based bioink during pre and post 3D bioprinting: A review. *Journal of Biomedical Materials Research Part B: Applied Biomaterials* **2021**, *109*, 279–293. DOI: 10.1002/jbm.b.34699.

[37] DeSimone, E.; Schacht, K.; Jungst, T.; Groll, J.; Scheibel, T. Biofabrication of 3D constructs: fabrication technologies and spider silk proteins as bioinks. *Pure and Applied Chemistry* **2015**, *87*, 737–749. DOI: 10.1515/pac-2015-0106.

[38] Schacht, K.; Jüngst, T.; Schweinlin, M.; Ewald, A.; Groll, J.; Scheibel, T. Biofabrication of cell-loaded 3D spider silk constructs. *Angewandte Chemie (International ed. in English)* **2015**, *54*, 2816–2820. DOI: 10.1002/anie.201409846.

[39] Bayram, C.; Jiang, X.; Gultekinoglu, M.; Ozturk, S.; Ulubayram, K.; Edirisinghe, M. Biofabrication of Gelatin Tissue Scaffolds with Uniform Pore Size via Microbubble Assembly. *Macro Materials & Eng* **2019**, *304*, 1900394. DOI: 10.1002/mame.201900394.

[40] Klotz, B. J.; Gawlitta, D.; Rosenberg, A. J. W. P.; Malda, J.; Melchels, F. P. W. Gelatin-Methacryloyl Hydrogels: Towards Biofabrication-Based Tissue Repair. *Trends in Biotechnology* **2016**, *34*, 394–407. DOI: 10.1016/j.tibtech.2016.01.002.

[41] Annamalai, R. T.; Naik, T.; Prout, H.; Putnam, A. J.; Stegemann, J. P. Biofabrication of injectable fibrin microtissues for minimally-invasive therapies: application of surfactants. *Biomedical Materials* **2018**, *13*, 45005. DOI: 10.1088/1748-605X/aab66f.

[42] Melo, B. A. G. de; Jodat, Y. A.; Cruz, E. M.; Benincasa, J. C.; Shin, S. R.; Porcionatto, M. A. Strategies to use fibrinogen as bioink for 3D bioprinting fibrin-based soft and hard tissues. *Acta biomaterialia* **2020**, *117*, 60–76. DOI: 10.1016/j.actbio.2020.09.024.

[43] Griffanti, G.; Fairag, R.; Rosenzweig, D. H.; Haglund, L.; Nazhat, S. N. Automated biofabrication of anisotropic dense fibrin gels accelerate osteoblastic differentiation of seeded mesenchymal stem cells. *Journal of Materials Research* **2021**, *36*, 4867–4882. DOI: 10.1557/s43578-021-00433-w.

[44] Sämfors, S.; Karlsson, K.; Sundberg, J.; Markstedt, K.; Gatenholm, P. Biofabrication of bacterial nanocellulose scaffolds with complex vascular structure. *Biofabrication* **2019**, *11*, 45010. DOI: 10.1088/1758-5090/ab2b4f.

[45] Wan, Y.; Wang, J.; Gama, M.; Guo, R.; Zhang, Q.; Zhang, P.; Yao, F.; Luo, H. Biofabrication of a novel bacteria/bacterial cellulose composite for improved adsorption capacity. *Composites Part A: Applied Science and Manufacturing* **2019**, *125*, 105560. DOI: 10.1016/j.compositesa.2019.105560.

[46] Yu, C.; Schimelman, J.; Wang, P.; Miller, K. L.; Ma, X.; You, S.; Guan, J.; Sun, B.; Zhu, W.; Chen, S. Photopolymerizable Biomaterials and Light-Based 3D Printing Strategies for Biomedical Applications. *Chemical reviews* **2020**, *120*, 10695–10743. DOI: 10.1021/acs.chemrev.9b00810.

[47] Ma, T.; Gao, X.; Dong, H.; He, H.; Cao, X. High-throughput generation of hyaluronic acid microgels via microfluidics-assisted enzymatic crosslinking and/or Diels–Alder click chemistry for cell encapsulation and delivery. *Applied Materials Today* **2017**, *9*, 49–59. DOI: 10.1016/j.apmt.2017.01.007.

[48] Utech, S.; Prodanovic, R.; Mao, A. S.; Ostafe, R.; Mooney, D. J.; Weitz, D. A. Microfluidic Generation of Monodisperse, Structurally Homogeneous Alginate Microgels for Cell Encapsulation and 3D Cell Culture. *Advanced healthcare materials* **2015**, *4*, 1628–1633. DOI: 10.1002/adhm.201500021.

[49] Nowicki, M.; Zhu, W.; Sarkar, K.; Rao, R.; Zhang, L. G. 3D printing multiphasic osteochondral tissue constructs with nano to micro features via PCL based bioink. *Bioprinting* **2020**, *17*, e00066. DOI: 10.1016/j.bprint.2019.e00066.

[50] Izgordu, M. S.; Uzgur, E. I.; Ulag, S.; Sahin, A.; Karademir Yilmaz, B.; Kilic, B.; Ekren, N.; Oktar, F. N.; Gunduz, O. Investigation of 3D-Printed Polycaprolactone-/Polyvinylpyrrolidone-Based Constructs. *Cartilage* **2021**, *13*, 626S-635S. DOI: 10.1177/1947603519897302.

[51] Wang, Y.; Lei, M.; Wei, Q.; Wang, Y.; Zhang, J.; Guo, Y.; Saroia, J. 3D printing biocompatible l-Arg/GNPs/PLA nanocomposites with enhanced mechanical property and thermal stability. *J Mater Sci* **2020**, *55*, 5064–5078. DOI: 10.1007/s10853-020-04353-8.

[52] Tan, Y. J.; Tan, X.; Yeong, W. Y.; Tor, S. B. Hybrid microscaffold-based 3D bioprinting of multi-cellular constructs with high compressive strength: A new biofabrication strategy. *Sci Rep* **2016**, *6*, 39140. DOI: 10.1038/srep39140.

[53] Xin, S.; Chimene, D.; Garza, J. E.; Gaharwar, A. K.; Alge, D. L. Clickable PEG hydrogel microspheres as building blocks for 3D bioprinting. *Biomater. Sci.* **2019**, *7*, 1179–1187. DOI: 10.1039/C8BM01286E.

[54] Rutz, A. L.; Gargus, E. S.; Hyland, K. E.; Lewis, P. L.; Setty, A.; Burghardt, W. R.; Shah, R. N. Employing PEG crosslinkers to optimize cell viability in gel phase bioinks and tailor post printing mechanical properties. *Acta biomaterialia* **2019**, *99*, 121–132. DOI: 10.1016/j.actbio.2019.09.007.

[55] Staudinger, H.; Schweitzer, O. Über hochpolymere Verbindungen, 20. Mitteil.: Über die Poly-äthylenoxyde. *Ber. Dtsch. Chem. Ges. A und B* **1929**, *62*, 2395.

[56] Herzberger, J.; Niederer, K.; Pohlit, H.; Seiwert, J.; Worm, M.; Wurm, F. R.; Frey, H. Polymerization of Ethylene Oxide, Propylene Oxide, and Other Alkylene Oxides: Synthesis, Novel Polymer Architectures, and Bioconjugation. *Chemical reviews* **2016**, *116*, 2170–2243. DOI: 10.1021/acs.chemrev.5b00441.

[57] Jana Herzberger, Kerstin Niederer, Hannah Pohlit, Jan Seiwert, Matthias Worm, Frederik R. Wurm, and Holger Frey. cr5b00441 1.74.

[58] Majumdar, R.; Alexander, K. S.; Riga, A. T. Physical characterization of polyethylene glycols by thermal analytical technique and the effect of humidity and molecular weight. *Pharmazie* **2010**, 343–347.

[59] Dingels, C.; Schömer, M.; Frey, H. Die vielen Gesichter des Poly(ethylenglykol)s. *Chemie in unserer Zeit* **2011**, *45*, 338–349. DOI: 10.1002/ciuz.201100551.

[60] Kjellander, R.; Florin, E. Water Structure and Changes in Thermal Stability of the System Poly(ethylene oxide)-Water. *J. Chem. Soc., Faraday Trans 1* **1981**, *77*, 2053–2077.

[61] Li, J.; Kao, W. J. Synthesis of polyethylene glycol (PEG) derivatives and PEGylated-peptide biopolymer conjugates. *Biomacromolecules* **2003**, *4*, 1055–1067. DOI: 10.1021/bm034069l.

[62] Fruijtier-Poelloth, C. Safety assessment on polyethylene glycols (PEGs) and their derivatives as used in cosmetic products. *Toxicology* **2005**, *214*, 1–38. DOI: 10.1016/j.tox.2005.06.001.

[63] Knop, K.; Hoogenboom, R.; Fischer, D.; Schubert, U. S. Poly(ethylene glycol) in drug delivery: pros and cons as well as potential alternatives. *Angewandte Chemie (International ed. in English)* **2010**, *49*, 6288–6308. DOI: 10.1002/anie.200902672.

[64] Casiraghi, A.; Selmin, F.; Minghetti, P.; Cilurzo, F.; Montanari, L. Nonionic Surfactants: Polyethylene Glycol (PEG) Ethers and Fatty Acid Esters as Penetration Enhancers. In *Percutaneous Penetration Enhancers Chemical Methods in Penetration Enhancement: Modification of the Stratum Corneum,* 1st ed. 2015; Dragicevic, N., Maibach, H. I., Eds.; Springer: Berlin, 2015; pp 251–271.

[65] Xue, Z.; He, D.; Xie, X. Poly(ethylene oxide)-based electrolytes for lithium-ion batteries. *J. Mater. Chem. A* **2015**, *3*, 19218–19253. DOI: 10.1039/C5TA03471J.

[66] Han, S.; Kim, C.; Kwon, D. Thermal degradation of poly(ethyleneglycol). *Polymer Degradation and Stability* **1995**, *47*, 203–208. DOI: 10.1016/0141-3910(94)00109-L.

[67] DeForest, C. A.; Anseth, K. S. Advances in bioactive hydrogels to probe and direct cell fate. *Annual review of chemical and biomolecular engineering* **2012**, *3*, 421–444. DOI: 10.1146/annurev-chembioeng-062011-080945.

[68] Levato, R.; Jungst, T.; Scheuring, R. G.; Blunk, T.; Groll, J.; Malda, J. From Shape to Function: The Next Step in Bioprinting. *Advanced Materials* **2020**, *32*, e1906423. DOI: 10.1002/adma.201906423.

[69] Buckwalter, D. J.; Dennis, J. M.; Long, T. E. Amide-containing segmented copolymers. *Progress in Polymer Science* **2015**, *45*, 1–22. DOI: 10.1016/j.progpolymsci.2014.11.003.

[70] Kojio, K.; Nakashima, S.; Furukawa, M. Microphase-separated structure and mechanical properties of norbornane diisocyanate-based polyurethanes. *Polymer* **2007**, *48*, 997–1004. DOI: 10.1016/j.polymer.2006.12.057.

[71] Buckwalter, D. J.; Zhang, M.; Inglefield, D. L.; Moore, R. B.; Long, T. E. Synthesis and characterization of siloxane-containing poly(urea oxamide) segmented copolymers. *Polymer* **2013**, *54*, 4849–4857. DOI: 10.1016/j.polymer.2013.07.025.

[72] Sheth, J. P.; Klinedinst, D. B.; Wilkes, G. L.; Yilgor, I.; Yilgor, E. Role of chain symmetry and hydrogen bonding in segmented copolymers with monodisperse hard segments. *Polymer* **2005**, *46*, 7317–7322. DOI: 10.1016/j.polymer.2005.04.041.

[73] Das, S.; Yilgor, I.; Yilgor, E.; Inci, B.; Tezgel, O.; Beyer, F. L.; Wilkes, G. L. Structure–property relationships and melt rheology of segmented, non-chain extended polyureas: Effect of soft segment molecular weight. *Polymer* **2007**, *48*, 290–301. DOI: 10.1016/j.polymer.2006.10.029.

[74] Toader, G.; Rusen, E.; Teodorescu, M.; Diacon, A.; Stanescu, P. O.; Rotariu, T.; Rotariu, A. Novel polyurea polymers with enhanced mechanical properties. *J. Appl. Polym. Sci.* **2016**, *133.* DOI: 10.1002/app.43967.

[75] Chalissery, D.; Schönfeld, D.; Walter, M.; Shklyar, I.; Andrae, H.; Schwörer, C.; Amann, T.; Weisheit, L.; Pretsch, T. Highly Shrinkable Objects as Obtained from 4D Printing. *Macro Materials & Eng* **2022**, *307*, 2100619. DOI: 10.1002/mame.202100619.

[76] Souza, F. M. de; Sulaiman, M. R.; Gupta, R. K. Materials and Chemistry of Polyurethanes. In *Materials and chemistry of flame-retardant polyurethanes*; Gupta, R. K., Ed.; American Chemical Society: Washington, DC, 2021; pp 1–36.

[77] Camberlin, Y.; Pascault, J. P. Phase segregation kinetics in segmented linear polyurethanes: Relations between equilibrium time and chain mobility and between equilibrium degree of segregation and interaction parameter. *J. Polym. Sci. Polym. Phys. Ed.* **1984**, *22*, 1835–1844. DOI: 10.1002/pol.1984.180221011.

[78] Eling, B.; Tomović, Ž.; Schädler, V. Current and Future Trends in Polyurethanes: An Industrial Perspective. *Macromol. Chem. Phys.* **2020**, *221*, 2000114. DOI: 10.1002/macp.202000114.

[79] Pervaiz, M.; Faruq, M.; Jawaid, M.; Sain, M. Polyamides: Developments and Applications Towards Next-Generation Engineered Plastics. Current Organic Synthesis, 14(2), 146-155. *COS* **2017**, *14*, 146–155. DOI: 10.2174/1570179413666160831112159.

[80] Brunette, C. M.; Hsu, S. L.; MacKnight, W. J. Hydrogen-Bonding Properties of Hard-Segment Model Compounds in Polyurethane Block Copolymers. *Macromolecules* **1982**, 71–77.

[81] Vasanthan, N. Crystallinity Determination of Nylon 66 by Density Measurement and Fourier Transform Infrared (FTIR) Spectroscopy. *J. Chem. Educ.* **2012**, *89*, 387–390. DOI: 10.1021/ed200398m.

[82] Ma, Y.; Zhou, T.; Su, G.; Li, Y.; Zhang, A. Understanding the crystallization behavior of polyamide 6/polyamide 66 alloys from the perspective of hydrogen bonds: projection moving-window 2D correlation FTIR spectroscopy and the enthalpy. *RSC Adv.* **2016**, *6*, 87405–87415. DOI: 10.1039/C6RA09611E.

[83] Nozaki, S.; Masuda, S.; Kamitani, K.; Kojio, K.; Takahara, A.; Kuwamura, G.; Hasegawa, D.; Moorthi, K.; Mita, K.; Yamasaki, S. Superior Properties of Polyurethane Elastomers Synthesized with Aliphatic Diisocyanate Bearing a Symmetric Structure. *Macromolecules* **2017**, *50*, 1008–1015. DOI: 10.1021/acs.macromol.6b02044.

[84] Riess, G.; Mendolia, M. S.; Schmidt, H.-W. Novel urea-siloxane polymers as gelling agents for silicone fluids. *Macromol. Symp.* **2002**, 123–134.

[85] Versteegen, R. M.; Sijbesma, R. P.; Meijer, E. W. Synthesis and Characterization of Segmented Copoly(ether urea)s with Uniform Hard Segments. *Macromolecules* **2005**, *38*, 3176–3184. DOI: 10.1021/ma0478207.

[86] Herzberger, J.; Sirrine, J. M.; Williams, C. B.; Long, T. E. Polymer Design for 3D Printing Elastomers: Recent Advances in Structure, Properties, and Printing. *Prog. Polym. Sci.* **2019**, *97*, 101144. DOI: 10.1016/j.progpolymsci.2019.101144.

[87] Hochleitner, G.; Fürsattel, E.; Giesa, R.; Groll, J.; Schmidt, H.-W.; Dalton, P. D. Melt Electrowriting of Thermoplastic Elastomers. *Macromolecular rapid communications* **2018**, *39*, e1800055. DOI: 10.1002/marc.201800055.

[88] Oguz, O.; Candau, N.; Stoclet, G.; Simsek, E.; Kosak Soz, C.; Yilgor, E.; Yilgor, I.; Menceloglu, Y. Z. Geometric Confinement Controls Stiffness, Strength, Extensibility, and Toughness in Poly(urethane–urea) Copolymers. *Macromolecules* **2021**, *54*, 4704–4725. DOI: 10.1021/acs.macromol.1c00596.

[89] Dankers, P. Y. W.; van Luyn, M. J. A.; Huizinga-van der Vlag, A.; van Gemert, G. M. L.; Petersen, A. H.; Meijer, E. W.; Janssen, H. M.; Bosman, A. W.; Popa, E. R. Development and in-vivo characterization of supramolecular hydrogels for intrarenal drug delivery. *Biomaterials* **2012**, *33*, 5144–5155. DOI: 10.1016/j.biomaterials.2012.03.052.

[90] Guo, M.; Pitet, L. M.; Wyss, H. M.; Vos, M.; Dankers, P. Y. W.; Meijer, E. W. Tough stimuli-responsive supramolecular hydrogels with hydrogen-bonding network junctions. *Journal of the American Chemical Society* **2014**, *136*, 6969–6977. DOI: 10.1021/ja500205v.

[91] Obert, E.; Bellot, M.; Bouteiller, L.; Andrioletti, F.; Lehen-Ferrenbach, C.; Boué, F. Both water- and organo-soluble supramolecular polymer stabilized by hydrogen-bonding and hydrophobic interactions. *Journal of the American Chemical Society* **2007**, *129*, 15601–15605. DOI: 10.1021/ja074296l.

[92] Wang, B.; Feng, C.; Dang, J.; Zhu, Y.; Yang, X.; Zhang, T.; Zhang, R.; Li, J.; Tang, J.; Shen, C.*; et al.* Preparation of Fibroblast Suppressive Poly(ethylene glycol)-b-poly(l-phenylalanine)/Poly(ethylene glycol) Hydrogel and Its Application in Intrauterine Fibrosis Prevention. *ACS biomaterials science & engineering* **2021**, *7*, 311–321. DOI: 10.1021/acsbiomaterials.0c01390.

[93] Pawar, G. M.; Koenigs, M.; Fahimi, Z.; Cox, M.; Voets, I. K.; Wyss, H. M.; Sijbesma, R. P. Injectable hydrogels from segmented PEG-bisurea copolymers. *Biomacromolecules* **2012**, *13*, 3966–3976. DOI: 10.1021/bm301242v.

[94] Cui, Y.; Tan, M.; Zhu, A.; Guo, M. Mechanically strong and stretchable PEG-based supramolecular hydrogel with water-responsive shape-memory property. *Journal of materials chemistry. B* **2014**, *2*, 2978–2982. DOI: 10.1039/c4tb00315b.

[95] Yang, N.; Yang, H.; Shao, Z.; Guo, M. Ultrastrong and Tough Supramolecular Hydrogels from Multiurea Linkage Segmented Copolymers with Tractable Processablity and Recyclability. *Macromolecular rapid communications* **2017**, *38.* DOI: 10.1002/marc.201700275.

[96] van Gaal, R. C.; van Sprang, J. F.; Borneman, Z.; Dankers, P. Y. W. Development of Poor Cell Adhesive Immersion Precipitation Membranes Based on Supramolecular Bis-Urea Polymers. *Macromolecular bioscience* **2020**, *20*, e1900277. DOI: 10.1002/mabi.201900277.

[97] Yu, J.; Chen, X.; Yang, Y.; Zhao, X.; Chen, X.; Jing, T.; Zhou, Y.; Xu, J.; Zhang, Y.; Cheng, Y. Construction of supramolecular hydrogels using imidazolidinyl urea as hydrogen bonding reinforced factor. *Journal of materials chemistry. B* **2020**, *8*, 3058–3063. DOI: 10.1039/d0tb00331j.

[98] Srivastava, M.; Rathee, S.; Patel, V.; Kumar, A.; Koppad, P. G. A review of various materials for additive manufacturing: Recent trends and processing issues. *Journal of Materials Research and Technology* **2022**, *21*, 2612–2641. DOI: 10.1016/j.jmrt.2022.10.015.

[99] Ligon, S. C.; Liska, R.; Stampfl, J.; Gurr, M.; Mulhaupt, R. Polymers for 3D Printing and Customized Additive Manufacturing. *Chem. Rev. (Washington, DC, U. S.)* **2017**, *117*, 10212–10290. DOI: 10.1021/acs.chemrev.7b00074.

[100] Huang, J.; Qin, Q.; Wang, J. A Review of Stereolithography: Processes and Systems. *Processes* **2020**, *8*, 1138. DOI: 10.3390/pr8091138.

[101] Melchels, F. P. W.; Feijen, J.; Grijpma, D. W. A review on stereolithography and its applications in biomedical engineering. *Biomaterials* **2010**, *31*, 6121–6130. DOI: 10.1016/j.biomaterials.2010.04.050.

[102] Chaudhary, R.; Fabbri, P.; Leoni, E.; Mazzanti, F.; Akbari, R.; Antonini, C. Additive manufacturing by digital light processing: a review. *Prog Addit Manuf* **2022**, 1–21. DOI: 10.1007/s40964-022-00336-0.

[103] Ding, H.; Dong, M.; Zheng, Q.; Wu, Z. L. Digital light processing 3D printing of hydrogels: a minireview. *Mol. Syst. Des. Eng.* **2022**, *7*, 1017–1029. DOI: 10.1039/D2ME00066K.

[104] Lipkowitz, G.; Samuelsen, T.; Hsiao, K.; Lee, B.; Dulay, M. T.; Coates, I.; Lin, H.; Pan, W.; Toth, G.; Tate, L.*; et al.* Injection continuous liquid interface production of 3D objects. *Science advances* **2022**, *8*, eabq3917. DOI: 10.1126/sciadv.abq3917.

[105] Li, L.; Fourkas, J. T. *Multiphoton polymerization*, 2007.

[106] Huang, Z.; Chi-Pong Tsui, G.; Deng, Y.; Tang, C.-Y. Two-photon polymerization nanolithography technology for fabrication of stimulus-responsive micro/nano-structures for biomedical applications. *Nanotechnology Reviews* **2020**, *9*, 1118–1136. DOI: 10.1515/ntrev-2020-0073.

[107] Brighenti, R.; Cosma, M. P.; Marsavina, L.; Spagnoli, A.; Terzano, M. Laser-based additively manufactured polymers: a review on processes and mechanical models. *J Mater Sci* **2021**, *56*, 961–998. DOI: 10.1007/s10853-020-05254-6.

[108] Han, W.; Kong, L.; Xu, M. Advances in selective laser sintering of polymers. *Int. J. Extrem. Manuf.* **2022**, *4*, 42002. DOI: 10.1088/2631-7990/ac9096.

[109] Sing, S. L.; Yeong, W. Y.; Wiria, F. E.; Tay, B. Y.; Zhao, Z.; Zhao, L.; Tian, Z.; Yang, S. Direct selective laser sintering and melting of ceramics: a review. *RPJ* **2017**, *23*, 611–623. DOI: 10.1108/RPJ-11-2015-0178.

[110] Zhang, L.-C.; Liu, Y.; Li, S.; Hao, Y. Additive Manufacturing of Titanium Alloys by Electron Beam Melting: A Review. *Adv. Eng. Mater.* **2018**, *20*, 1700842. DOI: 10.1002/adem.201700842.

[111] Galati, M.; Iuliano, L. A literature review of powder-based electron beam melting focusing on numerical simulations. *Additive Manufacturing* **2018**, *19*, 1–20. DOI: 10.1016/j.addma.2017.11.001.

[112] Gülcan, O.; Günaydın, K.; Tamer, A. The State of the Art of Material Jetting-A Critical Review. *Polymers* **2021**, *13.* DOI: 10.3390/polym13162829.

[113] Elkaseer, A.; Chen, K. J.; Janhsen, J. C.; Refle, O.; Hagenmeyer, V.; Scholz, S. G. Material jetting for advanced applications: A state-of-the-art review, gaps and future directions. *Additive Manufacturing* **2022**, *60*, 103270. DOI: 10.1016/j.addma.2022.103270.

[114] Ziaee, M.; Crane, N. B. Binder jetting: A review of process, materials, and methods. *Additive Manufacturing* **2019**, *28*, 781–801. DOI: 10.1016/j.addma.2019.05.031.

[115] Shakor, P.; Chu, S. H.; Puzatova, A.; Dini, E. Review of binder jetting 3D printing in the construction industry. *Prog Addit Manuf* **2022**, *7*, 643–669. DOI: 10.1007/s40964-021-00252-9.

[116] Gibson, I.; Rosen, D. W.; Stucker, B. Sheet Lamination Processes. *Additive Manufacturing Technologies*; Springer, Boston, MA, 2010; pp 223–252.

[117] Ahn, D.-G. Directed Energy Deposition (DED) Process: State of the Art. *Int. J. of Precis. Eng. and Manuf.-Green Tech.* **2021**, *8*, 703–742. DOI: 10.1007/s40684-020-00302-7.

[118] R. Comminal; M.P. Serdeczny; D.B. Pedersen; and J. Spangenberg. Numerical Modeling of the Material Deposition and Contouring Precision in Fused Deposition Modeling. *Am. Soc. Mech. Eng.* **1995**, 1225–1235.

[119] Mohamed, O. A.; Masood, S. H.; Bhowmik, J. L. Optimization of fused deposition modeling process parameters for dimensional accuracy using I-optimality criterion. *Measurement* **2016**, *81*, 174–196. DOI: 10.1016/j.measurement.2015.12.011.

[120] Kristiawan, R. B.; Imaduddin, F.; Ariawan, D.; Ubaidillah; Arifin, Z. A review on the fused deposition modeling (FDM) 3D printing: Filament processing, materials, and printing parameters. *Open Engineering* **2021**, *11*, 639–649. DOI: 10.1515/eng-2021-0063.

[121] Jin, M.; Giesa, R.; Neuber, C.; Schmidt, H.-W. Filament Materials Screening for FDM 3D Printing by Means of Injection-Molded Short Rods. *Macromol. Mater. Eng.* **2018**, *303*, 1800507. DOI: 10.1002/mame.201800507.

[122] Ferris, C. J.; Gilmore, K. G.; Wallace, G. G.; het Panhuis, M. in. Biofabrication: an overview of the approaches used for printing of living cells. *Applied microbiology and biotechnology* **2013**, *97*, 4243–4258. DOI: 10.1007/s00253-013-4853-6.

[123] Chang, C. C.; Boland, E. D.; Williams, S. K.; Hoying, J. B. Direct-write bioprinting three-dimensional biohybrid systems for future regenerative therapies. *Journal of biomedical materials research. Part B, Applied biomaterials* **2011**, *98*, 160–170. DOI: 10.1002/jbm.b.31831.

[124] Ozbolat, I. T.; Yu, Y. Bioprinting toward organ fabrication: challenges and future trends. *IEEE transactions on bio-medical engineering* **2013**, *60*, 691–699. DOI: 10.1109/TBME.2013.2243912.

[125] Koch, L.; Gruene, M.; Unger, C.; Chichkov, B. Laser Assisted Cell Printing. *Curr. Pharm. Biotechnol.* **2013**, *14*, 91–97.

[126] Calvert, P. Printing Cells. *Science (New York, N.Y.)* **2007**, *318*, 208–209. DOI: 10.1126/science.1148507.

[127] Derby, B. Bioprinting: inkjet printing proteins and hybrid cell-containing materials and structures. *J. Mater. Chem.* **2008**, *18*, 5717. DOI: 10.1039/b807560c.

[128] Attalla, R.; Puersten, E.; Jain, N.; Selvaganapathy, P. R. 3D bioprinting of heterogeneous bi- and tri-layered hollow channels within gel scaffolds using scalable multi-axial microfluidic extrusion nozzle. *Biofabrication* **2018**, *11*, 15012. DOI: 10.1088/1758-5090/aaf7c7.

[129] Costantini, M.; Colosi, C.; Święszkowski, W.; Barbetta, A. Co-axial wet-spinning in 3D bioprinting: state of the art and future perspective of microfluidic integration. *Biofabrication* **2018**, *11*, 12001. DOI: 10.1088/1758-5090/aae605.

[130] Lee, A.; Hudson, A. R.; Shiwarski, D. J.; Tashman, J. W.; Hinton, T. J.; Yerneni, S.; Bliley, J. M.; Campbell, P. G.; Feinberg, A. W. 3D bioprinting of collagen to rebuild components of the human heart. *Science (New York, N.Y.)* **2019**, *365*, 482–487. DOI: 10.1126/science.aav9051.

[131] Zhang, Y.; Ellison, S. T.; Duraivel, S.; Morley, C. D.; Taylor, C. R.; Angelini, T. E. 3D printed collagen structures at low concentrations supported by jammed microgels. *Bioprinting* **2021**, *21*, e00121. DOI: 10.1016/j.bprint.2020.e00121.

[132] Hinton, T. J.; Jallerat, Q.; Palchesko, R. N.; Park, J. H.; Grodzicki, M. S.; Shue, H.-J.; Ramadan, M. H.; Hudson, A. R.; Feinberg, A. W. Three-dimensional printing of complex biological structures by freeform reversible embedding of suspended hydrogels. *Science advances* **2015**, *1*, e1500758. DOI: 10.1126/sciadv.1500758.

[133] Highley, C. B.; Rodell, C. B.; Burdick, J. A. Direct 3D Printing of Shear-Thinning Hydrogels into Self-Healing Hydrogels. *Advanced materials (Deerfield Beach, Fla.)* **2015**, *27*, 5075–5079. DOI: 10.1002/adma.201501234.

[134] Noor, N.; Shapira, A.; Edri, R.; Gal, I.; Wertheim, L.; Dvir, T. 3D Printing of Personalized Thick and Perfusable Cardiac Patches and Hearts. *Advanced Science* **2019**, *6*, 1900344. DOI: 10.1002/advs.201900344.

[135] Ouyang, L.; Armstrong, J. P. K.; Chen, Q.; Lin, Y.; Stevens, M. M. Void-free 3D Bioprinting for In-situ Endothelialization and Microfluidic Perfusion. *Adv. Funct. Mater.* **2020**, *30*, 1908349. DOI: 10.1002/adfm.201908349.

[136] Davoodi, E.; Sarikhani, E.; Montazerian, H.; Ahadian, S.; Costantini, M.; Swieszkowski, W.; Willerth, S.; Walus, K.; Mofidfar, M.; Toyserkani, E.*; et al.* Extrusion and Microfluidic-based Bioprinting to Fabricate Biomimetic Tissues and Organs. *Advanced Materials Technologies* **2020**, *5*, 1901044. DOI: 10.1002/admt.201901044.

[137] Richard, C.; Neild, A.; Cadarso, V. J. The emerging role of microfluidics in multi-material 3D bioprinting. *Lab Chip* **2020**, *20*, 2044–2056. DOI: 10.1039/C9LC01184F.

[138] Brenken, B.; Barocio, E.; Favaloro, A.; Kunc, V.; Pipes, R. B. Fused filament fabrication of fiber-reinforced polymers: A review. *Additive Manufacturing* **2018**, *21*, 1–16. DOI: 10.1016/j.addma.2018.01.002.

[139] Mechau, J.; Frank, A.; Bakirci, E.; Gumbel, S.; Jungst, T.; Giesa, R.; Groll, J.; Dalton, P. D.; Schmidt, H.-W. Hydrophilic (AB) n Segmented Copolymers for Melt Extrusion-Based Additive Manufacturing. *Macromol. Chem. Phys.* **2021**, *222*, 2000265. DOI: 10.1002/macp.202000265.

[140] Cantrell, J. T.; Rohde, S.; Damiani, D.; Gurnani, R.; DiSandro, L.; Anton, J.; Young, A.; Jerez, A.; Steinbach, D.; Kroese, C.*; et al.* Experimental characterization of the mechanical properties of 3D-printed ABS and polycarbonate parts. *Rapid Prototyping Journal* **2017**, *23*, 811–824. DOI: 10.1108/RPJ-03-2016-0042.

[141] Gordeev, E. G.; Galushko, A. S.; Ananikov, V. P. Improvement of quality of 3D printed objects by elimination of microscopic structural defects in fused deposition modeling. *PloS one* **2018**, *13*, e0198370. DOI: 10.1371/journal.pone.0198370.

[142] Jin, M.; Neuber, C.; Schmidt, H.-W. Tailoring polypropylene for extrusion-based additive manufacturing. *Additive Manufacturing* **2020**, *33*, 101101. DOI: 10.1016/j.addma.2020.101101.

[143] Zein, I.; Hutmacher, D. W.; Tan, K. C.; Teoh, S. H. Fused deposition modeling of novel scaffold architectures for tissue engineering applications. *Biomaterials* **2002**, *23*, 1169–1185. DOI: 10.1016/S0142-9612(01)00232-0.

[144] Vaezi, M.; Yang, S. Extrusion-based additive manufacturing of PEEK for biomedical applications. *Virtual and Physical Prototyping* **2015**, *10*, 123–135. DOI: 10.1080/17452759.2015.1097053.

[145] Kishi, N.; Iizuka, H. The barus effect of polymer melts. *Polym. Lett.* **1964**, *2*, 399–402.

[146] Robinson, T. M.; Hutmacher, D. W.; Dalton, P. D. The Next Frontier in Melt Electrospinning: Taming the Jet. *Adv. Funct. Mater.* **2019**, *29*, 1904664. DOI: 10.1002/adfm.201904664.

[147] Nayak, R.; Padhye, R.; Kyratzis, I. L.; Truong, Y. B.; Arnold, L. Effect of viscosity and electrical conductivity on the morphology and fiber diameter in melt electrospinning of polypropylene. *Textile Research Journal* **2013**, *83*, 606–617. DOI: 10.1177/0040517512458347.

[148] Großhaus, C.; Bakirci, E.; Berthel, M.; Hrynevich, A.; Kade, J. C.; Hochleitner, G.; Groll, J.; Dalton, P. D. Melt Electrospinning of Nanofibers from Medical-Grade Poly(ε-Caprolactone) with a Modified Nozzle. *Small (Weinheim an der Bergstrasse, Germany)* **2020**, *16*, e2003471. DOI: 10.1002/smll.202003471.

[149] Christiansen, L.; Gurevich, L.; Wang, D.; Fojan, P. Melt Electrospinning of PET and Composite PET-Aerogel Fibers: An Experimental and Modeling Study. *Materials (Basel, Switzerland)* **2021**, *14.* DOI: 10.3390/ma14164699.

[150] Nazari, T.; Garmabi, H. Polylactic acid/polyethylene glycol blend fibres prepared via melt electrospinning: effect of polyethylene glycol content. *Micro & Nano Letters* **2014**, *9*, 686–690. DOI: 10.1049/mnl.2013.0735.

[151] Nazari, T.; Garmabi, H. Thermo-rheological and interfacial properties of polylactic acid/polyethylene glycol blends toward the melt electrospinning ability. *J Appl Polym Sci* **2016**, *133.* DOI: 10.1002/app.44120.

[152] Nazari, T.; Garmabi, H. The effects of processing parameters on the morphology of PLA/PEG melt electrospun fibers. *Polym Int* **2018**, *67*, 178–188. DOI: 10.1002/pi.5486.

[153] He, F.-L.; Deng, X.; Zhou, Y.-Q.; Zhang, T.-D.; Liu, Y.-L.; Ye, Y.-J.; Yin, D.-C. Controlled release of antibiotics from poly-ε-caprolactone/polyethylene glycol wound dressing fabricated by direct-writing melt electrospinning. *Polym. Adv. Technol.* **2019**, *30*, 425–434. DOI: 10.1002/pat.4481.

[154] Unnithan, A. R.; Arathyram, R. S.; Kim, C. S. Chapter 3 - Electrospinning of Polymers for Tissue Engineering. In *Nanotechnology applications for tissue engineering*; Thomas, S., Ed.; Elsevier: Amsterdam [u.a.], 2015; pp 45–55.

[155] Eichholz, K. F.; Gonçalves, I.; Barceló, X.; Federici, A. S.; Hoey, D. A.; Kelly, D. J. How to design, develop and build a fully-integrated melt electrowriting 3D printer. *Additive Manufacturing* **2022**, *58*, 102998. DOI: 10.1016/j.addma.2022.102998.

[156] Brown, T. D.; Dalton, P. D.; Hutmacher, D. W. Melt electrospinning today: An opportune time for an emerging polymer process. *Prog. Polym. Sci.* **2016**, *56*, 116–166. DOI: 10.1016/j.progpolymsci.2016.01.001.

[157] Hartman, R.; Brunner, D. J.; Camelot, D.; Marijnissen, J.; Scarlett, B. ELECTROHYDRODYNAMIC ATOMIZATION IN THE CONE–JET MODE PHYSICAL MODELING OF THE LIQUID CONE AND JET. *Journal of Aerosol Science* **1999**, *30*, 823–849. DOI: 10.1016/S0021-8502(99)00033-6.

[158] Kade, J. C.; Dalton, P. D. Polymers for Melt Electrowriting. *Advanced healthcare materials* **2021**, *10*, e2001232. DOI: 10.1002/adhm.202001232.

[159] Brown, T. D.; Dalton, P. D.; Hutmacher, D. W. Direct writing by way of melt electrospinning. *Advanced materials (Deerfield Beach, Fla.)* **2011**, *23*, 5651–5657. DOI: 10.1002/adma.201103482.

[160] Hochleitner, G.; Youssef, A.; Hrynevich, A.; Haigh, J. N.; Jungst, T.; Groll, J.; Dalton, P. D. Fibre pulsing during melt electrospinning writing. *BioNanoMaterials* **2016**, *17.* DOI: 10.1515/bnm-2015-0022.

[161] Hochleitner, G.; Jüngst, T.; Brown, T. D.; Hahn, K.; Moseke, C.; Jakob, F.; Dalton, P. D.; Groll, J. Additive manufacturing of scaffolds with sub-micron filaments via melt electrospinning writing. *Biofabrication* **2015**, *7*, 35002. DOI: 10.1088/1758-5090/7/3/035002.

[162] Hrynevich, A.; Elçi, B. Ş.; Haigh, J. N.; McMaster, R.; Youssef, A.; Blum, C.; Blunk, T.; Hochleitner, G.; Groll, J.; Dalton, P. D. Dimension-Based Design of Melt Electrowritten Scaffolds. *Small (Weinheim an der Bergstrasse, Germany)* **2018**, *14*, e1800232. DOI: 10.1002/smll.201800232.

[163] Daneshfar, A.; Edwards, S. L.; Dumée, L. F.; Kong, L.; Hughes, T. C. Predicting Operating Rules for Successful Melt Electrowriting. *ACS Appl. Polym. Mater.* **2021**, *3*, 1890–1898. DOI: 10.1021/acsapm.0c01421.

[164] Kim, J.; Bakirci, E.; O'Neill, K. L.; Hrynevich, A.; Dalton, P. D. Fiber Bridging during Melt Electrowriting of Poly(ε-Caprolactone) and the Influence of Fiber Diameter and Wall Height. *Macromol. Mater. Eng.* **2021**, *306*, 2000685. DOI: 10.1002/mame.202000685.

[165] Böhm, C.; Stahlhut, P.; Weichhold, J.; Hrynevich, A.; Teßmar, J.; Dalton, P. D. The Multiweek Thermal Stability of Medical-Grade Poly(ε-caprolactone) During Melt Electrowriting. *Small (Weinheim an der Bergstrasse, Germany)* **2022**, *18*, e2104193. DOI: 10.1002/smll.202104193.

[166] Woodruff, M. A.; Hutmacher, D. W. The return of a forgotten polymer—Polycaprolactone in the 21st century. *Prog. Polym. Sci.* **2010**, *35*, 1217–1256. DOI: 10.1016/j.progpolymsci.2010.04.002.

[167] Bartnikowski, M.; Dargaville, T. R.; Ivanovski, S.; Hutmacher, D. W. Degradation mechanisms of polycaprolactone in the context of chemistry, geometry and environment. *Prog. Polym. Sci.* **2019**, *96*, 1–20. DOI: 10.1016/j.progpolymsci.2019.05.004.

[168] Hewitt, E.; Mros, S.; McConnell, M.; Cabral, J. D.; Ali, A. Melt-electrowriting with novel milk protein/PCL biomaterials for skin regeneration. *Biomedical Materials* **2019**, *14*, 55013. DOI: 10.1088/1748-605X/ab3344.

[169] Wunner, F. M.; Wille, M.-L.; Noonan, T. G.; Bas, O.; Dalton, P. D.; De-Juan-Pardo, E. M.; Hutmacher, D. W. Melt Electrospinning Writing of Highly Ordered Large Volume Scaffold Architectures. *Advanced materials (Deerfield Beach, Fla.)* **2018**, *30*, e1706570. DOI: 10.1002/adma.201706570.

[170] Brown, T. D.; Slotosch, A.; Thibaudeau, L.; Taubenberger, A.; Loessner, D.; Vaquette, C.; Dalton, P. D.; Hutmacher, D. W. Design and fabrication of tubular scaffolds via direct writing in a melt electrospinning mode. *Biointerphases* **2012**, *7*, 13. DOI: 10.1007/s13758-011-0013-7.

[171] Paxton, N. C.; Daley, R.; Forrestal, D. P.; Allenby, M. C.; Woodruff, M. A. Auxetic tubular scaffolds via melt electrowriting. *Materials & Design* **2020**, *193*, 108787. DOI: 10.1016/j.matdes.2020.108787.

[172] Liashenko, I.; Hrynevich, A.; Dalton, P. D. Designing Outside the Box: Unlocking the Geometric Freedom of Melt Electrowriting using Microscale Layer Shifting. *Advanced materials (Deerfield Beach, Fla.)* **2020**, *32*, e2001874. DOI: 10.1002/adma.202001874.

[173] Saidy, N. T.; Shabab, T.; Bas, O.; Rojas-González, D. M.; Menne, M.; Henry, T.; Hutmacher, D. W.; Mela, P.; De-Juan-Pardo, E. M. Melt Electrowriting of Complex 3D Anatomically Relevant Scaffolds. *Frontiers in bioengineering and biotechnology* **2020**, *8*, 793. DOI: 10.3389/fbioe.2020.00793.

[174] Włodarczyk-Biegun, M. K.; Villiou, M.; Koch, M.; Muth, C.; Wang, P.; Ott, J.; Del Campo, A. Melt Electrowriting of Graded Porous Scaffolds to Mimic the Matrix Structure of the Human Trabecular Meshwork. *ACS biomaterials science & engineering* **2022**, *8*, 3899–3911. DOI: 10.1021/acsbiomaterials.2c00623.

[175] Visser, J.; Melchels, F. P. W.; Jeon, J. E.; van Bussel, E. M.; Kimpton, L. S.; Byrne, H. M.; Dhert, W. J. A.; Dalton, P. D.; Hutmacher, D. W.; Malda, J. Reinforcement of hydrogels using three-dimensionally printed microfibres. *Nature communications* **2015**, *6*, 6933. DOI: 10.1038/ncomms7933.

[176] Bas, O.; De-Juan-Pardo, E. M.; Meinert, C.; D'Angella, D.; Baldwin, J. G.; Bray, L. J.; Wellard, R. M.; Kollmannsberger, S.; Rank, E.; Werner, C.*; et al.* Biofabricated soft network composites for cartilage tissue engineering. *Biofabrication* **2017**, *9*, 25014. DOI: 10.1088/1758-5090/aa6b15.

[177] Castilho, M.; Hochleitner, G.; Wilson, W.; van Rietbergen, B.; Dalton, P. D.; Groll, J.; Malda, J.; Ito, K. Mechanical behavior of a soft hydrogel reinforced with three-dimensional printed microfibre scaffolds. *Scientific reports* **2018**, *8*, 1245. DOI: 10.1038/s41598-018-19502-y.

[178] Dubey, N.; Ferreira, J. A.; Daghrery, A.; Aytac, Z.; Malda, J.; Bhaduri, S. B.; Bottino, M. C. Highly tunable bioactive fiber-reinforced hydrogel for guided bone regeneration. *Acta biomaterialia* **2020.** DOI: 10.1016/j.actbio.2020.06.011.

[179] Saidy, N. T.; Wolf, F.; Bas, O.; Keijdener, H.; Hutmacher, D. W.; Mela, P.; De-Juan-Pardo, E. M. Biologically Inspired Scaffolds for Heart Valve Tissue Engineering via Melt Electrowriting. *Small* **2019**, *15*, e1900873. DOI: 10.1002/smll.201900873.

[180] Saidy, N. T.; Fernández-Colino, A.; Heidari, B. S.; Kent, R.; Vernon, M.; Bas, O.; Mulderrig, S.; Lubig, A.; Rodríguez-Cabello, J. C.; Doyle, B.*; et al.* Spatially Heterogeneous Tubular Scaffolds for In Situ Heart Valve Tissue Engineering Using Melt Electrowriting. *Adv Funct Materials* **2022**, *32*, 2110716. DOI: 10.1002/adfm.202110716.

[181] Dufour, A.; Gallostra, X. B.; O'Keeffe, C.; Eichholz, K.; Euw, S. von; Garcia, O.; Kelly, D. J. Integrating melt electrowriting and inkjet bioprinting for engineering structurally organized articular cartilage. *Biomaterials* **2022**, *283*, 121405. DOI: 10.1016/j.biomaterials.2022.121405.

[182] Ruijter, M. de; Ribeiro, A.; Dokter, I.; Castilho, M.; Malda, J. Simultaneous Micropatterning of Fibrous Meshes and Bioinks for the Fabrication of Living Tissue Constructs. *Advanced healthcare materials* **2019**, *8*, e1800418. DOI: 10.1002/adhm.201800418.

[183] Haigh, J. N.; Dargaville, T. R.; Dalton, P. D. Additive manufacturing with polypropylene microfibers. *Materials science & engineering. C, Materials for biological applications* **2017**, *77*, 883–887. DOI: 10.1016/j.msec.2017.03.286.

[184] Florczak, S.; Lorson, T.; Zheng, T.; Mrlik, M.; Hutmacher, D. W.; Higgins, M. J.; Luxenhofer, R.; Dalton, P. D. Melt electrowriting of electroactive poly(vinylidene difluoride) fibers. *Polym. Int.* **2019**, *68*, 735–745. DOI: 10.1002/pi.5759.

[185] Chala, T. F.; Wu, C.-M.; Chou, M.-H.; Guo, Z.-L. Melt Electrospun Reduced Tungsten Oxide /Polylactic Acid Fiber Membranes as a Photothermal Material for Light-Driven Interfacial Water Evaporation. *ACS applied materials & interfaces* **2018**, *10*, 28955–28962. DOI: 10.1021/acsami.8b07434.

[186] Castilho, M.; Feyen, D.; Flandes-Iparraguirre, M.; Hochleitner, G.; Groll, J.; Doevendans, P. A. F.; Vermonden, T.; Ito, K.; Sluijter, J. P. G.; Malda, J. Melt Electrospinning Writing of Poly-

Hydroxymethylglycolide-co-ε-Caprolactone-Based Scaffolds for Cardiac Tissue Engineering. *Advanced healthcare materials* **2017**, *6.* DOI: 10.1002/adhm.201700311.

[187] Luposchainsky, S.; Jörissen, S.; Nüchter, A.; Dalton, P. D. Melt Electrowriting of Poly(dioxanone) Filament Using a Multi-Axis Robot. *Macro Materials & Eng* **2022**, *307*, 2200450. DOI: 10.1002/mame.202200450.

[188] Böhm, C.; Tandon, B.; Hrynevich, A.; Teßmar, J.; Dalton, P. D. Processing of Poly(lactic- co -glycolic acid) Microfibers via Melt Electrowriting. *Macro Chemistry & Physics* **2022**, *223*, 2100417. DOI: 10.1002/macp.202100417.

[189] Kade, J. C.; Otto, P. F.; Luxenhofer, R.; Dalton, P. D. Melt electrowriting of poly(vinylidene difluoride) using a heated collector. *Polym Adv Technol* **2021**, *32*, 4951–4955. DOI: 10.1002/pat.5463.

[190] Uribe-Gomez, J.; Posada-Murcia, A.; Shukla, A.; Ergin, M.; Constante, G.; Apsite, I.; Martin, D.; Schwarzer, M.; Caspari, A.; Synytska, A.*; et al.* Shape-Morphing Fibrous Hydrogel/Elastomer Bilayers Fabricated by a Combination of 3D Printing and Melt Electrowriting for Muscle Tissue Regeneration. *ACS Appl. Bio Mater.* **2021**, *4*, 1720–1730. DOI: 10.1021/acsabm.0c01495.

[191] Nadernezhad, A.; Ryma, M.; Genç, H.; Cicha, I.; Jüngst, T.; Groll, J. Melt Electrowriting of Isomalt for High-Resolution Templating of Embedded Microchannels. *Adv. Mater. Technol.* **2021**, *6*, 2100221. DOI: 10.1002/admt.202100221.

[192] Hochleitner, G.; Kessler, M.; Schmitz, M.; Boccaccini, A. R.; Teßmar, J.; Groll, J. Melt electrospinning writing of defined scaffolds using polylactide-poly(ethylene glycol) blends with 45S5 bioactive glass particles. *Materials Letters* **2017**, *205*, 257–260. DOI: 10.1016/j.matlet.2017.06.096.

[193] Chen, F.; Hochleitner, G.; Woodfield, T.; Groll, J.; Dalton, P. D.; Amsden, B. G. Additive Manufacturing of a Photo-Cross-Linkable Polymer via Direct Melt Electrospinning Writing for Producing High Strength Structures. *Biomacromolecules* **2016**, *17*, 208–214. DOI: 10.1021/acs.biomac.5b01316.

[194] Hochleitner, G.; Chen, F.; Blum, C.; Dalton, P. D.; Amsden, B.; Groll, J. Melt electrowriting below the critical translation speed to fabricate crimped elastomer scaffolds with non-linear extension behaviour mimicking that of ligaments and tendons. *Acta biomaterialia* **2018**, *72*, 110–120. DOI: 10.1016/j.actbio.2018.03.023.

[195] Javadzadeh, M.; Del Barrio, J.; Sánchez-Somolinos, C. Melt Electrowriting of Liquid Crystal Elastomer Scaffolds with Programmed Mechanical Response. *Advanced Materials* **2023**, *35*, e2209244. DOI: 10.1002/adma.202209244.

[196] Nahm, D.; Weigl, F.; Schaefer, N.; Sancho, A.; Frank, A.; Groll, J.; Villmann, C.; Schmidt, H.-W.; Dalton, P. D.; Luxenhofer, R. A versatile biomaterial ink platform for the melt electrowriting of chemically-crosslinked hydrogels. *Mater. Horiz.* **2020**, *7*, 928–933. DOI: 10.1039/C9MH01654F.

[197] Wu, D. J.; Vonk, N. H.; Lamers, B. A.; Castilho, M.; Malda, J.; Hoefnagels, J. P.; Dankers, P. Y. Anisotropic hygro-expansion in hydrogel fibers owing to uniting 3D electrowriting and supramolecular polymer assembly. *European Polymer Journal* **2020**, *141*, 110099. DOI: 10.1016/j.eurpolymj.2020.110099.

[198] Shanks, R.; Kong, I. Thermoplastic Elastomers. In *Thermoplastic Elastomers*; El-Sonbati, A., Ed.; InTech: [Place of publication not identified], 2012.

[199] La Campa, J. G. de. Synthetic Methods in Step-Growth Polymers Edited by Martin E. Rogers, Timothy E. Long. *Macromol. Chem. Phys.* **2004**, *205*, 700. DOI: 10.1002/macp.200490012.

[200] Coleman, M. M.; Sobkowiak, M.; Pehlert, G. J.; Painter, P. C. Infrared temperature studies of a simple polyurea. *Macromol. Chem. Phys.* **1997**, 117–136.

[201] Frick, A.; Rochman, A. Characterization of TPU-elastomers by thermal analysis (DSC). *Polym. Test.* **2004**, *23*, 413–417. DOI: 10.1016/j.polymertesting.2003.09.013.

[202] Faucher, J. A.; Koleske, J. V.; Santee, E. R.; Stratta, J. J.; Wilson, C. W. Glass Transitions of Ethylene Oxide Polymers. *Journal of Applied Physics* **1966**, *37*, 3962–3964. DOI: 10.1063/1.1707961.

[203] Startsev, O. V.; Vapirov, Y. M.; Lebedev, M. P.; Kychkin, A. K. Comparison of Glass-Transition Temperatures for Epoxy Polymers Obtained by Methods of Thermal Analysis. *Mech Compos Mater* **2020**, *56*, 227–240. DOI: 10.1007/s11029-020-09875-5.

[204] Matyjaszewski, K.; Möller, M., Eds. *Polymer science: A comprehensive reference*; Elsevier: Amsterdam, 2012.

[205] W. L. Peticolas and J. M. Watkins. The Molecular Structure of Polyethylene. VII. Melt Viscosity and the Effect of Molecular Weight and Branching1 **1956**.

[206] Cox, W. P.; Merz, E. H. Correlation of dynamic and steady flow viscosities. *J. Polym. Sci.* **1958**, 619–622.

[207] Qiu, W.; Wunderlich, B. Reversible melting of high molar mass poly(oxyethylene). *Thermochim. Acta* **2006**, *448*, 136–146. DOI: 10.1016/j.tca.2006.07.005.

[208] Pielichowski, K.; Flejtuch, K. Differential scanning calorimetry studies on poly(ethylene glycol) with different molecular weights for thermal energy storage materials. *Polym. Adv. Technol.* **2002**, *13*, 690–696. DOI: 10.1002/pat.276.

[209] Garcia, D.; Starkweather Jr., H. W. Hydrogen bonding in nylon 66 and model compounds. *Journal of Polymer Science* **1985**, 537–555.

[210] Eshraghi, S.; Das, S. Mechanical and microstructural properties of polycaprolactone scaffolds with one-dimensional, two-dimensional, and three-dimensional orthogonally oriented porous architectures produced by selective laser sintering. *Acta Biomater.* **2010**, *6*, 2467–2476. DOI: 10.1016/j.actbio.2010.02.002.

[211] Wang, L.; Shi, X.; Wang, J. A temperature-responsive supramolecular hydrogel: preparation, gel-gel transition and molecular aggregation. *Soft matter* **2018**, *14*, 3090–3095. DOI: 10.1039/c8sm00220g.

[212] Tominaga, H.; Ishiyama, M.; Ohseto, F.; Sasamoto, K.; Hamamoto, T.; Suzukic, K.; Watanabe, M. A water-soluble tetrazolium salt useful for colorimetric cellviability assay. *Anal. Commun.* **1998**, 47–50.

[213] Hannah, R.; Beck, M.; Moravec, R.; Riss, T. CellTiter-Glo™ Luminescent Cell Viability Assay: A Sensitive and Rapid Method for Determining Cell Viability. *Cell Notes* **2001**, 10–13.

[214] Ahn, S. J.; Costa, J.; Emanuel, J. R. PicoGreen quantitation of DNA: effective evaluationof samples pre- or post-PCR. *Nucleic Acid Research* **1996**, *13*, 2623–2625.

[215] Sonebi, M.; Yahia, A. 1 - Mix design procedure, tests, and standards. In *Self-compacting concrete: Materials, properties and applications*; Siddique, R., Ed.; Woodhead Publishing: Duxford, Cambridge, Kidlington, 2020; pp 1–30.

[216] Dasdemir, M.; Topalbekiroglu, M.; Demir, A. Electrospinning of thermoplastic polyurethane microfibers and nanofibers from polymer solution and melt. *J. Appl. Polym. Sci.* **2013**, *127*, 1901–1908. DOI: 10.1002/app.37503.

[217] Gumbel, S. 3D-Druck von (AB)n-segmentierten Copolymeren und Stabilisierung weicher Hydrogele. Masterarbeit, Universität Bayreuth, 2019.

[218] Bakirci, E.; Frank, A.; Gumbel, S.; Otto, P. F.; Fürsattel, E.; Tessmer, I.; Schmidt, H.-W.; Dalton, P. D. Melt Electrowriting of Amphiphilic Physically Crosslinked Segmented Copolymers. *Macro Chemistry & Physics* **2021**, *222*, 2100259. DOI: 10.1002/macp.202100259.

# 8 Attachment

Attachment 1: DSC curves of copolymer **6a-2**

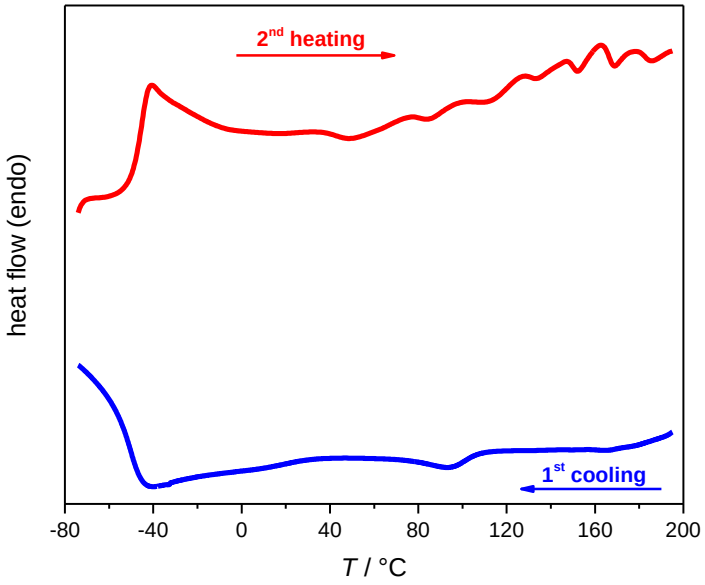


**Figure 8.1:** DSC curves of **6a-2** with 74 wt% PPG-PEG-PPG segments and 26 wt% hexamethylene bisurea segments. A glass transition of the PPG-PEG-PPG segments at -46 °C and a stepwise melting of the bisurea segments are visible.

Attachment 2: DSC of PPG-PEG-PPG diamine **1b** (Jeffamine ED-900)

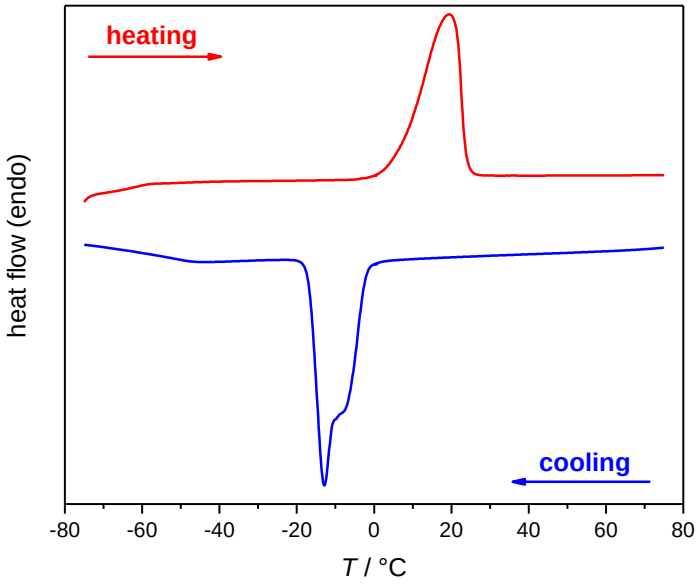


**Figure 8.2***:* DSC curves of Jeffamine ED-900 (**1b**). Upon first cooling a broad crystallization peak with a peak minimum of -13 °C is visible correlating to the PEG units. The second heating curve reveals a glass transition of the PPG-PEG-PPG segments at -46 °C and the melting of the PEG units with a peak maximum at 12 °C.

Attachment 3: DSC curves of copolymer **6b**

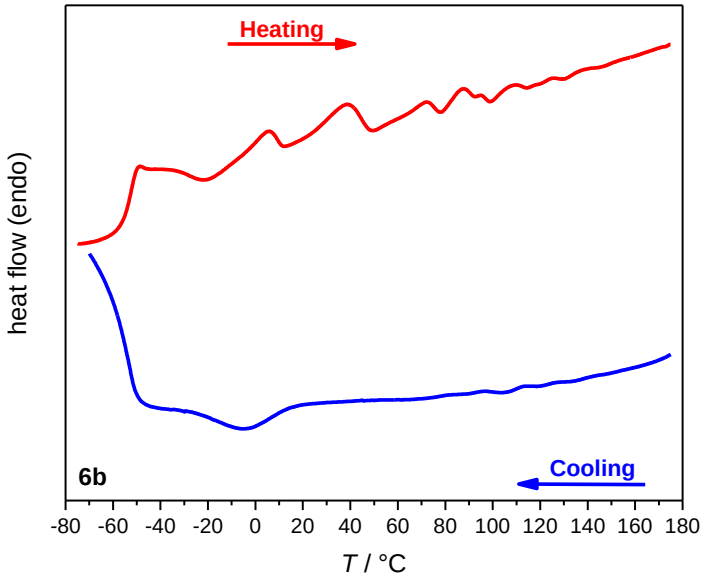


**Figure 8.3:** DSC curves of **6b** with 82 wt% PPG-PEG-PPG segments and 18 wt% hexamethylene bisurea segments. DSC curve reveals a glass transition at - 53 °C and a stepwise melting of the bisurea segments.

Attachment 4: DMTA tension geometry method of **6b**

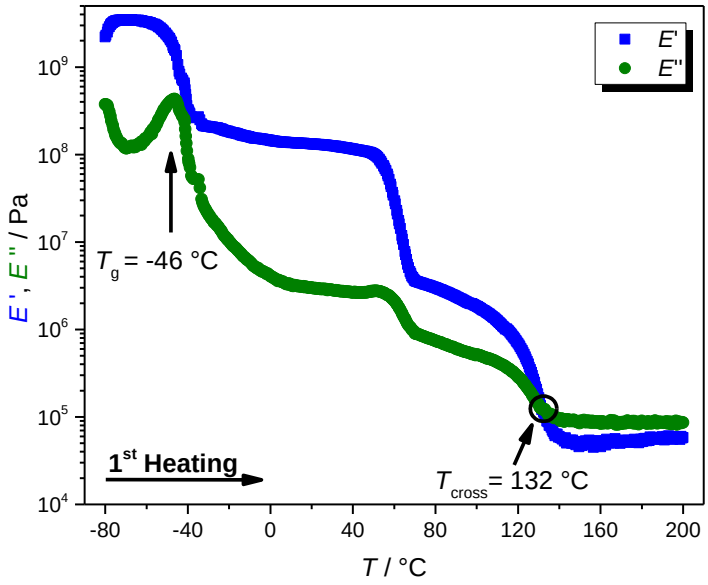


**Figure 8.4:** Dynamic mechanical thermal analysis of **6b** with 82 wt% PPG-PEG-PPG segments and 18 wt% hexamethylene bisurea segments using the tension geometry method. The turning point of the elastic modulus (E') is at -46 °C and corresponds to the glass transition of the PEG-PEG-PPG segments. The transition from elastic to viscous behavior is indicated by the intersection of the elastic (E') and viscous (E'') modulus occurring at 132 °C.

Attachment 5: DMTA tension geometry method of **6c**

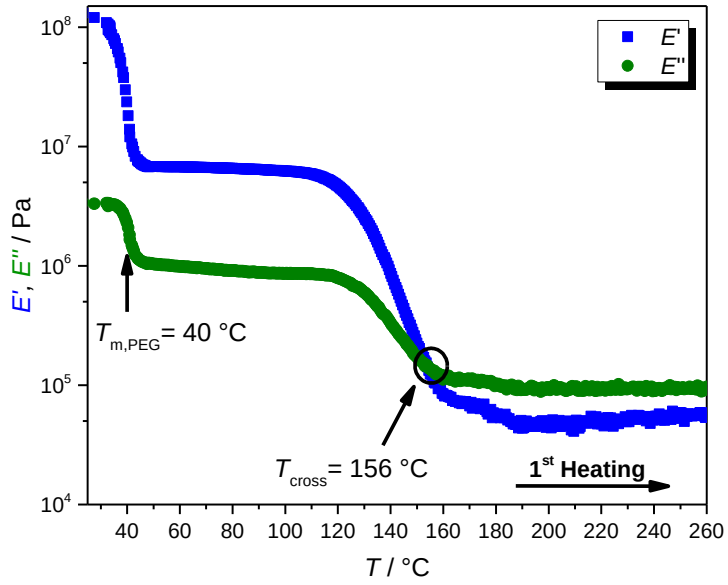


**Figure 8.5:** Dynamic mechanical thermal analysis of **6c** with 91 wt% PPG-PEG-PPG segments and 9 wt% hexamethylene bisurea segments using tension geometry experiment (heating rate: 2 K $min^{-1}$, frequency: 1 Hz). The transition at 41 °C describes the melting of the PEG units and the transition from elastic to viscous behavior ($T_{cross}$) occurs at 156 °C.

Attachment 6: DMTA tension geometry method of **6c-1**

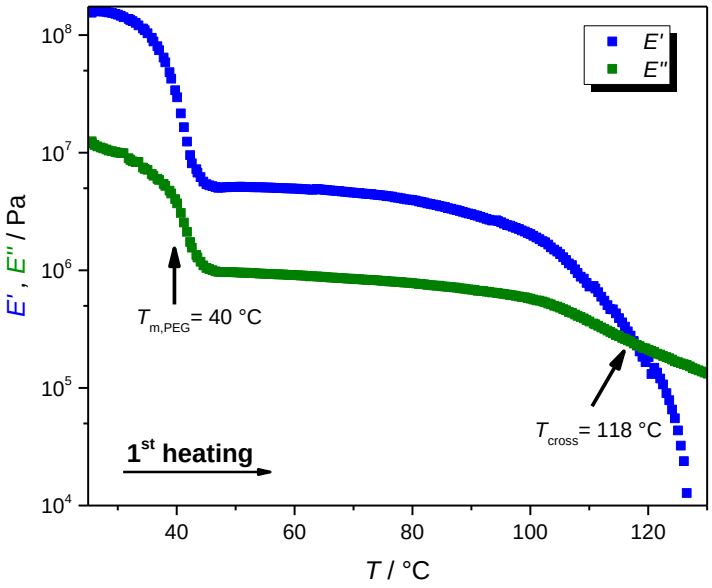


**Figure 8.6:** Dynamic mechanical thermal analysis of **6c-1** with 91 wt% PPG-PEG-PPG segments and 9 wt% hexamethylene bisurea segments using tension geometry experiment (heating rate: 2 K $min^{-1}$, frequency: 1 Hz). The transition at 40 °C describes the melting of the PEG units and the transition from elastic to viscous behavior ($T_{cross}$) occurs at 118 °C.

**(Eidesstattliche) Versicherungen und Erklärungen**

(§ 9 Satz 2 Nr. 3 PromO BayNAT)

*Hiermit versichere ich eidesstattlich, dass ich die Arbeit selbstständig verfasst und keine anderen als die von mir angegebenen Quellen und Hilfsmittel benutzt habe (vgl. Art. 97 Abs. 1 Satz 8 BayHIG).*

(§ 9 Satz 2 Nr. 3 PromO BayNAT)

*Hiermit erkläre ich, dass ich die Dissertation nicht bereits zur Erlangung eines akademischen Grades eingereicht habe und dass ich nicht bereits diese oder eine gleichartige Doktorprüfung endgültig nicht bestanden habe.*

(§ 9 Satz 2 Nr. 4 PromO BayNAT)

*Hiermit erkläre ich, dass ich Hilfe von gewerblichen Promotionsberatern bzw. -vermittlern oder ähnlichen Dienstleistern weder bisher in Anspruch genommen habe noch künftig in Anspruch nehmen werde.*

(§ 9 Satz 2 Nr. 7 PromO BayNAT)

*Hiermit erkläre ich mein Einverständnis, dass die elektronische Fassung meiner Dissertation unter Wahrung meiner Urheberrechte und des Datenschutzes einer gesonderten Überprüfung unterzogen werden kann.*

(§ 9 Satz 2 Nr. 8 PromO BayNAT)

*Hiermit erkläre ich mein Einverständnis, dass bei Verdacht wissenschaftlichen Fehlverhaltens Ermittlungen durch universitätsinterne Organe der wissenschaftlichen Selbstkontrolle stattfinden können.*

…….
Ort, Datum, Unterschrift